UNIVERSITY OF CALIFORNIA

Santa Barbara

N–H Hydrogen Atom Abstractions at Fe Complexes and Selective Capture and Release of Lithium Using Redox-Active Carborane Crown Ethers

A dissertation submitted in partial satisfaction of the

requirements for the degree Doctor of Philosophy

in Chemistry

by

Zongheng Wang

Committee in charge:

Professor Gabriel Ménard, Chair

Professor Trevor Hayton

Professor Mahdi Abu-Omar

Professor Armen Zakarian

September 2022

The dissertation of Zongheng Wang is approved.

_____

Trevor Hayton

_____

Mahdi Abu-Omar

_____

Armen Zakarian

_____

Gabriel Ménard, Committee Chair

August 2022

N–H Hydrogen Atom Abstractions at Fe Complexes and Selective Capture and Release of Lithium Using Redox-Active Carborane Crown Ethers

ACKNOWLEDGEMENTS

First, I would like to thank my supervisor Professor Gabriel Menard. Gab, thank you for letting me join the group and I learned so much from during my PhD study. Thank you for guiding me when I am lost in research and gave me all the freedom to follow my own research directions. Your tips on presentation were very helpful and I have become much more confident and comfortable when I give a talk. I am really appreciating all the funding you provided for me, so I didn't have to teach last two and half years and have a better work-time balance. Thank you for being patient with me.

Next, I would like to thank my past and current group members for help me adjust in grad school when I was just fresh out of undergrad and did not have a clue on what was going on. I really appreciate you guys being very patient with me, especially Dr. Jiaxiang Chu and Dr. Camden Hunt for guiding me through my first research project back then. I also enjoyed some late-night working with Dr. Sam Jacob and Dr. Anthony Wong. Later, as I understand more of the grad school and started my own research, I received so many useful advice from you guys and applied to my work. Your advice and feedbacks from practice talk also helped a lot on my research and getting better at presenting. As I became more senior member of the group, I also got chances to gain some mentorship experience from guiding new group members. Outside the lab, I was really enjoying all group social activities that helped me felt more relaxed. I am glad I get to know all your guys better, thank you!

I would also like to thank all the people I have made friends with in Santa Barbara. Socialization can be challenging for an international PhD student like me but knowing and hanging out with your guys have made my life in UCSB much more interesting. I got a nice

crew to play basketball with and participated the intramural league. Thanks to my friend and lab mate Dr. Sam Jacob, I also discovered my passion in playing volleyball and met more people in SB. I also started a team in one of the UCSB intramural volleyball leagues and won the tile (still mad that we could not get T-shirt prize)! I also had great times to play bowling, pool and tennis with many incredible friends. Other than sports, thank you for inviting me to many social activities that enriched my life outside of work. I also appreciate my friends from my home country China for many Mahjong and Karaoke nights, which helped me experience some of my lifestyle back home. I got to experience many cool events in SB because of my friends, thank you!

I would also like to thank my friends form undergrad, especially the 'CSF' crew of Luke, Lee, Maddy, Noreen and Lindy. We had a lot of fun in college from taking classes to hanging out! Although after undergrad we scattered across the country, we keep in touch and had some fun online activity. I really liked those times when we had the chance to gather in person!

Finally, I would like to thank my family back in China. Thank you for all the support for me to pursue my career in PhD study. Your life advice was incredibly valuable to me. Last couple years were hard for international travel and hopefully it will get easier for visiting!

Zongheng Wang

515-817-3991 | zongheng@ucsb.edu | linkedin.com/in/wang-zongheng-a38625206

EDUCATION

Ph.D. Inorganic Chemistry, *University of California, Santa Barbara*
Expected August 2022
Research advisor: Professor Gabriel Ménard
Award: 2021 Outstanding Service to the Department

B.S Chemistry, Minor in Mathematics, *Iowa State University*
Aug 2013 – May 2017
Research advisor: Professor Levi Stanley, Professor William Jenks
Award: 2016 Hudson Research Stipend

SKILLS

Technical

- Air free technique (Glove Box and Schlenk Line)
- Purification/separation techniques
- Cyclic Voltammetry
- Single-crystal X-ray Diffraction
- Mössbauer spectroscopy
- 1H, heteronuclear (^{7}Li/^{11}B/^{13}C/^{14}N/ ^{31}P/^{19}F/^{23}Na/^{39}K) and 2D NMR Spectroscopy
- GCMS, ESI and MALDI
- ICP-OES
- Organic and inorganic synthesis
- Thermogravimetric analysis
- Column Chromatography
- UV-Visible Spectroscopy
- FTIR Spectroscopy

Additional

- *Research website:* Scifinder, Reaxys, Mendeley
- *Data analysis software:* Chemdraw, MestReNova, Olex, Origin, Xshell, Mercury, Nova, MS office
- *Language:* Chinese (Native) and English (bilingual)

RESEARCH EXPERIENCE

Graduate Student Researcher, UCSB Sept 2017 – Present

- Designed and synthesize a series of novel redox-active carborane crown complexes for selective Lithium capture/release electrochemically for lithium recycle from seawater, patent pending in progress
- Applied synthesized carborane crown complexes with larger crown size for selective Cesium and Strontium capture/release electrochemically for nuclear waste treatment
- Utilized synthesized metal phthalocyanines on homogenous catalytic ammonia oxidation to N_2 and alkylamine N–H/C–H activation for fuel cell applications, collaborated with PNNL for DFT mechanistic calculation
- Synthesize and explore reactivity on bridging Iron phthalocyanine nitride for the development of flow batteries
- Research resulted in 2 publications, 3 conference presentations and funding from Mitsubishi Chemical Company with monthly project updates and quarterly oral presentation

- Maintain laboratory equipment (e.g., glove boxes and Mössbauer spectrometer) and train new users on protocols
- Design and manage projects through literature search, experiments, data analysis and communication

Iowa State University, Undergraduate Student Researcher Sept 2014 – May 2017

- Synthesized and studied several Metal-organic frameworks for their application on heterogeneous catalysis
- Investigated catalysts for Palladium catalyzed hydroheteroarylation and Cobalt-catalyzed hydroacylation
- Studied the radical polarizing agents for Dynamic Nuclear polarization NMR

LEADERSHIP EXPERIENCE

Liaison, Chemistry Professional Development (ChemPD), Organization, UCSB
Sept 2020 – Present

- Shared professional development opportunities and helped coordinate a virtual Career Day for graduate students.

Mentor, Tutor, & Teaching Assistant, UCSB & ISU
Sept 2017 – Sept 2021

- Taught 100+ student undergraduate chemistry courses involving intro to chemistry, general chemistry, organic chemistry, and advanced physical chemistry, helping students understand difficult concepts

Graduate Mentor, UCSB
Sept 2019 – present

- Mentored new graduate and undergraduate students to learn how to effectively conduct experiments safely, characterize and analyze results, and present their findings
    - Undergraduate mentee attended New York University for Chemistry PhD in Fall 2021
    - Designed metal capture projects for new graduate students

PUBLICATIONS

- **Wang, Z**.; Johnson, S. I.; Wu, G.; Ménard, G. Multiple N–H and C–H Hydrogen Atom Abstractions Through Coordination-Induced Bond Weakening at Fe-Amine Complexes. *Inorg. Chem*. **2021**, 60 (11), 8242–8251.
- **Wang, Z**.; Wu, G.; G.; Ménard. Selective lithium capture and release with redox switchable ortho-carborane based crown ether. *Manuscript in progress*.
- **Wang, Z**.; Heinrich, S.; Sepunaru, L.; Ménard, G. Selective Electrochemical Capture and Release of Lithium from Seawater. *Patent pending in progress*.
- Peterson, M.; Hunt, C.; **Wang, Z**.; Heinrich, S. E.; Wu, G.; Ménard, G. Synthesis, Characterization and Electrochemical Properties of a First-Row Metal Phthalocyanine Series. *Dalt. Trans*. **2020**, 49 (45), 16268–16277.

PRESENTATIONS

- **Wang, Z**.; Johnson, S. I.; Wu, G.; Ménard, G. "Multiple N–H and C–H Hydrogen Atom Abstractions Through Coordination-Induced Bond Weakening at Fe-Amine Complexes" *Talk presentation.* UC Chemical Symposium, online, March 2021

- Heinrich, S.; Mattejat, M.; **Wang, Z**.; Ménard, G. “Selective Electrochemical Capture and Release of Uranyl in Solution” *Poster presentation.* DOE Science Program Meeting, August 2021
- **Wang, Z**.; Johnson, S. I.; Wu, G.; Ménard, G. “Multiple N–H and C–H Hydrogen Atom Abstractions Through Coordination-Induced Bond Weakening at Fe-Amine Complexes” *Poster presentation.* Pacifichem December 2021.

ABSTRACT

N–H Hydrogen Atom Abstractions at Fe Complexes and Selective Capture and Release of Lithium Using Redox-Active Carborane Crown Ethers

by

Zongheng Wang

For the first part of this dissertation, we wanted to study new abundant-metal homogeneous ammonia oxidation catalysts in order to gain important mechanistic understandings of these molecular-level transformations. Our catalyst of choice was an Fe-phthalocyanine complex, PcFe (Pc = 1,4,8,11,15,18,22,25-octaethoxy-phthalocyanine), which we synthesized and with which we subsequently generated PcFe−amine complexes with ammonia and related alkylamines. Treatment of PcFe with an excess hydrogen atom abstractor, 2,4,6-tri-*tert*-butylphenoxyl radical (^{tBu}ArO•), in the presence of NH_3 resulted in catalytic H atom abstraction (HAA) and C−N coupling to produce 4-amino-2,4,6-tritert-butylcyclohexa-2,5-dien-1-one and ^{tBu}ArOH. Exposing FePc to an excess of the trityl (CPh_3) variant, 2,6-di-*tert*-butyl-4-tritylphenoxyl radical (^{Tr}ArO•), and NH_3 did not lead to catalytic ammonia oxidation as similarly reported in a related Ru-porphyrin complex. However, pronounced coordination-induced bond weakening of both α N−H and β C−H in the PcFe-alkylamine congeners, led to multiple HAA events in the presence of ^{tBu}ArO•, yielding a cyanide or an imine complex depending on which alkylamine was used. Detailed computational studies were also performed to elucidate the mechanisms involved in these transformations.

For the second half of this dissertation, we explored the selective, electrochemical capture and release of Li^+ from seawater using redox-switchable substituted *ortho*-carboranes (Cb). Reduction of the neutral "*closo*-Cb" to the 2 e^- reduced "*nido*-Cb" resulted in C–C bond cleavage and subsequent cage opening, increasing the bite angle of the Cb-appended donor groups. This structural change can be reversed by oxidation of *nido*-Cb back to *closo*-Cb. To capture Li^+ ions, we synthesized and fully characterized a series of Cb-substituted crown ether compounds, which are known to have high affinity and selectivity to Li^+. Li^+ binding affinity and selectivity was monitored via ^1H, ^7Li, ^{23}Na NMR spectroscopy, as well as with cyclic voltammetry. These measurements point to significant observed selectivity for Li^+ vs. other alkali metals in the *nido*-Cb form as described in this thesis. Furthermore, we also extended our studies to group 2 metals, specifically cesium and strontium capture/release, for nuclear waste treatment purposes using larger Cb-crown species. These preliminary results are also presented herein.

TABLE OF CONTENTS

ACKNOWLEDGEMENTS iv

Zongheng Wang vi

ABSTRACT ix

LIST OF FIGURES xv

LIST OF SCHEMES xxiii

LIST OF TABLES xxv

Chapter 1 1

1.1 Renewable energy storage 2

1.1.1 Renewable energy storage chemical vector 2

1.1.2 Storing energy in ammonia 3

1.1.3 Ammonia fuel cells 3

1.2 Lithium capture 5

1.2.1 Lithium demand and production 5

1.2.2 Lithium in seawater 6

1.2.3 Crown ethers 7

1.3 Carboranes 8

1.3.1 Carborane cluster 8

1.3.2 Redox active *ortho*-carborane 10

1.3.3 Electronic properties of substituted Cb 11

1.4 Scope of thesis 12

1.5 References 14

Chapter 2 22

2.1 Introduction 23

2.2 Results and Discussion 25

2.2.1 Synthesis and Characterization of ^{EtO}PcFe 25

2.2.2 Synthesis and Characterization of PcFe-Amine Precursors..... 27

2.2.2 N–H HAA at PcFe-NH_3..... 30

2.2.3 N–H and C–H HAA at PcFe-Alkylamines 35

2.2.4 Mechanistic Studies using DFT 41

2.3 Summary 44

2.4 Experimental 45

2.5 Appendix 53

2.6 References 56

Chapter 3 67

3.1 Introduction 68

3.2 Results and Discussion 69

3.2.1 Synthesis and characterization of *closo*- and *nido*- Cb 14-crown-4..... 69

3.2.2 Reactivity of *nido*- Cb 14-crown-4 74

3.2.3 Synthesis and characterization of Di-Carborane 14-crown-4 analog 80

3.2.4 Synthesis, characterization and reactivity of *nido*-Di-Carborane 14-crown-4 83

3.2.5 Synthesis and characterization of other Cb crown ethers 86

3.2.6 Carbon-spaced Cb-crown compounds 91

3.2.7 Phenyl phosphine oxide -PhPO- spacer 99

3.3 Summary 105

3.4 Experimental 106

3.5 Appendex 116

3.6 Reference 118

Chapter 4 122

4.1 Introduction 123

4.2 Results and Discussion 124

4.2.1 Li^+ measurements with 1 124

4.2.2 Li^+ capture studies with 1-*nido*-K using NMR spectroscopic measurements 131

4.2.3 Li^+ selectivity studies with 1-*nido*-K using NMR spectroscopic measurements 135

4.2.4 Electrochemical measurements on *nido*-form of 1 in DMF 137

4.2.4 NMR spectroscopic measurements on *nido*-form of 1 in DMF143

4.2.5 Other lithium interaction with *nido*-form of 1 146

4.2.6 Li^+ measurements on *closo*- and *nido*-system of 2 150

4.2.7 Li^+ measurements on other Cb crown ether 4, 5 and 8 155

4.3 Summary 158

4.4 Experimental 159

4.5 Appendix 163

4.6 Reference 163

Chapter 5 169

5.1 Introduction 170

5.2 Preliminary results and discussion 171

5.2.1. Attempt Cs capture with Cb crown ethers 171

5.2.2. Group 2 metal interaction with *nido*-Cb crown ethers..... 173

5.3 Summary and future work 176

5.4 Experimental 176

5.5 Reference 178

LIST OF FIGURES

Figure 1.1. Depiction of an AMFC 4

Figure 1.2. a) Examples of carborane clusters with different numbers of vertices. b) 12 vertices carborane clusters with different location and number of carbon atoms..... 9

Figure 1.3. (left) *closo*-*ortho*-carborane (Cb), 1,2-$C_2B_{10}H_{12}$ (12 vertices). (middle) *nido*-$C_2B_9H_{12}^-$ (11 vertices). (right) *arachno*-$C_2B_8H_{12}^{2-}$ (10 vertices). 10

Figure 1.4. Capture and release of metal cation using Cb with selective donors (L). 11

Figure 1.5. Iodine substitution on the Cb cage shifts the reduction potential..... 12

Figure 2.1. a) Various reported examples of α, β or γ E–H CIBW at metal complexes..... 24

Figure 2.2. Solid-state molecular structures of **2.1.** Ethoxy groups, co-crystallized solvent molecules, and all H atoms, except N–H, have been omitted for clarity. C, black; N, blue; O, red; Fe, yellow..... 26

Figure 2.3. a) Solid-state molecular structures of **2.1-$(NH_3)_2$, 2.1-$(MeNH_2)_2$,** and **2.1-$(Me_2NH)_2$**. Ethoxy groups, co-crystallized solvent molecules, and all H atoms, except N–H, have been omitted for clarity. Fe, orange; N, blue; C, black; H, gray. b) Zero-field ^{57}Fe Mössbauer spectra (90 K) of the corresponding complexes with isomer shift (δ) and quadrupole splitting ($|\Delta E_Q|$) values indicated. c) Partial ^{1}H NMR spectra of the corresponding complexes highlighting the strongly shielded amine N–H and C–H resonances. 29

Figure 2.4. GC of headspace sample taken from the catalytic C–N coupling of $^{t\text{Bu}}$ArO• with $^{15}NH_3$ and **2.1** (experimental details are found in the manuscript). a) GC trace, b) MS at retention time of 1.54 mins displaying no $^{15}N_2$ (m/z = 30)..... 31

Figure 2.5. (top) Synthesis of **2.1-OAr^{tBu}**. (bottom) Solid-state molecular structure of **2.1-OAr^{tBu}**..... 33

Figure 2.6. ^{57}Fe Mössbauer spectrum of **2.1-OAr^{tBu}** taken at 90 K 34

Figure 2.7. ^{1}H NMR (600 MHz) spectrum of **2.1-OAr^{tBu}** in C_6D_6. Integrated peaks are from this paramagnetic product. 34

Figure 2.8. Solid-state molecular structure of **2.1-(MeN=CH$_2$)$_2$**. Ethoxy groups, co-crystallized solvent molecules, and all H atoms, except imine N–H and C–H, have been omitted for clarity. Selected bond lengths: Fe1–N1 2.006(5) Å, N1–C1 1.324(9) Å, N1–C2 1.395(8) Å. 37

Figure 2.9. Solid-state molecular structure of **2.1-(MeNH$_2$)(CN)**. Ethoxy groups, co-crystallized solvent molecules, and all H atoms, except amine N–H and C–H, have been omitted for clarity. Selected bond lengths and angles: Fe1–C1 1.962(6) Å, C1–N1 1.155(7) Å, Fe1–N2 2.060(5) Å, Fe1–C1–N1 173.8(5)°..... 40

Figure 2.10. DFT-calculated free energy values (kcal/mol) in benzene for the conversions of **2.1-(NH$_3$)$_2$** (a), and **2.1-(MeNH$_2$)$_2$** (b). BDFEs are in red and ΔG values are in blue. All free energy values are calculated relative to the $^{t\text{Bu}}$ArO•/$^{t\text{Bu}}$ArOH BDFE in benzene (76.7 kcal/mol).[9] The most thermodynamically favorable pathways follow the green arrows..... 42

Figure 3.1. Depiction of the biphasic electrochemical selective capture and release of UO_2^{2+} 68

Figure 3.2. ^{11}B NMR (128 MHz) spectrum of **1-b** in $CDCl_3$..... 71

Figure 3.3. The cyclic voltammogram of **1** in THF at various scan rate. (Glassy carbon – WE, Pt wire – CE, Ag– RE) 72

Figure 3.4. ^{1}H (top, 400 MHz) and ^{11}B (bottom, 128 MHz) NMR spectra of **1-*nido*-K** after heating at 60°C for 3 hours. **1-*nido*-K** and **1-*nido*-b** labeled with blue and red dots, respectively 75

Figure 3.5. a) ^{1}H NMR spectra of **1-*nido*-b** from [NBu_4][PF_6] reaction in 400Hz and 600 Hz in selected range. Crown ether peaks were labeled with blue and red dots. b) Proposed rearrangement of *nido*-Cb 76

Figure 3.6. ^{11}B NMR (128 MHz) spectrum of **1-*nido*-K** with HBArF before and after LiHMDS with **1-*nido*-b** peaks labeled y blue dots 77

Figure 3.7. a) ^{1}H NMR spectra (400 MHz) of **1-*nido*-K** with 0, 1 and 2 equivs of kryptofix-222 and free kryptofix-222 at r.t. Crown ether peaks are labeled with dots. b) ^{11}B NMR (128 MHz) spectra of **1-*nido*-K** with 0, 1 and 2 equivs of kryptofix-222 at r.t. 78

Figure 3.8 a) ^{1}H NMR (400 MHz) spectra of **1-*nido*-K** with 2 equiv of kryptofix-222, 18-crown-6 and [NEt_4][Br] to form **1-*nido*-c** at r.t. **1-*nido*-K and 1-*nido*-c** peaks are labeled with red and blue dots, respectively. b) ^{11}B NMR (128 MHz) spectra of the same reactions. c) Proposed chemical structure of **1-*nido*-c** with different counter cation 80

Figure 3.9. Solid state structure of 3-b (low-resolution structure) 82

Figure 3.10. The cyclic voltammogram of **2** in THF at various scan rate. (Glassy carbon – WE, Pt wire – CE, Ag wire – RE) 83

Figure 3.11 ^{1}H NMR (400 MHz) spectrum of **2-*nido*-K** in MeCN-d_3**.** Crown ether peak are labeled with blue dots 84

Figure 3.12 ^{11}H (400 MHz) and ^{11}B NMR (128 MHz) spectra of **2-*nido*** with 2 equiv of [NEt_4][Br] at r.t. Crown ether peaks are labeled with dots. 85

Figure 3.13. Stacked ^{1}H (400 MHz) and ^{11}B (128 MHz) NMR spectra of **2-*nido*-K** before and after addition of 18-crown-6. Crown ether peak labeled in blue dots..... 86

Figure 3.14. Solid-state molecular structure of **3-b.** All H atoms have been omitted for clarity. B, pink; C, black; O, red; K purple..... 88

Figure 3.15. The cyclic voltammogram of **3** in THF at various scan rate. (Glassy carbon – WE, Pt wire – CE, Ag wire– RE) 88

Figure 3.16. Stacked a) ^{1}H (400 MHz) and b) ^{11}B NMR (128 MHz) spectra of **3** (top) and **3-*nido*-K** (bottom) in MeCN-d_3. Crown ether peaks are labeled with dots..... 90

Figure 3.17. The cyclic voltammogram of **5** in THF at various scan rate. (Glassy carbon – WE, Pt wire – CE, Ag wire– RE) 93

Figure 3.18. Solid-state molecular structure of **6-b** (low resolution)..... 95

Figure 3.19. The cyclic voltammogram of **6** in THF at various scan rate with presence of Fc. (Glassy carbon – WE, Pt wire – CE, Ag wire– RE) 96

Figure 3.20. The cyclic voltammogram of **7** in THF at 100 mV/s scan rate 97

Figure 3.21. The cyclic voltammogram of **8** in THF at various scan rate with presence of Fc. (Glassy carbon – WE, Pt wire – CE, Ag wire – RE) 99

Figure 3.22. ^{31}P NMR (162 MHz) spectra of reactions described in **Scheme 3.14** and **Scheme 3.15** 103

Figure 3.23. ^{1}H (400 MHz) and ^{11}B (128 MHz) NMR spectra of **3-b** and small contamination of **3** 116

Figure 3.24. ^{11}B NMR (128 MHz) spectra of **8** before and after add potassium naphthalenide 117

Figure 3.25. ^{31}P NMR (162 MHz) spectra of crude mixture from reactions described in **Scheme 3.17** 117

Figure 4.1 Depiction of NMR tube and insert for NMR measurement of Li^+ affinity of **1**. 125

Figure 4.2. Stacked ^{7}Li NMR (155 MHz) spectra of 0.006 M LiTFAB after mixing with different equivalent of **1** or 1 equiv 12-crown-4 in MeCN-d_3 with LiCl in D_2O as external standard 126

Figure 4.3. Stack ^{1}H NMR (400 MHz) and ^{7}Li NMR (155 MHz) spectra of 0.03 M **1** after mixing different equivalent of LiTFAB in MeCN-d_3 with LiTFAB in MeCN-d_3 as external standard. Compound **1** peaks are labeled with dots 128

Figure 4.4. ^{7}Li (155 MHz) and ^{23}Na (106 MHz) NMR spectroscopic measurement of mixing 1 equiv **1** with Li, Na and KTFAB at variable temperature..... 130

Figure 4.5. Solid-state molecular structure of **1-b-Li**. All except counter cation H atoms have been omitted for clarity. Li, pink purple; B, pink; C, black; O, red..... 130

Figure 4.6. ^{7}Li NMR (155 MHz) spectra of **1-*nido*-K** with different equivs of LiTFAB in MeCN-d_3 at r.t..... 132

Figure 4.7. ^{11}B NMR (128 MHz) spectra of **1-*nido*-K** with LiTFAB, LiCl and $LiPF_6$ at r.t. **1-*nido*-b** is labeled with blue dots..... 133

Figure 4.8. Stack ^{7}Li NMR (155 MHz) spectra of $LiPF_6$ with different equivs of **1-*nido*-K** at r.t. 134

Figure 4.9. ^{7}Li NMR (155 MHz) spectra of $LiPF_6$ with 1 equiv of **1-*nido*-K** at -38.5 °C and r.t. 135

Figure 4.10. a) ^{7}Li (155 MHz) and ^{23}Na NMR (106 MHz) spectra of $LiPF_6$ and $NaPF_6$ with 1 equivs of synthesized 14-crown-4 and 18-crown-6 at r.t. b) ^{7}Li (155 MHz) and ^{23}Na

(106 MHz) NMR spectra of 1:1 ratio of $LiPF_6$:$NaPF_6$ with different equiv of added **1-*nido*-K** at r.t. 137

Figure 4.11. a) Cyclic voltammogram of **1** with varying equivalents of $LiPF_6$. b) Cyclic voltammogram of **1** with varying equivalents of $NaPF_6$. c) Cyclic voltammogram of **1** with varying equivalents of KPF_6. 139

Figure 4.12. CV of 1 with 2 equivalents of $LiPF_6$, $NaPF_6$, or KPF_6 in DMF. 140

Figure 4.13. unlocked ^{11}B NMR spectrum of reaction solution after bulk electrolysis (top). **1-*nido*** and **1-*nido*-b** peaks labeled with blue and red dots, respectively. DPV of 0.003 M **1-*nido*** with 2 equivalents of $LiPF_6$, $NaPF_6$, KPF_6 or mixed metal in DMF with 0.1 M $[NBu_4][PF_6]$ (bottom)..... 142

Figure 4.14. Cyclic voltammograms in DMF with 0.1M $[NBu_4][PF_6]$ and 2.9mM of **1** at a 50mV/s scan rate for consistency test. 143

Figure 4.15. a) ^7Li NMR (155 MHz) spectra of $LiPF_6$ with aliquot DMF followed by 12-crown-4 in MeCN-d_3. b) Unlocked ^7Li NMR (155 MHz) spectra of $LiPF_6$ with different equiv of **1-*nido*-K** in DMF at r.t. followed by addition of $FcPF_6$ (LiTFAB peak ignored for clarity). c) unlocked ^{11}B NMR (128 MHz) spectra of the **1-*nido*-K** with $LiPF_6$ before and after $FcPF_6$..... 145

Figure 4.16. ^1H (400MHz), ^{11}B (128 MHz) and ^7Li (155 MHz) NMR spectra of **1-*nido*-K** with LiHMDS stacked ^{11}B NMR spectrum of **1-*nido*-K** and ^7Li NMR spectrum of LiHMDS 147

Figure 4.17. ^1H (400MHz), ^{11}B (128 MHz) and ^7Li (155 MHz) NMR spectra of **1-*nido*-Li** stacked with ^1H and ^{11}B NMR spectra of **1-*nido*-K.** Compounds peaks are labeled with blue and red dots. 148

Figure 4.18. ^{7}Li NMR (155 MHz) spectra of **1-*nido*-Li** before and after addition of $FcPF_6$ at r.t. and -38°C in d-THF 149

Figure 4.19. ^{7}Li NMR (155 MHz) spectra of **2** with different equivs of LiTFAB at r.t. 151

Figure 4.20. ^{7}Li NMR (155 MHz) spectra of **2-*nido*-K** with different equivalents of LiTFAB at r.t. 152

Figure 4.21. The cyclic voltammogram of **2** with different equivalent of $LiPF_6$ in THF at 100 mV/s scan rate. (Glassy carbon – WE, Pt wire – CE, Ag wire– RE) 153

Figure 4.22. ^{1}H (400 MHz), ^{11}B (128 MHz) and ^{7}Li NMR (155 MHz) spectra of **2-*nido*-Li** stacked with NMR spectra of **2-*nido*-K** (labeled with blue dots). Note: proton resonances in **2-*nido*-Li** are broad 155

Figure 4.23. ^{7}Li NMR (155 MHz) spectra of 4 with different equivs of LiTFAB at r.t. 156

Figure 4.24. The cyclic voltammogram of **5** before and after addition of $LiPF_6$ in THF at 100 mV/s scan rate. (Glassy carbon – WE, Pt wire – CE, Ag wire– RE) 157

Figure 4.25. The cyclic voltammogram of **8** before and after addition of $LiPF_6$ in THF at 100 mV/s scan rate. (Glassy carbon – WE, Pt wire – CE, Ag wire– RE) 158

Figure 4.26. Bulk electrolysis set for electrochemical reduction of **1** 163

Figure 5.1. Calixarene attached crown ether Cs Selective Chelators (left). Solid-state structure of **1-*nido*-K** (right) 171

Figure 5.2. ^{1}H NMR (400 MHz) spectra of **3** before and after addition of $CsNO_3$ 172

Figure 5.3. The cyclic voltammogram of **6** before and after addition of $CsNO_3$ in THF at 100 mV/s scan rate 173

Figure 5.4. ^{1}H (400 MHz) and ^{11}B (128 MHz) NMR spectra of **2-*nido*-K** with group 2 triflate. **2-*nido*-K** peak labeled with blue dots and new compound **2-d** labeled with red dots. Mixture generated with $Ba(OTf)_2$ labeled with orange dots 175

LIST OF SCHEMES

Scheme 1.1 Examples of crown ethers 7

Scheme 2.1. Reaction of with **2.1-(Me_2NH)$_2$** 1.25 equiv of $^{t\text{Bu}}$ArO• 36

Scheme 2.2. Addition of 2.6 equiv of PMe_3 to **2.1-(MeN=CH_2)$_2$** 38

Scheme 2.3. Proposed hyperconjugative interactions scheme led to the formation of **1-(MeN=CH_2)(Me_2NH)** 39

Scheme 3.1. Synthesis of Cb 14-crown-4 (**1**) and its solid-state molecular structure (bottom) 71

Scheme 3.2. Reduction of **1** to **1-*nido*-K** using potassium naphthalenide in THF and its solid-state molecular structure (bottom). Cocrystallized solvent molecules, all H atoms and the second K^+ have been omitted for clarity. 73

Scheme 3.3. Two step synthesis of Di-carborane 14-crown-4 (**2**) from $Cb(OH)_2$ and **2-b** 81

Scheme 3.4. Reaction of deprotonated $Cb(OK)_2$ with 1 equiv dibromopropane 82

Scheme 3.5. Reduction of **2** to the **2-*nido*-K** using potassium naphthalenide in THF 84

Scheme 3.6. Synthesis of Cb 18-crown-6 (**3**) and its solid-state molecular structure (bottom). All H atoms have been omitted for clarity. 87

Scheme 3.7. Reduction of **3** to the **3-*nido*-K** using potassium naphthalenide in THF 89

Scheme 3.8. Synthesis of **4** and its solid-state molecular structure (bottom). All H atoms have been omitted for clarity. Si, yellow; O, red; B, pink; C, black 91

Scheme 3.9. Synthesis of **5** and its solid-state molecular structure (bottom). All H atoms have been omitted for clarity 92

Scheme 3.10. Synthesis of **6** from Cb $(CH_2OH)_2$ 94

Scheme 3.11. Synthesis of **7** from Cb $(CH_2OH)_2$ 97

Scheme 3.12. Synthesis of **8** from Cb $(CH_2OH)_2$ and its solid-state molecular structure (bottom). All H atoms have been omitted for clarity. Si, yellow; O, red; C, black; B, pink 99

Scheme 3.13. Synthesis of **9** from Cb and its solid-state molecular structure (right). All H atoms have been omitted for clarity..... 100

Scheme 3.14. Ongoing synthesis step to produce **10** and its proposed Li+ capture/release scheme..... 101

Scheme 3.15. Synthesis of **11** with byproduct **11-b** and other impurities..... 102

Scheme 3.16. Ongoing synthesis to produce **12**..... 104

Scheme 3.17. Synthesis of **13** with byproduct **13-b** and other impurities..... 105

LIST OF TABLES

Table 2.1 Final Free Energies (with spin state)..... 54

Chapter 1

Introduction

1.1 Renewable energy storage

1.1.1 Renewable energy storage chemical vector

In the ongoing effort to battle climate change, we must reduce the emission of carbon dioxide (CO_2) from the use of fossil fuels and one of the alternatives is to increase the use of renewable energy (RE) based on solar, wind, geothermal, and other sources. Currently, RE storage is heavily relying on pumped hydro storage (95%) and batteries (~5%); however, their capacity only account for a small portion of total RE generation.[1] The sustained growth of the RE production relies on the development of chemical and electrochemical energy storage technologies to meet the mixed demands of the electric grid and transportation sectors, which in turn depends on exploring different systems for efficient energy storage, such as chemical bonds in chemical energy vectors (H_2, MeOH, NH_3).

With energy stored in chemical bonds, chemical energy vectors can be used for long-term energy storage and can stabilize RE grid fluctuations.[2-4] Hydrogen (H_2) is a popular candidate for RE storage due to its high gravimetric energy density (141.86 MJ/Kg) and carbon-free emissions with water as the only product; however, challenges in H_2 storage and transportation limit the wider utilization of H_2 in RE storage. Compressing H_2 into tanks requires high pressure conditions (750 bar) with only 40-50% efficiency and high compression costs.[5] In addition, handling and transporting hydrogen tanks raises safety concerns, especially with possible leakage from various storage containers due to the small size and rapid diffusion of hydrogen.[6, 7] To overcome these issues, storing H_2 in the form of ammonia (NH_3) has drawn increasing attention.

1.1.2 Storing energy in ammonia

Ammonia (NH_3) is an attractive chemical energy vectors for RE storage for its zero-carbon content, high energy density and high H_2-storage capacity (17.6%/wt). NH_3 production is low-cost ($1.4-1.7/kg) and can be processed on a megaton scale due to the commercially and industrially developed Haber-Bosch process.[8] Compared to H_2, NH_3 is much easier to compress or liquify at much lower pressures (8 bar) in tanks and is much safer to transport. NH_3 storage, transportation and its global distribution infrastructure are well established industrially due to its widespread application as in fertilizers.[9] Although NH_3 can be a promising candidate for RE storage, the majority of current NH_3 production is not environmental friendly, because of the hydrogen source for the Haber-Bosch process coming from steam reform of fossil fuels, which together accounts for 1.4% of total global CO_2 emission.[10] Therefore, there is an increasing push to use RE-powered electrolytic water splitting to generate H_2, followed by N_2 reduction to produce NH_3. Direct NH_3 generation from N_2 and H_2O in a single electrochemical reactor, has also been investigated.[3, 11, 12] New pilot plants based on those carbon free NH_3 production methods have been constructed. [2, 9]

1.1.3 Ammonia fuel cells

To utilize the energy stored in NH_3, there is increasing research on the use of NH_3 powered fuels cells. Polymer electrolyte membrane fuel cells (PEMFCs) is one of the well-developed fuel cells that NH_3 can be used to fuel indirectly.[13] After initial cracking of NH_3 to N_2/H_2 at high temperatures ranging from 500-1000 °C, the generated H_2 is oxidized at the anode and O_2 is reduced at the cathode (Equations 1 and 2) to release the energy stored in the chemical bonds that are initially from ammonia.[6, 14]

$$anode\ reaction\text{: } 2H_2 \rightarrow 2H^+ + 4e^- \quad (1)$$

$$cathode\ reaction: O_2 + 4H^+ + 4e^- \rightarrow 2H_2O \quad (2)$$

On the other hand, technologies based on alkaline membrane fuel cells (AMFCs) has emerged for the direct use of NH_3. The reported AMFCs utilize KOH aqueous solution as electrolyte or molten NaOH/KOH at temperature ranges of 200-450 °C (Equations 3 and 4, **Figure 1.1**).[14-16]

$$anode\ reaction: 2NH_3 + 6OH^- \rightarrow N_2 + 6H_2O + 6e^- \quad (3)$$

$$cathode\ reaction: 1.5O_2 + 3H_2O + 6e^- \rightarrow 6OH^- \quad (4)$$

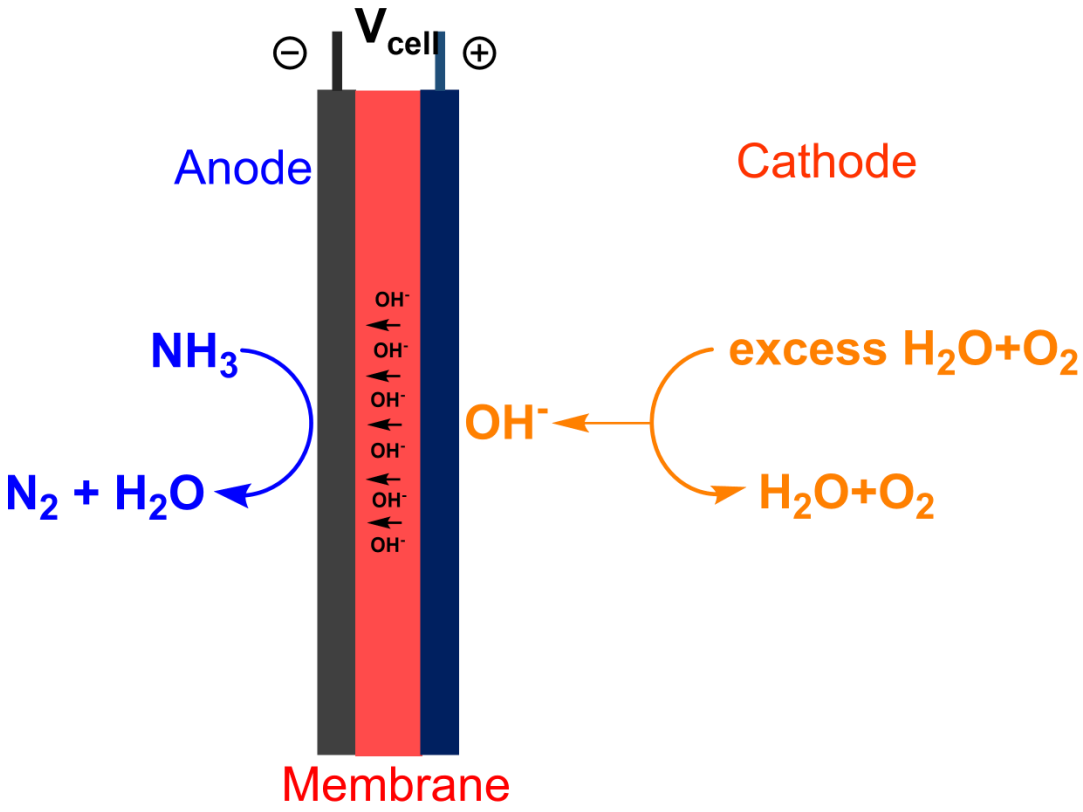

Figure 1.1. Depiction of an AMFC

Conversion of NH_3 to N_2/H_2 (for PEMFCs) or N_2/H_2O (for AMFCs) heterogeneously and electrocatalytically have been reported.[15-20] However, those catalytic NH_3 studies suffered

from significant overpotentials and low conversions, which limited the further utilization of these NH_3 fuel cells. These challenges emphasize the importance of understanding of the complex multielectron ammonia oxidation (AO) (Equations 5) reaction.

$$2NH_3 \rightarrow N_2 + 3H_2 \quad (5)$$

1.2 Lithium capture

1.2.1 Lithium demand and production

In addition to chemical energy vectors for RE storage, electrochemical RE storage technologies, such as with batteries, also underwent rapid development and deployment over the last two decades. Lithium-ion based batteries, in particular, have become the most popular commercially produced batteries and are widely applied in our daily lives (e.g., phones, laptops, electronics, etc.) and are increasingly being used for grid-scale RE storage. Therefore, lithium is increasingly considered a global strategic resource.[21] As a result, the demand for lithium has increased significantly and is projected to continue to increase in 6-9% rate annually, in turn predicted to consume one-third of the world's land-based lithium reserves in the next decade.[22, 23]

Current lithium production is land based and there are an estimated 21 million metric tons of lithium available.[24] Lithium production relies mostly on the lime-soda solar evaporation technique from Li-rich brines.[22, 24] The subsurface brine is pumped into large open evaporation ponds where it sits for 1-2 years to concentrate the lithium content under sunlight. The concentrated brine is then treated chemically to precipitate out lithium carbonate, followed by filtration and drying. This less costly method is limited to lithium rich locations such as the "Lithium Triangle" centered around Chile, Bolivia, and Argentina. Additionally, recovering

lithium from brine is time consuming, requires a lot of water, generates salt waste, and can contaminate water used for drinking and irrigation. Another industrial lithium production method involves extracting the metal from lithium-bearing mineral ores by using concentrated sulfuric acid to leach the ores, which generates environmental unfriendly acid by-products.[24, 25] With surging demand for lithium, it is expected that current production will very soon not meet projected market demands.[22] Therefore, there is a growing interest in exploring alternative lithium sources, such as from seawater.

1.2.2 Lithium in seawater

Dissolved lithium (Li^+) in seawater is at a very low concentration of 0.17 ppm; however, due to the vastness of the oceans, the total dissolved Li^+ content in seawater is estimated to be 180 billion tons, approximately 10,000× higher than the combined land-based reserves.[24, 26] This represents huge untapped resources which could be collected in an environmentally friendly manner. However, the capture of Li^+ in a selective and effective manner from seawater has been a major challenge due mainly to the high sodium ion (Na^+) concentration present which is 60,000× more concentrated than Li^+.

Seawater Li^+ capture has previously been investigated primarily using modified Mn_2O_4 or λ-Mn_2O_4 adsorbents which demonstrated high selectivity towards Li^+.[27, 28] Like the lime-soda solar evaporation technique, those Li^+ absorption process are time consuming (months) and required an acidic workup step which can lead to Mn leaching resulting in serious environmental concerns. Furthermore, extra purification for the released Li^+ concentrate is often required to remove the other co-captured metal ions from the adsorption process. For electrochemical seawater Li^+ extraction, studies showed these Mn_2O_4 and related $LiFePO_4$

adsorbents can be utilized as electrode materials, including conditions under a continuous flow of seawater.[22, 29-32] These promising electrochemical techniques drastically reduce the time required to capture Li^+ compared to commercially production methods. Nevertheless, these electrochemical techniques suffer from relatively high energy consumption, pH sensitivity, competing metal binding (e.g., Mg^{2+}) and Mn leaching,[32] indicating the need for the investigation of new electrochemical seawater lithium extraction methods, such as from seawater.

1.2.3 Crown ethers

Crown ethers are heterocyclic compounds that were first reported in the 1960s.[33] Simple crown ethers consist of a repeating unit of $–CH_2CH_2O–$, which repeats 4 times in 12-crown-4 and 6 times in 18-crown-6 (**Scheme 1.1**). More complicated crown ethers feature additional carbon atoms (e.g.,14-crown-4), different heteroatoms such as nitrogen (i.e., azo-12-crown-4) or addition of functional groups.

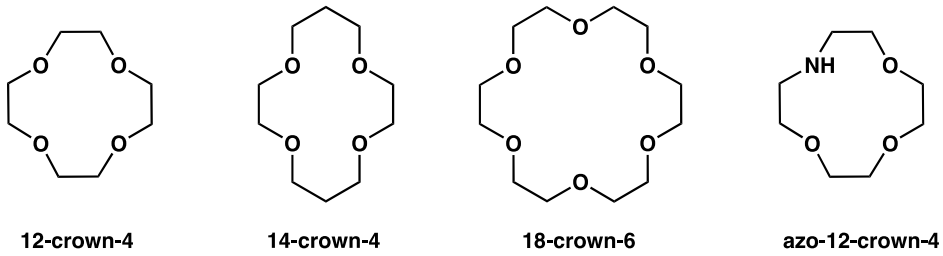

Scheme 1.1 Examples of crown ethers

Crowns ethers have been studied extensively for their ability to coordinate metal cations, especially alkali metal cations.[33] The heteroatom donors (mostly oxygen) in crown ethers provide several coordination sites for metal cation binding. In addition, by changing the size of the heterocycle, the crown ethers are capable of selectively coordinating different alkali

metal cations.[34] For example, 18-crown-6 has high selectivity for bigger cations, such as Na^+ and K^+.[33, 34] Smaller 14-crown-4 and 12-crown-4 demonstrated the highest selectivity toward Li^+, which can be used for Li^+ capture.[35-38] Adding electron-donating groups onto 14-crown-4 can further increase the Li^+ binding affinity and selectivity over Na^+.[39]

1.3 Carboranes

1.3.1 Carborane cluster

Carboranes ($C_xB_yH_z$) are polyhedral boron-carbon cluster that are stabilized by electron-delocalized σ covalent bonds. Inspired by the super stable polyhedral borane cluster $B_{12}H_{12}^{2-}$,[40] the isoelectronic analogue icosahedral carborane ($C_2B_{10}H_{12}$) was first synthesized in the 1950s and reported in 1963.[41] After more than 50 years of study, carborane chemistry has been developed and applied in the field of medicine, nanoscale engineering, catalysis, metal recovery, and so on for its unique electronic properties, geometry, and versatility.

The size of carborane clusters can vary from 5 (e.g., $C_2B_3H_5$)[42] to 14 (e.g., $C_2B_{12}H_{14}$)[43] vertices (total number of non–H atoms in cluster) resulting in structural patterns with different geometric shapes (**Figure 1.2a**). The location and number (1-5) of carbon atom in carboranes are not fixed (**Figure 1.2b**).

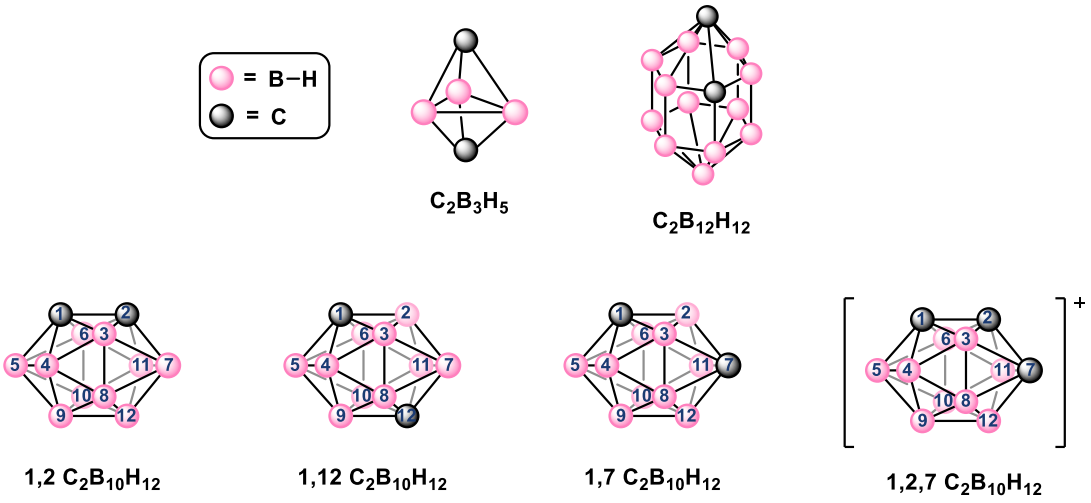

Figure 1.2. a) Examples of carborane clusters with different numbers of vertices. b) 12 vertices carborane clusters with different location and number of carbon atoms

Similar to B–H–B 3c2e (three-center, two-electron) localized electron-pair bonds, electrons in carboranes are delocalized in the skeletal boron and carbon atoms. Therefore, unlike organoboranes, the carbon atom in carborane can have at least 3 and as many as 6 neighboring atoms. The cluster geometry of carboranes is determined by the total number of skeletal electron pairs (SEP), contributed by both boron and carbon units. The prefix *closo*- refers to the carborane cage that has a closed polyhedron geometry with all faces triangular and SEP is based on number of vertices (n) under equation SEP = n+1. The prefixes *nido*-, *arachno*-, and *hypho*- designate polyhedral carborane cage (*closo*-) with one, two, or three missing vertices, respectively, which does not change the total number of SEP and electronic geometry. For example, in the *ortho*-carborane $C_2B_{10}H_{12}$ (Cb, **Figure 1.3**) case, both *nido*- and *arachno*-form with missing boron vertices still have total 13 SEP and their electronic geometry remained icosahedral.

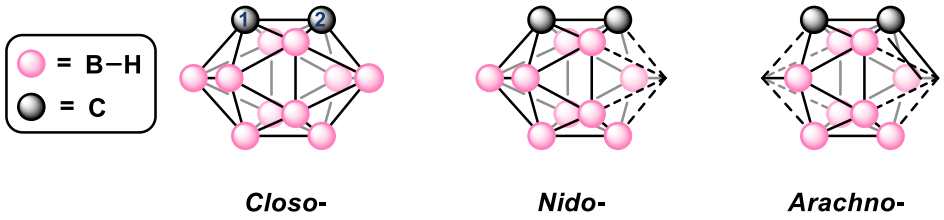

Figure 1.3. (left) *closo-ortho*-carborane (Cb), 1,2-$C_2B_{10}H_{12}$ (12 vertices). (middle) *nido*-$C_2B_9H_{12}^-$ (11 vertices). (right) *arachno*-$C_2B_8H_{12}^{2-}$ (10 vertices). Dash bonds highlight the missing vertices and are terminated by an H atom.

1.3.2 Redox active *ortho*-carborane

Among the family of carborane clusters, the *closo-ortho*-carborane (Cb), 1,2-$C_2B_{10}H_{12}$, (**Figure 1.3**, left) is of most interest to us. It was one of the first reported carboranes in the literature.[41] Like the parent borane $B_{12}H_{12}^{2-}$, the Cb consists of electron-deficient bonds and all SEP are fully delocalized in the Cb framework, resulting in 3D aromaticity and high stability. Studies have shown that the neutral Cb can undergo $2e^-$ reduction, increasing the total number of SEP to 14 and resulting in a change in the cluster geometry.[44-47] During this process, the C–C bond in Cb ruptures, leading to the cage opening to form the open *nido*-Cb ($C_2B_{10}H_{12}^{2-}$), where 12 vertices remain (different from 11 vertices *nido*-form depicted in **Figure 1.3** due to the change in number of SEP). The *nido*-Cb can be oxidized back to *closo*-Cb, highlighting its redox switchable property. Due to the electron delocalization and inductive effect, the C–H bonds in Cb can be readily substituted with different groups for various purposes. For example, donor ligands may be installed on both carbon atoms in the cluster. The ligand bite angle may then be significantly increased in the reduced *nido*-Cb relative to its neutral *closo*-form. The bigger bite angle in *nido*-Cb can be optimal for metal coordination, while the *closo*-form may have poor metal binding ability due to the smaller bite angle.[48] We previously reported the use

of such redox-switchable coordinating abilities for the electrochemical capture and release of uranyl ($M = UO_2^{2+}$) from biphasic solutions (**Figure 1.4**). [48, 49] By utilizing this redox switching function from the *closo*- to the *nido*-Cb, this system may also provide a potential pathway to achieving lithium ($M = Li^+$) capture and release from seawater.

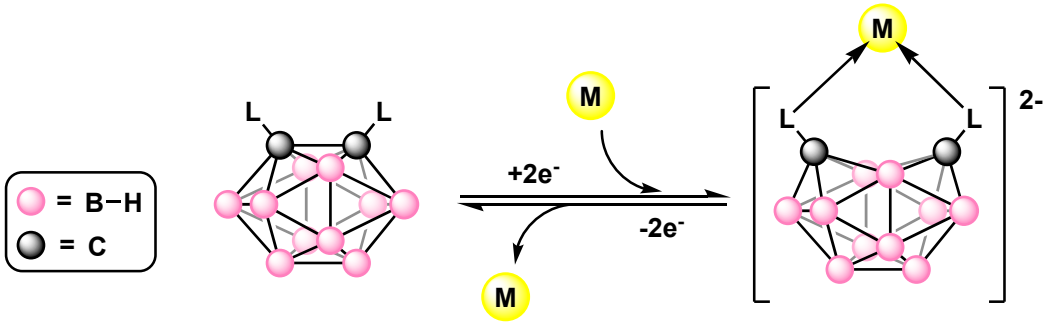

Figure 1.4. Capture and release of metal cation using Cb with selective donors (L).

1.3.3 Electronic properties of substituted Cb

Reduction of Cb is the key step to applying Cb-based chemistry for metal capture/release (**Figure 1.4**), highlighting the importance to study the electronic properties of the substituted Cb. Unsubstituted Cb has a reported reduction potential at -2.96 V vs the Fc/Fc^+ couple (Fc = ferrocene).[50] Such low reduction potential would result in instability of *nido*-Cb, especially under aqueous condition. The reduction potential of Cb can be shifted by changing the electronic nature of the substituents on boron or carbon.[46] Furthermore, these $2e^-$ reduction of substituted Cb can occur simultaneously or into two steps, depending on the stability of the mono reduced radical intermediate.[46, 51] For example, Cb with an iodine substitution on 9-position (9-I-Cb) has a more positive reduction potential at -2.53 V vs Fc/Fc^+.[50] The second iodine substitution on the 12-position (9,12-I_2-Cb) shifted the reduction potential anodically to -2.19 V (**Figure 1.5**).[50]

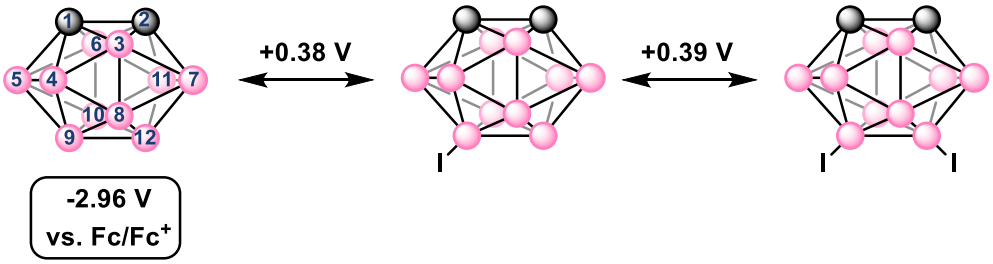

Figure 1.5. Iodine substitution on the Cb cage shifts the reduction potential(Position numbering highlighted on the left).

Similarly, adding electron-withdrawing groups, such as 4-$CF_3C_6H_4$ on both carbons resulted in a reduction potentials at -1.35 V and -1.61 V.[52] The bulkiness of the substituents is another factor that can affect the redox properties. For instance, the presence of two bulky phenyl substituents at both adjacent C atoms pushed the reduction potential to -1.51 V and -1.78V.[50] Overall, by modifying the electronic nature and bulkiness of the substituents, the redox potentials for the reduction of differently substituted Cb span a remarkable range of ~2.5 V. The redox properties of substituted Cb are also greatly affected by different solvents.[51, 52] Furthermore, the strong structural change from the C–C bond cleavage during reduction affects the electrochemical and chemical redox reversibility of the Cb, which is further dependent on the nature of the substituents.[53]

1.4 Scope of thesis

In the first half of this thesis, we sought to study homogeneous AO catalysts to provide important insights into these molecular-level transformations of NH_3 to N_2. Our investigation began with using a first-row transition metal complex, a substituted Fe-phthalocyanine (PcFe), for its simple synthesis, low cost and ability to bind NH_3. H atom abstracting reagents were

used to activate NH_3 in the presence of PcFe through coordination-induced bond weakening. To bolster the mechanistic study on ammonia oxidation, we also added related alkylamines onto PcFe and used H atom abstracting reagent on coordinated Fe-amines complexes to activate similar N–H bonds, unexpectedly cleaving adjacent C–H bond at the same time. DFT calculations were performed to correlate the experimental results and provide additional analysis to understanding this complex mechanism (Chapter 2).

We further extended our study on electrochemical RE storage by investigating a new redox-switchable system to capture and release Li^+ for lithium extraction in seawater. We utilized carborane chemistry for its unique redox behavior, which showed success for our previous work on selective Uranium capture and release. To achieve Li^+ capture and release, our approach was to attach various Li^+ selective donor group onto Cb. We synthesized and characterized a series of carbon substituted Cb featuring donor group such as crown ethers that were known for selective Li^+ binding. After studying the electrochemical properties of synthesized Cb-based compounds, we chemically reduced these substituted *closo*-Cb into *nido*-form as potential candidates for Li^+ capture (Chapter 3). With fully characterized *closo*- and *nido*- Cb crown ether compounds, we applied multiple analytical methods to investigate their Li^+ binding affinity, followed by probing Li^+ selectivity over other metal cation (Chapter 4). Next, we expanded our Cb redox-switchable scheme for other metals of interest, such as cesium, strontium and other group 2 metal. Using characterized Cb compounds, we obtained preliminary results on their interaction with these metal cations, providing important insights on future directions of metal capture and release projects (Chapter 5).

In Chapters 2-5, all compounds were prepared and characterized by the author except for Density Functional Theory (DFT) analysis by Sam Johnson at Pacific Northwest National

Laboratory. In Chapters 3, all electrochemical characterizations were performed by the author. In Chapter 4, all NMR experiments were performed by the author and the electrochemical methods were conduct by Shannon Heinrich. In Chapter 5, all NMR experiments and the electrochemical methods were performed by the author. At the time of this writing, Chapter 2 has been published. Portions of Chapter 3 and Chapter 4 are in preparation for publication.

Chapter 2: Peterson, M.; Hunt, C.; **Wang, Z**.; Heinrich, S. E.; Wu, G.; Ménard, G. Synthesis, Characterization and Electrochemical Properties of a First-Row Metal Phthalocyanine Series. Dalt. Trans. 2020, 49 (45), 16268–16277**.**

Wang, Z.; Johnson, S. I.; Wu, G.; Ménard, G. Multiple N–H and C–H Hydrogen Atom Abstractions Through Coordination-Induced Bond Weakening at Fe-Amine Complexes. *Inorganic Chemistry* **2021**, *60* (11), 8242-8251

Chapter 3: Manuscript in preparation

Chapter 4: Manuscript in preparation

Chapter 5: Preliminary investigation

1.5 References

(1) [Online], U. S. E. I. A. Most pumped storage electricity generators in the U.S. were built in the 1970s. **2019**.

(2) Service, R. F. Liquid sunshine. *Science* **2018**, *361* (6398), 120-123.

(3) Giddey, S.; Badwal, S. P. S.; Munnings, C.; Dolan, M. Ammonia as a Renewable Energy Transportation Media. *ACS Sustainable Chemistry & Engineering* **2017**, *5* (11), 10231-10239.

(4) Parkinson, G. Solar fuels could be Australia's biggest energy export. Renew Economy.

(5) Parks, G., Boyd, R., Cornish, J., and Remick, R. . Hydrogen Station Compression, Storage, and Dispensing Technical Status and Costs: Systems Integration. United States: N. p., 2014. Web. doi:10.2172/1130621.

(6) Adli, N. M.; Zhang, H.; Mukherjee, S.; Wu, G. Review—Ammonia Oxidation Electrocatalysis for Hydrogen Generation and Fuel Cells. *Journal of The Electrochemical Society* **2018**, *165* (15), J3130-J3147.

(7) Lototskyy, M. V.; Yartys, V. A.; Pollet, B. G.; Bowman, R. C. Metal hydride hydrogen compressors: A review. *International Journal of Hydrogen Energy* **2014**, *39* (11), 5818-5851.

(8) Lan, R.; Irvine, J. T. S.; Tao, S. Ammonia and related chemicals as potential indirect hydrogen storage materials. *International Journal of Hydrogen Energy* **2012**, *37* (2), 1482-1494.

(9) EA Producing ammonia and fertilizers: new opportunities from renewables. https://www.iea.org/media/news/2017/Fertilizer_manufacturing_Renewables_01102017.pdf (accessed 05/31).

(10) Capdevila-Cortada, M. Electrifying the Haber–Bosch. *Nature Catalysis* **2019**, *2* (12), 1055-1055.

(11) Giddey, S.; Badwal, S. P. S.; Kulkarni, A. Review of electrochemical ammonia production technologies and materials. *International Journal of Hydrogen Energy* **2013**, *38* (34), 14576-14594.

(12) Amar, I. A.; Lan, R.; Petit, C. T. G.; Tao, S. Solid-state electrochemical synthesis of ammonia: a review. *Journal of Solid State Electrochemistry* **2011**, *15* (9), 1845-1860.

(13) Miyaoka, H.; Miyaoka, H.; Ichikawa, T.; Ichikawa, T.; Kojima, Y. Highly purified hydrogen production from ammonia for PEM fuel cell. *International Journal of Hydrogen Energy* **2018**, *43* (31), 14486-14492.

(14) Jeerh, G.; Zhang, M.; Tao, S. Recent progress in ammonia fuel cells and their potential applications. *Journal of Materials Chemistry A* **2021**, *9* (2), 727-752, 10.1039/D0TA08810B.

(15) Lan, R.; Tao, S. Direct Ammonia Alkaline Anion-Exchange Membrane Fuel Cells. *Electrochemical and Solid-State Letters* **2010**, *13* (8), B83.

(16) Lan, R.; Tao, S. Ammonia as a Suitable Fuel for Fuel Cells. *Frontiers in Energy Research* **2014**, *2*, Mini Review.

(17) Gwak, J.; Choun, M.; Lee, J. Alkaline Ammonia Electrolysis on Electrodeposited Platinum for Controllable Hydrogen Production. *ChemSusChem* **2016**, *9* (4), 403-408, From NLM Medline.

(18) Cheddie, D. Ammonia as a Hydrogen Source for Fuel Cells: A Review. http://dx.doi.org/10.5772/47759.

(19) Suzuki, S.; Muroyama, H.; Matsui, T.; Eguchi, K. Fundamental studies on direct ammonia fuel cell employing anion exchange membrane. *Journal of Power Sources* **2012**, *208*, 257-262.

(20) Little, D. J.; Smith, I. I. I. M. R.; Hamann, T. W. Electrolysis of liquid ammonia for hydrogen generation. *Energy & Environmental Science* **2015**, *8* (9), 2775-2781, 10.1039/C5EE01840D.

(21) Dorn, F. M.; Ruiz Peyré, F. Lithium as a Strategic Resource: Geopolitics, Industrialization, and Mining in Argentina. *Journal of Latin American Geography* **2020**, *19* (4), 68-90.

(22) Battistel, A.; Palagonia, M. S.; Brogioli, D.; La Mantia, F.; Trocoli, R. Electrochemical Methods for Lithium Recovery: A Comprehensive and Critical Review. *Adv Mater* **2020**, *32* (23), e1905440, From NLM PubMed-not-MEDLINE.

(23) Martin, G.; Rentsch, L.; Höck, M.; Bertau, M. Lithium market research – global supply, future demand and price development. *Energy Storage Materials* **2017**, *6*, 171-179.

(24) Jacoby, M. Can seawater give us the lithium to meet our battery needs? https://cen.acs.org/materials/inorganic-chemistry/Can-seawater-give-us-lithium-to-meet-our-battery-needs/99/i36. **2021**, *99* (36).

(25) Thacker Pass Lithium Mine Project Final Environmental Impact Statement (Technical report). Bureau of Land Management and the U.S. Fish and Wildlife Service. 4 December 2020. DOI-BLM-NV-W010-2020-0012-EIS. Retrieved 16 March 2021.

(26) Loganathan, P.; Naidu, G.; Vigneswaran, S. Mining valuable minerals from seawater: a critical review. *Environmental Science: Water Research & Technology* **2017**, *3* (1), 37-53, 10.1039/C6EW00268D.

(27) Chitrakar, R.; Kanoh, H.; Miyai, Y.; Ooi, K. Recovery of Lithium from Seawater Using Manganese Oxide Adsorbent (H1.6Mn1.6O4) Derived from Li1.6Mn1.6O4. *Industrial & Engineering Chemistry Research* **2001**, *40* (9), 2054-2058.

(28) Nishihama, S.; Onishi, K.; Yoshizuka, K. Selective Recovery Process of Lithium from Seawater Using Integrated Ion Exchange Methods. *Solvent Extraction and Ion Exchange* **2011**, *29* (3), 421-431.

(29) Yu, J.; Fang, D.; Zhang, H.; Leong, Z. Y.; Zhang, J.; Li, X.; Yang, H. Y. Ocean Mining: A Fluidic Electrochemical Route for Lithium Extraction from Seawater. *ACS Materials Letters* **2020**, *2* (12), 1662-1668.

(30) Kanoh, H.; Ooi, K.; Miyai, Y.; Katoh, S. Electrochemical Recovery of Lithium Ions in the Aqueous Phase. *Separation Science and Technology* **1993**, *28* (1-3), 643-651.

(31) Kim, J.-S.; Lee, Y.-H.; Choi, S.; Shin, J.; Dinh, H.-C.; Choi, J. W. An Electrochemical Cell for Selective Lithium Capture from Seawater. *Environmental Science & Technology* **2015**, *49* (16), 9415-9422.

(32) Zhang, Y.; Sun, W.; Xu, R.; Wang, L.; Tang, H. Lithium extraction from water lithium resources through green electrochemical-battery approaches: A comprehensive review. *Journal of Cleaner Production* **2021**, *285*.

(33) Gokel, G. W.; Leevy, W. M.; Weber, M. E. Crown Ethers: Sensors for Ions and Molecular Scaffolds for Materials and Biological Models. *Chemical Reviews* **2004**, *104* (5), 2723-2750.

(34) Swain, B. Separation and purification of lithium by solvent extraction and supported liquid membrane, analysis of their mechanism: a review. *Journal of Chemical Technology and Biotechnology* **2016**, *91* (10), 2549-2562.

(35) Tian, Y.; Chen, W.; Zhao, Z.; Xu, L.; Tong, B. Interaction and selectivity of 14-crown-4 derivatives with Li+, Na+, and Mg2+ metal ions. *Journal of Molecular Modeling* **2020**.

(36) Torrejos, R. E. C.; Nisola, G. M.; Song, H. S.; Limjuco, L. A.; Lawagon, C. P.; Parohinog, K. J.; Koo, S.; Han, J. W.; Chung, W. J. Design of lithium selective crown ethers: Synthesis, extraction and theoretical binding studies. *Chemical Engineering Journal* **2017**, *326*, 921-933.

(37) Bartsch, R. A.; Czech, B. P.; Kang, S. I.; Stewart, L. E.; Walkowiak, W.; Charewicz, W. A.; Heo, G. S.; Son, B. High Lithium Selectivity in Competitive Alkali-Metal Solvent Extraction by Lipophilic Crown Carboxylic Acids. *Journal of the American Chemical Society* **1985**, *107* (17), 4997-4998.

(38) Sachleben, R. A.; Moyer, B. A. Ligand Design for Small Cations: The Li+/14-Crown-4 System. *ACS Symposium Series* **1999**, *716*, 114-132.

(39) Weisman, G. R.; Rogers, M. E.; Wong, E. H.; Jasinski, J. P.; Paight, E. S. Cross-Bridged Cyclam. Protonation and Li+ Complexation in a Diamond-Lattice Cleft. *Journal of the American Chemical Society* **1990**, *112* (23), 8604-8605.

(40) Wunderlich, J. A.; Lipscomb, W. N. STRUCTURE OF B12H12-2 ION. *Journal of the American Chemical Society* **1960**, *82* (16), 4427-4428.

(41) Fein, M. M.; Bobinski, J.; Mayes, N.; Schwartz, N.; Cohen, M. S. Carboranes. I. The Preparation and Chemistry of 1-Isopropenylcarborane and its Derivatives (a New Family of Stable Clovoboranes). *Inorganic Chemistry* **1963**, *2* (6), 1111-1115.

(42) Shapiro, I.; Good, C. D.; Williams, R. E. The Carborane Series: BnC2Hn+2. I. B3C2H5. *Journal of the American Chemical Society* **1962**, *84* (20), 3837-3840.

(43) Deng, L.; Chan, H. S.; Xie, Z. Synthesis, reactivity, and structural characterization of a 14-vertex carborane. *Angew Chem Int Ed Engl* **2005**, *44* (14), 2128-2131, From NLM PubMed-not-MEDLINE.

(44) Heying, T. L.; Ager, J. W.; Clark, S. L.; Mangold, D. J.; Goldstein, H. L.; Hillman, M.; Polak, R. J.; Szymanski, J. W. A New Series of Organoboranes. I. Carboranes from the Reaction of Decaborane with Acetylenic Compounds. *Inorganic Chemistry* **1963**, *2* (6), 1089-1092.

(45) Fisher, S. P.; Tomich, A. W.; Lovera, S. O.; Kleinsasser, J. F.; Guo, J.; Asay, M. J.; Nelson, H. M.; Lavallo, V. Nonclassical Applications of closo-Carborane Anions: From Main Group Chemistry and Catalysis to Energy Storage. *Chemical Reviews* **2019**, *119* (14), 8262-8290.

(46) Núñez, R.; Tarrés, M.; Ferrer-Ugalde, A.; de Biani, F. F.; Teixidor, F. Electrochemistry and Photoluminescence of Icosahedral Carboranes, Boranes, Metallacarboranes, and Their Derivatives. *Chemical Reviews* **2016**, *116* (23), 14307-14378.

(47) Grimes, R. N. *Carboranes*; Elsevier Inc., 2016.

(48) Keener, M.; Hunt, C.; Carroll, T. G.; Kampel, V.; Dobrovetsky, R.; Hayton, T. W.; Ménard, G. Redox-switchable carboranes for uranium capture and release. *Nature* **2020**, *577* (7792), 652-655.

(49) Keener, M.; Mattejat, M.; Zheng, S.-L.; Wu, G.; Hayton, T. W.; Ménard, G. Selective electrochemical capture and release of uranyl from aqueous alkali{,} lanthanide{,} and actinide mixtures using redox-switchable carboranes. *Chem. Sci.* **2022**, *13* (12), 3369-3374.

(50) Morris, J. H.; Gysling, H. J.; Reed, D. Electrochemistry of boron compounds. *Chemical Reviews* **1985**, *85* (1), 51-76.

(51) Weber, L.; Kahlert, J.; Böhling, L.; Brockhinke, A.; Stammler, H.-G.; Neumann, B.; Harder, R. A.; Low, P. J.; Fox, M. A. Electrochemical and spectroelectrochemical studies of C-benzodiazaborolyl-ortho-carboranes. *Dalton Transactions* **2013**, *42* (6), 2266-2281, 10.1039/C2DT32378H.

(52) Tricas, H.; Colon, M.; Ellis, D.; Macgregor, S. A.; McKay, D.; Rosair, G. M.; Welch, A. J.; Glukhov, I. V.; Rossi, F.; Laschi, F.; et al. Spectroscopic, structural, computational and (spectro)electrochemical studies of icosahedral carboranes bearing fluorinated aryl groups. *Dalton Transactions* **2011**, *40* (16), 4200-4211, 10.1039/C0DT01798A.

(53) Deng, L.; Cheung, M.-S.; Chan, H.-S.; Xie, Z. Reduction of 1,2-(CH2)n-1,2-C2B10H10 by Group 1 Metals. Effects of Bridge Length/Rigidity on the Formation of Carborane Anions. *Organometallics* **2005**, *24* (25), 6244-6249.

Chapter 2

Multiple N−H and C−H Hydrogen Atom Abstractions Through Coordination-Induced Bond Weakening at Fe-Amine Complexes

2.1 Introduction

As described in Chapter 1, ammonia is an attractive RE storage candidate[1, 2]; however, its end use requires a fundamental understanding of the complex multi-electron ammonia oxidation (AO) reaction. Homogeneous AO catalysts can provide important insight into these molecular-level transformations and several groups have recently reported important contributions to this field. For instance, the groups of Bullock,[3] Mock,[4] Nishibayashi,[5] and Hamann and Smith[6] have all reported Ru-based electro/chemical catalysts for AO. For first-row metal complexes, our group previously reported a pseudo-catalytic "synthetic" cycle using a Mn complex,[7] whereas Peters and coworkers have recently reported an Fe-based electrocatalyst for AO.[8] While the proposed AO mechanisms vary in all of these reports, the underlying challenge in converting NH_3 to N_2 lies in activating the strong N–H bonds sufficiently to prompt subsequent N–N bond formation (N–H bond dissociation free-energy ($BDFE_{N–H}$) = 99.4 kcal/mol).[9, 10]

Coordination-induced bond weakening (CIBW) of NH_3 or other ligands bound to redox-active metal centers can result in substantial decreases in E–H (E = C, N, O) BDFEs with effects seen at α positions [11-17] or downstream (β, γ, etc.) [18-20] of the metal center (**Figure 2.1a**). Bezdek and Chirik have recently demonstrated substantial N–H CIBW at a Mo–NH_3 complex leading to spontaneous H_2 formation,[16] whereas Mock, Bullock, and co-workers have utilized N–H bond weakening to target H-atom abstraction (HAA) at metal-coordinated NH_3.[4, 21, 22] In a recent example, catalytic C–N coupling versus AO was controlled by tuning the HAA agent from 2,4,6-*tert*-butylphenoxyl radical ($^{t\text{Bu}}$ArO•; $BDFE_{O–H}$ = 76.7 kcal/mol)[9] to the *para*-trityl variant, $^{\text{Tr}}$ArO•, respectively, using the porphyrin-based catalyst, **(TMP)Ru(NH_3)$_2$**, in the presence of excess NH_3 (TMP = tetramesitylporphyrin; **Figure 2.1b**).[3]

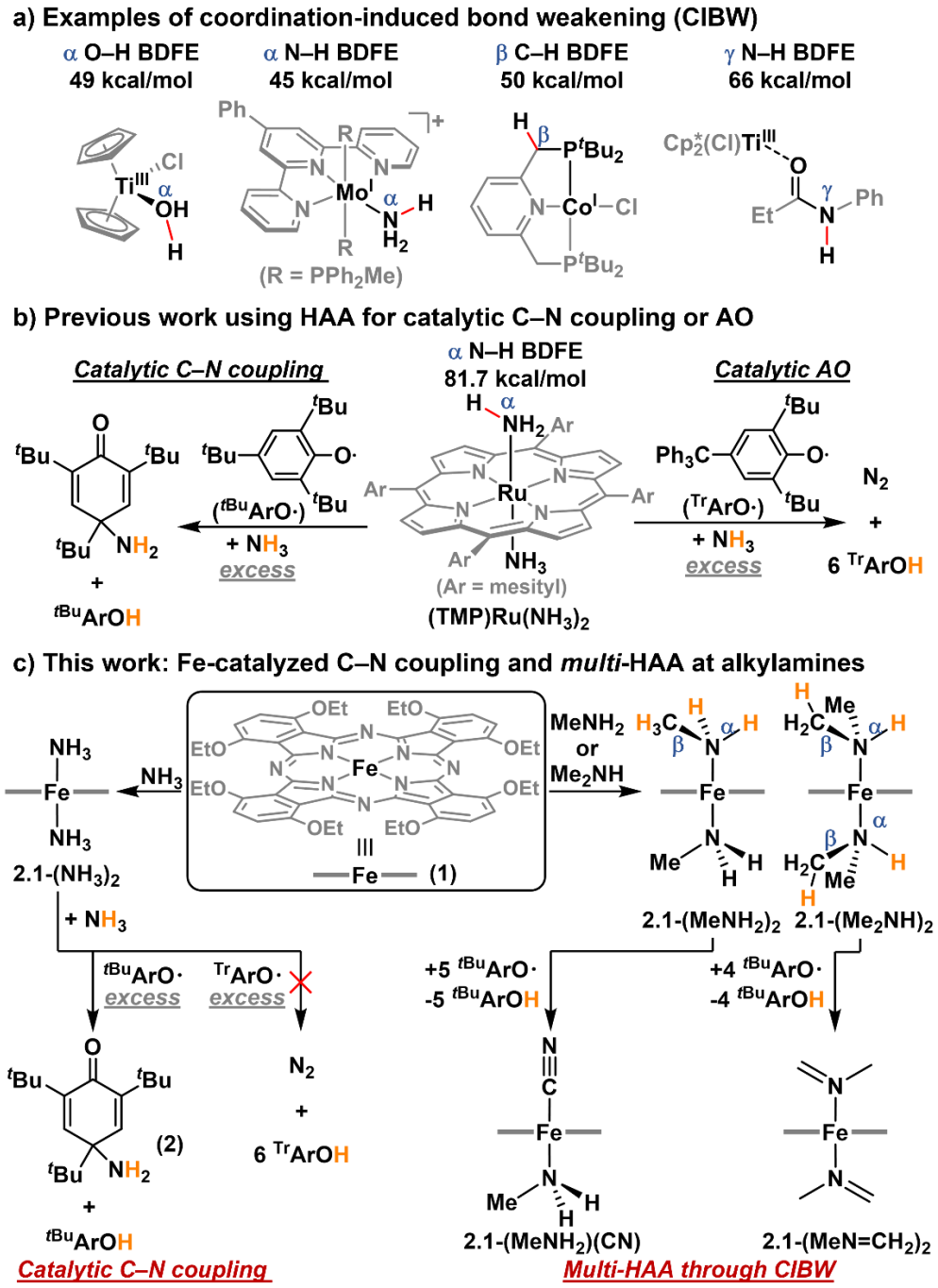

Figure 2.1. a) Various reported examples of α, β or γ E–H CIBW at metal complexes (E = C, N, O). Reported E–H (red) BDFEs are shown. b) Previously reported catalytic HAA for C–N coupling or AO at **(TMP)Ru(NH$_3$)$_2$**. c) This work featuring: (left) catalytic C–N coupling of NH$_3$ with ^{tBu}ArO• using **2.1-(NH$_3$)$_2$** through CIBW, and; (right) multiple α N–H and β C–H

HAA events enabled by CIBW at alkylamine complexes, **2.1-(MeNH$_2$)$_2$** and **2.1-(Me$_2$NH)$_2$**, using $^{t\text{Bu}}$ArO•.

Our interest lies in developing new first-row catalysts for AO, and understanding the mechanistic details underlying N–H activation and N–N bond forming pathways.[7] In parallel with Bullock and co-workers,[3] we investigated the use of our recently reported Fe-phthalocyanine (PcFe) complex (**2.1**),[23] analogous to **(TMP)Ru(NH$_3$)$_2$**, and its potential use as an AO catalyst (**Figure 2.1c**). While we discovered that **2.1** was a competent C–N coupling catalyst, we found it was mostly inactive for catalytic AO through HAA chemistry (**Figure 2.1c**, left). However, in an effort to bolster our mechanistic understanding of these transformations, we synthesized related alkylamine complexes and exposed these to similar HAA conditions. In these cases, we uncovered that pronounced CIBW led to multiple α N–H and β C–H events, generating unsaturated C–N bonds (**Figure 2.1c**, right).[24-28] In one case, subsequent C–N bond formation could be induced. The details of these transformations are presented herein.

2.2 Results and Discussion

2.2.1 Synthesis and Characterization of $^{\text{EtO}}$PcFe

The starting complex $^{\text{EtO}}$PcFe (**2.1)**, was synthesized from free ligand $^{\text{EtO}}$PcH$_2$ reacting with Fe(OAc)$_2$ in toluene with reflux for 24h.[23] After work-up, **2.1** was isolated and identified by NMR spectroscopy and the solid-state structure obtained by single crystal XRD studies (**Figure 2.2**). The ^{1}H NMR spectrum of **2.1** displayed arene C–H resonances upfield at 3.44 ppm relative to the ethoxy peaks at 4.32 ppm (triplet) and 9.90 ppm (quartet). **2.1** was further

analyzed by zero-field ^{57}Fe Mössbauer spectroscopy. The 90 K spectrum revealed a quadrupole doublet with an isomer shift value at $\delta = 0.33$ mm s^{-1} and a quadrupole split- ting value ($|\Delta E_Q|$) of 1.37 mm s^{-1}. These values are consistent with an expected intermediate spin (S = 1) square planar Fe center.[29] Our quadrupole splitting is roughly half of what would be expected by comparison with unsubstituted Pcs, which may be attributed to the electron donating ethoxy groups.[30 31]

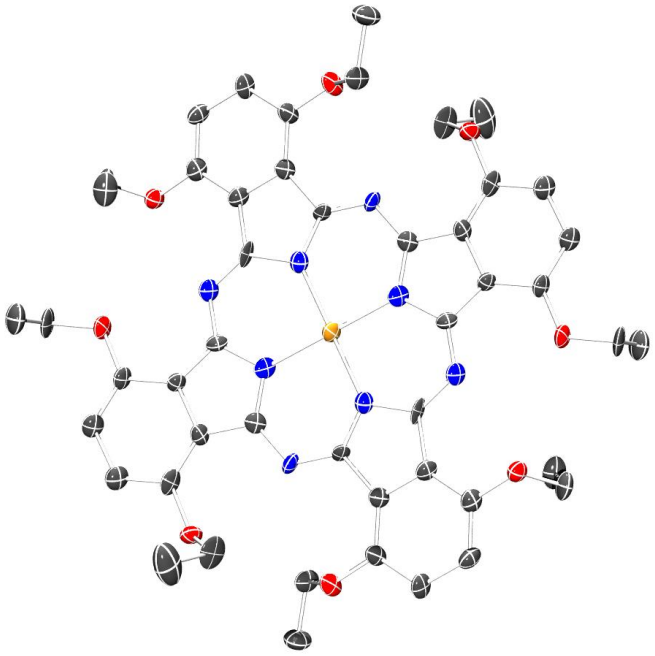

Figure 2.2. Solid-state molecular structures of **2.1.** Ethoxy groups, co-crystallized solvent molecules, and all H atoms, except N–H, have been omitted for clarity. C, black; N, blue; O, red; Fe, yellow

2.2.2 Synthesis and Characterization of PcFe-Amine Precursors

Treatment of **2.1** with excess NH_3, $MeNH_2$, or Me_2NH afforded the green products **2.1-$(NH_3)_2$**, **2.1-$(MeNH_2)_2$**, or **2.1-$(Me_2NH)_2$**, respectively, in high yields (**Figure 2.1c**). Each new complex was unambiguously identified by single crystal X-ray diffraction (XRD) studies, with the solid-state structures shown in **Figure 2.3a**. Observed Fe–N_{amine} bond distances of 2.017(4), 2.037(6), and 2.087(5) Å for **2.1-$(NH_3)_2$**, **2.1-$(MeNH_2)_2$**, and **2.1-$(Me_2NH)_2$**, respectively, are consistent with increasing amine bulk and similar to previous reports.[32-34] Pc ring distortions are most pronounced for **2.1-$(MeNH_2)_2$** and may be due to packing effects observed in the extended structure.[23] The zero-field ^{57}Fe Mössbauer spectra of each complex were collected at 90 K and revealed very similar quadrupole doublets with isomer shift and quadrupole splitting (δ, $|\Delta E_Q|$ (mm/s)) values of: **2.1-$(NH_3)_2$** (0.29, *1.14*), **2.1-$(MeNH_2)_2$** (0.24, *0.87*), and **2.1-$(Me_2NH)_2$** (0.25, *0.99*) (**Figure 2.3b**). While the δ values are similar to previously reported axially substituted PcFe species,[30] their $|\Delta E_Q|$ values are significantly reduced, similar to what was previously observed in **2.1** and which is again tentatively attributed to the electron donating EtO groups (**Figure 2.1c**).[23] We note also that the spectral parameters of the amine-substituted complexes are all smaller than those in **1** (0.33, *1.37*), which is attributed to the addition of axially-bound σ-donating ligands, resulting in a spin-state change from $S = 1$ (**2.1**) to $S = 0$ (**2.1-$(NH_3)_2$**, **2.1-$(MeNH_2)_2$**, and **2.1-$(Me_2NH)_2$**).[23, 30, 35] The ^{1}H NMR spectra of each compound revealed diamagnetic species with heavily shielded amine resonances due to their axial coordination above the strong, diatropic Pc ring current.[36] As expected, this effect was more pronounced for the closer N–H resonances than the further C–H resonances (**Figure 2.3c**). Lastly, the UV-Vis absorption spectra displayed nearly identical prominent Q-band (HOMO(π)→LUMO(π^*)) absorption peaks at 714 nm (ε = 47,432 M^{-1} cm^{-1}), 716 nm (ε =

36,102 M^{-1} cm^{-1}), and 713 nm (ε = 37,992 M^{-1} cm^{-1}) for **2.1-$(NH_3)_2$**, **2.1-$(MeNH_2)_2$**, and **2.1-$(Me_2NH)_2$**, respectively, all of which are significantly blue-shifted relative to **2.1** (765 nm (ε = 41,868 M^{-1} cm^{-1})).[23] In contrast to **2.1**, the substituted complexes all contained distinct absorptions in the 400-500 nm region assigned to Fe→Pc metal-to-ligand charge transfer (MLCT) bands previously observed in axially substituted low-spin $PcFe^{II}$ complexes[37, 38]: **2.1-$(NH_3)_2$** (433 nm), **2.1-$(MeNH_2)_2$** (438 nm), **2.1-$(Me_2NH)_2$** (436 nm).

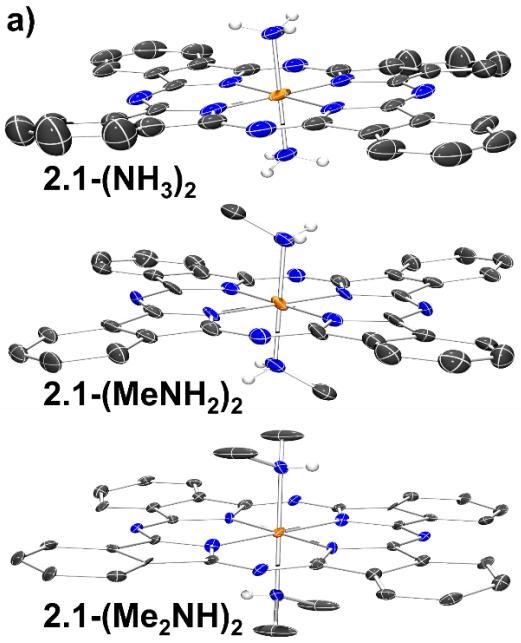

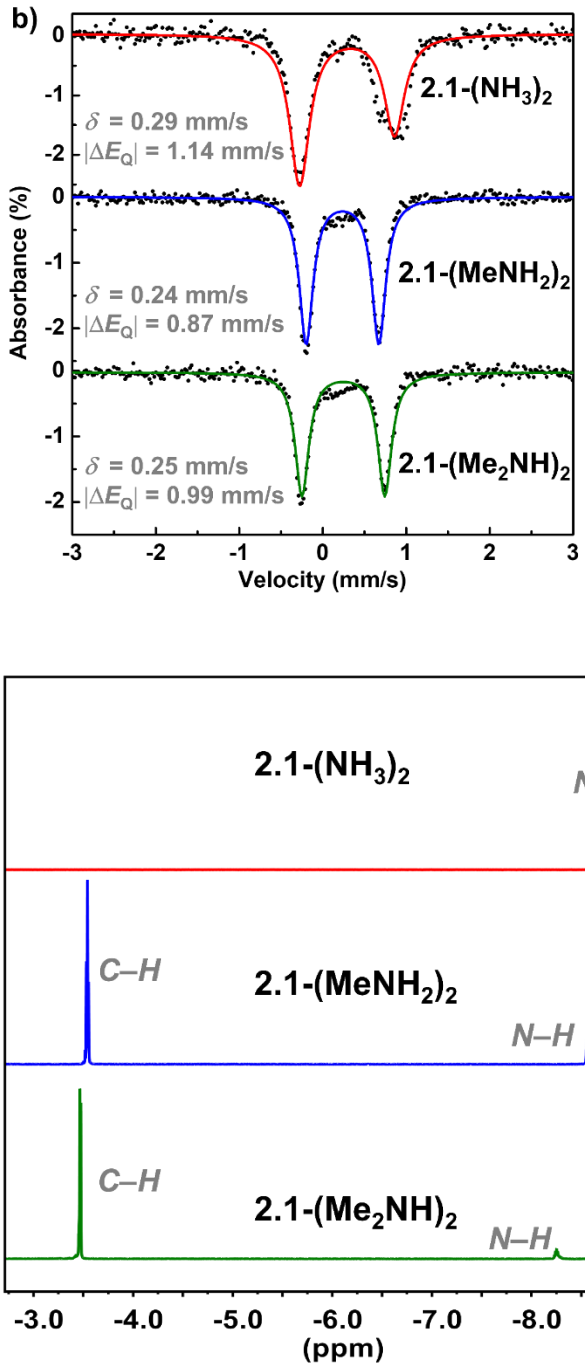

Figure 2.3. a) Solid-state molecular structures of **2.1-(NH$_3$)$_2$**, **2.1-(MeNH$_2$)$_2$**, and **2.1-(Me$_2$NH)$_2$**. Ethoxy groups, co-crystallized solvent molecules, and all H atoms, except N–H, have been omitted for clarity. Fe, orange; N, blue; C, black; H, gray. b) Zero-field ^{57}Fe

Mössbauer spectra (90 K) of the corresponding complexes with isomer shift (δ) and quadrupole splitting ($|\Delta E_Q|$) values indicated. c) Partial ^{1}H NMR spectra of the corresponding complexes highlighting the strongly shielded amine N–H and C–H resonances.

2.2.2 N–H HAA at PcFe-NH_3.

In order to test possible AO catalysis with **2.1** via HAA chemistry, we investigated the reactivity of this compound with $^{t\text{Bu}}$ArO• or $^{\text{Tr}}$ArO• under an atmosphere of NH_3. Similar to the **(TMP)Ru(NH_3)$_2$** system reported by Bullock and co-workers,[3] we observed that **2.1** was a competent C–N coupling catalyst (**Figure 2.1b**(left), **2.1c** (left)). For instance, treatment of **2.1** to 300 equiv of $^{t\text{Bu}}$ArO• under an atmosphere of NH_3 in C_6D_6 revealed the formation of $^{t\text{Bu}}$ArOH and the reported species, 4-amino-2,4,6-tri-*tert*-butylcyclohexa-2,5-dien-1-one (**2.2**; **Figure 2.1c**),[3] as observed by ^{1}H NMR spectroscopy after 24 h. The ratio of $^{t\text{Bu}}$ArOH to **2.2** was slightly elevated (ca. 1.5:1) and may be due to adventitious water from the NH_3 gas or decomposition of $^{t\text{Bu}}$ArO• (*vide infra*). A turnover number (TON) of 303 was calculated using 0.05% of **2.1** after 27 h, similar to the reported reactivity of **(TMP)Ru(NH_3)$_2$**.[3] The headspace gas of a reaction performed under an $^{15}NH_3$ atmosphere was analyzed by GC-MS and revealed some isobutylene, attributed to the decomposition of $^{t\text{Bu}}$ArO•,[39] but no $^{15}N_2$ (**Figure 2.4**).

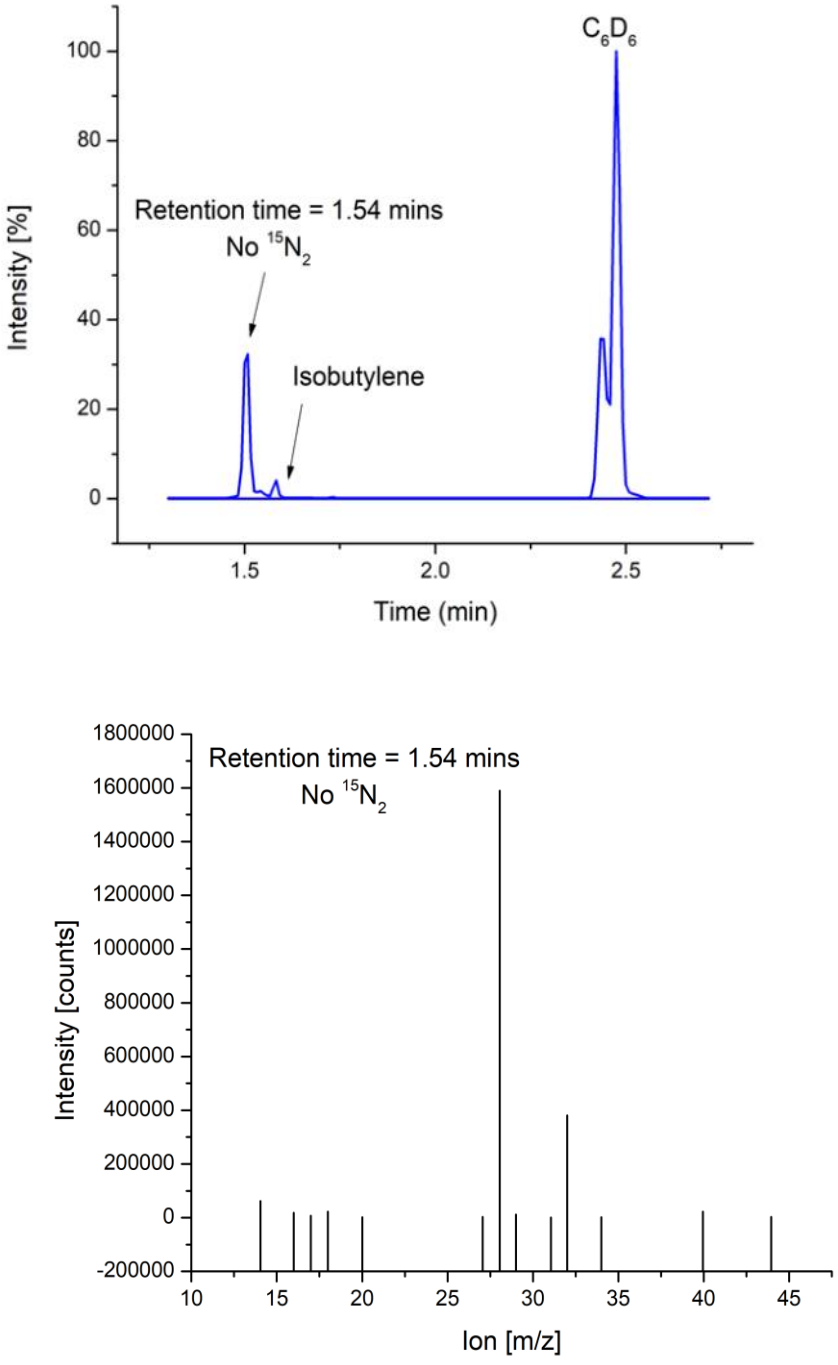

Figure 2.4. GC of headspace sample taken from the catalytic C–N coupling of $^{t\text{Bu}}$ArO• with $^{15}NH_3$ and **2.1** (experimental details are found in the manuscript). a) GC trace, b) MS at retention time of 1.54 mins displaying no $^{15}N_2$ (m/z = 30).

A control experiment involving the reaction of $^{t\text{Bu}}$ArO• ($BDFE_{ArO–H}$ = 76.7 kcal/mol) with NH_3 ($BDFE_{N–H}$ = 99.4 kcal/mol) in the absence of **2.1** revealed no reactivity, indicating that significant N–H CIBW occurred upon coordination to **2.1**.[9] HAA from the isolated complex, **2.1-(NH$_3$)$_2$**, also occurred using $^{t\text{Bu}}$ArO•. Treatment of **2.1-(NH$_3$)$_2$** to 6.1 equiv of $^{t\text{Bu}}$ArO• resulted in the formation of 2 equiv of **2.2**, as well as an excess of $^{t\text{Bu}}$ArOH (3 equiv) as observed by ^{1}H NMR spectroscopy, and confirmed by ^{2}H NMR spectroscopy using **2.1-(ND$_3$)$_2$**. We further observed the formation of a new, dark green, paramagnetic product. The identity of this product was confirmed by independent synthesis by reacting **2.1** with $^{t\text{Bu}}$ArO• in dichloromethane (DCM). The solid-state structure obtained by XRD studies revealed the formation of the adduct, **2.1-OAr$^{t\text{Bu}}$** (**Figure 2.5**). The complex featured a domed $^{\text{EtO}}$Pc ligand with a nearly linear Fe1–O1–C1 bond (177.3(7)°),[40] and an elongated Fe1–O1 bond (1.836(6) Å).[40-44] The C1–O1 bond (1.370(11) Å) is average relative to reported Fe–OAr$^{t\text{Bu}}$ species,[40, 43-45] and longer than in free $^{t\text{Bu}}$ArO• (1.246(2) Å).[46]

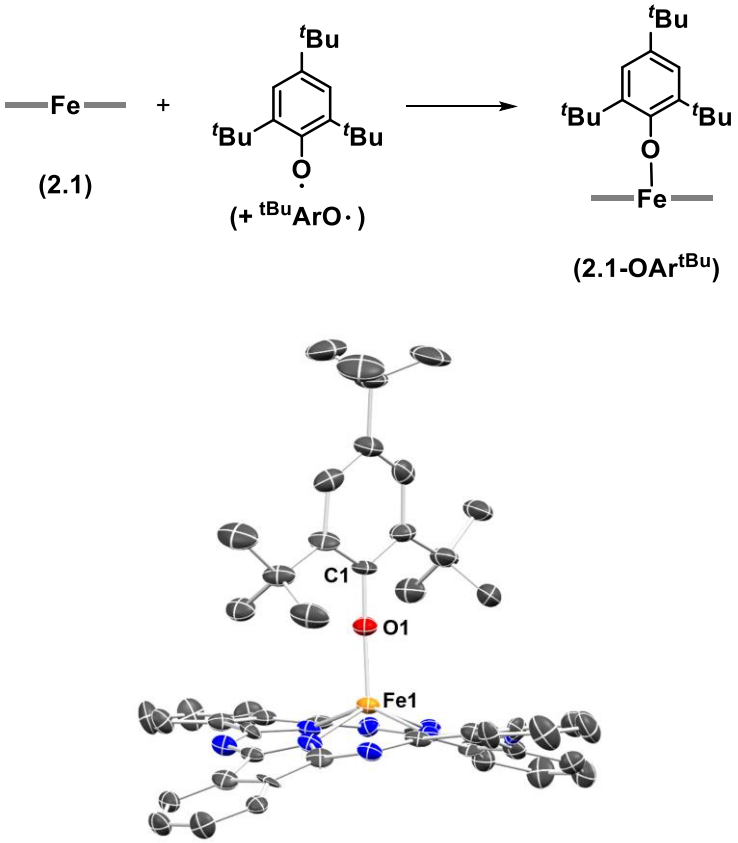

Figure 2.5. (top) Synthesis of **2.1-OAr^{tBu}**. (bottom) Solid-state molecular structure of **2.1-OAr^{tBu}**. Ethoxy groups, co-crystallized solvent molecules, and all H atoms have been omitted for clarity. Selected bond lengths and angles: Fe–O1 1.836(6) Å, O1–C1 1.370(11) Å, Fe1–O1–C1 177.3(7)°.

The zero-field ^{57}Fe Mössbauer spectrum of **2.1-OAr^{tBu}** (90 K) revealed a $\delta = 0.26$ mm/s and a narrow $|\Delta E_Q| = 0.28$ mm/s, consistent with formal oxidation to Fe^{III} (**Figure 2.6**).[47] This was further supported by the appearance of broadened, paramagnetically shifted resonances in the ^{1}H NMR spectrum (**Figure 2.7**). Treatment of **2.1-OAr^{tBu}** to an atmosphere of NH_3 resulted in the formation of **2.1-(NH$_3$)$_2$**, ^{tBu}ArOH, and **2.2** in similar ratios to above.

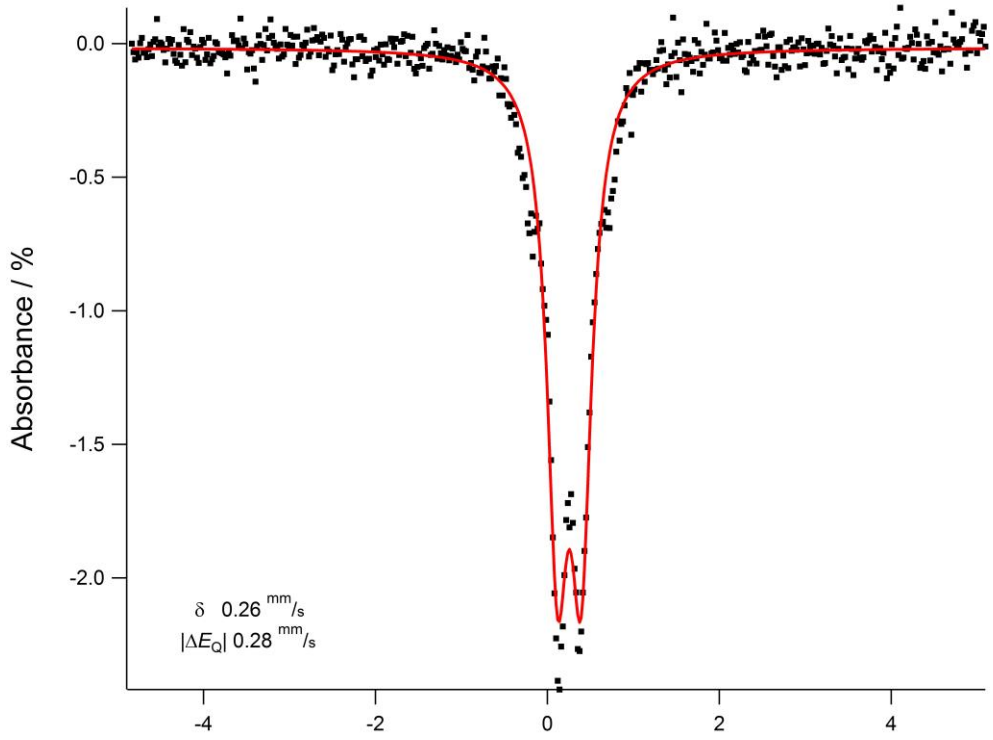

Figure 2.6. ^{57}Fe Mössbauer spectrum of **2.1-OAr^{tBu}** taken at 90 K

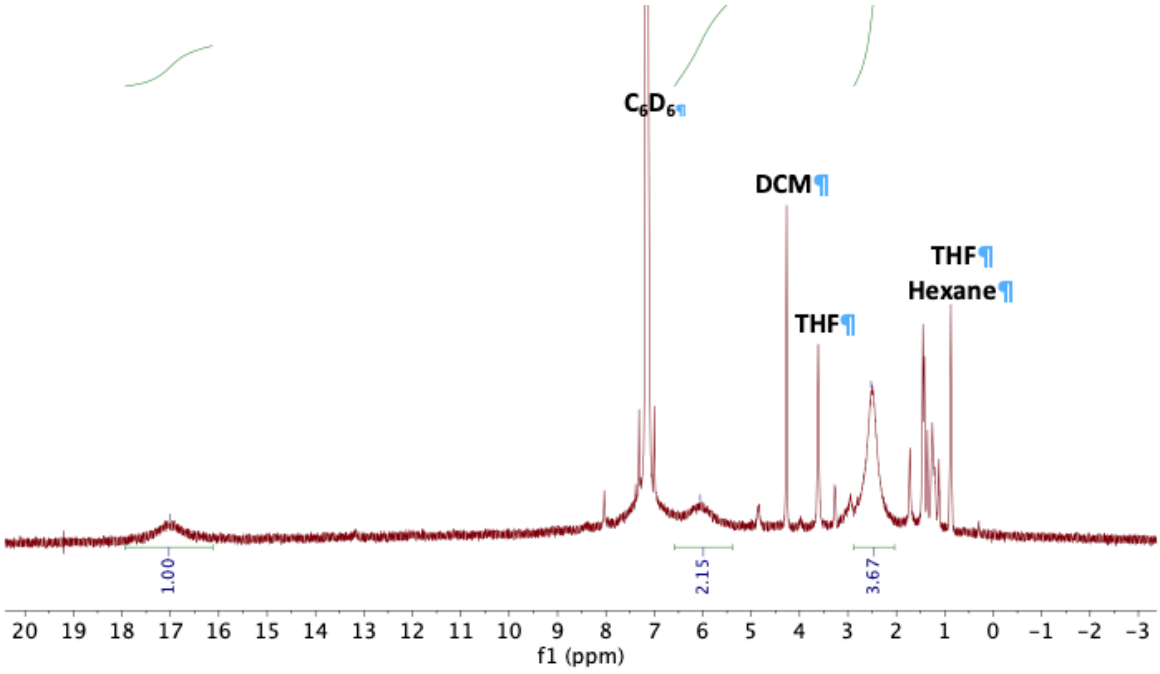

Figure 2.7. ^{1}H NMR (600 MHz) spectrum of **2.1-OAr^{tBu}** in C_6D_6. Integrated peaks are from this paramagnetic product.

In order to circumvent the catalytic formation of **2.2**, we investigated AO using the bulkier congener, ^{Tr}ArO• (**Figure 2.1b-c**), bearing the trityl (CPh_3) group in the *para* position.[3] Under an atmosphere of $^{15}NH_3$, 93 equiv of ^{Tr}ArO• were added to **2.1** and stirred in benzene for 16 h. Analysis of the headspace gas by GC-MS revealed only trace $^{15}N_2$. A parallel concentrated reaction in a J. Young NMR tube monitored after 48 h revealed no detectable $^{15}N_2$ by ^{15}N NMR spectroscopy. These data suggest that **2.1** is at best a very poor catalyst for AO, in contrast to the related **(TMP)Ru(NH$_3$)$_2$** system (**Figure 2.1b-c**).[3] While a substantial amount (~ 70-90%) of ^{Tr}ArO• was converted to ^{Tr}ArOH, as observed by ^{1}H NMR spectroscopy and perhaps attributable to HAA at NH_3, a significant quantity of isobutylene was also observed suggesting a competing ^{Tr}ArO• decomposition pathway. Stoichiometric reactions of ^{Tr}ArO• with **2.1-(NH$_3$)$_2$** were also inconclusive. In order to shed more light on these transformations, we decided to investigate this chemistry further using model ^{EtO}PcFe–alkylamine complexes.

2.2.3 N–H and C–H HAA at PcFe-Alkylamines

In an attempt to simplify our system and reduce the total number of N–H bonds in **2.1-(NH$_3$)$_2$**, we synthesized the dimethylamine variant, **2.1-(Me$_2$NH)$_2$** (*vide supra*), containing only two N–H bonds. Exposure of this compound to 1.25 equiv of $^{t\text{Bu}}$ArO• led to the clean formation of two new products (ca. 60%) as observed by ^{1}H NMR spectroscopy, along with residual **2.1-(Me$_2$NH)$_2$** (ca. 40%). The major new product contained a set of resonances in the ^{1}H NMR spectrum consistent with amine (Me_2NH) and *imine* ($MeN{=}CH_2$) coordination to Fe, with each integrating in a 1:1 ratio. We assign this as the putative intermediate, **2.1-(MeN=CH$_2$)(Me$_2$NH)**, although efforts to isolate this single product have failed (**Scheme 2.1**).

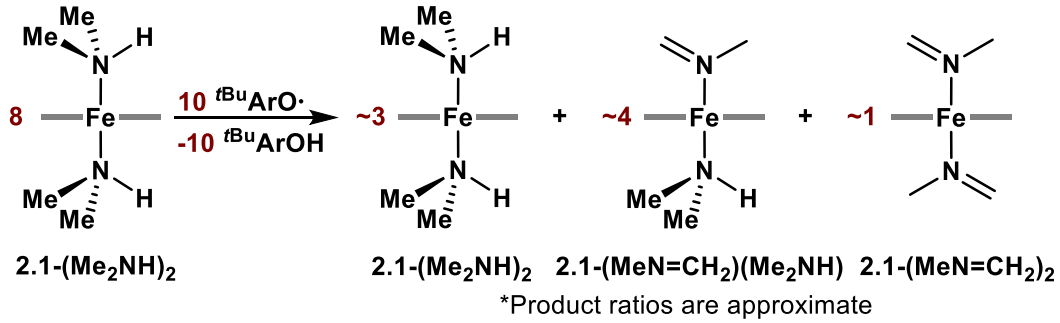

Scheme 2.1. Reaction of with **2.1-(Me$_2$NH)$_2$** 1.25 equiv of $^{t\text{Bu}}$ArO•

The minor (ca. 15%) of the two new products could be cleanly formed by addition of 4 equiv of $^{t\text{Bu}}$ArO• to **2.1-(Me$_2$NH)$_2$**. A singlet at -2.19 ppm (6H) correlating to a set of doublets (2H each) at 2.18 and 0.71 ppm was observed and together suggested *N*-methylmethan*imine* (MeN=CH$_2$) coordination to Fe. The solid-state structure obtained by single crystal XRD studies indeed unambiguously confirmed the structure as the bis-*imine* product, **2.1-(MeN=CH$_2$)$_2$** (**Figure 2.1c**, **Figure 2.8**). The structure revealed distinctively shortened N1–C1 bonds (1.324(9) Å), relative to the N1–C2 bonds (1.395(8) Å). However, we note that these bond differences are not as pronounced as the only other crystallographically characterized σ-coordinated *N*-methylmethanimine complex (bound to Co) reported by Power and co-workers which contained C–N and C=N bond lengths of 1.451(3) and 1.262(3) Å, respectively.[48] The smaller difference in **2.1-(MeN=CH$_2$)$_2$** may be due to crystallographic averaging of the single and double bonds in the symmetry-generated XRD structure. Given the pure imine σ coordination to Fe, and similar Fe–N$_{\text{imine}}$ (2.006(5) Å) to Fe–N$_{\text{amine}}$ (2.087(5) Å) bond lengths in **2.1-(MeN=CH$_2$)$_2$** and **2.1-(Me$_2$NH)$_2$**, respectively, the Mössbauer spectral parameters are also nearly identical (δ, $|\Delta E_Q|$ (mm/s)): **2.1-(MeN=CH$_2$)$_2$** (0.25, *0.92*), **2.1-(Me$_2$NH)$_2$** (0.25, *0.99*). UV-Vis absorption features are also very similar for both.

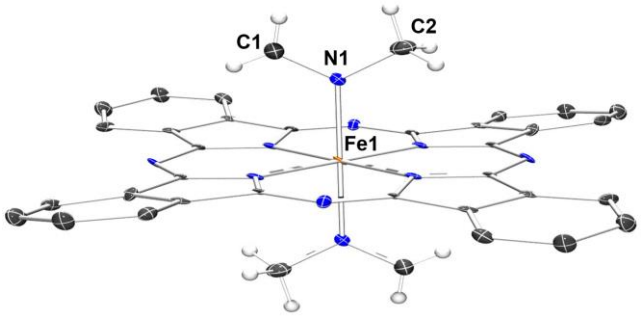

Figure 2.8. Solid-state molecular structure of **2.1-(MeN=CH$_2$)$_2$**. Ethoxy groups, co-crystallized solvent molecules, and all H atoms, except imine N–H and C–H, have been omitted for clarity. Selected bond lengths: Fe1–N1 2.006(5) Å, N1–C1 1.324(9) Å, N1–C2 1.395(8) Å.

We observed that the MeN=CH$_2$ ligands were labile towards high heat as observed by a thermogravimetric analysis (TGA) of **2.1-(MeN=CH$_2$)$_2$** which revealed a 7.5% mass drop from 120°C to 170°C, in the range expected for loss of both imine ligands (8.5%). Room temperature substitution was achieved by addition of 2.6 equiv of PMe$_3$ to **2.1-(MeN=CH$_2$)$_2$**, which led to the formation of a new diamagnetic FePc complex, as observed by ^{1}H and ^{31}P NMR spectroscopy. We assigned this new species as the bis-trimethylphosphine species, **2.1-(PMe$_3$)$_2$**. Interestingly, release of MeN=CH$_2$ led to its spontaneous cyclization via C–N bond formation to the 6-membered product, 1,3,5-trimethyl-1,3,5-triazinane, as observed by ^{1}H NMR spectroscopy (**Scheme 2.2**).[49]

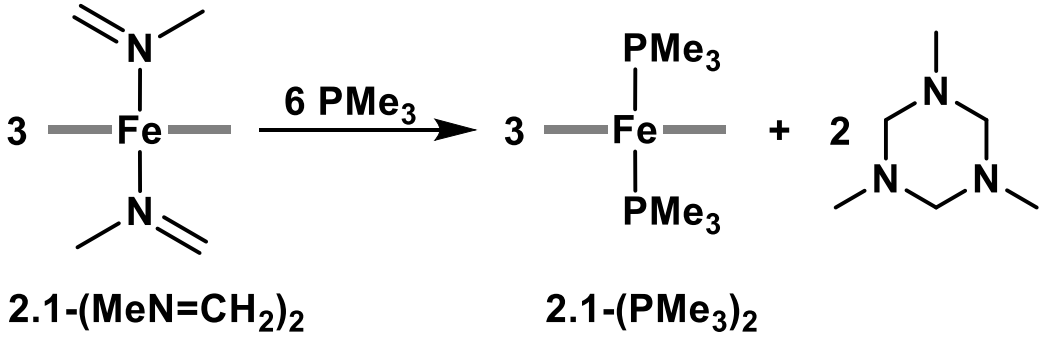

Scheme 2.2. Addition of 2.6 equiv of PMe_3 to **2.1-(MeN=CH$_2$)$_2$**

While the oxidative dehydrogenation of coordinated amines has been reported,[24-28] we next wanted to elucidate the specific mechanistic pathway for the specific conversion of **2.1-(Me$_2$NH)$_2$** to **2.1-(MeN=CH$_2$)$_2$**. To do so, we first performed the control reaction of $^{t\text{Bu}}$ArO• with Me_2NH in the absence of **1**. In contrast to the control reaction of $^{t\text{Bu}}$ArO• with NH_3, an HAA reaction was observed upon mixing $^{t\text{Bu}}$ArO• with Me_2NH. Analysis of the reaction mixture by ^{1}H NMR spectroscopy and GC-MS revealed the formation of $^{t\text{Bu}}$ArOH in addition to a second product assigned as the dimethylamine analog of **2.2** (**Figure 2.1c**), **2.2-NMe$_2$**, in a 1.5:1 ratio. The observed reactivity was surprising given the reported experimentally determined N–H and C–H bond dissociation *enthalpy* values of related Et_2NH ($BDE_{N–H/C–H(avg)} \approx 87$ kcal/mol) and calculated values for Me_2NH ($BDE_{C–H} = 91.7$ kcal/mol; $BDE_{N–H} = 95.4$ kcal/mol) were significantly higher than the reported experimental value for $^{t\text{Bu}}$ArO–H ($BDE_{O–H} = 81.6$ kcal/mol).[50, 51] Moreover, previous kinetic studies revealed faster C–H than N–H HAA rates with the alkyloxide radical, *t*BuO•, in contrast to our observed results with $^{t\text{Bu}}$ArO•.[52] In addition, no further HAA events were observed when exposing **2.2-NMe$_2$** to excess $^{t\text{Bu}}$ArO•. These results highlight the important role of CIBW in enabling multiple HAA events at Me_2NH. We propose that initial N–H HAA at the Fe-coordinated complex, **2.1-(Me$_2$NH)$_2$**, results in pronounced C–H bond weakening due to available hyperconjugative interactions between the β C–H σ bond and the newly formed semi-occupied Fe–N π* orbital (**Scheme 2.3**). This may enable the subsequent, thermodynamically favorable β C–H HAA reaction to proceed, generating the observed intermediate, **2.1-(MeN=CH$_2$)(Me$_2$NH)**, and

subsequently **2.1-(MeN=CH$_2$)$_2$**. This hypothesis is supported by computational studies we performed (*vide infra*).

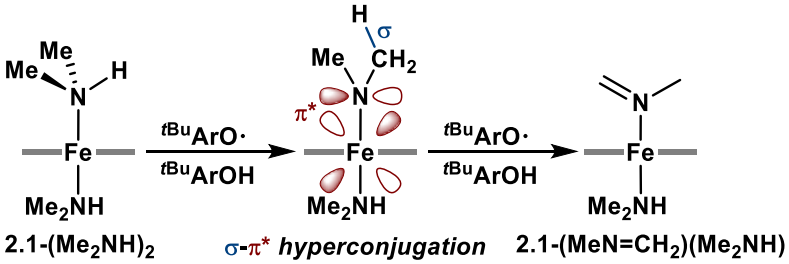

Scheme 2.3. Proposed hyperconjugative interactions scheme led to the formation of **1-(MeN=CH$_2$)(Me$_2$NH)**

We next explored similar HAA chemistry at the related methylamine complex, **2.1-(MeNH$_2$)$_2$** (**Figure 2.1c**, **Figure 2.3a**). Exposure of this to 1, 2, or 4 equiv of $^{t\text{Bu}}$ArO• led to the increased production of $^{t\text{Bu}}$ArOH with concurrent reduction in the intensity of the resonances attributed to **2.1-(MeNH$_2$)$_2$** as observed by ^{1}H NMR spectroscopy. While new diamagnetic resonances were observed, the growth of these was not commensurate with the quantity of $^{t\text{Bu}}$ArO• added, suggesting these were from an unknown by-product and that the major product formed was likely paramagnetic. Addition of 5 equiv of $^{t\text{Bu}}$ArO• led to the complete disappearance of the resonances for **2.1-(MeNH$_2$)$_2$**. Following workup, a paramagnetic species was isolated and unambiguously identified by single crystal XRD studies as the cyanide product, **2.1-(MeNH$_2$)(CN)** (**Figure 2.9**). The Fe1–C1 (1.962(6) Å) and C1–N1 (1.155(7) Å) bond distances are similar to previous reports,[53, 54] whereas the *trans* Fe1–N2 (2.060(5) Å) distance is longer than in **2.1-(MeNH$_2$)$_2$** (2.037(6) Å), and expected due to the *trans*-influence of the cyanide group. FT-IR spectroscopy revealed a C≡N stretching frequency at 2102 cm^{-1}, similar to previously reported Fe-cyanide complexes.[55] The ^{57}Fe Mössbauer

spectrum of **2.1-(MeNH$_2$)(CN)** revealed contracted δ (0.16 mm/s) and $|\Delta E_Q|$ (*0.71* mm/s) values relative to **2.1-(MeNH$_2$)$_2$** (0.24, *0.87*, respectively), suggesting formal oxidation to Fe^{III}.[47] This was further supported by the disappearance of the MLCT band for the precursor, **2.1-(MeNH$_2$)$_2$** (438 nm), observed in axially substituted low-spin $PcFe^{II}$ complexes.[37, 38] We note, however, that while these data support oxidation to a formal Fe^{III} state, significant Pc structural distortions observed in **2.1-(MeNH$_2$)(CN)** may also suggest some ligand-based contributions (Figure 2.5).[36]

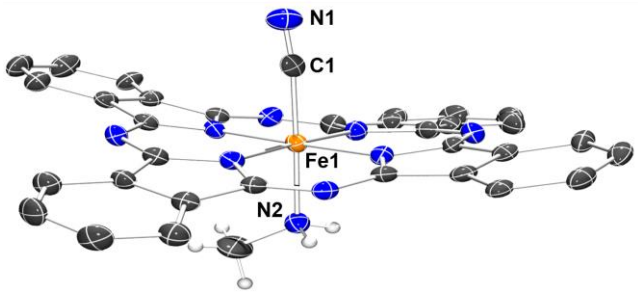

Figure 2.9. Solid-state molecular structure of **2.1-(MeNH$_2$)(CN)**. Ethoxy groups, co-crystallized solvent molecules, and all H atoms, except amine N–H and C–H, have been omitted for clarity. Selected bond lengths and angles: Fe1–C1 1.962(6) Å, C1–N1 1.155(7) Å, Fe1–N2 2.060(5) Å, Fe1–C1–N1 173.8(5)°.

In contrast to Me_2NH, the control reaction of $^{t\text{Bu}}$ArO• with $MeNH_2$ revealed no reaction, similar to NH_3, highlighting again the role of CIBW. Similar to the conversion of **2.1-(Me$_2$NH)$_2$** to **2.1-(MeN=CH$_2$)$_2$**, we propose that initial N–H HAA at **2.1-(MeNH$_2$)$_2$** leads to significant C–H bond weakening, due in part to hyperconjugative interactions (**Scheme 2.3**), enabling multiple alternating N–H/C–H HAA reactions to yield **2.1-(MeNH$_2$)(CN)**. We note that addition of excess $^{t\text{Bu}}$ArO• to **2.1-(MeNH$_2$)(CN)** did not result in additional reactivity suggesting a reduced CIBW effect at the higher valent Fe^{III} center. We next proceeded to

evaluate the possible common mechanisms at play leading to these multiple HAA reactions at PcFe-alkylamines (**2.1-$(Me_2NH)_2$**, **2.1-$(MeNH_2)_2$**) and contrast this to the reactions at **2.1-$(NH_3)_2$** using computational methods.

2.2.4 Mechanistic Studies using DFT

In order to shed light on the mechanistic pathways for the catalytic conversion of **2.1-$(NH_3)_2$** to **2.2**, as well as the multi-step N–H and C–H HAA reactions for the conversion of **2.1-$(MeNH_2)_2$** to **2.1-$(MeNH_2)$(CN)** (**Figure 2.1c**), free energy calculations were performed on the likely stepwise intermediate products (**Figure 2.10**).

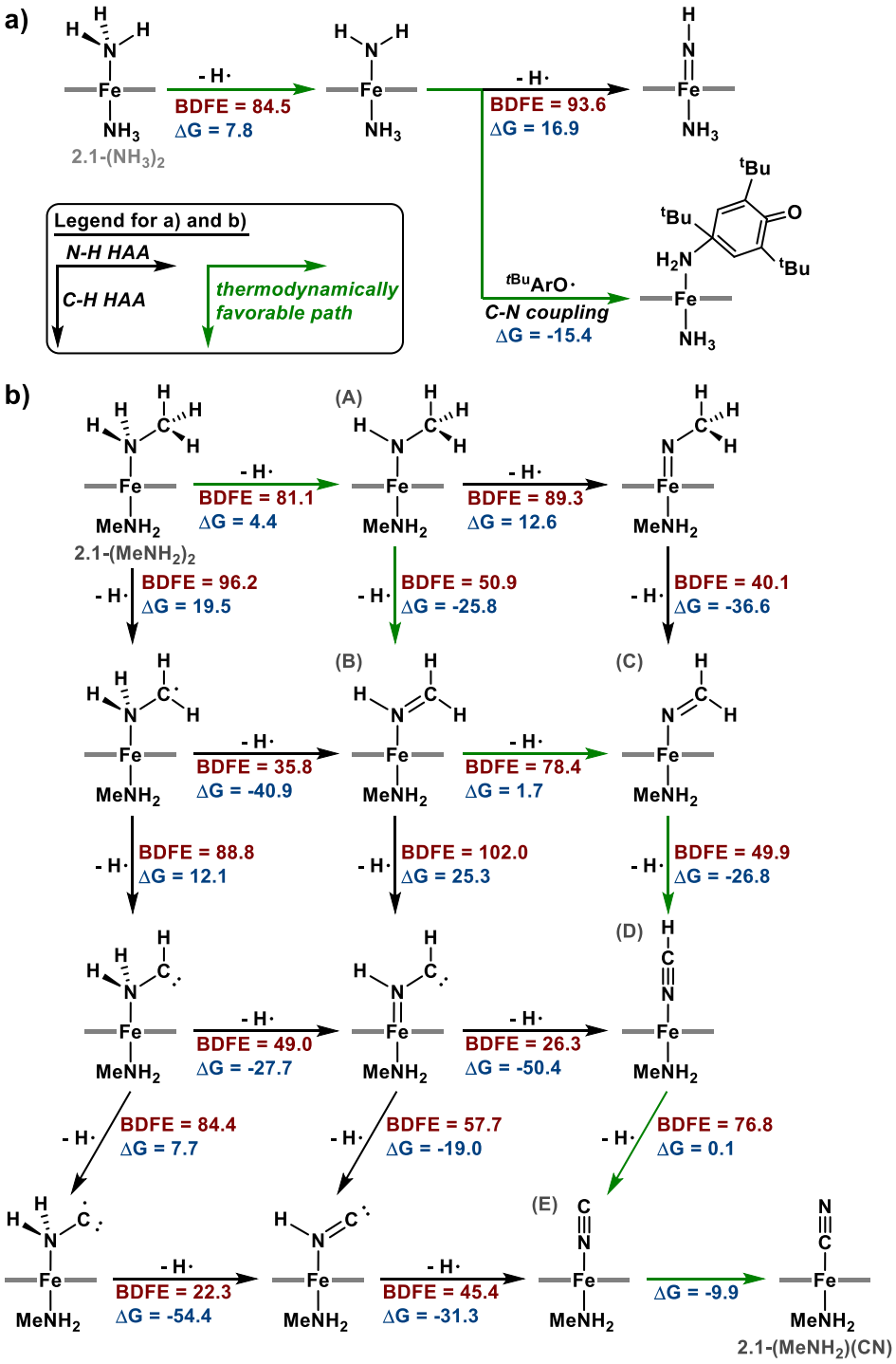

Figure 2.10. DFT-calculated free energy values (kcal/mol) in benzene for the conversions of **2.1-(NH3)2** (a), and **2.1-(MeNH2)2** (b). BDFEs are in red and ΔG values are in blue. All free

energy values are calculated relative to the $^{t\text{Bu}}$ArO•/$^{t\text{Bu}}$ArOH BDFE in benzene (76.7 kcal/mol).[9] The most thermodynamically favorable pathways follow the green arrows.

The calculated BDFEs for the first two sequential N–H HAA reactions at a single N site in **2.1-$(NH_3)_2$** (84.5 and 93.6 kcal/mol) were similar to the values in the related **(TMP)Ru$(NH_3)_2$** system (81.7 and 92.9 kcal/mol) (**Figure 2.1b**, **Figure 2.10a**). The corresponding ΔG of reaction for the initial HAA was slightly higher in **2.1-$(NH_3)_2$** (7.8 kcal/mol) relative to **(TMP)Ru$(NH_3)_2$** (5.0 kcal/mol), yet the second HAA events in each case were nearly identical (16.9 and 16.2 kcal/mol, respectively). Interestingly, the competing C–N coupling step of the intermediate **2.1-$(NH_3)(NH_2)$** with $^{t\text{Bu}}$ArO• was significantly more exergonic (-15.4 kcal/mol) than in the related intermediate **(TMP)Ru$(NH_3)(NH_2)$** (-0.9 kcal/mol).[3] This less favorable value in **(TMP)Ru$(NH_3)(NH_2)$** is likely the result of the increased steric protection offered by the flanking mesityl groups. This steric clash is also likely what drives catalytic AO at **(TMP)Ru$(NH_3)_2$** with the bulkier $^{\text{Tr}}$ArO•, something not observed in our sterically unprotected compound, **2.1-$(NH_3)_2$** (**Figure 2.1b-c**). While these data demonstrate a clear thermodynamic pathway to catalytic C–N bond formation using **2.1-$(NH_3)_2$** to generate **2.2**, the identity of the Fe product following possible N–H HAA with $^{\text{Tr}}$ArO• (*vida supra*) remains unclear (**Figure 2.1c**).

Calculations performed on the amine compound, **2.1-$(MeNH_2)_2$**, revealed a significantly weaker N–H vs. C–H bond with respective calculated BDFE values of 81.1 and 96.2 kcal/mol. These data support initial N–H HAA using $^{t\text{Bu}}$ArO• (**Figure 2.10b**). Calculations performed on intermediate **A** further highlight significant C–H CIBW resulting in a drastic drop in its BDFE (50.9 kcal/mol) relative to the residual N–H bond (89.3 kcal/mol), perhaps due to proposed hyperconjugative interactions (**Scheme 2.3**). Subsequent N–H HAA

at the imine intermediate **B** is significantly more facile than the corresponding C–H HAA, similar in pattern to the proposed reactivity in **2.1-(Me$_2$NH)$_2$** (**Scheme 2.3**). The resulting favorable intermediate, **C**, can then undergo 2 facile C–H HAA reactions through intermediate **D** to yield the isocyano intermediate, **E**. The coordination mode for **D** features an end-on –NCH group. A side-on coordinated –NCH was also explored as a potential concerted route to **2.1-(MeNH$_2$)(CN)** which would avoid the thermoneutral formation of **E**. However, side-on configurations were higher in energy by over 30 kcal/mol, requiring all H atoms to be removed before isomerization could occur. Conversion of **E** to the final product **2.1-(MeNH$_2$)(CN)** was calculated to be exergonic by -9.9 kcal/mol (**Figure 2.10b**).

Other pathways were also studied for the conversion of **2.1-(MeNH$_2$)$_2$** to **2.1-(MeNH$_2$)(CN)**; however, these were ultimately deemed unlikely due to unfavorable thermodynamic values. Together, these data outline an alternating mechanism involving sequential N–H and C–H HAA pathways to form the final cyanide product, **2.1-(MeNH$_2$)(CN)**. We propose that an analogous pathway is likely at play with **2.1-(Me$_2$NH)$_2$**, but that subsequent HAA reactions are arrested due to a lack of N–H bonds, thereby resulting in the final bis-imine product, **2.1-(MeN=CH$_2$)$_2$**.

2.3 Summary

In summary, we have described the synthesis of a series of PcFe-amine complexes, **2.1-(NH$_3$)$_2$**, **2.1-(MeNH$_2$)$_2$**, and **2.1-(Me$_2$NH)$_2$**, as well as their reactivity with aryloxide radicals, $^{t\text{Bu}}$ArO• and $^{\text{Tr}}$ArO•. CIBW led to facile HAA at **2.1-(NH$_3$)$_2$** and subsequent catalytic C–N coupling in the presence of NH_3 to generate **2.2**. Significant CIBW at **2.1-(MeNH$_2$)$_2$** and **2.1-(Me$_2$NH)$_2$** also led to multiple α N–H *and* β C–H HAA reactions when treated to excess

$^{t\text{Bu}}$ArO• generating the unsaturated products, **2.1-(MeNH$_2$)(CN)** and **2.1-(MeN=CH$_2$)$_2$**, respectively, similar to previous studies.[24-28] Detailed computational studies supported an alternating mechanism involving sequential N–H and C–H HAA to generate these unsaturated products. These fundamental transformations may enable the development of more complex new catalytic substrate activation reactions through CIBW functionalization.

2.4 Experimental

General Considerations. All manipulations were performed under an atmosphere of dry, oxygen-free N_2 within an MBraun glovebox (MBRAUN UNIlab Pro SP Eco equipped with a -35 °C freezer), or by standard Schlenk techniques. Pentane, hexanes, benzene, Et_2O, DCM and THF (inhibitor-free) were dried and degassed on an MBraun Solvent Purification System and stored over activated 4 Å molecular sieves. All other solvents were degassed by freeze-pump-thaw and stored on activated 4 Å molecular sieves prior to use. Celite® and 4 Å molecular sieves were dried at 250 °C under dynamic vacuum (<0.1 Torr) for 24 h prior to use. Elemental analyses were recorded at the University of California, Berkeley using a Perkin Elmer 2400 Series II combustion analyzer. Hexamethylbenzene and dimethylamine (2 M in THF) were purchased from Fisher Scientific, ammonia gas, methylamine (2 M in THF) from Sigma-Aldrich and all were used without further purification. $^{\text{EtO}}$PcFe,[23] $^{t\text{Bu}}$ArO•,[46] and $^{\text{Tr}}$ArO•[56] were prepared following previous reports. All other reagents were obtained from Sigma-Aldrich, Fisher Scientific, or VWR and used without further purification.

Spectroscopic Measurements. NMR spectra were obtained on an Agilent Technologies 400 MHz DD2, Varian Unity Inova 500 MHz, Bruker Avance NEO 500 MHz,

or a Varian 600 MHz spectrometer, and referenced to residual solvent. Chemical shifts (δ) are recorded in ppm and the coupling constants are in Hz. ^{1}H NMR assignments are supported by 2D NMR experiments. J. Young air-tight adaptors were used for air- and water-sensitive compounds. UV-Vis spectra were collected on a Shimadzu UV-2401PC spectrophotometer. All measurements were performed on recrystallized product. All stock solutions and dilutions were prepared by mass. ATR FT-IR spectra were collected on a Bruker Alpha Platinum with an ATR Quicksnap® Sampling Module. All measurements were performed on recrystallized product. ^{57}Fe Mössbauer spectroscopy was performed using a SEECo Model W304 resonant gamma-ray spectrometer (activity = 50 mCi +/- 10 %, ^{57}Co/Rh source manufactured by Ritverc) equipped with a Janis Research Model SVT-400 cryostat system. The source linewidth was <0.12 mm/s for the innermost lines of a 25 micron □-Fe foil standard. Isomer shifts are referenced to Fe foil at room temperature. All ^{57}Fe Mössbauer samples were prepared using 20-30 mg of powdered material and measured at 90 K unless otherwise stated. Data was fitted using a custom Igor Pro (Wavemetrics) macro package developed by the Betley group at Harvard University.

Mass Spectrometry. Mass spectra were collected on a Shimadzu GC-2010 gas chromatograph coupled to a Shimadzu GCMS-QP2010 mass spectrometer. The instrument is equipped with a 30 m × 0.25 mm Agilent DB-1 column with a dimethylpolysiloxane stationary phase (0.25 μm). Helium was used as the carrier gas.

X-ray Crystallography. Data was collected on a Bruker KAPPA APEX II diffractometer equipped with an APEX II CCD detector using a TRIUMPH monochromator with a Mo Kα X-ray source (α = 0.71073 Å). The crystals were mounted on a cryoloop under

Paratone-N oil, and all data were collected at 110 K using an Oxford nitrogen gas cryostream system. A hemisphere of data was collected using ω scans with 0.5° frame widths. Data collection and cell parameter determination were conducted using the SMART program. Integration of the data frames and final cell parameter refinement were performed using SAINT software. Absorption correction of the data was carried out using SADABS. Structure determination was done using direct or Patterson methods and difference Fourier techniques. All hydrogen atom positions were idealized and rode on the atom of attachment. Structure solution, refinement, graphics, and creation of publication materials were performed using SHELXTL or OLEX[2].

Density Functional Theory Calculations. DFT calculations were carried out on a modified version of PcFe wherein ethoxide groups were exchanged for methoxide groups to avoid issues with rotation in the ethyl groups. All calculations employed the BP86 functional[57, 58] with Grimme's D3 dispersion correction with Becke-Johnson damping.[59, 60] Geometry optimization calculations were carried out using the Karlsruhe double-ζ def2-SVP basis set.[61] Subsequent frequency calculations at the same level of theory were used to obtain zero-point energy (ZPE) and entropic and enthalpic corrections at 298.15 K. These frequency calculations were also used to validate that each point was indeed a minimum on the potential energy surface. The final electronic energies were obtained from a single point calculation at the previous geometry using the def2-TZVP basis set.[61] Solvation in benzene was approximated using the SMD solvation method.[62] The electronic energy is combined with ZPE, entropic/enthalpic contributions, and solvation energy to give the free energies of all complexes reported here. Bond dissociation energies were referenced to 2,4,6-tri-*tert*-butyl phenoxyl radical using the experimental BDFE in benzene.[9] While all low-, mid-, and high

spin geometries were calculated, only the lowest energy state is presented here. The preferred spin state of each complex can be found in the supplementary information. All calculations were completed using Orca 4.1.2.[63]

Synthesis of 2.1. Under an inert atmosphere, $^{EtO}PcH_2$ (1.00 g, 1.15 mmol, 1 equiv.) and $Fe(OAc)_2$ (0.24 g, 1.38 mmol, 1.2 equiv.) were slurred in 15 mL of toluene and heated to reflux for 24 h resulting in a dark green solution. After cooling, all volatiles were removed under reduced pressure, yielding a dark green powder. The crude product was transferred to a glass frit and washed with 25 mL of pentane and 25 mL of EtO_2. The resulting dark green filter was extracted with 50 mL of DCM and the filtrate was reduced to ca. 10 mL under reduced pressure, and layered with pentane (10 mL) at room temperature. Yield: 0.840 g (75.8%). Single crystals suitable for XRD studies were obtained by vapor diffusion of hexanes into a con- centrated solution of the product in benzene at room temperature. ^{1}H NMR (600 MHz, CD_2Cl_2): δ 9.90 (q, J = 7 Hz, 16H, OCH_2CH_3), 4.32 (t, J = 7 Hz, 24H, OCH_2CH_3), 3.44 (s, 8H, C_6H_2). λ_{max} (ε) = 765 nm (41 868 M^{-1} cm^{-1}). MS (MALDI-TOF): calculated 920.29 (M^+) found 920.40 (M^+).

Synthesis of 2.1-$(NH_3)_2$. In the glovebox, 0.300 g (0.326 mmol, 1 equiv) of **1** was mixed in ca. 6 mL benzene or THF in a 100 mL Schlenk flask equipped with a magnetic stir bar. The mixture was brought to the Schlenk line and degassed using three freeze-pump-thaw cycles, followed by addition of ca. 1.5 atm of NH_3 (excess). The solution was allowed to stir for 1 h under NH_3. All volatiles were removed under reduced pressure, resulting in a green crude powder of **2.1-$(NH_3)_2$**. The crude product was purified by dissolving in minimal benzene or THF and layering with pentane. Yield: 0.24 g (78%). Single crystals suitable for XRD studies were obtained by vapor diffusion of Et_2O over a saturated THF solution of **2.1-$(NH_3)_2$** at -35 °C. ^{1}H NMR (500 MHz, C_6D_6): δ 7.42 (s, 8H, C_6H_2), 5.14 (q, *J* = 7.5 Hz, 16H,

OC*H*$_2$CH$_3$), 1.82 (t, *J* = 7.4 Hz, 24H, OCH$_2$C*H*$_3$), -9.17 (s, 6H, N*H*$_3$). $^{13}C^{64}$ NMR (500 MHz, C_6D_6): δ 150.9, 147.6, 133.9, 118.0, 68.2, 15.9. Mössbauer: δ = 0.29 mm/s, $|\Delta E_Q|$ = 1.14 mm/s. UV-Vis: λ_{max} = 714 nm (ε = 47,432 M^{-1} cm^{-1}). Anal. Calc. for $C_{48}H_{54}FeN_{10}O_8$: C, 60.38; H, 5.70; N, 14.67. Found: C, 60.11; H, 5.73; N, 14.46.

Synthesis of 2.1-(MeNH$_2$)$_2$. In the glovebox, 0.500 g (0.543 mmol, 1 equiv) of **1** was mixed in ca. 4 mL of THF in a vial equipped with a magnetic stir bar. To this, 1.0 mL of 2 M $MeNH_2$ in THF solution (2.00 mmol, 3.7 equiv) was added dropwise and the resulting green solution was stirred for 1 h. All volatiles were removed under reduced pressure resulting in a dark green powder of **2.1-(MeNH$_2$)$_2$**. Yield: 0.51 g (96%). Single crystals suitable for XRD studies were obtained by vapor diffusion of Et_2O over a saturated DCM solution of **2.1-(MeNH$_2$)$_2$** at -35 °C. ^{1}H NMR (500 MHz, C_6D_6): δ 7.41 (s, 8H, C_6H_2), 5.12 (q, *J* = 7.0 Hz, 16H, OC*H*$_2$CH$_3$), 1.81 (t, *J* = 7.0 Hz, 24H, OCH$_2$C*H*$_3$), -3.54 (t, *J* = 6.6 Hz, 6H, C*H*$_3$NH$_2$), -8.58 (q, *J* = 7.0 Hz, 4H, CH$_3$N*H*$_2$). $^{13}C^{64}$ NMR (500 MHz, C_6D_6): δ 151.01, 147.5, 133.6, 117.7, 68.0, 25.6 (*C*H$_3$NH$_2$), 15.7. Mössbauer: δ = 0.24 mm/s, $|\Delta E_Q|$ = 0.87 mm/s. UV-Vis: λ_{max} = 716 nm (ε = 36,102 M^{-1} cm^{-1}). Anal. Calc. for $C_{50}H_{58}FeN_{10}O_8$: C, 61.10; H, 5.95; N, 14.25. Found: C, 61.18; H, 5.71; N, 14.04.

Synthesis of 2.1-(Me$_2$NH)$_2$. In the glovebox, 0.300 g (0.326 mmol, 1 equiv) of **1** was mixed in ca. 3 mL of THF in a vial equipped with a magnetic stir bar. To this, 0.6 mL of 2 M Me_2NH in THF solution (1.20 mmol 3.7 equiv) was added dropwise and the resulting green solution was stirred for 1 h. All volatiles were removed under reduced pressure, resulting in a dark green powder of **2.1-(Me$_2$NH)$_2$**. Yield: 0.32 g (97%). Single crystals suitable for XRD studies were obtained by vapor diffusion of Et_2O over a saturated DCM solution of **2.1-(Me$_2$NH)$_2$** at -35 °C. ^{1}H NMR (400 MHz, C_6D_6): δ 7.40 (s, 8H, C_6H_2), 5.09 (q, *J* = 7.0 Hz,

16H, OC*H*$_2$CH$_3$), 1.79 (t, *J* = 7.0 Hz, 24H, OCH$_2$C*H*$_3$), -3.47 (d, *J* = 6.2 Hz, 12H, (C*H*$_3$)$_2$NH), -8.28 (m, 2H, (CH$_3$)$_2$N*H*). $^{13}C^{64}$ NMR (500 MHz, C_6D_6): δ 151.0, 148.0, 133.9, 117.6, 68.1, 35.2 ((*C*H$_3$)$_2$NH), 15.8. Mössbauer: δ = 0.25 mm/s, $|\Delta E_Q|$ = 0.99 mm/s. UV-Vis: λ_{max} = 713 nm (ε = 37,992 M^{-1} cm^{-1}). Anal. Calc. for $C_{52}H_{62}FeN_{10}O_8$: C, 61.78; H, 6.18; N, 13.85. Found: C, 61.59; H, 5.91; N, 13.67.

Synthesis of 2.1-OAr^{tBu}. In the glovebox, 0.050 g (0.0543 mmol, 1 equiv) of **1** was dissolved in ca. 1.5 mL of DCM in a vial equipped with a magnetic stir bar. To this, $^{t\text{Bu}}$ArO• (0.0155 g, 0.0594 mmol, 1.1 equiv) in ca. 1 mL of DCM was added dropwise and the resulting green solution was stirred overnight. All volatiles were removed under reduced pressure, resulting in a dark green powder. The crude mixture was washed with pentane (3 x 3 mL) over Celite on a glass frit and extracted with ca. 5 mL of DCM. The DCM fraction was brought to dryness under reduced pressure, affording a dark green powder of **2.1-OAr^{tBu}**. The crude product was further purified by dissolving in minimal DCM and layering with pentane. Yield: 0.0533 g (83%). Single crystals suitable for XRD studies were obtained by vapor diffusion of Et$_2$O over a saturated DCM solution at -35 °C. ^{1}H NMR (500 MHz, C_6D_6): δ 17.10 (b, 8H), 6.07 (b, 16H), 2.51 (b, 24H). Mössbauer: δ = 0.26 mm/s, $|\Delta E_Q|$ = 0.28 mm/s. UV-Vis: λ_{max} = 775 nm (ε = 96154 M^{-1} cm^{-1}).

Synthesis of 2.1-(MeN=CH$_2$)$_2$. In the glovebox, 0.050 g (0.049 mmol, 1 equiv) of **2.1-(Me$_2$NH)$_2$** was dissolved in ca. 1.5 mL of benzene in a vial equipped with a magnetic stir bar. To this, 0.053 g of $^{t\text{Bu}}$ArO• (0.203 mmol, 4.1 equiv) in ca. 1.5 ml of benzene was added dropwise and the resulting green solution was stirred for 4 h. All volatiles were removed under reduced pressure, resulting in a dark green powder. The crude solid was transferred to a glass frit with Celite and washed with pentane (3 x 3 mL), then extracted with ca. 5 mL of DCM.

The DCM fraction was then brought to dryness under reduced pressure, affording a dark green powder of **2.1-(MeN=CH$_2$)$_2$**. The crude product was further purified by dissolving in minimal DCM and layering with pentane. Yield: 0.0368 g (73.9%). Single crystals suitable for XRD studies were obtained by vapor diffusion of Et_2O over a saturated DCM solution at -35 °C. ^{1}H NMR (500 MHz, C_6D_6): 7.41 (s, 8H, C_6H_2), 5.07 (q, J = 7.0 Hz, 16H, OCH_2CH_3), 2.19 (d, J = 13.1 Hz, 2H, CH_3NCH_2), 1.77 (t, J = 7.0 Hz, 24H, OCH_2CH_3), 0.72 (d, J = 13.0 Hz, 2H, CH_3NCH_2), -2.19 (s, 6H, CH_3NCH_2). $^{13}C^{64}$ NMR (500 MHz, C_6D_6): δ 161.1(CH_3NCH_2), 151.1, 147.2, 133.5, 117.9, 68.2, 45.4 (CH_3NCH_2), 15.8. Mössbauer: δ = 0.25 mm/s, $|\Delta E_Q|$ = 0.92 mm/s. UV-Vis: λ_{max} = 706 nm (ε = 100,976 M^{-1} cm^{-1}). Anal. Calc. for $C_{52}H_{58}FeN_{10}O_8$: C, 62.03; H, 5.81; N, 13.91. Found: C, 61.79; H, 5.57; N, 13.67.

Synthesis of 2.1-(MeNH$_2$)(CN). In the glovebox, 0.046 g (0.047 mmol, 1 equiv) of **2.1-(MeNH$_2$)$_2$** was dissolved in ca. 1.5 mL of benzene in a vial equipped with a magnetic stir bar. To this, 0.0633 g of $^{t\text{Bu}}$ArO• (0.243 mmol, 5.1 equiv) in ca. 2 mL of benzene was added dropwise. The resulting green solution was stirred for 3 h and all volatiles were removed under reduced pressure, resulting in a dark blue green powder. The crude solid was transferred to a glass frit with Celite and washed with pentane (3 x 3 mL), then extracted with ca. 5 mL of DCM. The DCM fraction was brought to dryness under reduced pressure, affording a dark green powder of **2.1-(MeNH$_2$)(CN)**. The crude product was further purified by dissolving in minimal DCM and layering with pentane. Yield: 39.6 mg (86.7%). Single crystals suitable for XRD studies were obtained by vapor diffusion of pentane onto a saturated THF solution at -35 °C. NMR spectra are silent due to paramagnetism. Mössbauer: δ = 0.25 mm/s, $|\Delta E_Q|$ = 0.92 mm/s. UV-Vis: λ_{max} = 763 nm (ε = 48,645 M^{-1} cm^{-1}). Anal. Calc. for $C_{50}H_{53}FeN_{10}O_8$: C, 61.41; H, 5.46; N, 14.32. Found: C, 60.68; H, 5.13; N, 14.05.

Catalytic C–N coupling of $^{t\mathrm{Bu}}$ArO• with NH_3. In the glovebox, 0.001 g (0.001 mmol, 1 equiv) of **2.1** was dissolved in ca. 0.2 mL of C_6D_6 and transferred to a J. Young NMR tube. To this, a C_6D_6 (0.4 mL) solution of $^{t\mathrm{Bu}}$ArO• (0.085 g, 0.300 mmol, 300 equiv) was added. The tube was sealed and connected to the Schlenk line. The solution was degassed using three freeze-pump-thaw cycles, followed by addition of ca. 1.5 atm of NH_3. All volatiles were removed under reduced pressure after 24 h. The crude solid was dissolved in ca. 3 mL of pentane and insoluble material was filtered over Celite. The pentane fraction was then brought to dryness under reduced pressure, affording a mixture of $^{t\mathrm{Bu}}$ArOH and **2.2**. The mixture was analyzed by ^{1}H NMR spectroscopy (see Supporting Information).

Stoichiometric C–N coupling of $^{t\mathrm{Bu}}$ArO• with 2.1-$(NH_3)_2$. In the glovebox, **2.1-$(NH_3)_2$** (0.005 g, 0.005 mmol, 1 equiv) was dissolved in ca. 0.2 mL of C_6D_6 and transferred to an NMR tube. To this, a C_6D_6 (0.3 mL) solution of $^{t\mathrm{Bu}}$ArO• (0.0083 g, 0.032 mmol, 6.1 equiv) and hexamethylbenzene (0.0017 g, 0.010 mmol, 2 equiv) was added. The reaction was monitored by ^{1}H NMR spectroscopy (see Supporting Information). The analogous study with **1-$(ND_3)_2$** in C_6H_6 was also performed and was monitored by ^{2}H NMR spectroscopy**.**

Attempted catalytic ammonia oxidation with $^{\mathrm{Tr}}$ArO•. In the glovebox, 0.002 g (0.002 mmol, 1 equiv) of **1** was dissolved in ca. 0.3 mL of C_6D_6 and transferred to a J. Young NMR tube. To this, a C_6D_6 (0.3 mL) solution of $^{\mathrm{Tr}}$ArO• (0.090 g, 0.200 mmol, 93 equiv) was added. The tube was sealed and connected to the Schlenk line. The solution was degassed using three freeze-pump-thaw cycles, followed by addition of ca. 1.5 atm of NH_3 or $^{15}NH_3$. The reactions were monitored by ^{1}H and ^{15}N NMR spectroscopy, respectively (see Supporting Information).

Generation of 1,3,5-trimethyl-1,3,5-triazinane and 2.1-$(PMe_3)_2$ through C–N bond formation. In the glovebox, **2.1-$(MeN{=}CH_2)_2$** (0.019 g, 0.020 mmol, 1 equiv) was dissolved in ca. 0.5 mL of C_6D_6 and transferred to a J. Young NMR tube. To this, 0.005 mL of PMe_3 (0.049 mmol, 2.6 equiv) was added and the tube was sealed. The reaction was monitored by ^1H and ^{31}P NMR spectroscopy (see Supporting Information).

Control reaction of ^{tBu}ArO• with Me_2NH: Observation of 2.2-NMe_2. In the glovebox, $^{t\text{Bu}}$ArO• (0.028 g, 0.1 mmol, 1 equiv) was dissolved in ca. 0.4 mL of C_6D_6 and transferred to a J. Young NMR tube. The tube was sealed and connected to the Schlenk line. The solution was degassed using three freeze-pump-thaw cycles, followed by addition of ca. 1.5 atm of Me_2NH_2. The reaction was monitored by ^1H NMR spectroscopy and GC-MS (see Supporting Information).

2.5 Appendix

Computational Methods Density functional theory calculations were completed in order to understand the order in which hydrogen atom abstraction occurs from amine-bound Fe-phthlalocyanine complexes. In order to simplify the ligand and eliminate extra rotational degrees of freedom, methoxy groups were substituted for the ethoxy groups in the synthesized compounds with the understanding that their electronic properties would be similar.[65] All calculations were completed using the BP86 functional[57] with Grimme's D3 dispersion correction with the Becke-Johnson damping scheme.[59, 60] Geometry optimization, frequency calculations, and single point solvation energies were calculated using the Karlsruhe def2-SVP basis set[61] with the def2/J auxiliary basis set.[66] Frequency calculations at 298.15 K were the source of zero-point energies (ZPE) and thermal corrections to the free energy. They also were

used to ensure that intermediates were minima on the potential energy surface. A large basis set single point calculation was used as the source for the final electronic energy and employed a def2-TZVP basis set.[61] Single point solvation in benzene was calculated using the SMD implicit solvation model.[62] All free energy calculations were completed in Orca 4.1.2.[67] Follow up NBO calculations were completed using the standalone NBO 6.0 program.[68]

Molecular Geometries

All structures referenced in this work can be found in the accompanying XYZ file. This can be opened with free software like MacmolPLT or Mercury, which can be found online. (https://www.ccdc.cam.ac.uk/mercury/).

Table 2.1 Final Free Energies (with spin state). Names correspond to name in .xyz file.

Molecule	**Free energy (kcal/mol)**
Fe_Pc_CHN_sing_geom1	-2533498.614
Fe_Pc_CN_doub_geom1	-2533135.968
Fe_Pc_NC_doub_geom1	-2533126.097
Fe_Pc_NCH_sing_geom1 (end on)	-2533514.443
Fe_Pc_NCH_sing_geom2 (side on)	-2533498.671

Fe_Pc_NCH2_doub_geom1	-2533875.928
Fe_Pc_NCH3_sing_geom1	-2534227.558
Fe_Pc_NCH3_trip_geom1	-2534222.262
Fe_Pc_NH2C_doub_geom1	-2533816.990
Fe_Pc_NH2C_doub_geom1	-2533816.990
Fe_Pc_NH2CH_sing_geom1	-2534212.926
Fe_Pc_NH2CH_trip_geom1	-2534191.180
Fe_Pc_NH2CH2_doub_geom1	-2534613.286
Fe_Pc_NHC_trip_geom1	-2533488.513
Fe_Pc_NHCH_doub_geom1	-2533852.345
Fe_Pc_NHCH2_sing_geom1	-2534265.899
Fe_Pc_NHCH3_doub_geom1	-2534628.404
Fe_Pc_2NH3_sing_geom1	-2485707.878
Fe_Pc_NH2_NH3_doub_geom2	-2485311.773
Fe_Pc_NH_NH3_trip_geom1	-2484906.594
Fe_Pc_ArONH2_NH3_sing_geom1	-2973896.705
Fe_Pc_2NH2CH3_sing_geom1	-2535021.051

2.6 References

(1) IEA. *Producing ammonia and fertilizers: new opportunities from renewables*. IEA, 2017. https://www.ee.co.za/wp-content/uploads/2017/06/Producing-ammonia-and-fertilizers-new-opportunities-from-renewables.pdf (accessed 2020 12/19/2020).

(2) Service, R. F. Liquid sunshine. *Science* **2018**, *361* (6398), 120-123.

(3) Dunn, P. L.; Johnson, S. I.; Kaminsky, W.; Bullock, R. M. Diversion of Catalytic C–N Bond Formation to Catalytic Oxidation of NH_3 through Modification of the Hydrogen Atom Abstractor. *Journal of the American Chemical Society* **2020**, *142* (7), 3361-3365.

(4) Bhattacharya, P.; Heiden, Z. M.; Chambers, G. M.; Johnson, S. I.; Bullock, R. M.; Mock, M. T. Catalytic Ammonia Oxidation to Dinitrogen by Hydrogen Atom Abstraction. *Angewandte Chemie International Edition* **2019**, *58*, 11618-11624.

(5) Nakajima, K.; Toda, H.; Sakata, K.; Nishibayashi, Y. Ruthenium-catalysed oxidative conversion of ammonia into dinitrogen. *Nature Chemistry* **2019**, *11* (8), 702-709.

(6) Habibzadeh, F.; Miller, S. L.; Hamann, T. W.; Smith, M. R. Homogeneous electrocatalytic oxidation of ammonia to N_2 under mild conditions. *Proceedings of the National Academy of Sciences* **2019**, *116* (8), 2849-2853.

(7) Keener, M.; Peterson, M.; Hernández Sánchez, R.; Oswald, V. F.; Wu, G.; Ménard, G. Towards Catalytic Ammonia Oxidation to Dinitrogen: A Synthetic Cycle by Using a Simple Manganese Complex. *Chemistry - A European Journal* **2017**, *23* (48), 11479-11484.

(8) Zott, M. D.; Garrido-Barros, P.; Peters, J. C. Electrocatalytic Ammonia Oxidation Mediated by a Polypyridyl Iron Catalyst. *ACS Catalysis* **2019**, *9* (11), 10101-10108.

(9) Warren, J. J.; Tronic, T. A.; Mayer, J. M. Thermochemistry of Proton-Coupled Electron Transfer Reagents and its Implications. *Chemical Reviews* **2010**, *110* (12), 6961-7001.

(10) Dunn, P. L.; Cook, B. J.; Johnson, S. I.; Appel, A. M.; Bullock, R. M. Oxidation of Ammonia with Molecular Complexes. *Journal of the American Chemical Society* **2020**, *142* (42), 17845-17858.

(11) Spiegel, D. A.; Wiberg, K. B.; Schacherer, L. N.; Medeiros, M. R.; Wood, J. L. Deoxygenation of Alcohols Employing Water as the Hydrogen Atom Source. *Journal of the American Chemical Society* **2005**, *127* (36), 12513-12515.

(12) Cuerva, J. M.; Campaña, A. G.; Justicia, J.; Rosales, A.; Oller-López, J. L.; Robles, R.; Cárdenas, D. J.; Buñuel, E.; Oltra, J. E. Water: The Ideal Hydrogen-Atom Source in Free-Radical Chemistry Mediated by Ti^{III} and Other Single-Electron-Transfer Metals? *Angewandte Chemie International Edition* **2006**, *45* (33), 5522-5526.

(13) Hulley, E. B.; Bonanno, J. B.; Wolczanski, P. T.; Cundari, T. R.; Lobkovsky, E. B. Pnictogen-Hydride Activation by $(silox)_3Ta$ (silox = $^tBu_3SiO$); Attempts to Circumvent the Constraints of Orbital Symmetry in N_2 Activation. *Inorganic Chemistry* **2010**, *49* (18), 8524-8544.

(14) Paradas, M.; Campaña, A. G.; Jiménez, T.; Robles, R.; Oltra, J. E.; Buñuel, E.; Justicia, J.; Cárdenas, D. J.; Cuerva, J. M. Understanding the Exceptional Hydrogen-Atom Donor

Characteristics of Water in Ti^{III}-Mediated Free-Radical Chemistry. *Journal of the American Chemical Society* **2010**, *132* (36), 12748-12756.

(15) Fang, H.; Ling, Z.; Lang, K.; Brothers, P. J.; de Bruin, B.; Fu, X. Germanium(III) corrole complex: reactivity and mechanistic studies of visible-light promoted N–H bond activations. *Chemical Science* **2014**, *5* (3), 916-921, 10.1039/C3SC52326H.

(16) Bezdek, M. J.; Guo, S.; Chirik, P. J. Coordination-induced weakening of ammonia, water, and hydrazine X–H bonds in a molybdenum complex. *Science* **2016**, *354* (6313), 730-733.

(17) Bezdek, M. J.; Chirik, P. J. Interconversion of Molybdenum Imido and Amido Complexes by Proton-Coupled Electron Transfer. *Angewandte Chemie International Edition* **2018**, *57*, 2224-2228.

(18) Estes, D. P.; Grills, D. C.; Norton, J. R. The Reaction of Cobaloximes with Hydrogen: Products and Thermodynamics. *Journal of the American Chemical Society* **2014**, *136* (50), 17362-17365.

(19) Semproni, S. P.; Milsmann, C.; Chirik, P. J. Four-Coordinate Cobalt Pincer Complexes: Electronic Structure Studies and Ligand Modification by Homolytic and Heterolytic Pathways. *Journal of the American Chemical Society* **2014**, *136* (25), 9211-9224.

(20) Tarantino, K. T.; Miller, D. C.; Callon, T. A.; Knowles, R. R. Bond-Weakening Catalysis: Conjugate Aminations Enabled by the Soft Homolysis of Strong N–H Bonds. *Journal of the American Chemical Society* **2015**, *137* (20), 6440-6443.

(21) Bhattacharya, P.; Heiden, Z. M.; Wiedner, E. S.; Raugei, S.; Piro, N. A.; Kassel, W. S.; Bullock, R. M.; Mock, M. T. Ammonia Oxidation by Abstraction of Three Hydrogen Atoms from a Mo–NH_3 Complex. *Journal of the American Chemical Society* **2017**, *139*, 2916-2919.

(22) Cook, B. J.; Johnson, S. I.; Chambers, G. M.; Kaminsky, W.; Bullock, R. M. Triple hydrogen atom abstraction from Mn–NH_3 complexes results in cyclophosphazenium cations. *Chemical Communications* **2019**, *55* (93), 14058-14061, 10.1039/C9CC06915A.

(23) Peterson, M.; Hunt, C.; Wang, Z.; Heinrich, S. E.; Wu, G.; Ménard, G. Synthesis, characterization, and electrochemical properties of a first-row metal phthalocyanine series. *Dalton Transactions* **2020**, *49*, 16268-16277, 10.1039/D0DT01372B.

(24) Diamond, S. E.; Tom, G. M.; Taube, H. Ruthenium promoted oxidation of amines. *Journal of the American Chemical Society* **1975**, *97* (10), 2661-2664.

(25) Keene, F. R.; Salmon, D. J.; Meyer, T. J. Oxidation of primary amines bound to bis(2,2'-bipyridine)ruthenium(II). *Journal of the American Chemical Society* **1976**, *98* (7), 1884-1889.

(26) Chen, B.; Wang, L.; Gao, S. Recent Advances in Aerobic Oxidation of Alcohols and Amines to Imines. *ACS Catalysis* **2015**, *5* (10), 5851-5876.

(27) Clares, M. P.; Acosta-Rueda, L.; Castillo, C. E.; Blasco, S.; Jiménez, H. R.; García-España, E.; Basallote, M. G. Iron(II) Complexes with Scorpiand-Like Macrocyclic Polyamines: Kinetico-Mechanistic Aspects of Complex Formation and Oxidative Dehydrogenation of Coordinated Amines. *Inorganic Chemistry* **2017**, *56* (8), 4400-4412.

(28) Dutta, I.; Yadav, S.; Sarbajna, A.; De, S.; Hölscher, M.; Leitner, W.; Bera, J. K. Double Dehydrogenation of Primary Amines to Nitriles by a Ruthenium Complex Featuring Pyrazole Functionality. *Journal of the American Chemical Society* **2018**, *140* (28), 8662-8666.

(29) Evans, D. F. 400. The determination of the paramagnetic susceptibility of substances in solution by nuclear magnetic resonance. *Journal of the Chemical Society (Resumed)* **1959**, (0), 2003-2005, 10.1039/JR9590002003.

(30) Dale, B. W.; Williams, R. J. P.; Edwards, P. R.; Johnson, C. E. Mössbauer spectra of compounds containing iron(II) in strong-field tetragonal environments. *Transactions of the Faraday Society* **1968**, *64* (0), 620-629, 10.1039/TF9686400620.

(31) Bell, N. A.; Brooks, J. S.; Robinson, J. K.; Thorpe, S. C. Variable-temperature 57Fe Mössbauer studies of the α and β phases of iron phthalocyanine. *Journal of the Chemical Society, Faraday Transactions* **1998**, *94* (20), 3155-3159, 10.1039/A804848G.

(32) Tomyn, S.; Haukka, M.; Nedelkov, R. Diammine{N-[2-(hydroxyimino)propionyl]-N'-[2-(oxidoimino)propionyl]propane-1,3-diaminido-[kappa]^{4}N,N',N'',N'''}iron(III). *Acta Crystallographica Section E* **2012**, *68* (12), m1568-m1569.

(33) McQuarters, A. B.; Goodrich, L. E.; Goodrich, C. M.; Lehnert, N. Disproportionation of O-Benzylhydroxylamine Catalyzed by a Ferric Bis-Picket Fence Porphyrin Complex. *Zeitschrift für anorganische und allgemeine Chemie* **2013**, *639* (8-9), 1520-1526.

(34) Bouwkamp, M. W.; Lobkovsky, E.; Chirik, P. J. Bis(imino)pyridine Ligand Deprotonation Promoted by a Transient Iron Amide. *Inorganic Chemistry* **2006**, *45* (1), 2-4.

(35) Ouedraogo, G. V.; More, C.; Richard, Y.; Benlian, D. Charge-transfer and Moessbauer spectra of axially substituted iron phthalocyanines. *Inorganic Chemistry* **1981**, *20* (12), 4387-4393.

(36) Hunt, C.; Peterson, M.; Anderson, C.; Chang, T.; Wu, G.; Scheiner, S.; Ménard, G. Switchable Aromaticity in an Isostructural Mn Phthalocyanine Series Isolated in Five Separate Redox States. *Journal of the American Chemical Society* **2019**, *141* (6), 2604-2613.

(37) Dale, B. W. Effect of axial ligands upon the electronic absorption spectrum of phthalocyanineiron(II). *Transactions of the Faraday Society* **1969**, *65* (0), 331-339, 10.1039/TF9696500331.

(38) Ough, E. A.; Stillman, M. J. Analysis of the absorption and magnetic circular dichroism spectra of iron(II) phthalocyanine. *Inorganic Chemistry* **1994**, *33* (3), 573-583.

(39) Hedoyatullah, M.; Thevenet, F. Oxydation d'Amines Aromatiques Primaires en Présence du Radical Tritertiobutyl-2,4,6 Phénoxyle. *Bulletin des Sociétés Chimiques Belges* **1987**, *96* (4), 311-323.

(40) Müller, H.; Seidel, W.; Görls, H. Zur Chemie des Dimesityleisens. X. Mesityleisenkomplexe $[FeMes(X)]_2$ mit zentraler $\{Fe_2(\mu\text{-}Mes)_2\}$-Einheit (Mes = C_6H_2-2,4,6-$(CH_3)_3$). *Zeitschrift für anorganische und allgemeine Chemie* **1996**, *622* (11), 1968-1974.

(41) Ercolani, C.; Monacelli, F.; Dzugan, S.; Goedken, V. L.; Pennesi, G.; Rossi, G. X-Ray crystal structure of μ-oxo-bis[(1-methylimidazole)-phthalocyaninatoiron(III)] and comments on the molecular structure and chemistry of oxo-bridged iron phthalocyaninate dimers. *Journal of the Chemical Society, Dalton Transactions* **1991**, (5), 1309-1315, 10.1039/DT9910001309.

(42) Gorun, S. M.; Rathke, J. W.; Chen, M. J. Long-range solid-state ordering and high geometric distortions induced in phthalocyanines by small fluoroalkyl groups. *Dalton Transactions* **2009**, (7), 1095-1097, 10.1039/B821000B.

(43) Walter, M. D.; White, P. S. Reactivity Studies on $[Cp'FeI]_2$: Monomeric Amido, Phenoxo, and Alkyl Complexes. *Inorganic Chemistry* **2012**, *51* (21), 11860-11872.

(44) MacLeod, K. C.; McWilliams, S. F.; Mercado, B. Q.; Holland, P. L. Stepwise N–H bond formation from N_2-derived iron nitride, imide and amide intermediates to ammonia. *Chemical Science* **2016**, *7* (9), 5736-5746, 10.1039/C6SC00423G.

(45) Bartlett, R. A.; Ellison, J. J.; Power, P. P.; Shoner, S. C. Synthesis and characterization of the homoleptic aryloxides $[M\{O(2,4,6\text{-tert-}Bu_3C_6H_2)\}_2]_2$ (M = manganese, iron), the adducts $[Mn(OCPh_3)_2(py)_2]$ and $[Fe(OCPh_3)_2(THF)_2]$, and the mixed complex $[Fe\{N(SiMe_3)_2\}\{.mu.\text{-}O(2,4,6\text{-tert-}Bu_3C_6H_2)\}]_2$: evidence for primarily ionic metal-oxygen bonding. *Inorganic Chemistry* **1991**, *30* (14), 2888-2894.

(46) Manner, V. W.; Markle, T. F.; Freudenthal, J. H.; Roth, J. P.; Mayer, J. M. The first crystal structure of a monomeric phenoxyl radical: 2,4,6-tri-tert-butylphenoxyl radical. *Chemical Communications* **2008**, (2), 256-258, 10.1039/B712872J.

(47) Mekhryakova, N. G.; Gulina, T. Y.; Li, V. D.; Bundina, N. I.; Kaliya, O. L.; Luk'yanets, E. A. Reaction of Iron Phthalocyanine with Oxygen: Critical Survey and New Data on the Structure of the Forming PcFe(II) μ-Oxo Dimer. *Russian Journal of General Chemistry* **2001**, *71* (4), 570-590.

(48) Ni, C.; Long, G. J.; Grandjean, F.; Power, P. P. Synthesis, Characterization, and Magnetism of Divalent Aryl Transition-Metal Complexes of the Simplest Dialkylamide, NMe_2: Rare T-Shaped Coordination at Chromium. *Inorganic Chemistry* **2009**, *48* (24), 11594-11600.

(49) Guillemin, J. C.; Denis, J. M. Flash vacuum thermolysis of α-aminonitriles and subsequent HCN removal on solid base, a 'one line' multistep sequence to reactive N-methyleneamines. *Journal of the Chemical Society, Chemical Communications* **1985**, (14), 951-952, 10.1039/C39850000951.

(50) Lalevée, J.; Allonas, X.; Fouassier, J.-P. N−H and α(C−H) Bond Dissociation Enthalpies of Aliphatic Amines. *Journal of the American Chemical Society* **2002**, *124* (32), 9613-9621.

(51) Mader, E. A.; Manner, V. W.; Markle, T. F.; Wu, A.; Franz, J. A.; Mayer, J. M. Trends in Ground-State Entropies for Transition Metal Based Hydrogen Atom Transfer Reactions. *Journal of the American Chemical Society* **2009**, *131* (12), 4335-4345.

(52) Nazran, A. S.; Griller, D. Hydrogen abstraction from amines: formation of aminyl vs. .alpha.-aminoalkyl radicals. *Journal of the American Chemical Society* **1983**, *105* (7), 1970-1971.

(53) Rittle, J.; Peters, J. C. Proton-Coupled Reduction of an Iron Cyanide Complex to Methane and Ammonia. *Angewandte Chemie International Edition* **2016**, *55* (40), 12262-12265.

(54) Masaki, M.; Takehiro, A.; Toshio, N.; Tamotsu, I.; Noriaki, H.; Hiroyuki, T. Structure and Physical Properties of Low-Dimensional Molecular Conductors, $[PXX][Fe^{III}(Pc)(CN)_2]$ and $[PXX][Co^{III}(Pc)(CN)_2]$ (PXX = *peri*-xanthenoxanthene, Pc = phthalocyaninato). *Bulletin of the Chemical Society of Japan* **2003**, *76* (10), 1935-1940.

(55) Geiss, A.; Vahrenkamp, H. M(μ-CN)Fe(μ-CN)M‘ Chains with Phthalocyanine Iron Centers: Preparation, Structures, and Isomerization. *Inorganic Chemistry* **2000**, *39* (18), 4029-4036.

(56) Teuber, H.-J.; Gross, H.-J. Beweis des monovalenten Charakters von Oxidationsreaktionen mit Kalium-nitrosodisulfonat durch ESR-Messungen, insbesondere an diffundierenden Lösungen. *Chemische Berichte* **1975**, *108* (6), 2097-2106.

(57) Becke, A. D. Density-functional exchange-energy approximation with correct asymptotic behavior. *Physical Review A* **1988**, *38* (6), 3098-3100.

(58) Perdew, J. P. Density-functional approximation for the correlation energy of the inhomogeneous electron gas. *Physical Review B* **1986**, *33* (12), 8822-8824.

(59) Grimme, S.; Antony, J.; Ehrlich, S.; Krieg, H. A consistent and accurate ab initio parametrization of density functional dispersion correction (DFT-D) for the 94 elements H-Pu. *The Journal of Chemical Physics* **2010**, *132* (15), 154104.

(60) Grimme, S.; Ehrlich, S.; Goerigk, L. Effect of the damping function in dispersion corrected density functional theory. *Journal of Computational Chemistry* **2011**, *32* (7), 1456-1465.

(61) Weigend, F.; Ahlrichs, R. Balanced basis sets of split valence, triple zeta valence and quadruple zeta valence quality for H to Rn: Design and assessment of accuracy. *Physical Chemistry Chemical Physics* **2005**, *7* (18), 3297-3305, 10.1039/B508541A.

(62) Marenich, A. V.; Cramer, C. J.; Truhlar, D. G. Universal Solvation Model Based on Solute Electron Density and on a Continuum Model of the Solvent Defined by the Bulk Dielectric Constant and Atomic Surface Tensions. *The Journal of Physical Chemistry B* **2009**, *113* (18), 6378-6396.

(63) Neese, F. Software update: the ORCA program system, version 4.0. *WIREs Computational Molecular Science* **2018**, *8* (1), e1327.

(64) Chitrakar, R.; Kanoh, H.; Miyai, Y.; Ooi, K. Recovery of Lithium from Seawater Using Manganese Oxide Adsorbent (H1.6Mn1.6O4) Derived from Li1.6Mn1.6O4. *Industrial & Engineering Chemistry Research* **2001**, *40* (9), 2054-2058.

(65) Hansch, C.; Leo, A.; Taft, R. W. A survey of Hammett substituent constants and resonance and field parameters. *Chem. Rev.* **1991**, *91* (2), 165-195.

(66) Weigend, F. Accurate Coulomb-fitting basis sets for H to Rn. *Phys. Chem. Chem. Phys.* **2006**, *8* (9), 1057-1065, 10.1039/B515623H.

(67) Neese, F. Software update: the ORCA program system, version 4.0. *Wiley Interdiscip. Rev. Comput. Mol. Sci.* **2017**, *8* (1), e1327, (acccessed 2018/05/23).

(68) Glendening, E. D.; Landis, C. R.; Weinhold, F. NBO 6.0: Natural bond orbital analysis program. *J. Comp. Chem.* **2013**, *34* (16), 1429-1437, (acccessed 2019/02/07).

Chapter 3

Synthesis and characterization of substituted carborane based chelating compounds

3.1 Introduction

As mentioned in chapter 1, studies have shown that reduction of *closo*-Cb to the *nido*-Cb results in cleavage of the C–C bond, cluster opening, and an increased bite angle from substituted donor ligands (**Figure 1.1**).[1-4] This redox-controlled chelation scheme was recently applied to the electrochemical capture and release of UO_2^{2+} from spent nuclear fuel mimics (**Figure 3.1**).[5] Diphenyl phosphine oxide ligand (-Ph_2P=O) were attached on to both carbon atoms in Cb as the donor groups to chelate UO_2^{2+}. The cycling experiments and NMR measurements demonstrated UO_2^{2+} was captured in the *nido*-form and released in the *closo*-form. Furthermore, Cb based capture of UO_2^{2+} can also be achieved in biphasic condition by extracting UO_2^{2+} from aqueous solution to organic DCE solution containing *nido*-Cb that was generated electrochemically. After removal of the aqueous layer post capture, the organic layer underwent electrochemical oxidation to regenerate *closo*-Cb and a fresh water layer was added to extract the released UO_2^{2+}. Cb based capture/release cycling was selective towards UO_2^{2+} over other heavy metal ions from the aqueous layer that mimic spent nuclear fuel **(Figure 3.1**).[6]

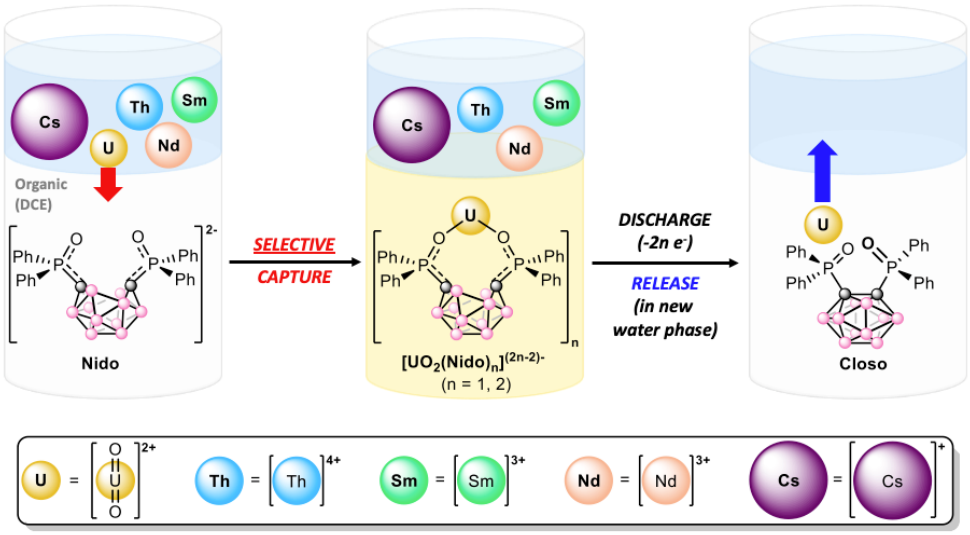

Figure 3.1. Depiction of the biphasic electrochemical selective capture and release of UO_2^{2+}

With the promising results from the UO_2^{2+} study, we extended this Cb based redox-controlled chelation scheme for lithium extraction as mentioned in Chapter 1. Our strategy to capture and release was to integrate Li^+ size selective crown ether donor groups onto Cb by linking the two carbons in the cluster. Studies showed when the cyclic donor group like crown ether was short and rigid, the carbon atoms remained adjacent during the reduction process instead of C–C cleavage.[3, 7, 8] Therefore, different sizes of crown ether was considered to attach on to the Cb as the donor groups. We synthesized and characterized a series of Cb based crown ethers as well as their *nido*-form, with details presented in this chapter.

3.2 Results and Discussion

3.2.1 Synthesis and characterization of *closo*- and *nido*- Cb 14-crown-4

We first targeted 14-crown-4 as the donor group for its high selectivity towards Li^+ over the other alkali metals (Chapter 1) by integrating onto Cb.[9] The Cb diol ($Cb(OH)_2$) precursor was synthesized first according to reported procedure.[10] We noticed the byproduct Cb mono-alcohol (Cb-OH) can also be used as starting material to produce more $Cb(OH)_2$ under the same experimental conditions. Next, potassium hydride (KH) was added to deprotonate $Cb(OH)_2$ to generate a better nucleophile and the resulting $Cb(OK)_2$ can be isolated after filtration, which contained 3 broad boron resonances as observed by ^{11}B NMR spectroscopy. Cb 14-crown-4 **(1)** was synthesized from $Cb(OK)_2$ (isolated or *in situ*) and the reported poly-ether, $TsO(CH_2)_3O(CR_2)_2O(CH_2)_3OTs$ ($R = CH_3$)[11] with tosylate (Ts) as the leaving group via a S_N2 reaction (**Scheme 3.1**). Four additional methyl groups were attached to the poly-ether linker for improving Li^+ selectivity.[12] The reaction mixture was heated

overnight in DMF at 75°C and after work-up, **1** can be isolated and identified by ^{1}H and ^{11}B NMR spectroscopy, with the solid-state structure of **1** shown in **Scheme 3.1**. The solid-state structure obtained by single crystal XRD studies revealed an elongated C–C bond distance of 1.767 Å in the Cb cluster due to donation of the oxygen lone pairs into the Cb cage. Under basic conditions, Cb cages are known to lose an BH group to form the deboronated $C_2B_9H_{11}^-$ species (11 vertices).[13] From this reaction of synthesis **1**, debronated Cb 14-crown-4 was also isolated (**1-b**) as a byproduct with distinct boron resonance at -35.68 and -39.33 ppm (**Figure 3.2**).

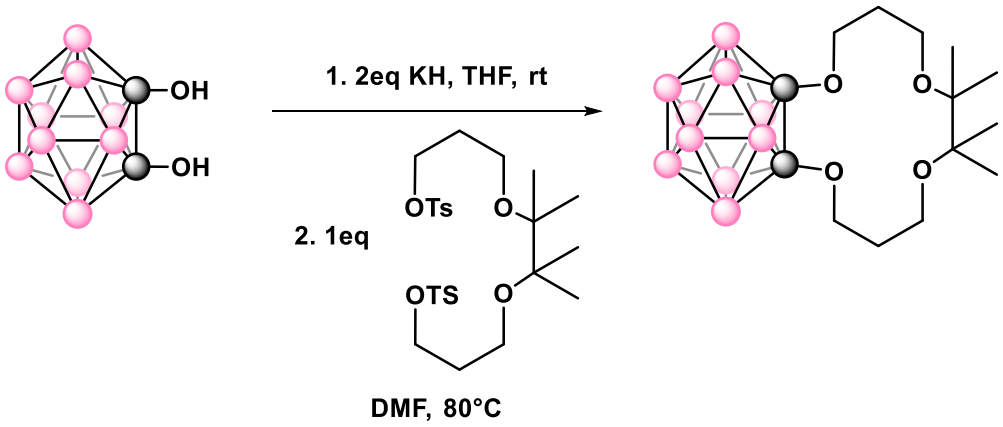

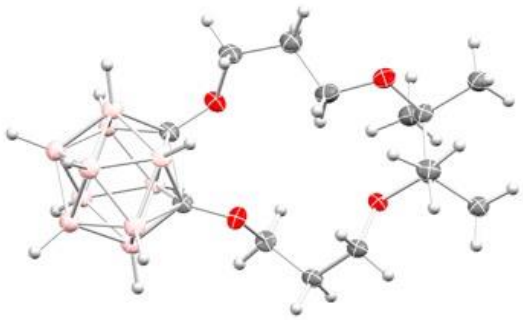

Scheme 3.1. Synthesis of Cb 14-crown-4 (**1**) and its solid-state molecular structure (bottom)

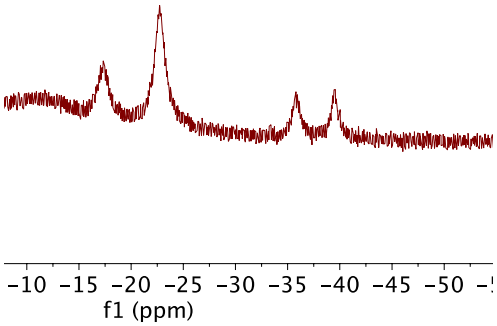

Figure 3.2. ^{11}B NMR (128 MHz) spectrum of **1-b** in $CDCl_3$

Compound **1** was analyzed by cyclic voltammetry (CV) in THF and revealed an electrochemically irreversible event with a peak reduction (**Figure 3.3**), which was far more negative than the potentials of phosphine oxide substituted Cb (−0.93 V and −1.11 V, **Figure 3.1**) likely due to the more electron-donating crown ether group donating into the cluster.[5] The addition of decamethyl cobaltocene or grinded Mg powder failed to reduce **1** to its *nido*-form because of its significant negative potential.

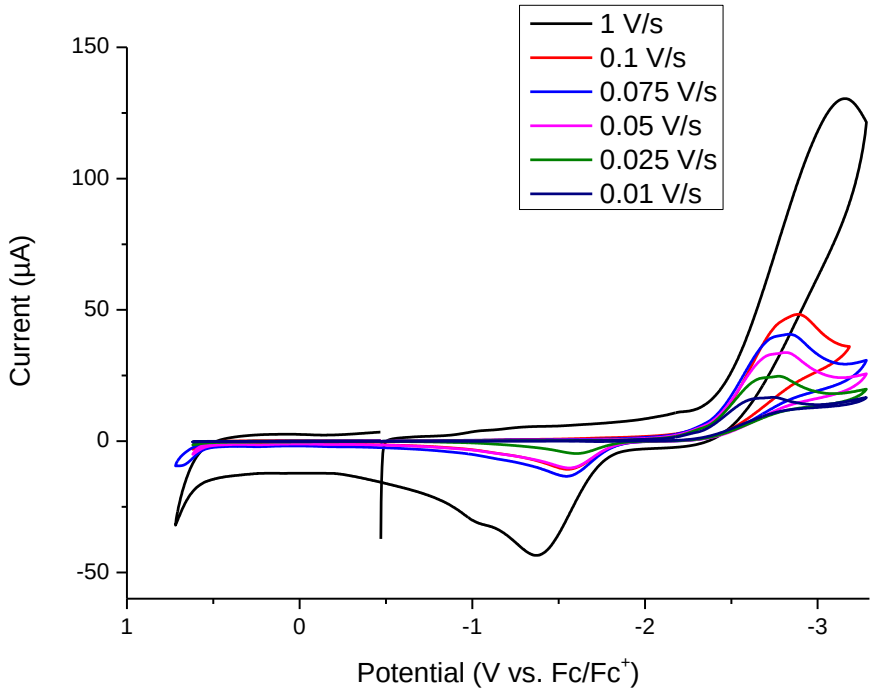

Figure 3.3. The cyclic voltammogram of **1** in THF at various scan rate. (Glassy carbon – WE, Pt wire – CE, Ag– RE)

Reduction of **1** was achieved by addition of 2.0 equiv of the strong reductant potassium naphthalenide (generated *in situ*) in dry THF, affording the *nido*-Cb 14-crown-4 with 2 potassium counter cations (**1-*nido*-K**, **Scheme 3.2**). Compared to **1**, the proton resonance from the crown ether shifted upfield after the reduction in ^{1}H NMR spectroscopy and the *nido*-Cb cluster had two broad boron peaks in ^{11}B NMR spectroscopy.

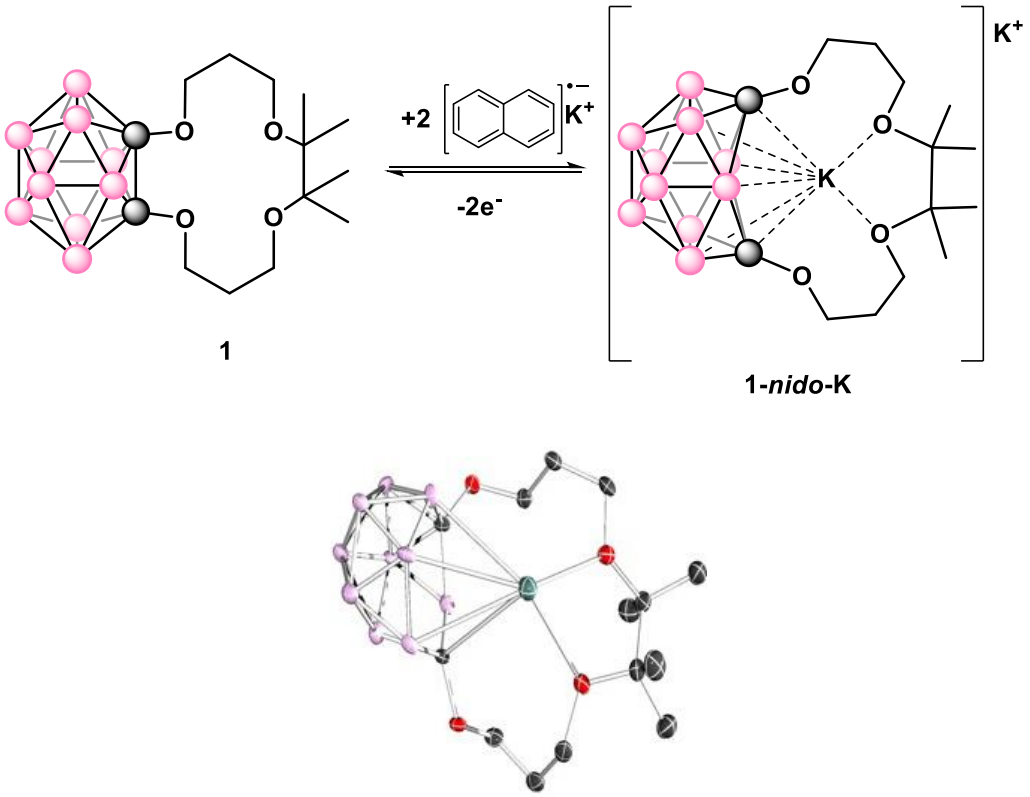

Scheme 3.2. Reduction of **1** to **1-*nido*-K** using potassium naphthalenide in THF and its solid-state molecular structure (bottom). Cocrystallized solvent molecules, all H atoms and the second K^+ have been omitted for clarity.

The solid-state structure of **1-*nido*-K** confirmed an open cage Cb cluster with C–C bond cleavage, and the donor bite angles became wider as the O–O distance (closest to Cb) increased from 2.931 Å to 5.040 Å after reduction. While one of the outer-sphere K^+ bridged between *nido*-Cb molecules, we noticed the second K^+ was partially inside the crown pocket, coordinated by 2 out of 4 crown ether oxygens along with the *nido*-Cb cluster which coordinated in an open-face η^6 fashion.[14, 15] These results indicate that a metal cation can be captured by Cb crown compounds. Addition of 2 equiv of ferrocenium hexafluorophosphate ([Fc][PF_6]) to **1-*nido*-K** resulted in its oxidation back to **1** cleanly, as confirmed by ^{1}H and ^{11}B NMR spectroscopy, indicating switching between the *closo*- and the *nido* forms was

chemically reversible for **1**. The mono reduced radical intermediate was unstable and unable to be obtained, evidenced by mixing 1 equiv potassium naphthalenide and **1** resulting in a mixture of **1** and **1-*nido*-K**.

3.2.2 Reactivity of *nido*- Cb 14-crown-4

Compound **1-*nido*-K** was found to be quite reactive as it slowly self-reacted in MeCN to form a new *nido*-Cb 14-crown-4 (**1-*nido*-b**) species at room temperature under inert atmosphere (**Figure 3.4**) with a small amount of deboronated byproduct being observed. Formation of **1-*nido*-b** can be accelerated by applying heat or adding water, acid, metal salts with smaller ion radius ($CaCl_2$, $Mg(OTf)_2$), or $[Bu_4N][Cl]$.

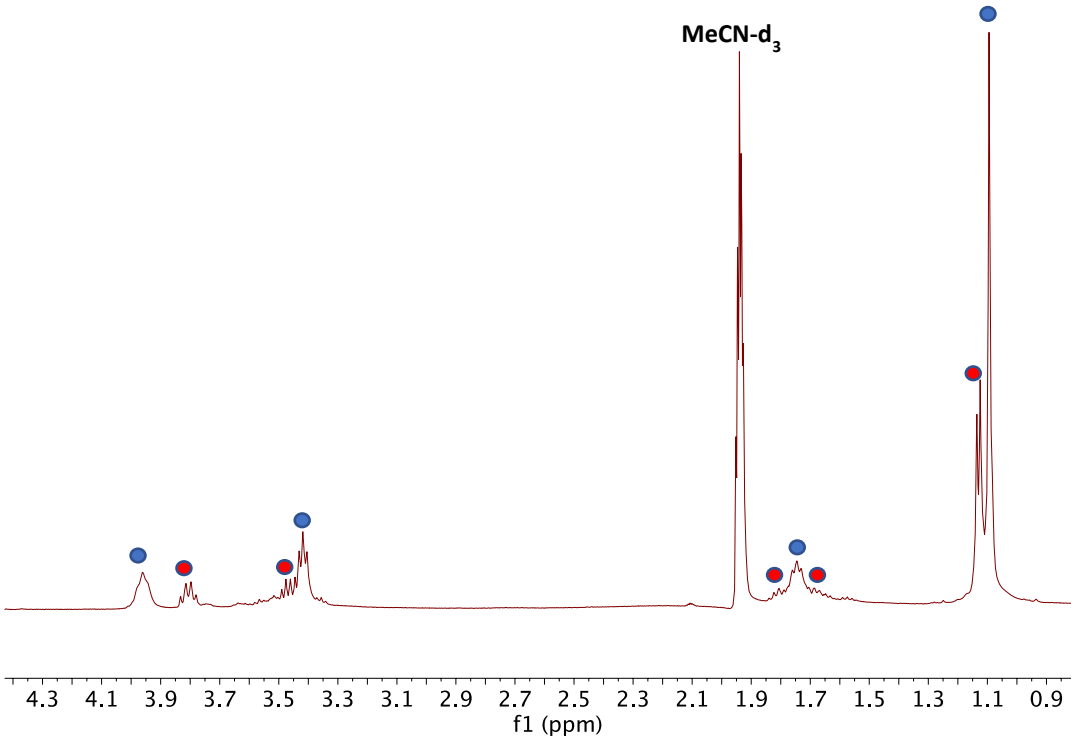

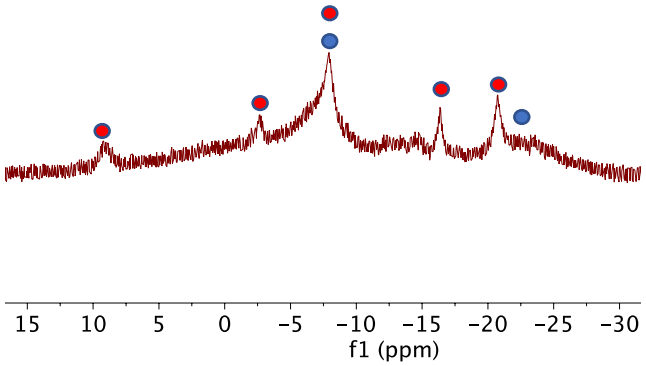

Figure 3.4. ^{1}H (top, 400 MHz) and ^{11}B (bottom, 128 MHz) NMR spectra of **1-*nido*-K** after heating at 60°C for 3 hours. **1-*nido*-K** and **1-*nido*-b** labeled with blue and red dots, respectively

While the exact structure of **1-*nido*-b** remains unknown, analysis of the scalar coupling patterns in the ^{1}H NMR spectrum revealed two sets of doublet of triplet resonances from protons in the crown ether donor group which emerged as **1-*nido*-K** was converted to **1-*nido*-b** at room temperature over a week (**Figure 3.5a**). The two triplet peaks from **1-*nido*-K** transformed to two sets of doublet of triplet resonances in **1-*nido*-b**, highlighting that the crown ether environment in **1-*nido*-b** became asymmetric, which we propose is due to the known possible rearrangement of *nido*-Cb (**Figure 3.5b**).[16]

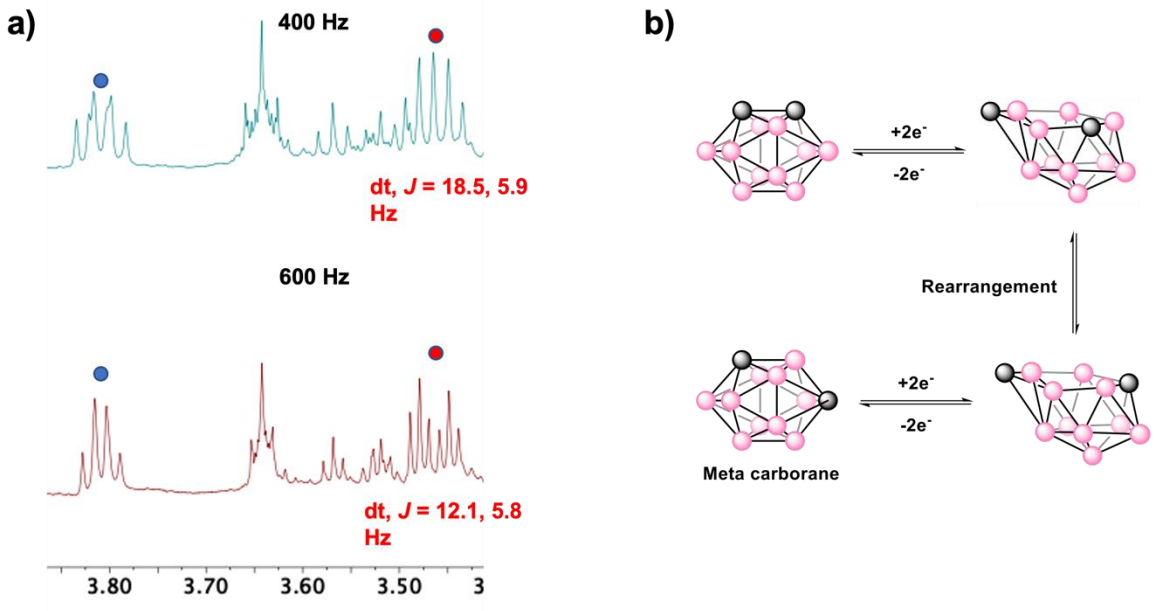

Figure 3.5. a) ^{1}H NMR spectra of **1-*nido*-b** from [NBu_4][PF_6] reaction in 400Hz and 600 Hz in selected range. Crown ether peaks were labeled with blue and red dots. b) Proposed rearrangement of *nido*-Cb

We previously reported that the carbon atoms in *nido*-Cb cluster can be protonated even after substitution with a donor group.[5] This unwanted byproduct was observed for phosphine oxide donors in our previous uranium studies, causing lower metal binding affinity and reducing the number of Cb redox cycles.[5, 6] Protonation on **1-*nido*-K** may be more profound due to the more electron donating crown ether group. To understand **1-*nido*-K** basicity, tetrakis[3,5-bis(trifluoromethyl)phenyl] borate acid (HBArF) was used to purposely protonate **1-*nido*-K**, resulting in a mixture of **1-*nido*-b** and a new Cb species (**Figure 3.6**). We next added excess strong base, LiHMDS, in this reaction mixture and only **1-*nido*-b** peaks were observed after deprotonation, indicating the new Cb species (**1-*nido*-H**) after mixing **1-*nido*-K** and HBArF was likely the protonated *Nido*-Cb.

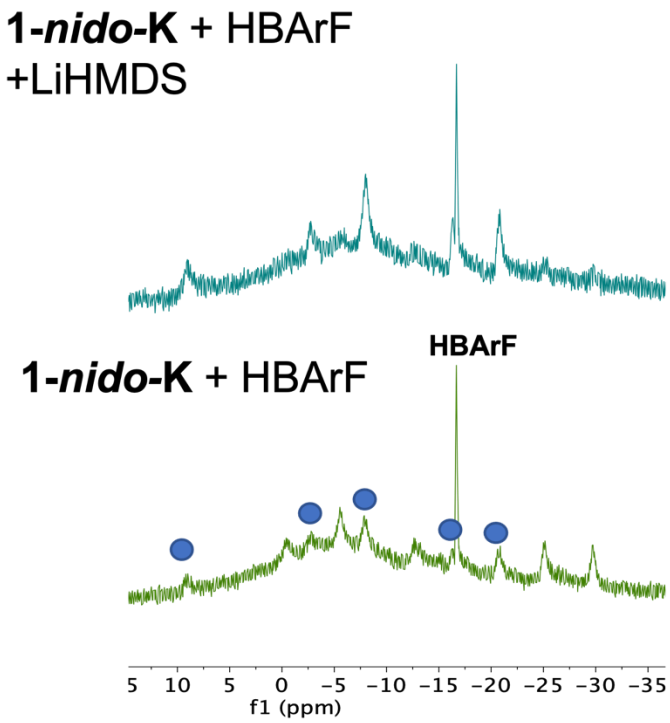

Figure 3.6. ^{11}B NMR (128 MHz) spectrum of **1-*nido*-K** with HBArF before and after LiHMDS with **1-*nido*-b** peaks labeled y blue dots

Due to the negative reduction potential of **1**, chemically producing **1-*nido*-K** required a strong reductant such as potassium napthalenide. Two K^+ counter ions in **1-*nido*-K** may cause interference on measuring accurate Li^+ binding affinity and selectivity. Therefore, we attempted to remove the K^+ ions from **1-*nido*-K** to provide full access to the crown pocket. We first applied different equivalents of kryptofix-222 which is known to strongly bind K^+ in a 1:1 ratio.[17]

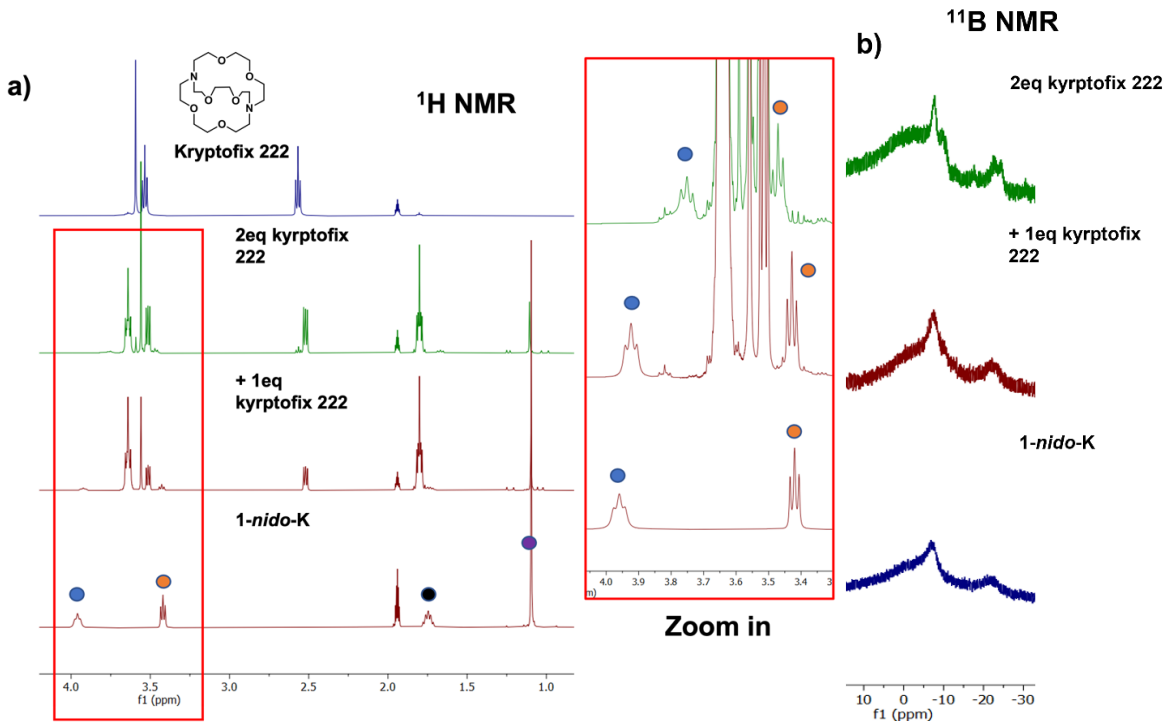

Figure 3.7. a) ^{1}H NMR spectra (400 MHz) of **1-*nido*-K** with 0, 1 and 2 equivs of kryptofix-222 and free kryptofix-222 at r.t. Crown ether peaks are labeled with dots. b) ^{11}B NMR (128 MHz) spectra of **1-*nido*-K** with 0, 1 and 2 equivs of kryptofix-222 at r.t.

Shifts in the ^{1}H NMR resonances attributed to kryptofix-222 and **1-*nido*-K** suggested that the outer-sphere K^{+} most likely was coordinated by kryptofix-222 (**Figure 3.7a**). As more kryptofix-222 was added, two crown ether proton resonance coalesced, indicating a fast exchange process occurred during the reaction, which we proposed was originated from interaction between kryptofix-222 and the second K^{+} that was inside the crown pocket **1-*nido*-K**. Boron resonances in the ^{11}B NMR spectrum became slightly sharper without any chemical shift change, indicating that the *nido*-Cb cluster remained mostly intact. We are pending an XRD study of this new *nido*-Cb 14-crown-4 (**1-*nido*-c**) to confirm whether the second K^{+} in the crown ether pocket was removed by kryptofix-222. Similarly, addition of 2 equivs of K^{+}

selective 18-crown-6 to **1-*nido*-K** generated **1-*nido*-c** as well, which was confirmed by ^{1}H and ^{11}B NMR spectroscopy (**Figure 3.8**). To our surprise, addition of 2 equiv tetraethylammonium bromide ([NEt_4][Br]), which is not known to bind K^+, also resulted in the formation of **1-*nido*-c**. We proposed the K^+ in the crown pocket in **1-*nido*-K** remained chelated after these metathesis reactions, indicating that *nido*-form of **1** had strong binding affinity towards group 1 metal cation. Heating **1-*nido*-c** at 60°C overnight resulted the formation of **1-*nido*-b**, suggesting **1-*nido*-c** shared similar reactivity as **1-*nido*-K**.

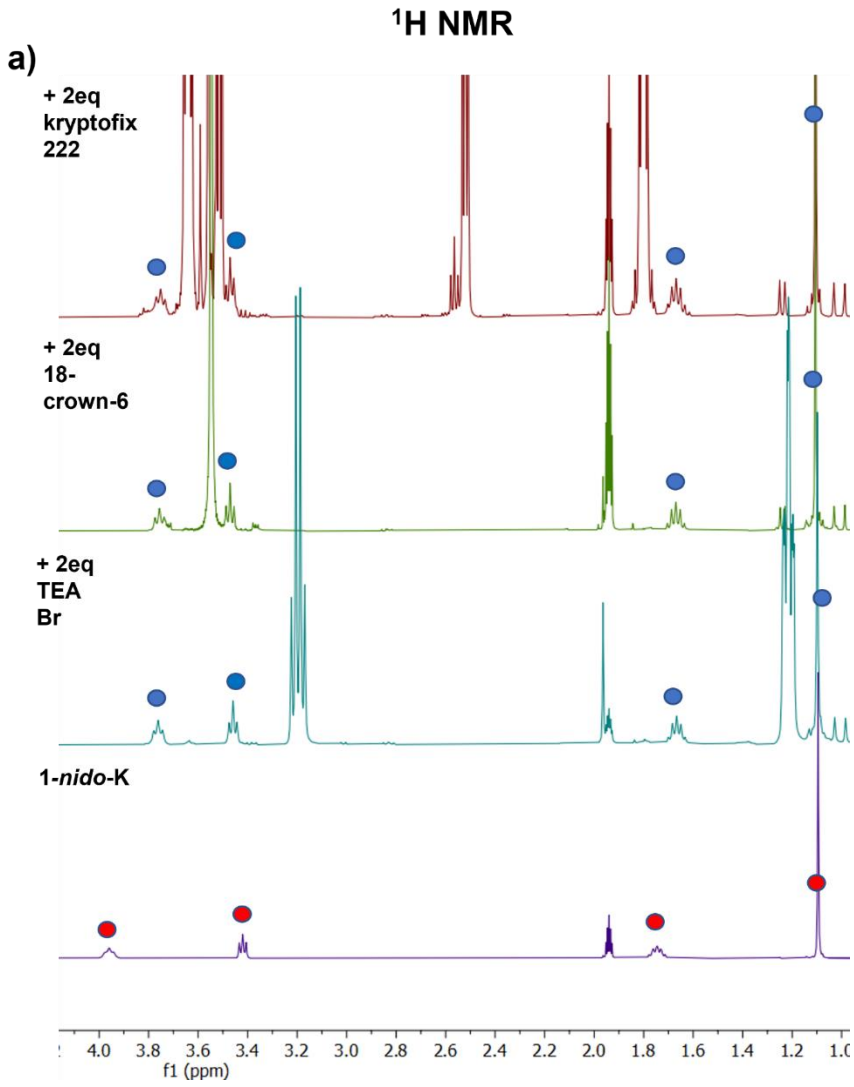

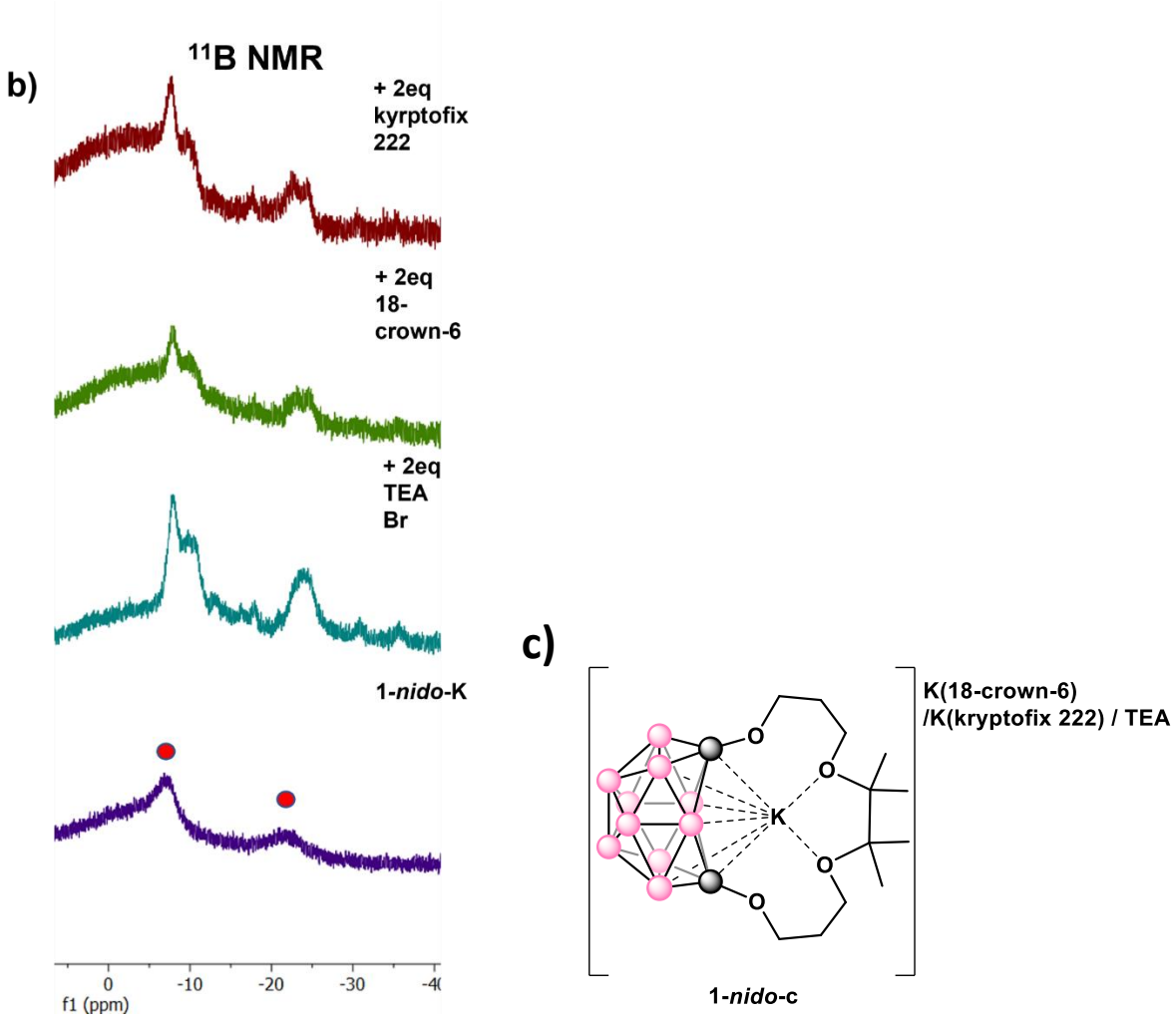

Figure 3.8 a) ^{1}H NMR (400 MHz) spectra of **1-*nido*-K** with 2 equiv of kryptofix-222, 18-crown-6 and [NEt_4][Br] to form **1-*nido*-c** at r.t. **1-*nido*-K and 1-*nido*-c** peaks are labeled with red and blue dots, respectively. b) ^{11}B NMR (128 MHz) spectra of the same reactions. c) Proposed chemical structure of **1-*nido*-c** with different counter cation

3.2.3 Synthesis and characterization of Di-Carborane 14-crown-4 analog

Next, we designed another Cb crown by integrating Li^+ selective 14-crown-4 between two Cb clusters according to the two-step synthesis plan shown in **Scheme 3.3**. The first approach involved first adding excess dibromopropane to $Cb(OH)_2$ in the presence of the base

KH to produce the partial Cb crown compound (**2-b**), followed by another equivalent of KH deprotonated $Cb(OK)_2$ to close the crown ether ring. After work-up, di-Cb 14-crown-4 (**2**) was isolated and identified by ^{1}H and ^{11}B NMR spectroscopy, as well as by GCMS.

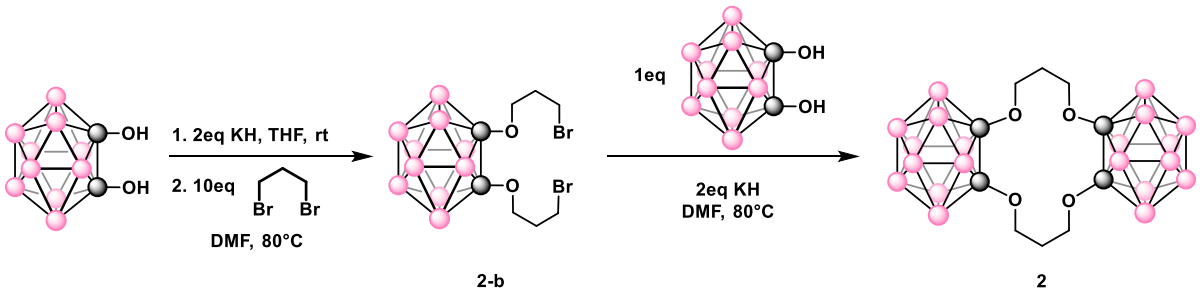

Scheme 3.3. Two step synthesis of Di-carborane 14-crown-4 (**2**) from $Cb(OH)_2$ and **2-b**

We also attempted to generate **2** in one step by mixing the *in situ*-generated $Cb(OK)_2$ with 1 equiv dibromopropane in DMF at 80°C; however, this resulted in a mixture of **2**, **2-b** and a new Cb compound along with unavoidable deboronated byproduct (**Scheme 3.4**). After purification, the new Cb compound was identified as the smaller Cb crown species (**2-c**) as confirmed by the solid-state structure obtained by XRD studies

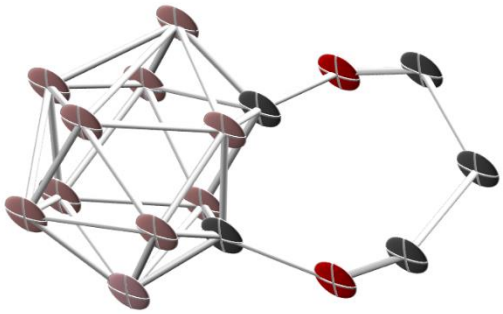

(

Figure 3.9).

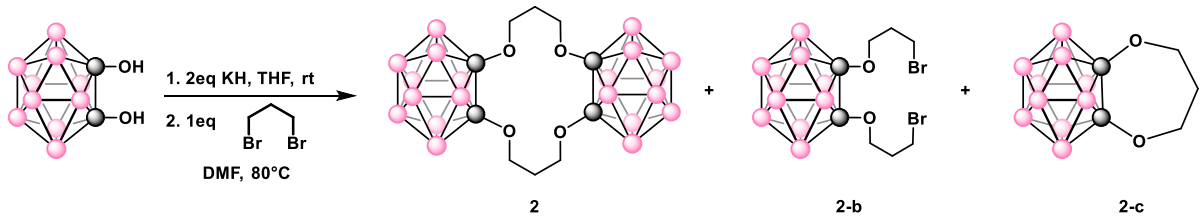

Scheme 3.4. Reaction of deprotonated $Cb(OK)_2$ with 1 equiv dibromopropane

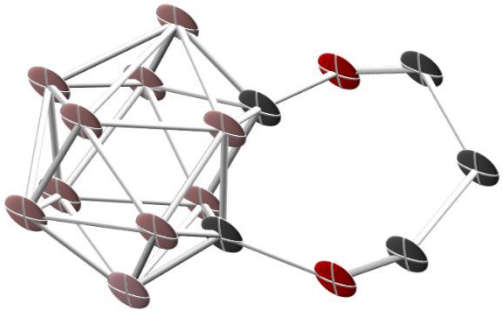

Figure 3.9. Solid state structure of 3-b (low-resolution structure)

The CV of **2** in THF revealed an electrochemically irreversible wave with a peakreduction potential at −2.72V relative to the Fc/Fc^+ redox couple at 100 mV/s scan rate (**Figure 3.10**). Compared to the peak reduction peak of **1** at -2.92 V, this reduction potential was slightly more positive with improved reversibility.

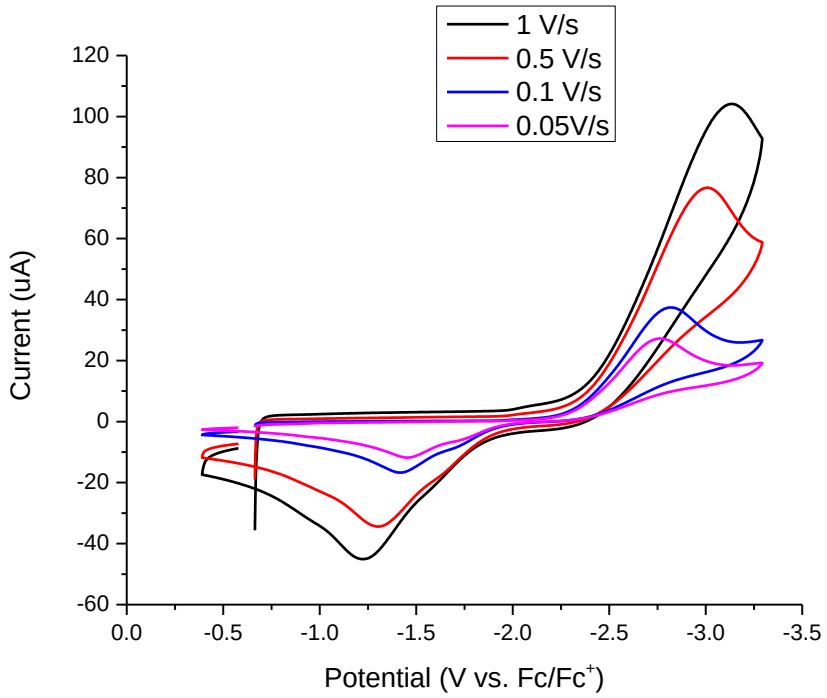

Figure 3.10. The cyclic voltammogram of **2** in THF at various scan rate. (Glassy carbon – WE, Pt wire – CE, Ag wire – RE)

3.2.4 Synthesis, characterization and reactivity of *nido*-Di-Carborane 14-crown-4

Similar to **1**, the reduction of **2** was achieved with 4.0 equiv of potassium naphthalenide (generated *in situ*) in dry THF and its *nido* from (**2-*nido*-K**) was isolated with MeCN wash (**Scheme 3.5**). Two proton resonances from the crown ether are shifted upfield after reduction and two broad boron peaks are observed similar to **1-*nido*-K**, and confirming opening of both Cb cages (**Figure 3.11**). Addition of 4 equiv $FcPF_6$ resulted in reoxidation of **2-*nido*-K** back to **2**, as evidenced by ^{1}H and ^{11}B NMR spectroscopy. With chelating ability from two *nido*-Cb clusters and crown ether in **2-*nido*-K**, four K^+ cations were likely in multiple coordinating

environments. Therefore, attempts to perform a salt swap with [NEt$_4$][Br] resulted in the formation of multiple products that were difficult to separate (**Figure 3.12**).

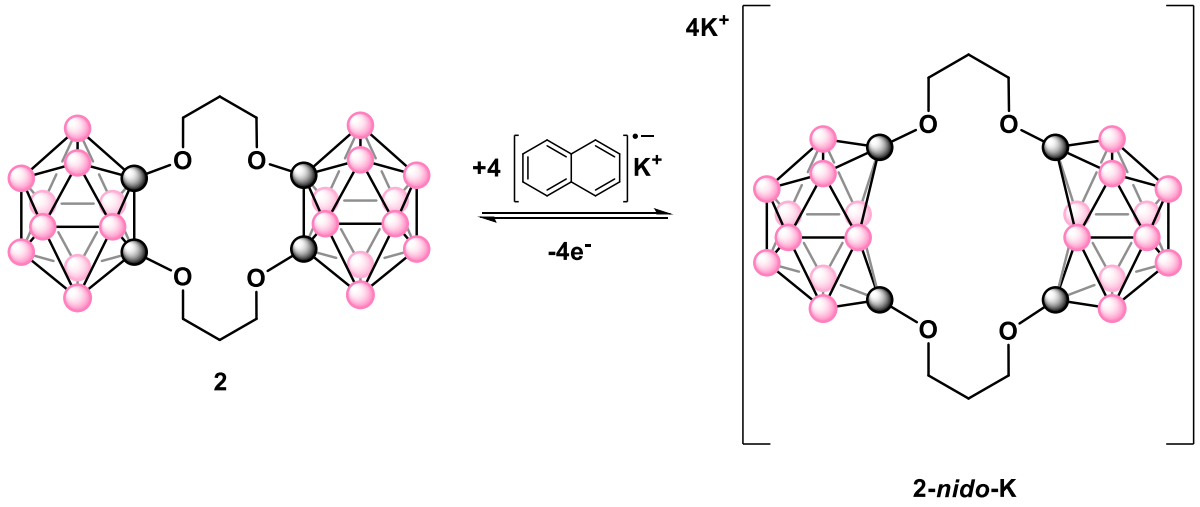

Scheme 3.5. Reduction of **2** to the **2-*nido*-K** using potassium naphthalenide in THF

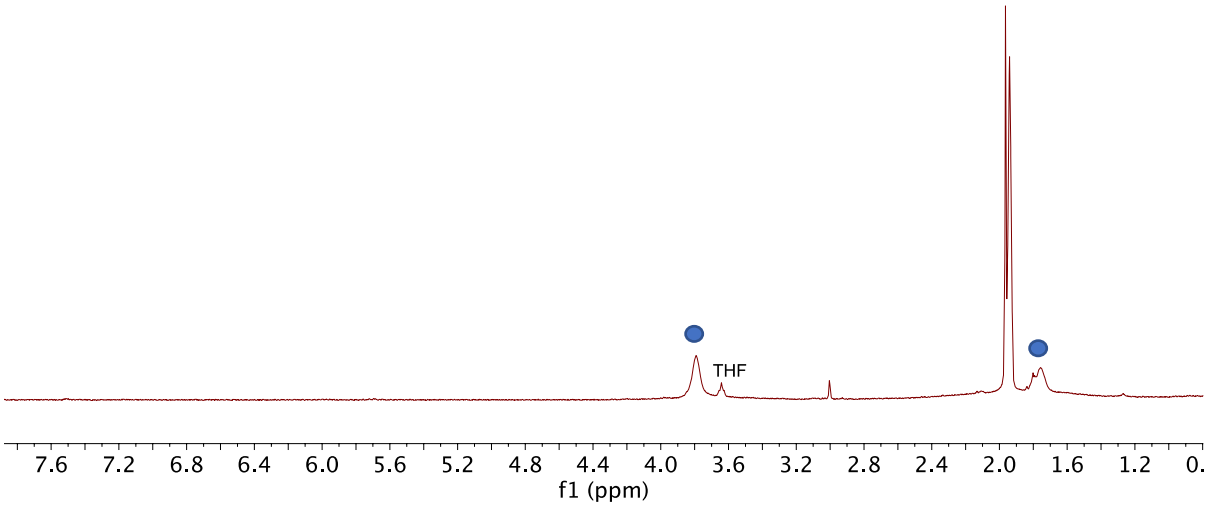

Figure 3.11 ^{1}H NMR (400 MHz) spectrum of **2-*nido*-K** in MeCN-d$_3$**.** Crown ether peak are labeled with blue dots

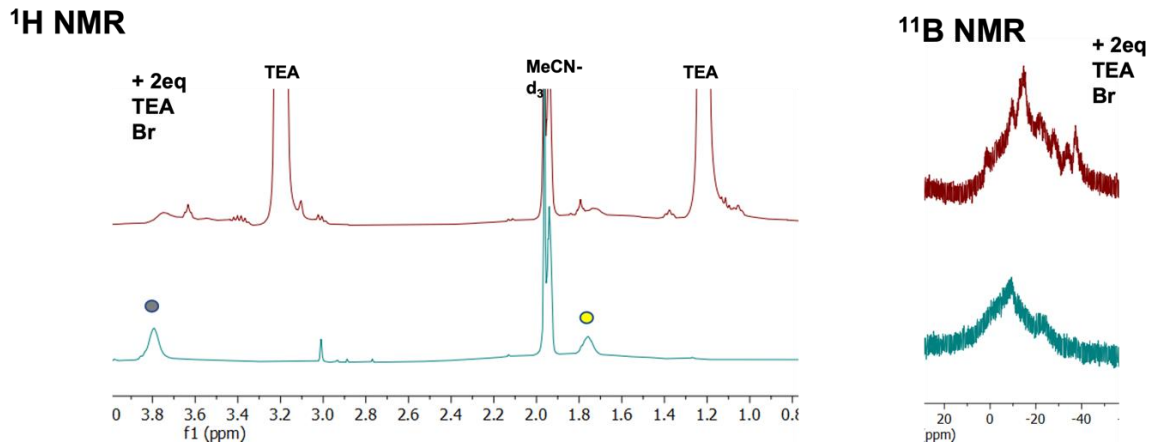

Figure 3.12 ^{11}H (400 MHz) and ^{11}B NMR (128 MHz) spectra of **2-*nido*** with 2 equiv of [NEt_4][Br] at r.t. Crown ether peaks are labeled with dots.

On the other hand, addition of excess 18-crown-6 to **2-*nido*-K** resulted in shifted resonances in the ^{1}H NMR spectra (**Figure 3.13**). The unchanged broad boron resonances observed in the ^{11}B NMR spectrum confirmed both *nido*-Cb clusters remain intact after the addition of 18-crown-6. The multiplicity and chemical shift change in the 18-crown-6 proton resonances confirmed the coordination of K^+ to 18-crown-6. Lastly, the most downfield proton resonance in crown ether shifted upfield, suggesting the removal of outer sphere K^+ ions; however, interaction of possible inner crown pocket K^+ was unclear. Unambiguous confirmation of these structural changes by single crystal XRD studies is pending.

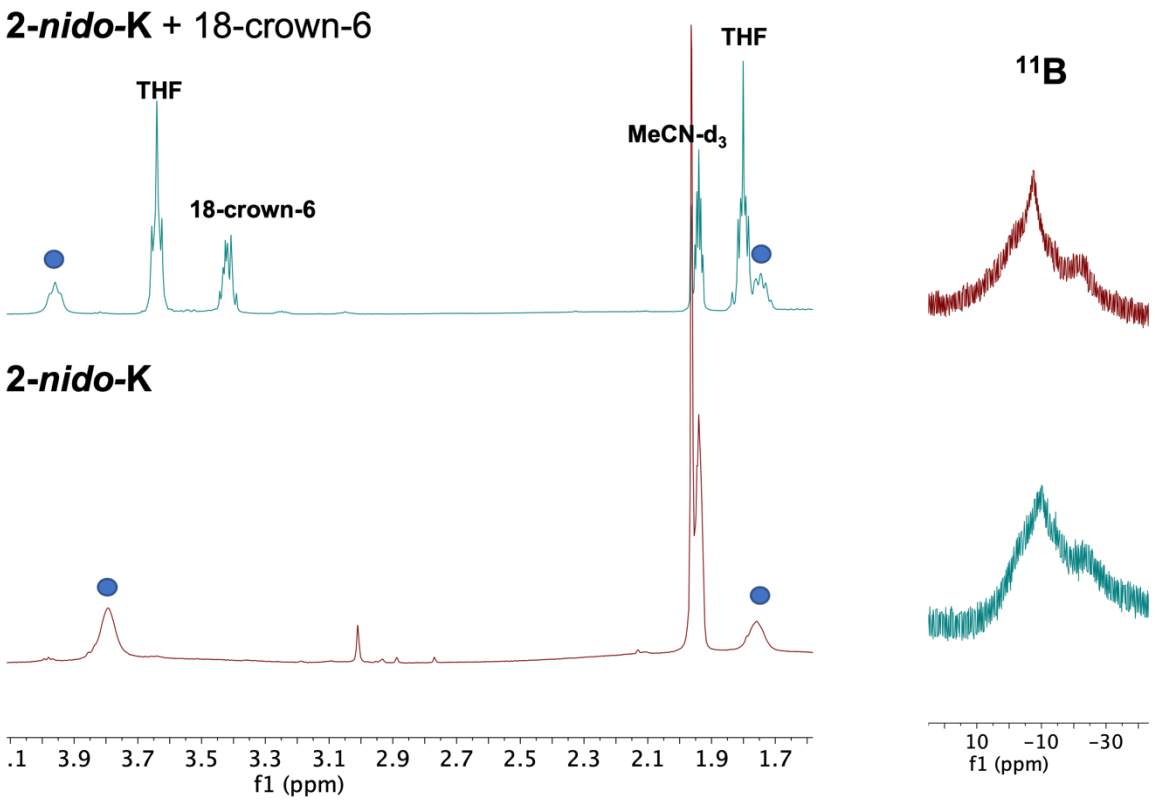

Figure 3.13. Stacked ^{1}H (400 MHz) and ^{11}B (128 MHz) NMR spectra of **2-*nido*-K** before and after addition of 18-crown-6. Crown ether peak labeled in blue dots

3.2.5 Synthesis and characterization of other Cb crown ethers

The 14-crown-4 donor group in **1-*nido*-K** showed different pocket size relative to regular 14-crown-4 and may affect their selectivity towards Li^{+}. In addition, two oxygen atoms in crown ether did not participate in the coordination of the inner sphere K^{+}. Therefore, other sizes or types of crown ethers were considered to optimize the Li^{+} selectivity. Cb 18-crown-6 (**3**) was synthesized by mixing KH deprotonated $Cb(OH)_2$ with longer poly-ether, $TsO(CH_2)_2(OCH_2CH_2)_4OTs$ (**Scheme 3.6**). The solid-state structure revealed a C–C bond distance of 1.751 Å in Cb cluster, very similar to **1** (1.767 Å).

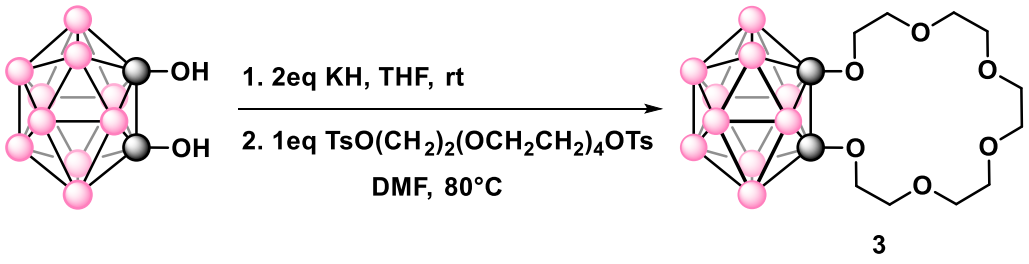

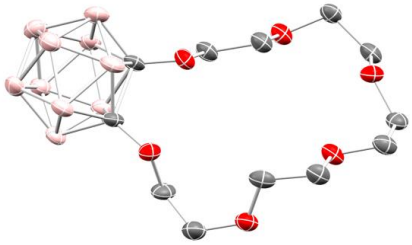

Scheme 3.6. Synthesis of Cb 18-crown-6 (**3**) and its solid-state molecular structure (bottom). All H atoms have been omitted for clarity.

The deboronated byproduct (**3-b**) was co-crystalized from crude mixture and the solid-state structure obtained by single crystal XRD studies (**Figure 3.14**). Interestingly, the K^+ counter cation was coordinated slightly outside the 18-crown-6 plane. The ^1H NMR spectrum indicated asymmetric crown ether proton resonance due to the extra K^+ and a missing boron in cluster with the diagnostic deboronation resonances in the ^{11}B NMR spectrum (**Figure 3.23**).

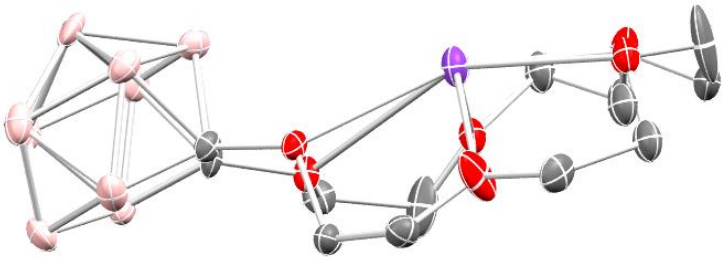

Figure 3.14. Solid-state molecular structure of **3-b.** All H atoms have been omitted for clarity. B, pink; C, black; O, red; K purple

The CV of **3** in THF revealed an electrochemical irreversible wave with reduction potential at −3.01V relative to the Fc/Fc^+ redox couple at a 100 mV/s scan rate (**Figure 3.15**).

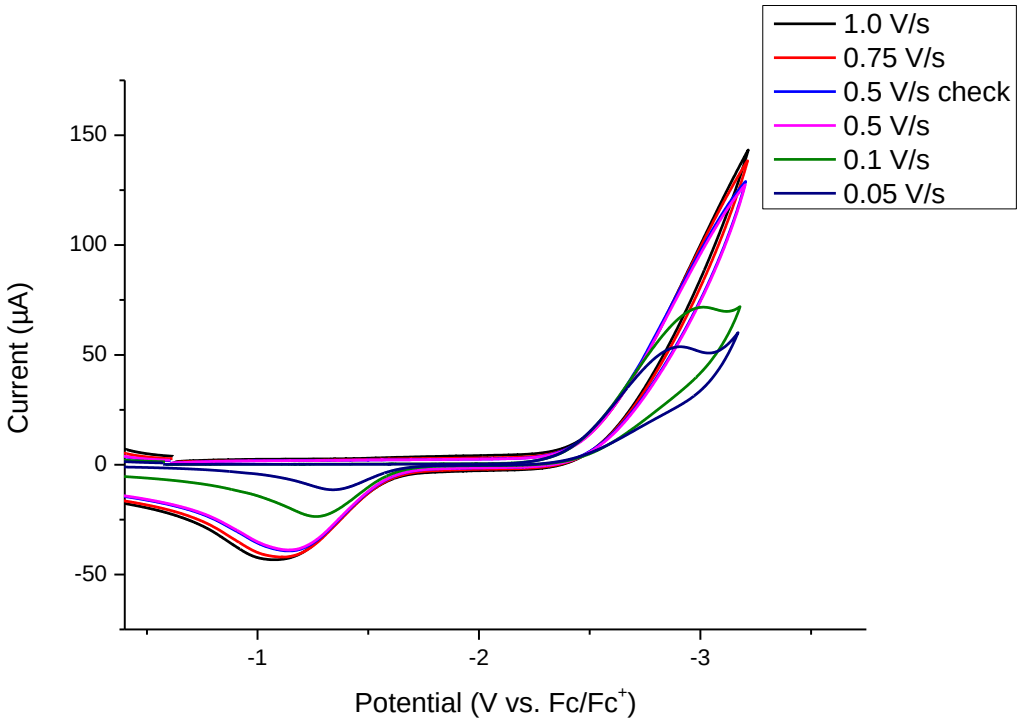

Figure 3.15. The cyclic voltammogram of **3** in THF at various scan rate. (Glassy carbon – WE, Pt wire – CE, Ag wire– RE)

The reduction of **3** was carried out by adding 2.0 equiv of potassium naphthalenide (generated *in situ*) in dry THF and its *nido*-form (**3-*nido*-K**) was isolated with MeCN wash

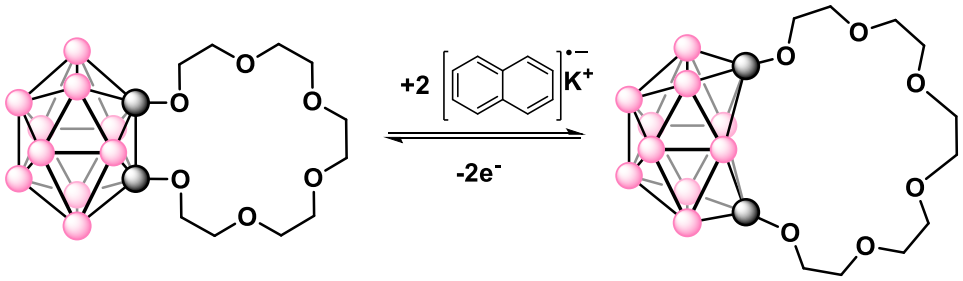

(**Scheme 3.7**). Similar to the reduction of **1** and **2**, upfield shifted crown ether proton resonance and *nido*-Cb cluster broad boron peaks were observed by ^{1}H NMR spectroscopy after reduction (**Figure 3.16**).

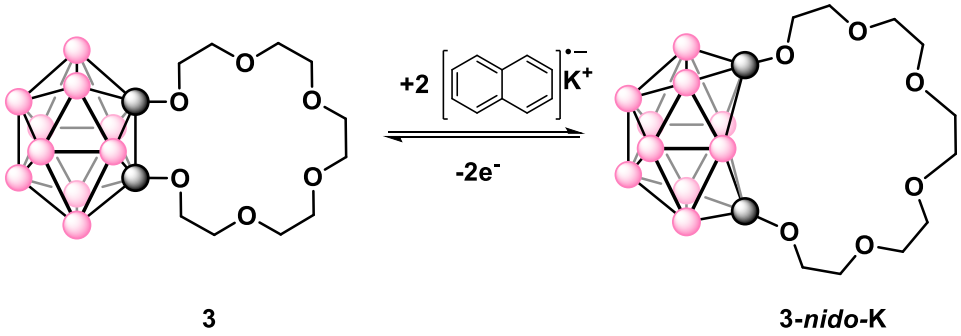

Scheme 3.7. Reduction of **3** to the **3-*nido*-K** using potassium naphthalenide in THF

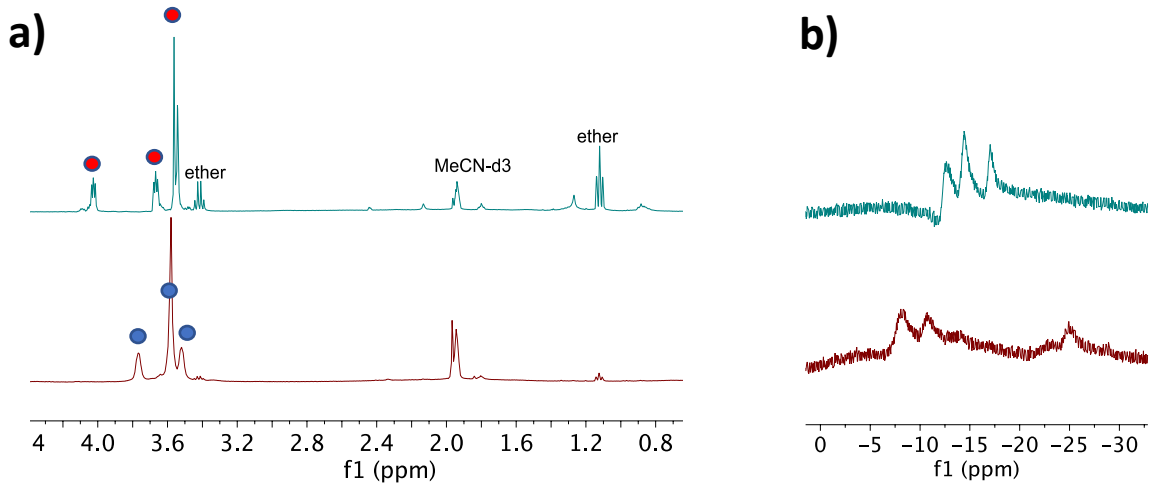

Figure 3.16. Stacked a) ^{1}H (400 MHz) and b) ^{11}B NMR (128 MHz) spectra of **3** (top) and **3-*nido*-K** (bottom) in MeCN-d_3. Crown ether peaks are labeled with dots

A smaller silicon-based crown ether previously demonstrated the ability to coordinate to Li^{+},[18] which drew our interest as a donor ligand for Cb. Reaction of KH deprotonated $Cb(OK)_2$ and 1,3-Dichloro-1,1,3,3-tetramethyldisiloxane resulted in the formation of silicone based Cb crown (**4**) and solid-state structure was obtained after purification (**Scheme 3.8**). The solid-state structure of **4** revealed the C–C bond distance at 1.732 Å in Cb cluster, similar to **1** (1.767 Å); however, compared to **1**, the silicon crown had a much smaller crown pocket size.

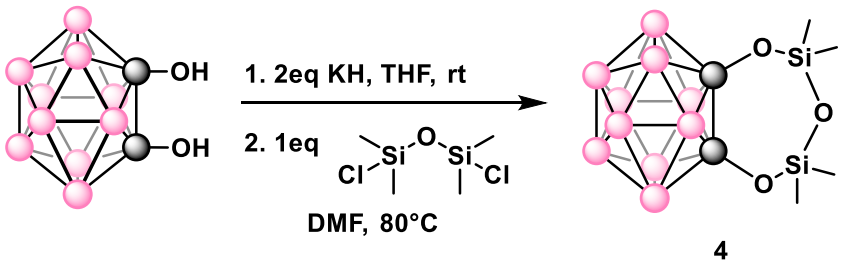

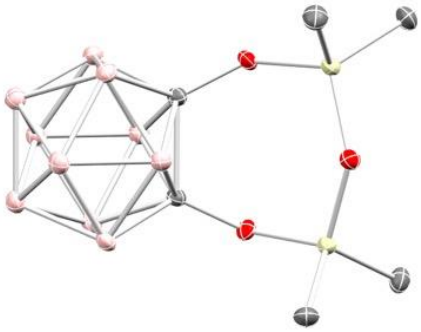

Scheme 3.8. Synthesis of **4** and its solid-state molecular structure (bottom). All H atoms have been omitted for clarity. Si, yellow; O, red; B, pink; C, black

3.2.6 Carbon-spaced Cb-crown compounds

Although the integration of crown ether onto Cb were successfully achieved, all these Cb crown ether compounds had very negative reduction potentials and their *nido*-forms were highly water sensitive for the end goal of seawater extraction. Therefore, in an attempt to the shift Cb crown reduction potential anodically, our approach was to integrate additional -CH_2- (carbon spacer) groups between the Cb cluster and crown ether linker to reduce the electron donating affect from crown ether into the cage.[3] We first incorporated carbon spacer onto **1** for 14-crown-4 case and designed a Cb 16-crown-4 (**5**) compound. To synthesize **5**, we first followed a reported procedure to generate the precursor Cb $(CH_2OH)_2$[19], followed by deprotonation with KH and addition of $TsO(CH_2)_3O(CR_2)_2O(CR_2)_3OTs$ ($R=CH_3$) using the same conditions as in the synthesis of **1** (**Scheme 3.9**).

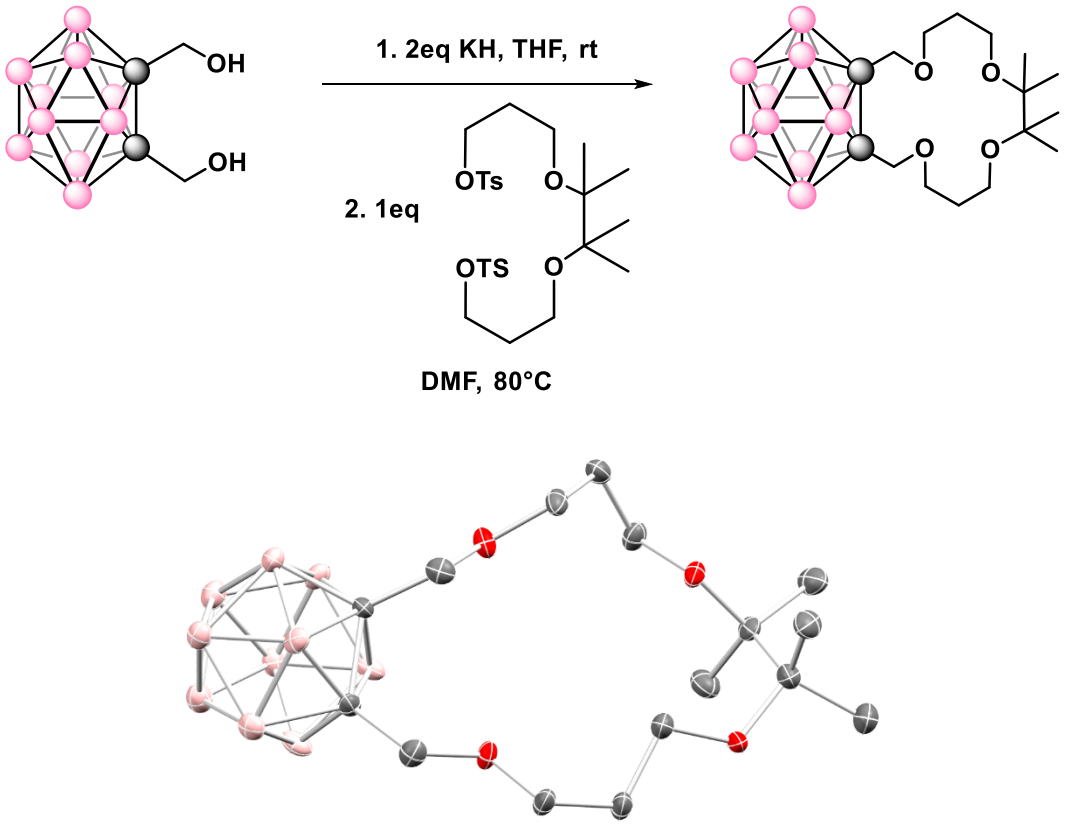

Scheme 3.9. Synthesis of **5** and its solid-state molecular structure (bottom). All H atoms have been omitted for clarity

After work-up, **5** was isolated and identified by ^{1}H, ^{11}B NMR spectroscopy and the solid-state structure obtained by single crystal XRD studies. The solid-state structure revealed a Cb C–C distance of 1.673 Å, shorter than Cb C–C bond (1.767 Å) in **1**. The CV of **5** in THF revealed an electrochemical irreversible wave with reduction potential at −3.15 V relative to the Fc/Fc^{+} redox couple at a 100 mV/s scan rate (**Figure 3.17**), which was surprisingly more negative than **1** (-2.92V). Furthermore, two reoxidation events were observed, unlike previous Cb crown compounds, suggesting mono reduced radical intermediate was more stable to be

generated with carbon spacer. However, such negative reduction potentials were challenging to access using chemical reduction and we have not yet been able to access these.

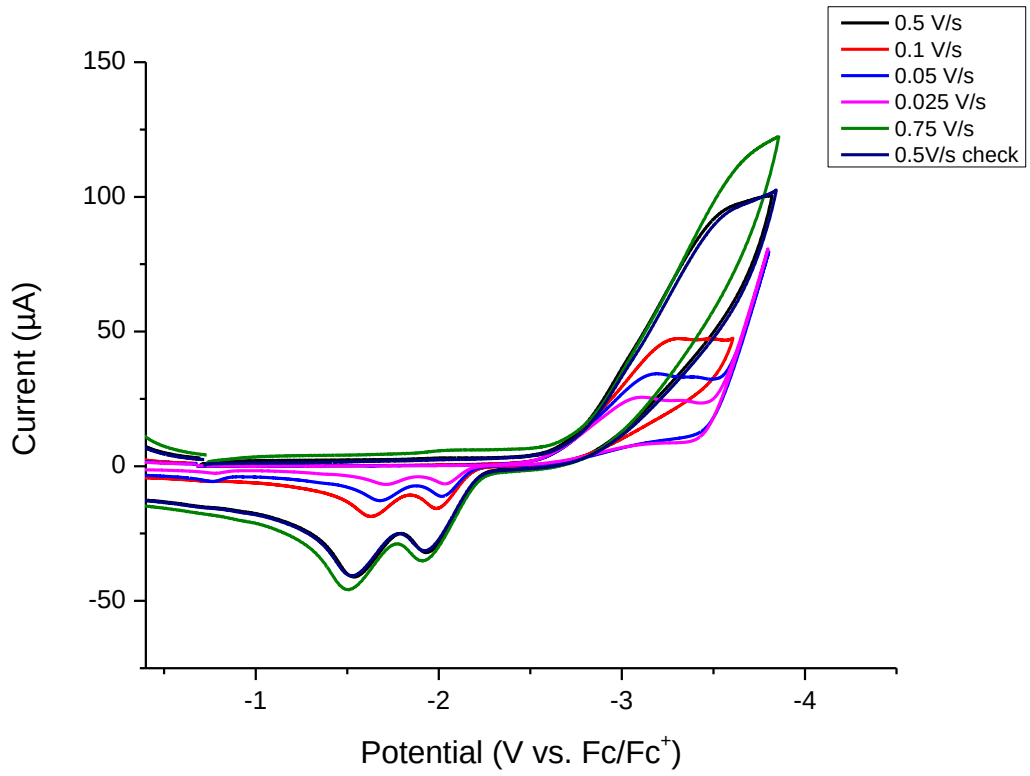

Figure 3.17. The cyclic voltammogram of **5** in THF at various scan rate. (Glassy carbon – WE, Pt wire – CE, Ag wire– RE)

We similarly attempted the incorporation of carbon spacers onto the 18-crown-6 donor ligand. By following synthetic step as shown in **Scheme 3.10**, Cb 20-crown-6 (**6**) was isolated and identified by ^{1}H and ^{11}B NMR spectroscopy. However, this reaction suffered small conversion of the starting material Cb $(CH_2OH)_2$, low yield in generating **6** and difficulty to separate tosylate linker starting material. The deboronated species (**6-b**) was also identified by

NMR spectroscopy and solid-state structure obtained by XRD studies

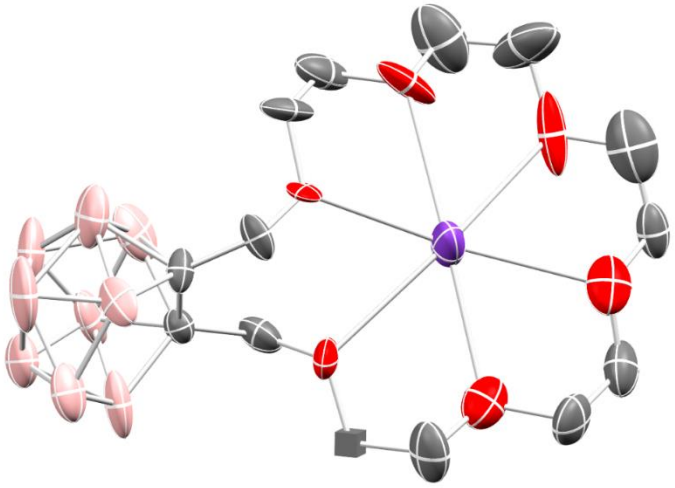

(

Figure 3.18, low resolution) as a major by-product.

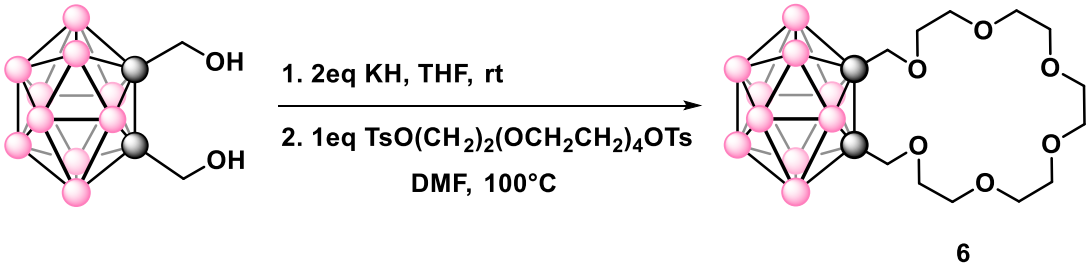

Scheme 3.10. Synthesis of **6** from Cb $(CH_2OH)_2$

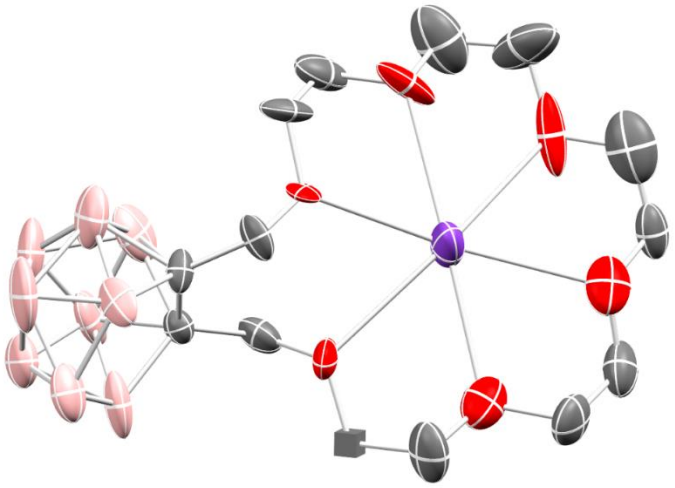

Figure 3.18. Solid-state molecular structure of **6-b** (low resolution)

The CV of **6** in THF was obtained and revealed a quasi-reversible reduction event with an $E_{1/2}$ = -2.10 V as well as a quasi-reversible oxidation event with $E_{1/2}$ = 0.35 V (**Figure 3.19**), different from all previous Cb crowns. Compared with **3**, reduction potential shifted more positive, and the reversibility was significantly improved, in contrast to **1** and **5**. One hypothesis was the longer 20-crown-6 chain offers more flexibility that favors Cb C–C bond cleavage, relative to the more rigid 16-crown-4.[3] The similar a quasi-reversible oxidation events in **6** was previously observed for B_{12}^{2-} borane cluster, which the radical cation can be chemically generated.[20]

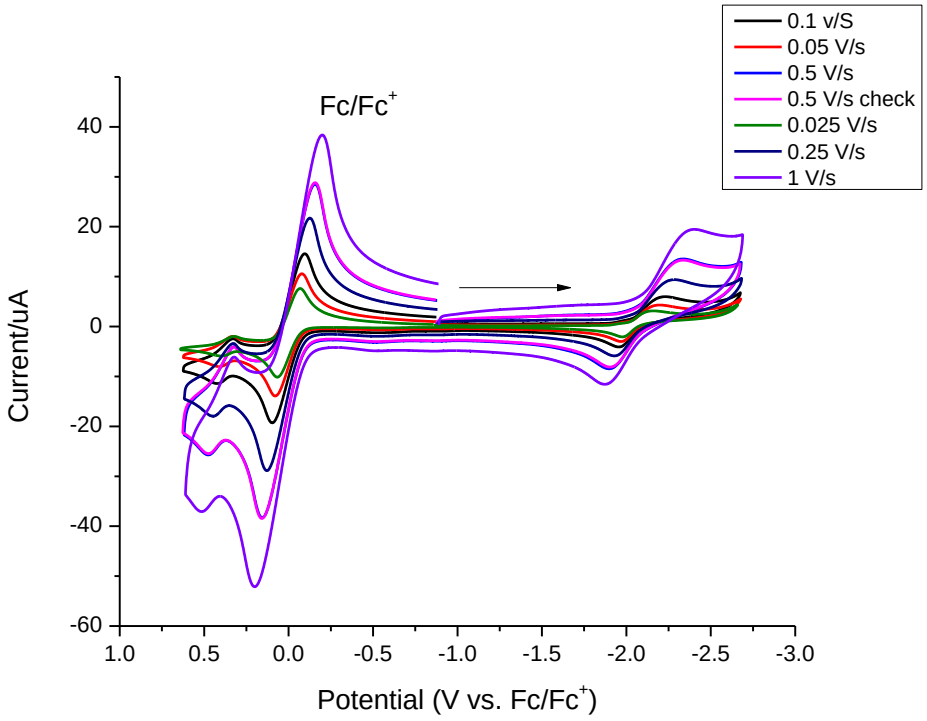

Figure 3.19. The cyclic voltammogram of **6** in THF at various scan rate with presence of Fc. (Glassy carbon – WE, Pt wire – CE, Ag wire– RE)

The smaller carbon spacer crown Cb 11-crown-3 (**7**) was also synthesized from deprotonated Cb $(OK)_2$ and Bis(2-bromoethyl) Ether, (**Scheme 3.11**) which was identified by ^{1}H and ^{11}B NMR spectroscopy after purification. The CV of **7** in THF revealed a small irreversible reduction event near the solvent window (**Figure 3.20**), indicating the challenge to achieve its *nido*-form from chemical reduction. The lack of reduction wave further supported that the length of the crown ether played an important role on electronic property of the Cb cluster by changing steric hindrance and rigidity of the donor group.[3]

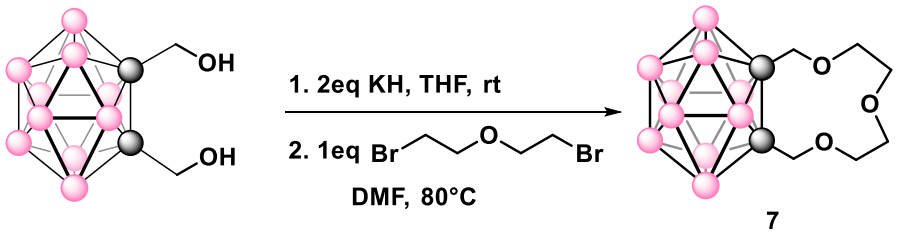

Scheme 3.11. Synthesis of **7** from Cb $(CH_2OH)_2$

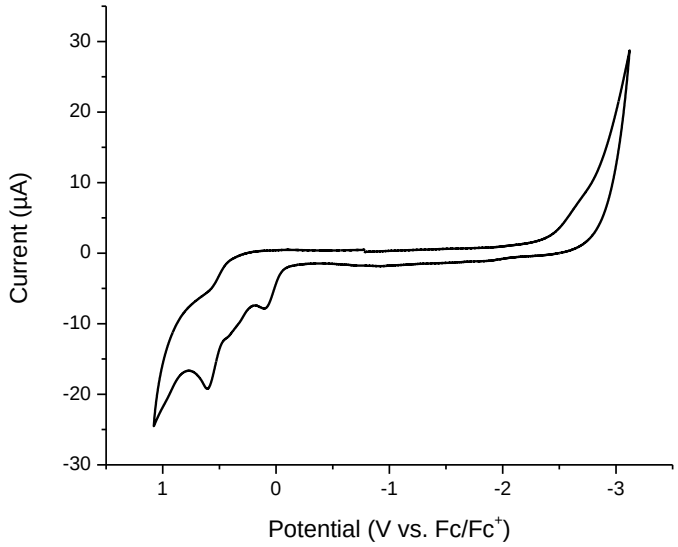

Figure 3.20. The cyclic voltammogram of **7** in THF at 100 mV/s scan rate. (Glassy carbon – WE, Pt wire – CE, Ag wire – RE)

Integrating a carbon spacer into the silicon-based crown ethers was also achieved synthetically (**Scheme 3.12**) in an attempt to improve the redox behavior of smaller Cb crown **5**. After work-up, Cb silicone crown (**8**) with carbon spacer was isolated and identified by NMR spectroscopy along with the solid-state structure obtained by single crystal XRD studies. **8** has a short Cb C–C distance of 1.674 Å and only a small irreversible reduction event near -2.8 V was observed in CV of **8** in THF (**Figure 3.21**). The chemical reduction of **8** with

potassium naphthalenide resulted in a mixture of unreacted **8**, deboronated products and unknown Cb species (**Figure 3.24**). The shorter cyclizing donor group may make it more difficult to access the desired *nido*-form of **8**.[3, 7, 8]

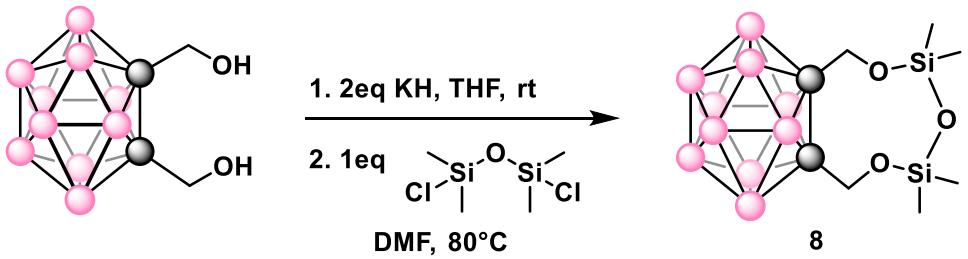

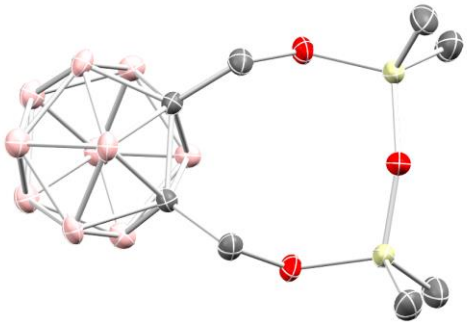

Scheme 3.12. Synthesis of **8** from Cb $(CH_2OH)_2$ and its solid-state molecular structure (bottom). All H atoms have been omitted for clarity. Si, yellow; O, red; C, black; B, pink

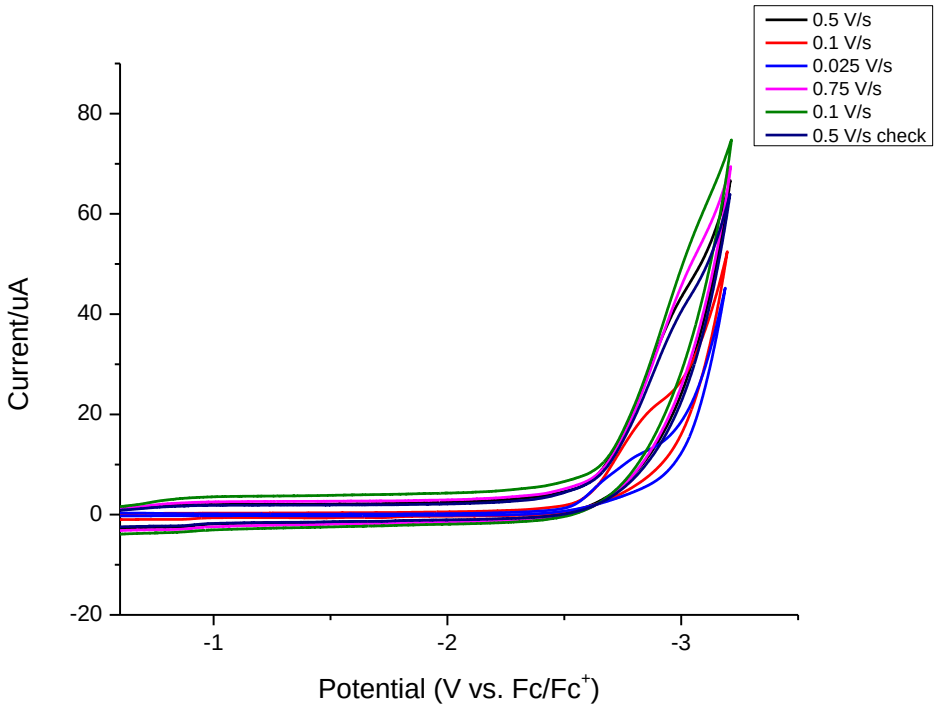

Figure 3.21. The cyclic voltammogram of **8** in THF at various scan rate with presence of Fc. (Glassy carbon – WE, Pt wire – CE, Ag wire – RE)

3.2.7 Phenyl phosphine oxide -PhPO- spacer

The CV showed carbon spacer Cb crown ether also had quite negative reduction potentials, highlighting the need of integrating more electron withdrawing spacers on the donor group. The previous study in our group on uranium capture showed Cb with phosphine oxide (P=O) donor group had reduction potential of -1.1 V. Therefore, our next approach to shift Cb reduction potential anodically was to integrate a P=O spacer with a phenyl attachment (-PhPO-) in between Cb crown compounds. The first step was to generate Cb PhP=O precursor according to **Scheme 3.13**. After work-up and recrystallization, two products were isolated in

diethyl ether and DCM filtrate, respectively. The ether fraction contained the desired product Cb $(PhPOCl)_2$ (**9**), identified by NMR spectroscopy and the solid-state structure obtained by single crystal XRD studies. The solid-state structure of **9** indicated one phosphorus chiral center is adopting R configuration and the other phosphorus was in S configuration. The product in DCM fraction (**9-b**) showed more downfield shifted peaks in ^{1}H and ^{31}P NMR spectroscopy than **9**; however, it shared the same boron resonances and identical unit cell with **9** from XRD analysis, indicating **9-b** was likely an meso-isomer of **9**.

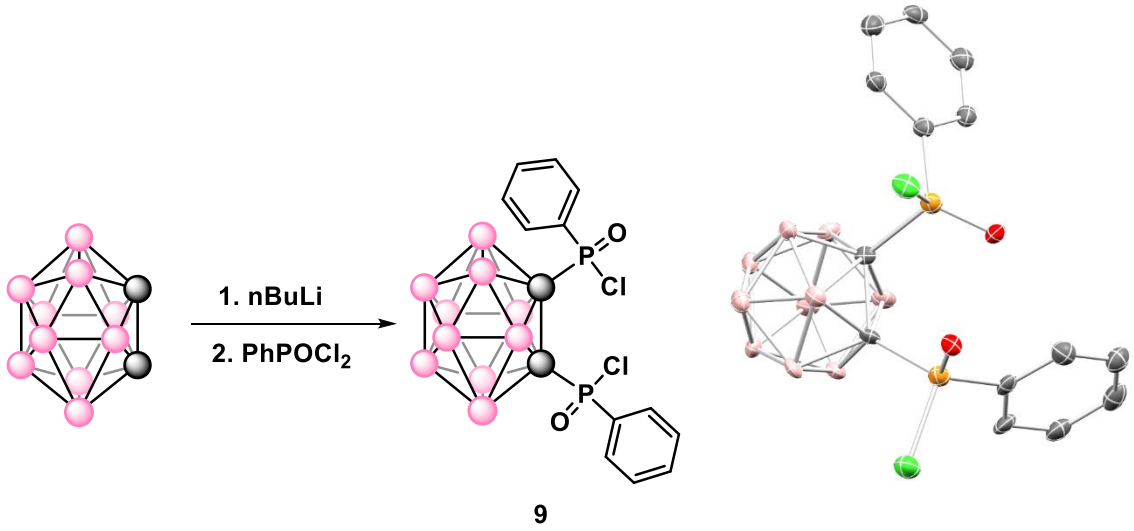

Scheme 3.13. Synthesis of **9** from Cb and its solid-state molecular structure (right). All H atoms have been omitted for clarity

With the leaving group -Cl in precursor **9**, the next step was to add crown ether diol in presence of base to cyclize the crown ether donor. Compared to Cb crown ether without spacer group, we proposed the attachment of P=O should allow the use of all oxygen donor from crown ether potion for Li^{+} coordination in *nido*-form (**Scheme 3.14**). Therefore, we first

integrated a smaller crown ether onto **9** and attempted to produce Cb 11-crown-3 P=O spacer species (**10**). The synthesis plan was to treat **9** with 1 equiv diethylene Glycol and 2 equiv base.

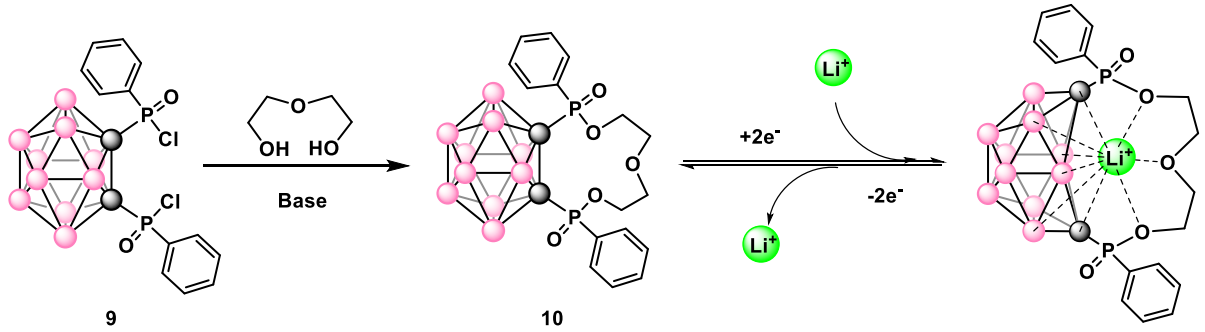

Scheme 3.14. Ongoing synthesis step to produce **10** and its proposed Li+ capture/release scheme

The first base we chose was KH that showed success to synthesize previous Cb crown ethers. No reaction of **9** was observed after 1 day when the reaction took place in ether, likely due to the low solubility of KH. Under the same conditions in a different solvent (i.e., THF), more than half of **9** reacted and we observed a set of boron resonances in the ^{11}B NMR spectrum matching perfectly the unsubstituted Cb starting material, suggesting that cleavage of C–P bond in **9** occurred during the reaction. The ^{31}P NMR spectrum of the crude mixture showed the multiple new peaks which were shifted upfield by 18-21 ppm relative to **9** (**Figure 3.22**). Increasing the equivalents of KH or diethylene glycol, as well as heating overnight at 60 °C in THF resulted in the same peaks in ^{11}B and ^{31}P NMR spectroscopy with more conversion of **9**, indicating the cleavage of C–P bonds, which suggested KH basicity might be too aggressive.

To estimate the change of phosphorus resonance in desired product **10** from **9**, we set up a control reaction of attaching two $PhPOCl_2$ onto diethylene Glycol (**11**) with 2 equiv of

triethylamine (Et_3N) as base (**Scheme 3.15**). After work-up, the ^1H NMR spectrum of the ether fraction confirmed the formation of **11** with matched integration values. Compared to the starting material $PhPOCl_2$, the phosphorus resonance in **11** was shifted upfield by 5.8 ppm after switching Cl groups to ether groups. The ^{31}P NMR spectrum of the benzene fraction indicated a mixture of **11** and multiple further upfield peaks (**Figure 3.22** top). We assigned the peak near 19.6 ppm as 1:1 $PhPOCl_2$ diethylene Glycol product (**11-b**), which was shifted upfield by 16.4 ppm relative to $PhPOCl_2$. The phosphorus resonance from reaction of **9** with diethylene Glycol using KH as base matched well with **11-b** and some unknown impurities from the control reaction**.**

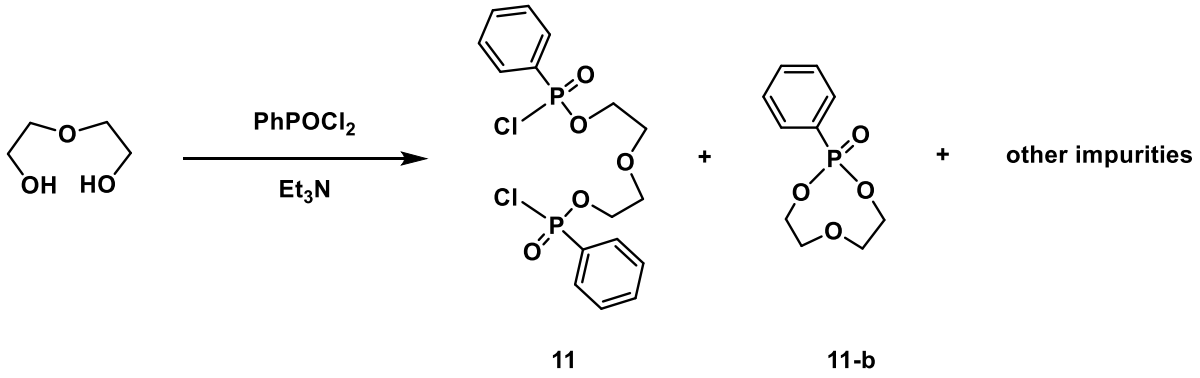

Scheme 3.15. Synthesis of **11** with byproduct **11-b** and other impurities

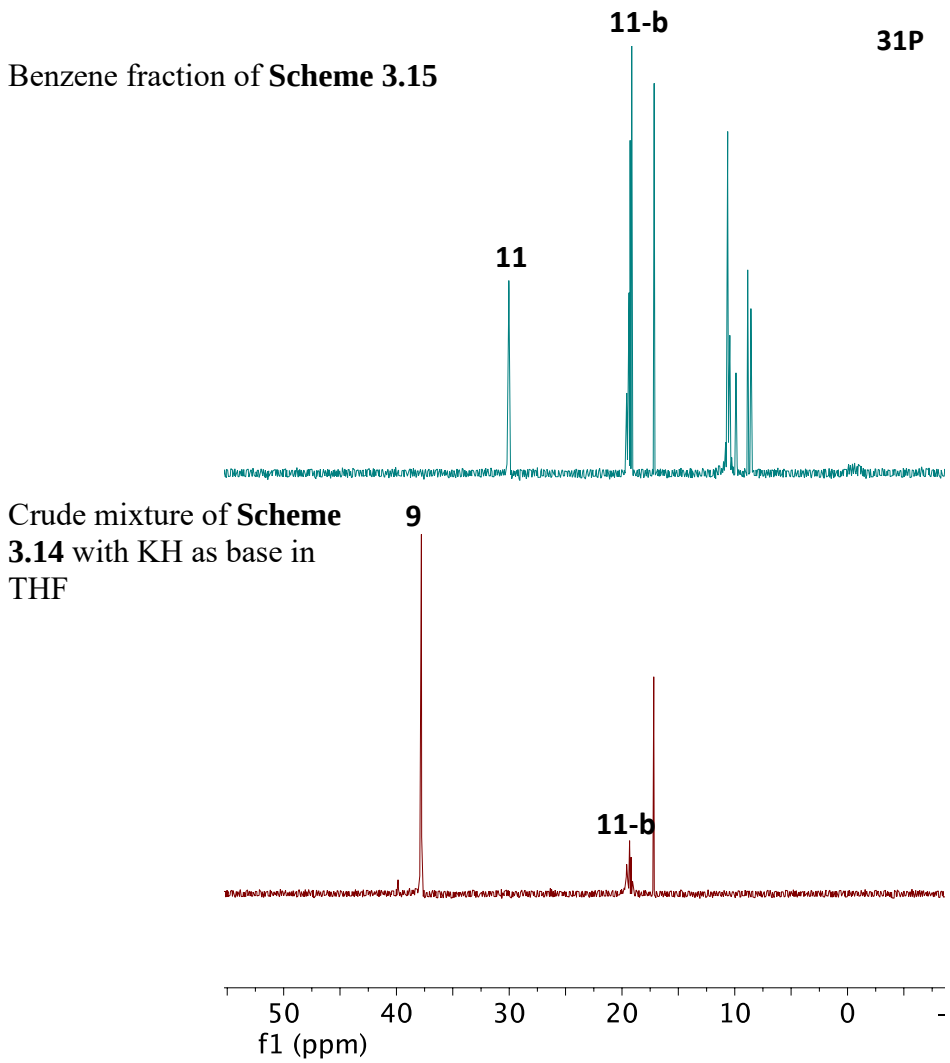

Figure 3.22. ^{31}P NMR (162 MHz) spectra of reactions described in **Scheme 3.14** and **Scheme 3.15**

Addition of 1 equiv **11** to n-butyllithium deprotonated Cb yielded an insoluble solid, suggesting the possible formation of polymerized products. Next, we turned to the compound **9-b**, which we suspected was the isomer of **9**, as the precursor for attaching the ether linker (**Scheme 3.14**). The benzene solution of **9-b** was added to the mixture of 1 equiv diethylene glycol and 2 equiv Et_3N for 1 day. The formation of Et_3N•HCl was observed in ^{1}H NMR

spectroscopy and single crystal XRD studies, confirming the S_N2 reaction occurred. After the work-up, the resulting product shared almost the identical boron resonances as **9-b**. The resulting major phosphorus peak and phenyl proton resonances were shifted upfield 0.35 ppm and 0.01 ppm relative to **9-b**, respectively, smaller than expected value from the control reaction (**Scheme 3.15**). On the other hand, one of the CH_2 proton resonances that was in diethylene glycol downfield shifted and the integration in ^1H NMR matched well with desired product **10**. Further characterization is underway currently.

We also attempted to integrate a bigger crown ether onto **9** to produce Cb 20-crown-6 P=O spacer species (**12**) using pentaethylene glycol as nucleophile (**Scheme 3.16**). To estimate the change of phosphorus resonance in desired product **12** from **9**, we set up a control reaction of attaching two $PhPOCl_2$ onto pentaethylene glycol (**13**) with 2 equiv Et_3N (**Scheme 3.17**). Similar to the diethylene glycol case (**Scheme 3.15**), the ^{31}P NMR spectrum indicated **13** shifted 5.97 ppm upfield and the assigned 1:1 diol : PhP=O species (**13-b**) shifted upfield 16.35 ppm (**Figure 3.25**).

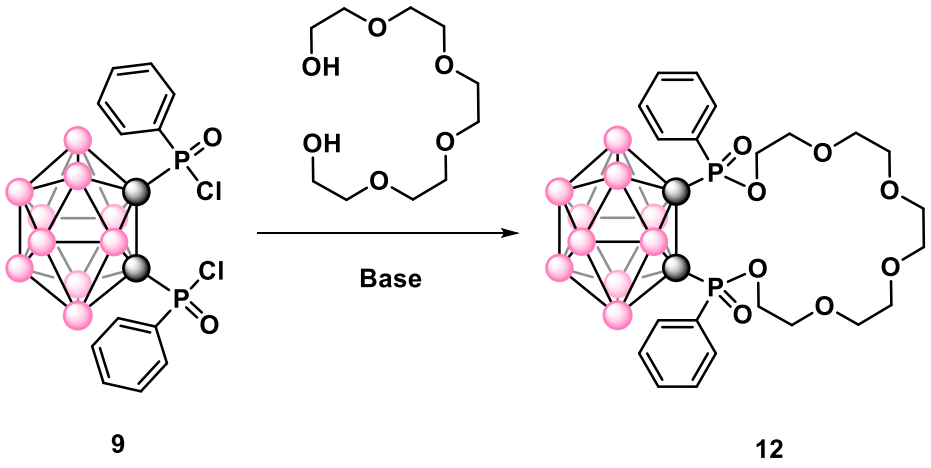

Scheme 3.16. Ongoing synthesis to produce **12**

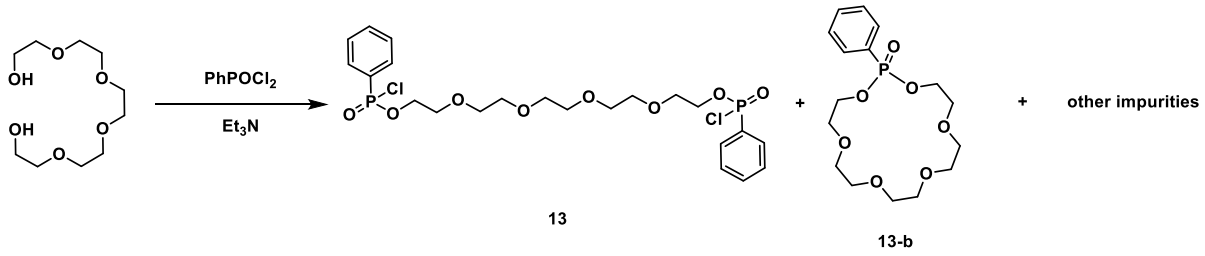

Scheme 3.17. Synthesis of **13** with byproduct **13-b** and other impurities

When KH was used as base for the reaction of **9** with pentaethylene glycol (**Scheme 3.16**), formation of Cb and **13-b** were also observed, as evidenced by ^{1}H, ^{11}B, ^{31}P NMR spectroscopy, indicating the dissociation of PhP=O group in **9**. Addition of 1 equiv **13** to the deprotonated Cb ($CbLi_2$) also yielded insoluble polymerized products. Like the diethylene glycol case, mixing **9-b** and pentaethylene glycol in the presence of Et_3N resulted in almost no change to the ^{11}B NMR spectra with upfield shift on phosphorus and proton resonance at 0.37 ppm and 0.02 ppm, respectively. The shift and integration of the crown ether proton resonances were close to the desired product **12**. Ongoing further characterization of **12** is currently underway.

3.3 Summary

In summary, we described the synthesis and characterization of a series of crown ether Cb compounds. After measuring the electrochemical properties of these species, we performed chemical reduction to access their *nido*-form. The *nido*-Cb crown ethers were quite reactive due to their strong negative reduction events, highlighting the importance of anodically shifting their reduction potentials. Surprisingly, our attempt to incorporate carbon spacer groups further increased these species' reduction potentials. To address this concern further, we next

introduced a more electron withdrawing spacer group, -PhPO-, into the Cb crown ether and worked on synthesizing the desired products. With the fully characterized *closo*- and *nido*-Cb crown ethers, we will next study the capture and release of Li which will be described in Chapter 4.

3.4 Experimental

General Considerations. All manipulations were carried out under an atmosphere of dry, oxygen-free N_2 within an MBraun glovebox (MBRAUN UNIlab Pro SP Eco equipped with a −35 °C freezer), or by standard Schlenk techniques. Pentane, hexanes, benzene, Et_2O, DCM, and THF (inhibitor-free) were dried and degassed on an MBraun Solvent Purification System and stored over activated 4 Å molecular sieves. All other solvents were degassed by freeze−pump−thaw and stored on activated 4 Å molecular sieves pubs.acs.org/IC Article prior to use. Celite and 4 Å molecular sieves were dried at 250 °C under dynamic vacuum (<0.1 Torr) for 24 h prior to use. Elemental analyses were recorded at the University of California, Berkeley, using a PerkinElmer 2400 Series II combustion analyzer. $Cb(OH)_2$[10] and poly-ether ($TsO(CH_2)_3O(CH_2)_2O(CH_2)_3OTs$)[11] were prepared following previous reports. Ortho-carborane, naphthalene, potassium metal, Kryptofix 222, 18-crown-6, [NEt_4][Br], dibromopropane, KH, Pentaethylene glycol di-p-toluenesulfonate, Bis(2-bromoethyl) Ether, 1,3-Dichloro-1,1,3,3-tetramethyldisiloxane and other reagents were obtained from Sigma-Aldrich, Fisher Scientific, or VWR and used without further purification.

Spectroscopic Measurements. NMR spectra were obtained on an Agilent Technologies 400 MHz DD2, Varian Unity Inova 500 MHz, Bruker Avance NEO 500 MHz, or a Varian 600 MHz spectrometer, and referenced to residual solvent. Chemical shifts (δ) are

recorded in ppm and the coupling constants are in Hz. J. Young airtight adaptors were used for air- and water-sensitive compounds. All measurements were carried out on recrystallized product. All stock solutions and dilutions were prepared by mass or volume.

Mass Spectrometry. Mass spectra were collected on a Shimadzu GC-2010 gas chromatograph coupled to a Shimadzu GCMS-QP2010 mass spectrometer. The instrument is equipped with a 30 m × 0.25 mm Agilent DB-1 column with a dimethylpolysiloxane stationary phase (0.25 μm). Helium was used as the carrier gas.

X-ray Crystallography. Data was collected on a Bruker KAPPA APEX II diffractometer equipped with an APEX II CCD detector using a TRIUMPH monochromator with a Mo Kα X-ray source (α = 0.71073 Å). The crystals were mounted on a cryoloop under Paratone-N oil, and all data were collected at 110 K using an Oxford nitrogen gas cryostream system. A hemisphere of data was collected using ω scans with 0.5° frame widths. Data collection and cell parameter determination were conducted using the SMART program. Integration of the data frames and final cell parameter refinement were carried out using SAINT software. Absorption correction of the data was carried out using SADABS. Structure determination was done using direct or Patterson methods and difference Fourier techniques. All hydrogen atom positions were idealized and rode on the atom of attachment. Structure solution, refinement, graphics, and creation of publication materials were carried out using SHELXTL or OLEX.2

Electrochemical measurements. CV was performed on a CH Instruments 630E Electrochemical Analysis Potentiostat. The working electrode was a 3 mm diameter glassy carbon (CH Instruments) electrode and was cleaned prior to each experiment by sequentially polishing with a gradient of 1.0 μm, 0.3 μm, and 0.05 μm alumina (CH Instruments) on a cloth

pad, followed by rinsing with distilled water and acetone. The Ag wire pseudo-reference were rinsed with distilled water and acetone. The Pt wire counter electrodes were rinsed with distilled water and acetone and heated white-hot with a butane torch. All measurements were performed on recrystallized product and referenced to the Fc/Fc^+ redox couple unless otherwise stated.

Synthesis of 1 In the glovebox, 0.070 g (0.4 mmol, 1 equiv) of $Cb(OH)_2$ was dissolving in 1 ml THF in a vial equipped with a magnetic stir bar and cooled to -25°C. To this, a THF suspension of 0.033 g KH (0.81 mmol, 2.05 equiv) was added and the resulting orange solution was stirred for 0.5h at RT. All volatiles were removed under reduced pressure and the resulting light yellow solid mixture was redissolved in DMF in a 100ml round bottom flask equipped with a magnetic stir bar. To this, 0.215 g $TsO(CH_2)_3O(CH_2)_2O(CH_2)_3OTs$ (0.4 mmol, 1 equiv) in ca. 5 mL of DMF was added dropwise and the resulting mixture was heat at 75°C overnight. After cooling, the DMF layer was extracted with 2x hexane. The hexane layer was washed with water 2 times, followed by brine wash. The hexane layer was dried over anhydrous $MgSO_4$ and concentrated by evaporation to yield 0.065 g (43.8%) of the compound **1** as white solid. To collect more 1, the residual DMF layer was dissolve in DCM and the organic phase was washed with water two times, followed by a brine wash. The organic layer was dried over anhydrous $MgSO_4$ and concentrated by evaporation. The raw mixture was purified by column chromatography (silica gel, hexane / ethyl acetate 9:1) to yield more **1** and **1-b**. Single crystals suitable for XRD studies were obtained by recrystallization from saturated diethyl ether solution at −25 °C. **^{1}H NMR** (400 Hz, $CDCl_3$): δ 3.97 (t, *J* = 5.4 Hz, 4H), 3.55 (t, *J* = 6.3 Hz, 4H), 1.84 (p, 4H), 1.15 (s, 12H). **^{1}H NMR** (400 Hz, MeCN-d_3): δ 4.00 (t, *J* = 5.4 Hz, 4H), 3.53 (t, *J* = 6.3 Hz, 4H), 1.77 (p, *J* = 5.9 Hz, 4H), 1.12 (s, 12H). Note: Cb B–**H** resonances are too

broad to be observed. **$^{11}B\{^{1}H\}$ NMR** (128 Hz, $CDCl_3$): δ -12.25, -14.19, -16.92. **$^{11}B\{^{1}H\}$ NMR** (128 Hz, MeCN-d_3): δ -12.65, -14.28, -17.23. **$^{11}B\{^{1}H\}$ NMR** of **1-b** (128 Hz, $CDCl_3$): δ -17.06, -22.70, -35.74, -39.60. Anal. Calcd for $B_{10}C_{14}O_4H_{34}$: C, 44.90; H, 9.15. Found: C, 45.27; H, 9.26.

Synthesis of 1-*nido*-K In the glove box, 0.055 g (0.4 mmol, 2 equiv) of naphthalene was dissolving in 1 ml anhydrous THF and added to a vial containing potassium metal (excess). The resulting dark green solution of potassium naphthalenide was stirred for 0.5h. In a separated vial equipped with a magnetic stir bar, 0.080 g (0.2 mmol, 1 equiv) of **1** was dissolving in 1 ml anhydrous THF and cooled to -25°C. To this, the THF solution of potassium naphthalenide in situ was added dropwise and the resulting colorless solution was stirred for 4h. The cloudy solution of THF solution was transferred to a glass frit with Celite and washed with THF (3 × 3 mL), then extracted with ca. 3 mL of MeCN. The MeCN fraction was brought to dryness under reduced pressure, affording a white powder of **1-*nido*-K**. Yield: 0.042 g (%). Single crystals suitable for XRD studies were obtained by recrystallization from saturated MeCN solution at −25 °C. **^{1}H NMR** (400 Hz, MeCN-d_3): δ 3.96 (d, *J* = 7.6 Hz, 4H), 3.43 (t, *J* = 5.5 Hz, 4H), 1.75 (p, *J* = 6.7 Hz, 4H), 1.10 (s, 12H). Note: Cb B–**H** resonances are too broad to be observed. **$^{11}B\{^{1}H\}$ NMR** (128 Hz, MeCN-d_3): δ -8.08, -22.95.

Synthesis of 2-b In the glovebox, 0.271 g (1.54 mmol, 1 equiv) of $Cb(OH)_2$ was dissolving in 1 ml THF in a vial equipped with a magnetic stir bar and cooled to -25°C. To this, a THF suspension of 0.126 g KH (3.15 mmol, 2.05 equiv) was added and the resulting orange solution was stirred for 0.5h at RT. All volatiles were removed under reduced pressure and the resulting light-yellow solid mixture was redissolved in DMF in a 100ml round bottom flask equipped with a magnetic stir bar. To this, 4.9 ml (12.3 mmol, 8 equiv) 1,3-Dibromopropane

in ca. 5 mL of DMF was added dropwise and the resulting mixture was heat at 75°C overnight. After cooling, the DMF layer was dissolve in DCM and the organic phase was washed with water two times, followed by a brine wash. The organic layer was dried over anhydrous $MgSO_4$ and concentrated by evaporation. The raw mixture was washed with ~30 ml diethyl ether and dried under reduced pressure. The crude product was purified by column chromatography (silica gel, hexane / ethyl acetate 4:1) to yield 0.31g (48.2%) of **2-b**. **^{1}H NMR** (400 Hz, $CDCl_3$): δ 4.05 (t, *J* = 5.7 Hz, 4H), 3.48 (t, *J* = 6.2 Hz, 4H), 2.20 (p, 4H). Note: Cb B–**H** resonances are too broad to be observed. **^{11}B{^{1}H} NMR** (128 Hz, $CDCl_3$): δ -11.97, -13.11, -14.39, -16.71

Synthesis of 2 In the glovebox, 0.130 g (0.74 mmol, 1 equiv) of Cb $Cb(OH)_2$ was dissolving in 1 ml THF in a vial equipped with a magnetic stir bar and cooled to -25°C. To this, a THF suspension of 0.061 g KH (1.52 mmol, 2.05 equiv) was added and the resulting orange solution was stirred for 0.5h at RT. All volatiles were removed under reduced pressure and the resulting light-yellow solid mixture was redissolved in DMF in a 100ml round bottom flask equipped with a magnetic stir bar. To this, 0.31g (0.74 mmol, 1 equiv) **2-b** in ca. 5 mL of DMF was added dropwise and the resulting mixture was heat at 75°C overnight. After cooling, the DMF layer was dissolve in DCM and the organic phase was washed with water two times, followed by a brine wash. The organic layer was dried over anhydrous $MgSO_4$ and concentrated by evaporation. The raw mixture was purified by column chromatography (silica gel, hexane / ethyl acetate 4:1) to yield 0.27g (84.3%) of **2**. **^{1}H NMR** (400 Hz, $CDCl_3$): δ 3.96 (t, *J* = 5.3 Hz, 8H), 2.01 (p, *J* = 5.2 Hz, 4H). Note: Cb B–**H** resonances are too broad to be observed. **^{11}B{^{1}H} NMR** (128 Hz, $CDCl_3$): δ -11.70, -13.81, -16.74.

1 step synthesis between $Cb(OH)_2$ and dibromopropane In the glovebox, 0.040 g (0.23 mmol, 1 equiv) of $Cb(OH)_2$ was dissolving in 1 ml THF in a vial equipped with a

magnetic stir bar and cooled to -25°C. To this, a THF suspension of 0.019 g KH (0.46 mmol, 2.05 equiv) was added and the resulting orange solution was stirred for 0.5h at RT. All volatiles were removed under reduced pressure and the resulting light-yellow solid mixture was redissolved in DMF in a 100ml round bottom flask equipped with a magnetic stir bar. To this, 0.019 g 1,3 dibromopropane (0.23 mmol, 1 equiv) in ca. 5 mL of DMF was added dropwise and the resulting mixture was heat at 80°C overnight. After cooling, the DMF layer was dissolve in DCM and the organic phase was washed with water three times, followed by a brine wash. The organic layer was dried over anhydrous $MgSO_4$ and concentrated by evaporation. Single crystals suitable for XRD studies of **2-c** were obtained by recrystallization from saturated diethyl ether solution at −25 °C. **^{1}H NMR** of **2-c** (400 Hz, $CDCl_3$): δ 4.16 (t, 8H), 2.12 (p, 4H). Note: Cb B–**H** resonances are too broad to be observed.

Reduction of 2 In the glove box, 0.012 g (0.09mmol, 4 equiv) of naphthalene was dissolving in 1 ml anhydrous THF and added to a vial containing potassium metal (excess). The resulting dark green solution of potassium naphthalenide was stirred for 0.5h. In a separated vial equipped with a magnetic stir bar, 0.01 g (0.02 mmol, 1 equiv) of **2** was dissolving in 1 ml anhydrous THF and cooled to -25°C. To this, the THF solution of potassium naphthalenide in situ was added dropwise and the resulting colorless solution was stirred for 4h. The cloudy solution of THF solution was transferred to a glass frit with Celite and washed with THF (3 × 3 mL), then extracted with ca. 3 mL of MeCN. The MeCN fraction was brought to dryness under reduced pressure, affording a white powder of **2-*nido***. Yield: 0.0093 g. **^{1}H NMR** (400 Hz, MeCN-d_3): δ 3.80 (broad, 8H), 1.75 (broad, 4H). Note: Cb B–**H** resonances are too broad to be observed. **^{11}B{^{1}H} NMR** (128 Hz, MeCN-d_3): δ -9.42, -23.86.

Synthesis of 3 In the glovebox, 0.109 g (0.62 mmol, 1 equiv) of $Cb(OH)_2$ was dissolving in 1 ml THF in a vial equipped with a magnetic stir bar and cooled to -25°C. To this, a THF suspension of 0.051 g KH (1.27 mmol, 2.05 equiv) was added and the resulting orange solution was stirred for 0.5h at RT. All volatiles were removed under reduced pressure and the resulting light-yellow solid mixture was redissolved in DMF in a 100ml round bottom flask equipped with a magnetic stir bar. To this, 0.338g (0.62 mmol, 1 equiv) Pentaethylene glycol di-p-toluenesulfonate in ca. 5 mL of DMF was added dropwise and the resulting mixture was heat at 75°C overnight. After cooling, the DMF layer was dissolve in DCM and the organic phase was washed with water two times, followed by a brine wash. The organic layer was dried over anhydrous $MgSO_4$ and concentrated by evaporation. The raw mixture was washed with ~20 ml hexane and dried under reduced pressure, yielding 0.1g of **3** (42.6%). Single crystals suitable for XRD studies of **3** and **3-b** were obtained by slow evaporation from saturated ether solution at room temperature. **^{1}H NMR** of **3** (400 Hz, $CDCl_3$): δ 4.01 (t, 4H), 3.73 (td, J = 4.9, 1.2 Hz, 4H), 3.61-3.68 (m, 16H). **^{11}B{^{1}H} NMR** (128 Hz, $CDCl_3$): δ -11.97, -14.22, -16.67. **^{1}H NMR** (400 Hz, MeCN-d_3): 4.02 (t, 4H), 3.67 (t, 4H), 3.60 – 3.51 (m, 16H). **^{11}B{^{1}H} NMR** (128 Hz, MeCN-d_3): δ -12.54, -14.40, -17.07. **^{1}H NMR** of **3-b** (400 Hz, $(CD_3)_2CO$): δ 3.61-3.93 (m, 24H). **^{11}B{^{1}H} NMR** (128 Hz, $(CD_3)_2CO$): δ -12.31, -15.85, -22.19, -22.88, -36.11, -39.19. Note: Cb B–**H** resonances are too broad to be observed.

Reduction of 3 In the glove box, 0.007 g (0.06mmol, 2 equiv) of naphthalene was dissolving in 1 ml anhydrous THF and added to a vial containing potassium metal (excess). The resulting dark green solution of potassium naphthalenide was stirred for 0.5h. In a separated vial equipped with a magnetic stir bar, 0.011 g (0.03 mmol, 1 equiv) of **2** was dissolving in 1 ml anhydrous THF and cooled to -25°C. To this, the THF solution of potassium

naphthalenide in situ was added dropwise and the resulting colorless solution was stirred for 4h. The cloudy solution of THF solution was transferred to a glass frit with Celite and washed with THF (3 × 3 mL), then extracted with ca. 3 mL of MeCN. The MeCN fraction was brought to dryness under reduced pressure, affording a white powder of **3-*nido***. Yield: 0.004 g. **^{1}H NMR** (400 Hz, MeCN-d_3): δ 3.76 (broad, 4H), 3.58 (broad, 16H), 3.52 (broad, 4H). Note: Cb B–**H** resonances are too broad to be observed. **^{11}B{^{1}H} NMR** (128 Hz, MeCN-d_3): δ -8.10, -10.73, -23.17, -24.92.

Synthesis of 4 In the glovebox, 0.02 g (0.1 mmol, 1 equiv) of $Cb(OH)_2$ was dissolving in 1 ml THF in a vial equipped with a magnetic stir bar and cooled to -25°C. To this, a THF suspension of 0.009 g KH (0.2 mmol, 2.05 equiv) was added and the resulting orange solution was stirred for 0.5h at RT. All volatiles were removed under reduced pressure and the resulting light-yellow solid mixture was redissolved in DMF in a 100ml round bottom flask equipped with a magnetic stir bar. To this, 0.022 ml (0.1 mmol, 1 equiv) 1,3-Dichloro-1,1,3,3-tetramethyldisiloxane in ca. 5 mL of DMF was added dropwise and the resulting mixture was heat at 75°C overnight. After cooling, the DMF layer was dissolve in DCM and the organic phase was washed with water two times, followed by a brine wash. The organic layer was dried over anhydrous $MgSO_4$ and concentrated by evaporation. The raw mixture was washed with ~20 ml hexane and dried under reduced pressure, yielding 0.019g of **3** (54.7%). Single crystals suitable for XRD studies of **3** were obtained by slow evaporation from saturated hexane solution at room temperature. **^{1}H NMR** (400 Hz, MeCN-d_3): δ 0.33 (s, 12H). Note: Cb B–**H** resonances are too broad to be observed. **^{11}B{^{1}H} NMR** (128 Hz, MeCN-d_3): δ -10.15, -13.28, -16.77.

General procedure for synthesis of carbon spacer Cb crown ether In the glovebox, 1 equiv of Cb $(CH_2OH)_2$ was dissolving in THF in a vial equipped with a magnetic stir bar and cooled to -25°C. To this, a THF suspension of 2.05 equiv KH was added and the resulting orange solution was stirred for 0.5h at RT. All volatiles were removed under reduced pressure and the resulting light-yellow solid mixture was redissolved in DMF in a 100ml round bottom flask equipped with a magnetic stir bar. To this, 1 equiv different electrophile crown ether linker in ca. 5 mL of DMF was added dropwise and the resulting mixture was heat at 80-100°C overnight. After cooling, the DMF layer was dissolve in DCM and the organic phase was washed with water two times, followed by a brine wash. The organic layer was dried over anhydrous $MgSO_4$ and concentrated by evaporation and afford the raw mixture, which was further purified in detail below depends on the compound.

Cb 20-crown-4 (5). 1 equiv $TsO(CH_2)_3O(CH_2)_2O(CH_2)_3OTs$ was used as the electrophile for integrating crown ether. The crude mixture after extraction was washed with ~20 ml diethyl ether and dried under reduced pressure. The further purification by column chromatography (silica gel, hexane / ethyl acetate 4:1) resulted in 62.6% yield of **5**. Single crystals suitable for XRD studies of **5** were obtained by slow evaporation from saturated hexane solution at room temperature. **^{1}H NMR** (400 Hz, $CDCl_3$): δ 3.92 (s, 4H), 3.53 (dt, *J* = 8.3, 5.8 Hz, 8H), 1.72 (p, *J* = 5.8 Hz, 4H), 1.12 (s, 12H). **^{11}B{^{1}H} NMR** (128 Hz, $CDCl_3$): δ -3.57, -11.25.

Cb 20-crown-6 (6) and deboronation product (6-b). 1 equiv Pentaethylene glycol di-p-toluenesulfonate was used as the electrophile for integrating crown ether. The crude mixture after extraction was washed with ~20 ml diethyl ether and dried under reduced pressure. The further purification by column chromatography (silica gel, hexane / ethyl acetate

4:1) resulted in 7.9% yield of **6** and 25% yield of **6-b**. Single crystals suitable for XRD studies of **6-b** were obtained by slow evaporation from saturated ether solution at room temperature.

Cb 11-crown-4 (7). 1 equiv Bis(2-bromoethyl) Ether was used as the electrophile for integrating crown ether. The crude mixture after extraction was washed with ~20 ml diethyl ether and dried under reduced pressure, resulted in 55.5% yield of **5**. **^{1}H NMR** of **6** (400 Hz, $CDCl_3$): δ 3.56-3.76 (m, 24H). **^{11}B{^{1}H} NMR** (128 Hz, $CDCl_3$): δ -3.57, -11.19.

Cb silicone crown with carbon spacer (8). 1 equiv 1,3-Dichloro-1,1,3,3-tetramethyldisiloxane was used as the electrophile for integrating crown ether. The crude mixture after extraction was washed with ~20 ml diethyl ether and dried under reduced pressure. resulted in 62% yield of **8**. Single crystals suitable for XRD studies of **8** were obtained by slow evaporation from saturated hexane solution at room temperature. **^{1}H NMR** (400 Hz, $CDCl_3$): δ 4.19 (s, 4H), 0.12-0.19 (m, 8H). **^{11}B{^{1}H} NMR** (128 Hz, $CDCl_3$): δ -3.80, -10.93

Synthesis of 9. In the glovebox, 0.176g (1.22 mmol, 1 equiv) of Cb was dissolving in 4 mL diethyl ether in a 20 ml vial equipped with a magnetic stir bar and cooled to -25°C. To this, a 1 mL of 2.5 M n-butyllithium in hexane solution (2.5 mmol, 2.05 equiv) was added and the resulting colorless suspension was stirred for 1h at RT. The suspension was filtered and washed with ~5 mL hexane and ~5 mL diethyl ether over a frit. The resulting white solid of Cb Li_2 was transferred to a 20 mL vial and dried under vacuum. ~4 mL diethyl ether was added, and the suspension was cooled to -78°C in a cold well inside the glove box. To this, 0.489 g (2.5 mmol, 2.05 equiv) Phenylphosphonic dichloride in ca. 8 mL of diethyl ether was added dropwise at -78°C. The resulting light orange solution with suspension was stirred overnight while ambient environment slowly warm to room temperature. The reaction mixture in ether was filtered washed with ca. 5 mL of diethyl ether followed by ca. 5 mL of DCM. All volatiles

in ether and DCM fraction were removed under reduced pressure respectively. The dried ether fraction was washed with hexane and yielded 0.46g of **9** (81.5%). The dried DCM fraction yield g of **9-b**. Single crystals suitable for XRD studies of **9** were obtained by Recrystallization from saturated diethyl ether solution at -25°C. **^{1}H NMR** of **9** (400 Hz, $CDCl_3$): δ 8.05 (td, 4H), 7.72 (dd, 2H), 7.59 (td, *J* = 7.7, 5.5 Hz, 4H), 1.45-3.72 (broad, 10H, BH). **^{11}B{^{1}H} NMR** (128 Hz, $CDCl_3$): δ 1.59, -7.20, -9.41. **^{31}P NMR** (162Hz, $CDCl_3$): δ 38.04. **^{1}H NMR** of **9b** (400 Hz, $CDCl_3$): δ 7.98 (td, 4H), 7.69 (dd, 2H), 7.55 (td, 4H), 1.40-3.30 (broad, 10H, BH). **^{11}B{^{1}H} NMR** (128 Hz, $CDCl_3$): δ 1.71z, -7.10, -8.90. **^{31}P NMR** (162Hz, $CDCl_3$): δ 37.80.

3.5 Appendex

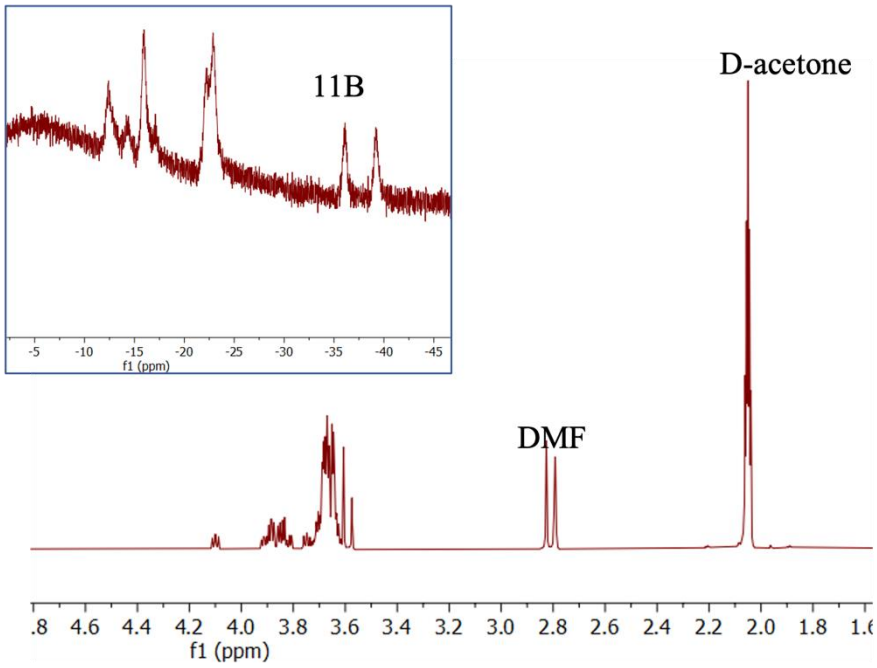

Figure 3.23. ^{1}H (400 MHz) and ^{11}B (128 MHz) NMR spectra of **3-b** and small contamination of **3**

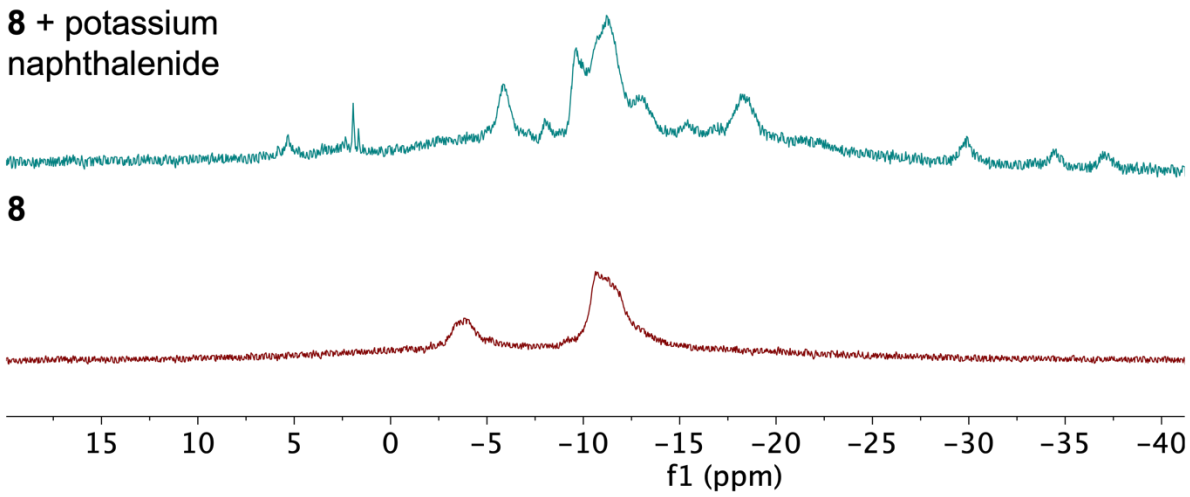

Figure 3.24. ^{11}B NMR (128 MHz) spectra of **8** before and after add potassium naphthalenide

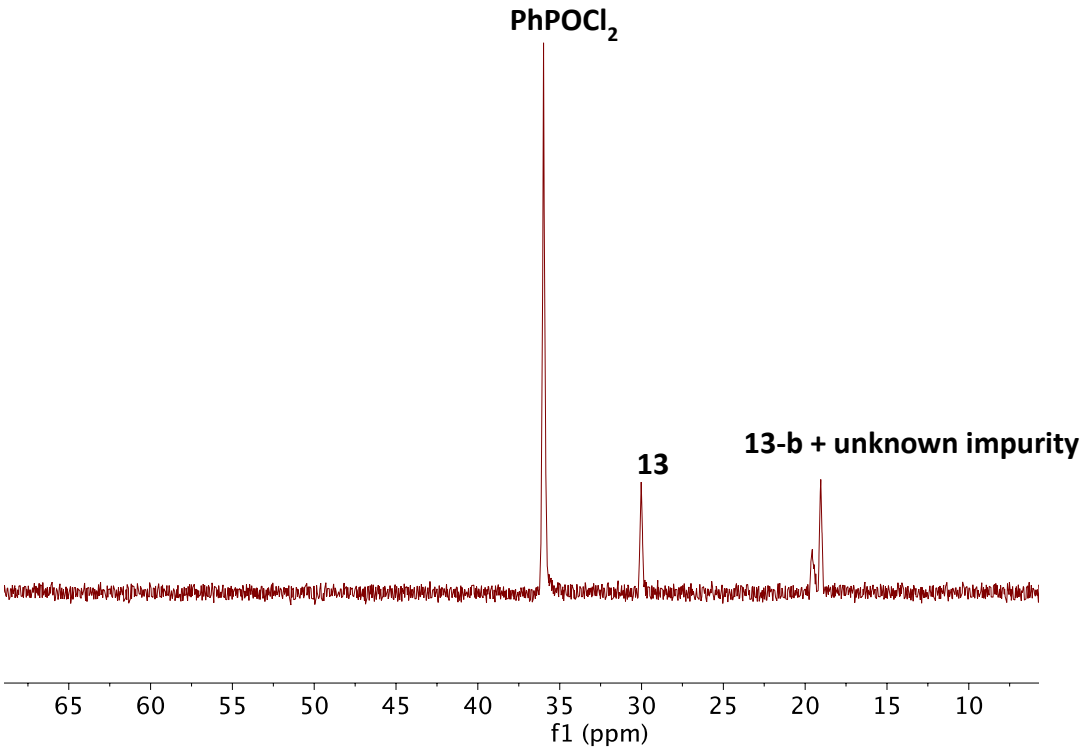

Figure 3.25. ^{31}P NMR (162 MHz) spectra of crude mixture from reactions described in **Scheme 3.17**

3.6 Reference

(1) Heying, T. L.; Ager, J. W.; Clark, S. L.; Mangold, D. J.; Goldstein, H. L.; Hillman, M.; Polak, R. J.; Szymanski, J. W. A New Series of Organoboranes. I. Carboranes from the Reaction of Decaborane with Acetylenic Compounds. *Inorganic Chemistry* **1963**, *2* (6), 1089-1092.

(2) Fisher, S. P.; Tomich, A. W.; Lovera, S. O.; Kleinsasser, J. F.; Guo, J.; Asay, M. J.; Nelson, H. M.; Lavallo, V. Nonclassical Applications of closo-Carborane Anions: From Main Group Chemistry and Catalysis to Energy Storage. *Chemical Reviews* **2019**, *119* (14), 8262-8290.

(3) Núñez, R.; Tarrés, M.; Ferrer-Ugalde, A.; de Biani, F. F.; Teixidor, F. Electrochemistry and Photoluminescence of Icosahedral Carboranes, Boranes, Metallacarboranes, and Their Derivatives. *Chemical Reviews* **2016**, *116* (23), 14307-14378.

(4) Grimes, R. N. *Carboranes*; Elsevier Inc., 2016.

(5) Keener, M.; Hunt, C.; Carroll, T. G.; Kampel, V.; Dobrovetsky, R.; Hayton, T. W.; Ménard, G. Redox-switchable carboranes for uranium capture and release. *Nature* **2020**, *577* (7792), 652-655.

(6) Keener, M.; Mattejat, M.; Zheng, S.-L.; Wu, G.; Hayton, T. W.; Ménard, G. Selective electrochemical capture and release of uranyl from aqueous alkali{,} lanthanide{,} and actinide mixtures using redox-switchable carboranes. *Chem. Sci.* **2022**, *13* (12), 3369-3374.

(7) Deng, L.; Cheung, M.-S.; Chan, H.-S.; Xie, Z. Reduction of 1,2-(CH2)n-1,2-C2B10H10 by Group 1 Metals. Effects of Bridge Length/Rigidity on the Formation of Carborane Anions. *Organometallics* **2005**, *24* (25), 6244-6249.

(8) Teixidor, F.; Pedrajas, J.; Vinas, C. Cathodic Cleavage of C-S and C-P in Carboranyl Derivatives. *Inorganic Chemistry* **1995**, *34* (7), 1726-1729.

(9) Bartsch, R. A.; Czech, B. P.; Kang, S. I.; Stewart, L. E.; Walkowiak, W.; Charewicz, W. A.; Heo, G. S.; Son, B. High Lithium Selectivity in Competitive Alkali-Metal Solvent Extraction by Lipophilic Crown Carboxylic Acids. *Journal of the American Chemical Society* **1985**, *107* (17), 4997-4998.

(10) Ohta, K.; Goto, T.; Yamazaki, H.; Pichierri, F.; Endo, Y. Facile and efficient synthesis of C-hydroxycarboranes and C,C′-dihydroxycarboranes. *Inorganic Chemistry* **2007**, *46* (10), 3966-3970.

(11) Citterio, D.; Takeda, J.; Kosugi, M.; Hisamoto, H.; Sasaki, S. I.; Komatsu, H.; Suzuki, K. pH-independent fluorescent chemosensor for highly selective lithium ion sensing. *Analytical Chemistry* **2007**.

(12) Sachleben, R. A.; Moyer, B. A. Ligand Design for Small Cations: The Li+/14-Crown-4 System. *ACS Symposium Series* **1999**, *716*, 114-132.

(13) Barberà, G.; Vaca, A.; Teixidor, F.; Sillanpää, R.; Kivekäs, R.; Viñas, C. Designed synthesis of new ortho-carborane derivatives: From mono- to polysubstituted frameworks. *Inorganic Chemistry* **2008**, *47* (16), 7309-7316.

(14) Chui, K.; Li, H.-W.; Xie, Z. Synthesis and Structural Characterization of closo-exo, exo-nido, and pseudocloso Group 1 Carborane Compounds of the C2B10 System. *Organometallics* **2000**, *19* (25), 5447-5453.

(15) Yinghuai, Z.; Hosmane, N. S. Carborane-based transition metal complexes and their catalytic applications for olefin polymerization: Current and future perspectives. *Journal of Organometallic Chemistry* **2013**, *747*, 25-29.

(16) Stanko, V. I.; Brattsev, V. A.; Knyazev, S. P. Structural Rearrangements in Carbaboranes and Related Compounds. *Russian Chemical Reviews* **1979**, *48* (2), 130-152.

(17) Szabo, M.; Wallace, M. I. Imaging potassium-flux through individual electropores in droplet interface bilayers. *Biochimica et Biophysica Acta (BBA) - Biomembranes* **2016**, *1858* (3), 613-617.

(18) Dankert, F.; Richter, R. M.; Weigend, F.; Xie, X.; Balmer, M.; von Hanisch, C. Construction of Inorganic Crown Ethers by s-Block-Metal-Templated Si-O Bond Activation. *Angew Chem Int Ed Engl* **2021**, *60* (18), 10393-10401, From NLM PubMed-not-MEDLINE.

(19) Li, N.; Zeng, F.; Qu, D.; Zhang, J.; Shao, L.; Bai, Y. Synthesis and characterization of carborane-containing polyester with excellent thermal and ultrahigh char yield. *Journal of Applied Polymer Science* **2016**.

(20) Stauber, J. M.; Schwan, J.; Zhang, X.; Axtell, J. C.; Jung, D.; McNicholas, B. J.; Oyala, P. H.; Martinolich, A. J.; Winkler, J. R.; See, K. A.; et al. A Super-Oxidized Radical Cationic Icosahedral Boron Cluster. *Journal of the American Chemical Society* **2020**, *142* (30), 12948-12953.

Chapter 4

Lithium capture and release with redox switchable ortho-carborane based compounds

4.1 Introduction

As mentioned in Chapter 1, Li^+ extraction from seawater has drawn increasing attention due to the lithium demand is predicted to outpace supply (land-based lithium production) in next two decades.[1-6] Low Li^+ concentration and other competing metal cations (Na^+, K^+, Mg^{2+}, etc.) remain the major challenges for selectively extracting Li^+ from seawater. Our approach for selective Li^+ extraction is to utilize redox switchable Cb compounds, which was applied in previous uranium studies.[7, 8] Our investigation on Li^+ capture/release began with the series of Cb based compounds that were synthesized and characterized as described in Chapter 3.

To achieve effective and efficient Li^+ extraction, the key factors for Li^+ chelating species are having high Li^+ affinity and selectivity, which can be measured by multiple analytical methods. For monophasic Li^+ measurement, UV-Vis spectroscopy is a common method for UV-active Li^+ coordinating species, where their distinctive UV absorption bands have been shown to change as a function of Li^+ concentration.[9, 10] Another method involves NMR spectroscopic measurements and commonly by monitoring proton and Li^+ resonances.[11, 12] For example, chelating Li^+ with crown ether is a fast exchange process, in which coordinated Li^+ and free Li^+ reach an equilibrium that is faster than the NMR timescale. As the result, the chemical shift of crown ether proton resonances in ^1H NMR spectroscopy and Li^+ resonances in ^7Li NMR spectroscopy change as the amount of the coordinating ligand increases, which is different from slow exchange reactions where starting material disappear with the concomitant appearance of product resonances. Studies with crown ethers have shown that binding constants (K) for Li^+, as well as K_{Li}/K_{Na} selectivity measurements, can be calculated by plotting chemical shift changes as a function of crown ether concentrations.[11] Another method to determine Li^+ affinity and selectivity is through biphasic studies by using ICP-OES to measure

[Li^+] or other metal concentrations in the aqueous phase before and after extraction to an organic phase.[10, 13-16]

To the best our knowledge, our Cb crown species are rare examples of redox active Li^+ coordinating species.[17, 18] Therefore, we took this opportunity to study the affinity and selectivity of metal cations using electrochemistry.[19-21] Using in cyclic voltammetry (CV), the potential shift of the redox events in the presence of metal binding interaction can be correlated to the Gibb's Free Energy using the Nernst equation, $\Delta G = -nFE^o$ and binding affinity K for each metal can be calculated through equation $\Delta G = -RTlnK$.[22-25] By utilizing these analytical methods, we performed measurements on the Li^+ affinity and selectivity of synthesized *closo*- and *nido*- Cb crown species to probe their abilities to achieve Li^+ capture/release cycle (**Figure 1.4**), with details presented in this chapter.

4.2 Results and Discussion

4.2.1 Li^+ measurements with 1

We first started our Li^+ affinity and selectivity measurement on compound **1** featuring 14-crown-4 donor ligand. UV-Vis spectroscopy was ineffective for **1** due to a lack of useful absorption bands in the spectral window. Next, we turned to ^{7}Li NMR spectroscopy to measure the Li^+ affinity of **1**. LiTFAB (TFAB = $[B(C_6F_5)_4]^-$, a non-coordinating anion) was used as the Li^+source for its solubility in organic solvents, such as MeCN-d_3. With a fixed concentration of LiTFAB, we monitored the change in the Li^+ chemical shift by increasing the equivalents of **1.** A sealed capillary of 1M LiCl in D_2O was added to the NMR tube as external standard for accurate chemical shift measurement (**Figure 4.1**).

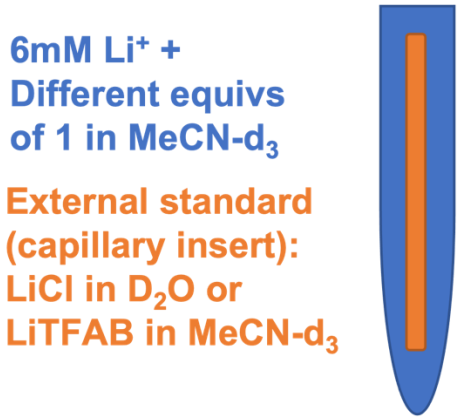

Figure 4.1 Depiction of NMR tube and insert for NMR measurement of Li^+ affinity of **1**

With the LiTFAB concentration set to 0.006 M in MeCN-d_3, 0-3.7 equivs of **1** was added and each sample was analyzed by ^{7}Li NMR spectroscopy as shown in **Figure 4.2**. At 0 equiv, the free LiTFAB had a sharp Li^+ resonance at -2.7 ppm. After increasing the equivalents of **1** at room temperature, the Li^+ resonance became broader and after 3.7 equiv **1** was added, the full width at half maximum of Li^+ resonance changed from 1.28 to 17.32. The chemical shift of Li^+ resonance moved upfield by ~0.0046 ppm, further indicating the existence of a very weak crown/Li^+ interaction, which was similar but much smaller to the peak shifts in reported crown ethers lithium studies that are fast exchange processes.[12, 26] The Cb cluster in **1** had no interaction with LiTFAB evidenced by no shift in ^{11}B NMR spectroscopy. A control study was conducted by mixing LiTFAB with 1 equiv of substituted 14-crown-4 that we chemically synthesized that was structurally similar as **1** (without Cb cluster), which is known to bind Li^+ strongly and selectively.[27] The ^{7}Li NMR spectrum of this control showed the 12-crown-4 coordinated Li^+ resonance shifted 1.12 ppm upfield relative to free Li^+, which was 100 times more than the observed shift in ^{7}Li NMR spectroscopic measurement of **1** under the

same condition. The control measurement further confirmed **1** had a poor Li^+ affinity, which was likely due to the strong electron withdrawing Cb cluster.

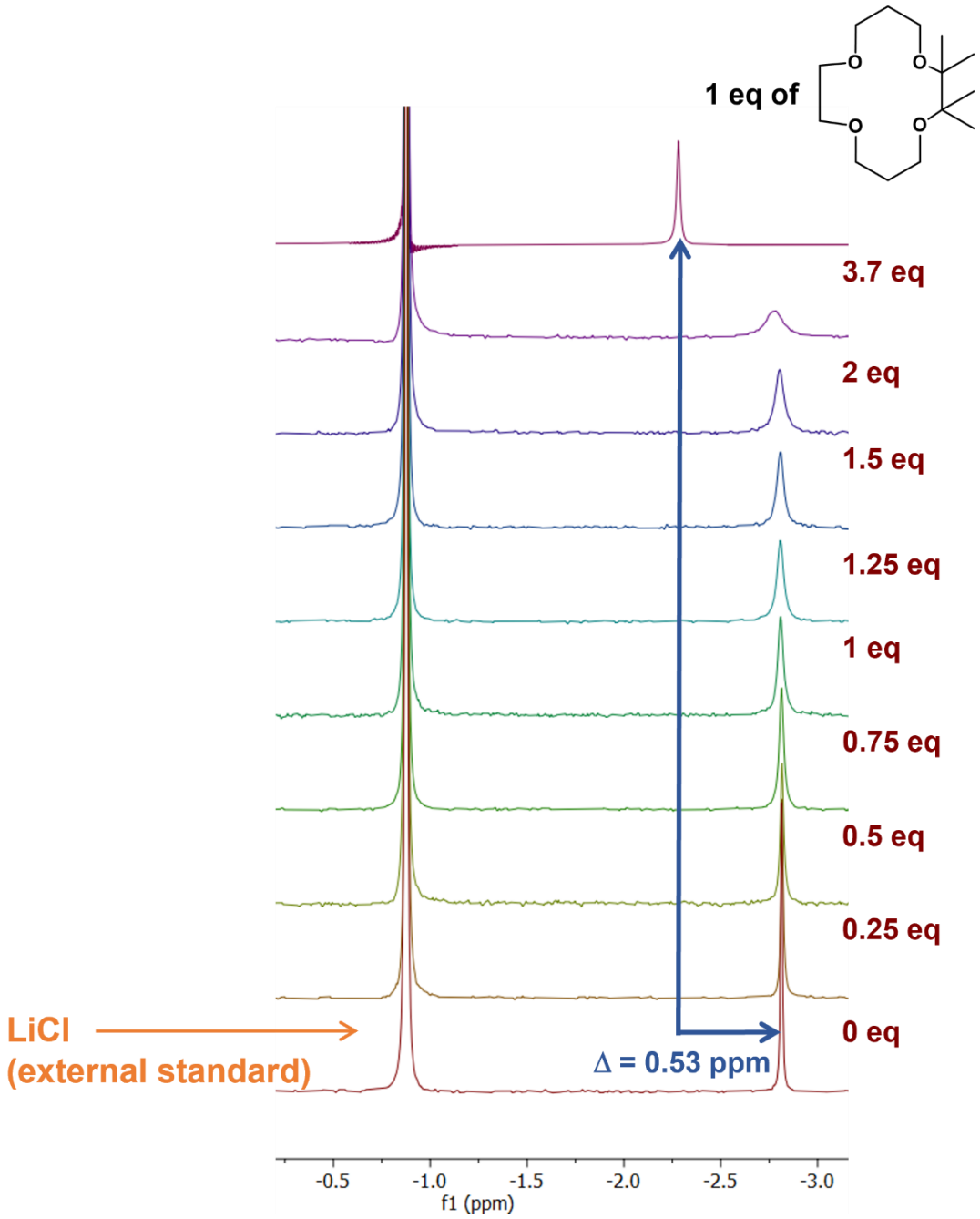

Figure 4.2. Stacked ^{7}Li NMR (155 MHz) spectra of 0.006 M LiTFAB after mixing with different equivalent of **1** or 1 equiv 12-crown-4 in MeCN-d_3 with LiCl in D_2O as external standard

The weak interaction between **1** and Li^+ can be further confirmed with ^1H NMR spectroscopy by tracking the proton resonances of the crown ether in **1**. For this measurement, the concentration of **1** was held constant and different equivs of LiTFAB were added. The proton resonance of **1** shifted upfield and broadened as equivalents of LiTFAB increased, confirming the existence of interaction between **1** and Li^+ (**Figure 4.2 top**). The small Li^+ chemical shift changes after 2 equiv LiTFAB further suggested the poor Li^+ affinity. Interestingly, at 1.25 equiv LiTFAB addition, both ^1H and ^7Li NMR spectra indicated a second set of crown Li^+ exchange that may originated from the sandwich type binding mode of two crown ether stacking Li^+.[28, 29] The residual water likely interfered with LiTFAB coordination as the water proton peak in ^1H NMR spectroscopy also shifted upfield. The small shift on proton resonance was also observed with LiCl or $LiBF_4$ after mixing **1**.

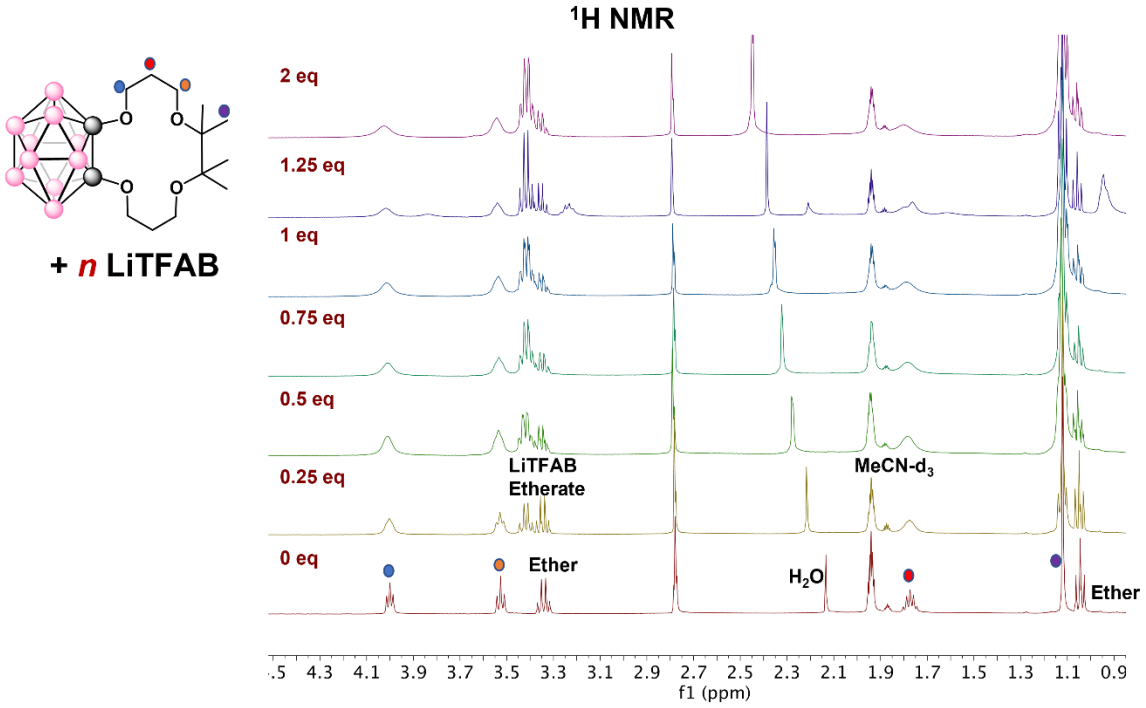

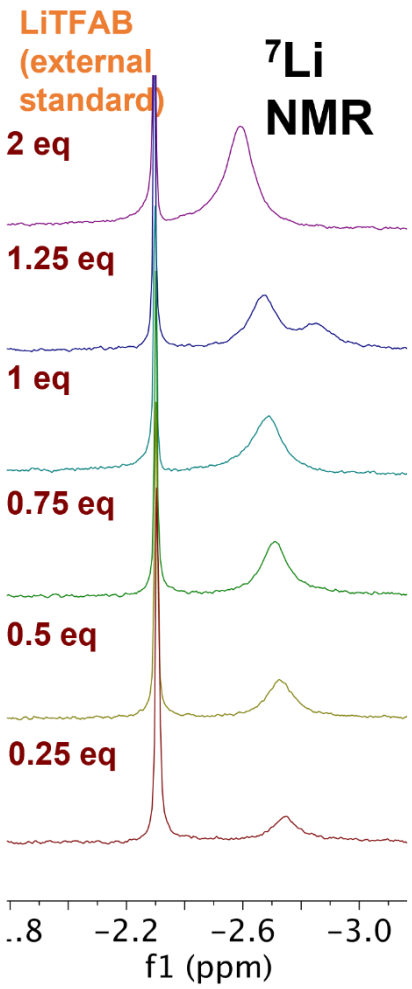

Figure 4.3. Stack ^{1}H NMR (400 MHz) and ^{7}Li NMR (155 MHz) spectra of 0.03 M **1** after mixing different equivalent of LiTFAB in MeCN-d_3 with LiTFAB in MeCN-d_3 as external standard. Compound **1** peaks are labeled with dots

A selectivity study was next conducted by adding a mixture of Li, Na and KTFAB to a MeCN-d_3 solution of **1**. The weak Li^+ interaction was still observed in the presence of competing Na^+ and K^+, confirmed by ^{1}H and ^{7}Li NMR spectroscopy. Furthermore, addition of only NaTFAB or KTFAB to **1** resulted in no proton resonance shift or broadening in the ^{1}H

NMR spectroscopy, suggesting that **1** was Li^+ selective for the small amount of Li^+ that can be chelated.

The fast exchange between Li^+ and crown can be slowed down at cooler temperatures to distinguish different Li^+ environments using variable temperature (VT) NMR experiments, as shown in **Figure 4.4**. Here, 1 equiv of **1** was added to a mixture of Li, Na and KTFAB with an external standard in place. As the temperature decreased, the broad Li^+ resonance split into two peaks, confirming the existence of multiple lithium interactions. In the ^1H NMR spectrum at -38.5 °C, we assigned the large sharp downfield peak near -2.8 ppm as the free Li^+, and the small upfield peak near -1.7 ppm as **1** coordinating to Li^+, further demonstrating the poor Li^+ affinity of **1**. The Na^+ resonance observed by ^{23}Na NMR spectroscopy remained almost unchanged with decreasing temperatures, confirming that 1 had higher Li^+ affinity than Na^+ (**Figure 4.4**).

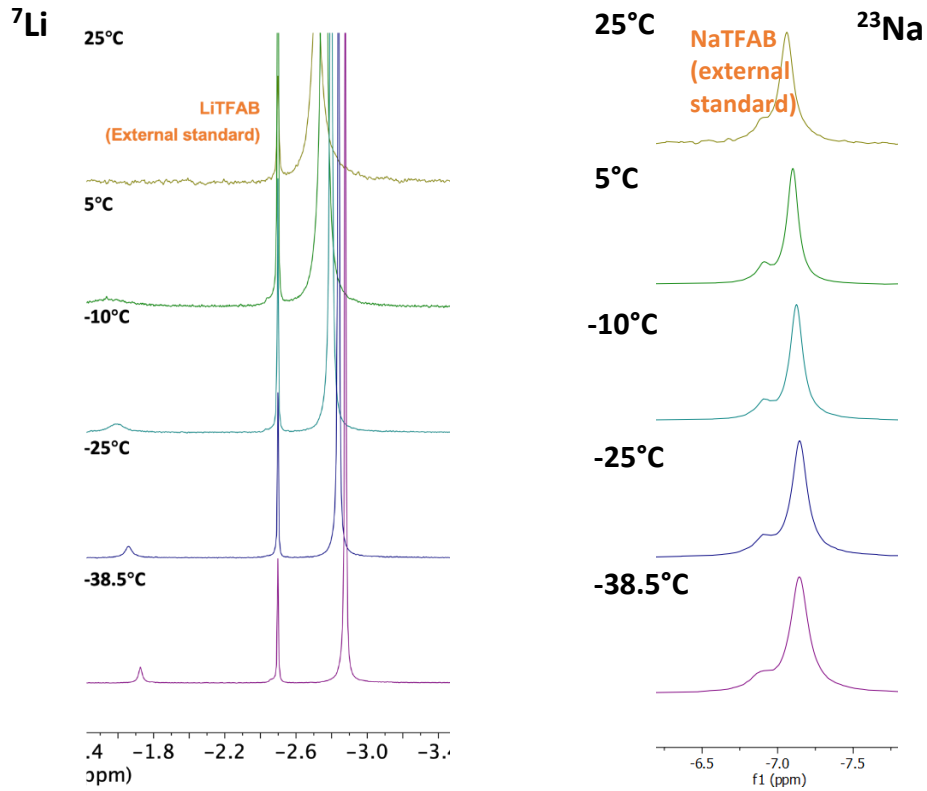

Figure 4.4. ^{7}Li (155 MHz) and ^{23}Na (106 MHz) NMR spectroscopic measurement of mixing 1 equiv **1** with Li, Na and KTFAB at variable temperature

We further conducted biphasic extraction studies using aqueous solutions of LiCl and chloroform or nitrobenzene solutions of **1**. ICP-OES was used to analyze the aqueous phase after calibration curved was constructed with standards LiCl solutions. After mixing LiCl aqueous layer and organic solutions of **1** with stirring for 16h, no Li^+ concentration change was observed before and after the extraction, confirming the weak Li^+ affinity of **1** from NMR spectroscopic measurements. Additionally, attempts to grow crystals of **1** with Li^+ coordinating were all proved unsuccessful after mixing **1** with 1 equiv of LiCl, $LiPF_6$, $LiBF_4$ and LiTFAB. Interestingly, reaction with 1 equiv strong base LiOH in ethanol led to a boron dissociation on Cb cage and formed deboronated Cb 14-crown-4 chelated LiOEt (**1-b-Li**) with solid-state structure shown in **Figure 4.5**.

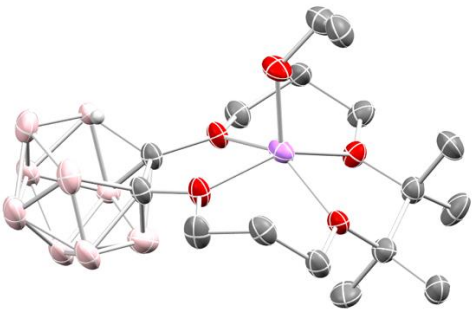

Figure 4.5. Solid-state molecular structure of **1-b-Li**. All except counter cation H atoms have been omitted for clarity. Li, pink purple; B, pink; C, black; O, red

The combined measurements suggested **1** was selective towards Li^+, similar to 14-crown-4, but with much weaker Li^+ affinity. Nevertheless, the poor Li^+ affinity of **1** may be beneficial for the Li^+ release step (**Figure 1.4**), which more captured Li^+ can be released in *closo*-form.

4.2.2 Li^+ capture studies with 1-*nido*-K using NMR spectroscopic measurements

After showing poor Li^+ affinity of **1**, we next moved on to its *nido*-form **1-*nido*-K** that was chemically synthesized. Due to the significant negative reduction potential, **1-*nido*-K** was extremely water sensitive. Therefore, ICP-OES analysis for biphasic conditions was not applicable for **1-*nido*-K** measurements. Next, we turned to NMR spectroscopic measurements to probe the Li^+ affinity and selectivity of **1-*nido*-K**. Our first attempt involved adding different equivs of LiTFAB to a fixed concentration of **1-*nido*-K** under same condition as the ^1H NMR studies of **1** (**Figure 4.6**). New downfield Li^+ peaks appeared and their intensity grew upon increasing the equivs of LiTFAB, unlike the crown/Li^+ interactions we observed for **1**. While a Li^+ interaction seems to exist, it was unclear if K^+ displacement from the crown pocket in **1-*nido*-K** occurred.

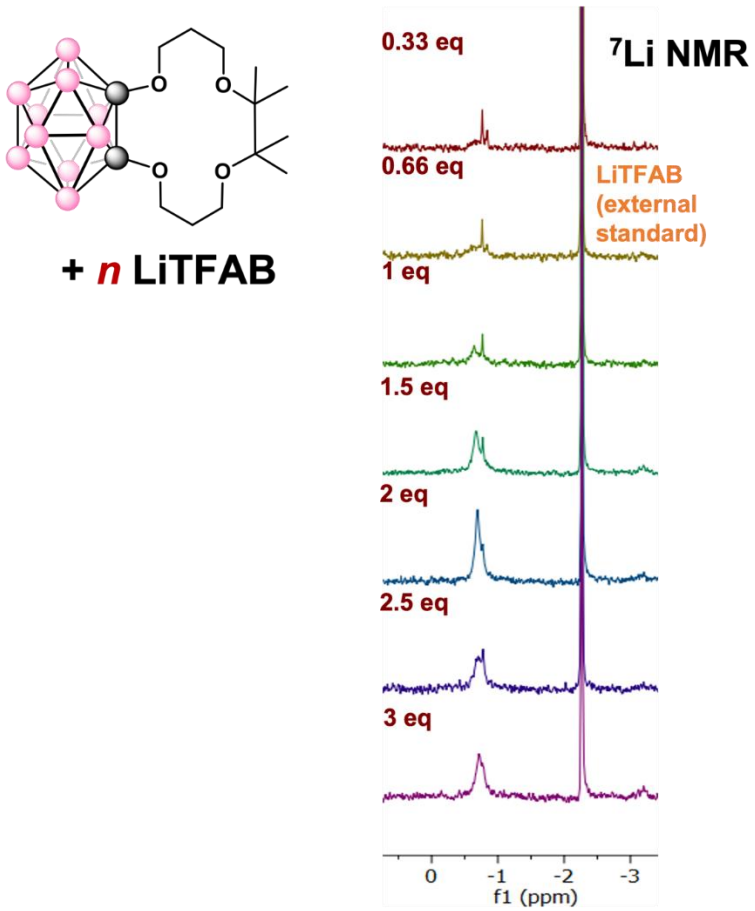

Figure 4.6. ^{7}Li NMR (155 MHz) spectra of **1-*nido*-K** with different equivs of LiTFAB in MeCN-d_3 at r.t.

With 2 equivs LiTFAB added to **1-*nido*-K**, we noticed the formation of **1-*nido*-b** (**Figure 3.4**, Chapter 3) and some deboronation biproducts in ^{11}B NMR spectroscopy, which were also observed after excess LiCl was added (**Figure 4.7**). To minimize interference from unwanted byproducts for binding affinity study of **1-*nido*-K**, a Li^+ salt with a more redox stable anion may be required. ^{11}B NMR spectrum of the reaction of **1-*nido*-K** with $LiPF_6$ showed the degradation peaks were much less pronounced compared to LiCl or LiTFAB. Therefore, we began to investigate the binding affinity of **1-*nido*-K** with $LiPF_6$ using NMR spectroscopy.

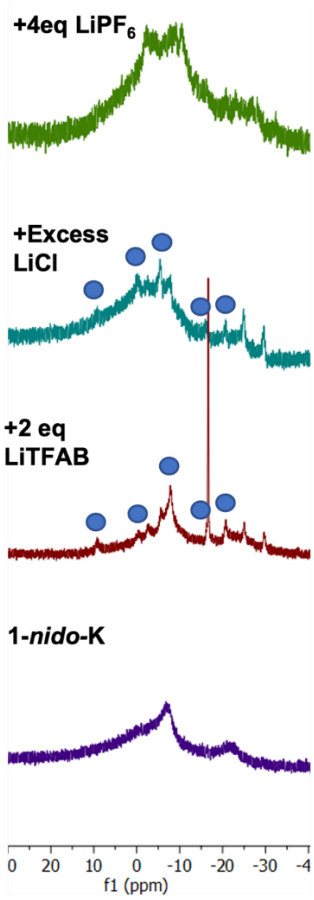

Figure 4.7. ^{11}B NMR (128 MHz) spectra of **1-*nido*-K** with LiTFAB, LiCl and $LiPF_6$ at r.t. **1-*nido*-b** is labeled with blue dots.

For the NMR spectroscopic measurements with $LiPF_6$, we set the concentration of $LiPF_6$ to 0.006M in MeCN-d_3, followed by monitored the change of Li^+ resonance and its chemical shift by increasing the equivalent of **1-*nido*-K** with a sealed capillary of LiTFAB in MeCN-d_3 as external standard (**Figure 4.8**), similar to ^{7}Li NMR spectroscopic measurement of **1**.

We observed that as we increased the ratio of **1-*nido*-K** to $LiPF_6$, the Li^+ resonance shifted significantly downfield as shown in **Figure 4.8**, similar to reported strong Li^+ chelating

species.[11, 12] The Li^+ resonance after adding 1 equiv of **1-*nido*-K** shifted 3.416 ppm, far more than the 1.12 ppm observed with 12-crown-4 and significantly more than the 0.0046 ppm shift with **1** (**Figure 4.2**), indicating that **1-*nido*-K** strongly binds to Li^+. The Li^+ peaks became notably broader, suggesting the existence of multiple Li^+ coordination environments. These different environments were observed upon collecting the ^7Li NMR spectrum at -38.5 °C, revealing 2 sharp peaks (**Figure 4.9**). We suspect that one Li^+ ion acts as an outer-sphere counter cation and the second Li^+ ion was captured in the crown ether pocket, similar to what we observe with the two K^+ ion environments in the solid-state molecular structure of **1-*nido*-K** (**Scheme 3.2**).

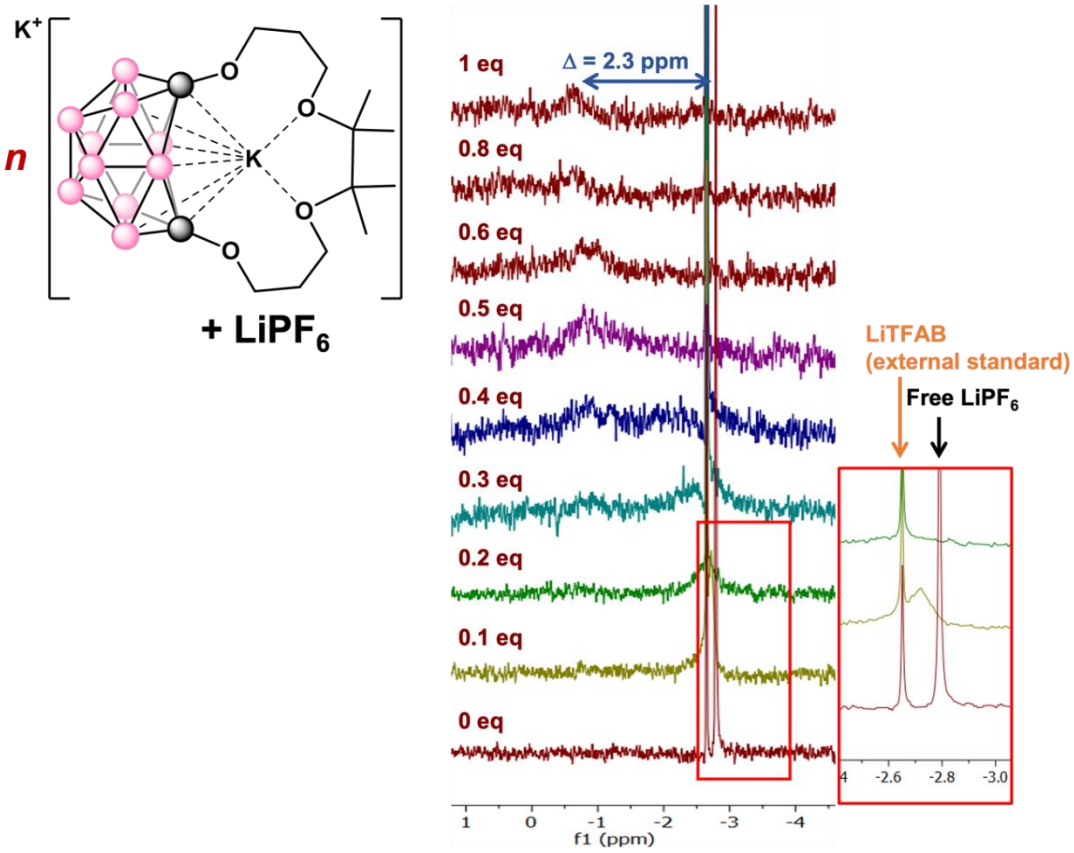

Figure 4.8. Stack ^7Li NMR (155 MHz) spectra of $LiPF_6$ with different equivs of **1-*nido*-K** at r.t.

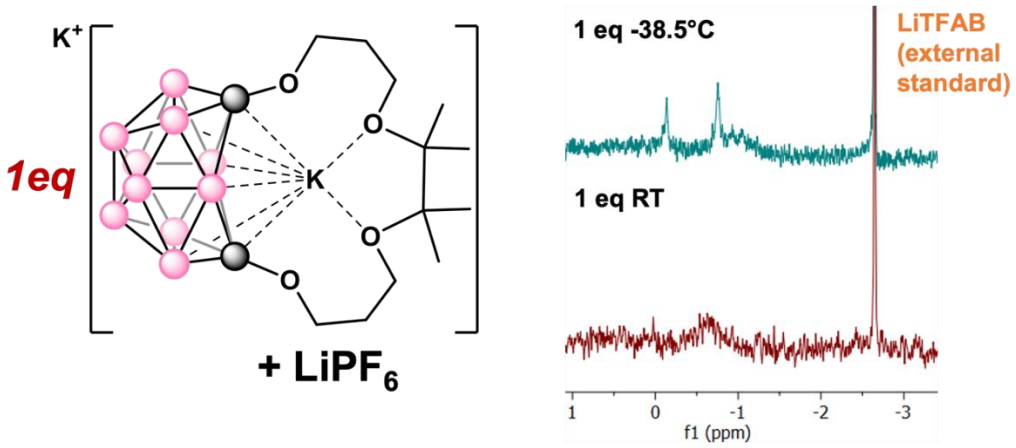

Figure 4.9. ^{7}Li NMR (155 MHz) spectra of $LiPF_6$ with 1 equiv of **1-*nido*-K** at -38.5 °C and r.t.

4.2.3 Li^+ selectivity studies with 1-*nido*-K using NMR spectroscopic measurements

The selectivity study was conducted by adding different equivalent of **1-*nido*-K** to a mixture of Li and $NaPF_6$ in MeCN-d_3 and the chemical shifts were monitored by both ^{7}Li and ^{23}Na NMR spectroscopy (**Figure 4.10a**). To correlate the selectivity of **1-*nido*-K**, several control studies were performed with crown ethers that have high Li^+ or Na^+ selectivity. We used the previously synthesized 14-crown-4 for better comparison of the effects of Cb cluster on Li^+ capture. 18-crown-6 was applied in the same condition for its selectivity towards Na^+ over Li^+ (**Figure 4.10b**).

As 1 equiv of 14-crown-4 was mixed with $LiPF_6$ and $NaPF_6$, the Li^+ peak shifted 0.3 ppm downfield in ^{7}Li NMR spectroscopy and sodium resonance shifted only -0.03 ppm. For 18-crown-6, which is known to have higher Na^+ selectivity, the Li^+ peak only shifted 0.01 ppm and the Na^+ signal shifted significantly by 4.9 ppm.

The changes in chemical shift from these control reactions set great reference values for measuring the selectivity of **1-*nido*-K**. We observed that as we increased the ratio of **1-*nido*-K** to $LiPF_6$, the Li^+ resonance became broader and shifted downfield by 0.23 ppm. This change was less than the observed shift in 14-crown-4 control but much more than the shift with 18-crown-6, as well as the observed shift by **1**. The change in ^{23}Na NMR spectroscopy was less significant at 0.08 ppm at 0.8 equiv, suggesting a higher Na^+ interaction relative to 14-crown-4 but much lower than 18-crown-6. The combined NMR spectroscopy data indicated **1-*nido*-K** had a decent Li^+ selectivity over Na^+, closed to level of 14-crown-4 that has the highest Li^+ selectivity among all crown ethers.[16]

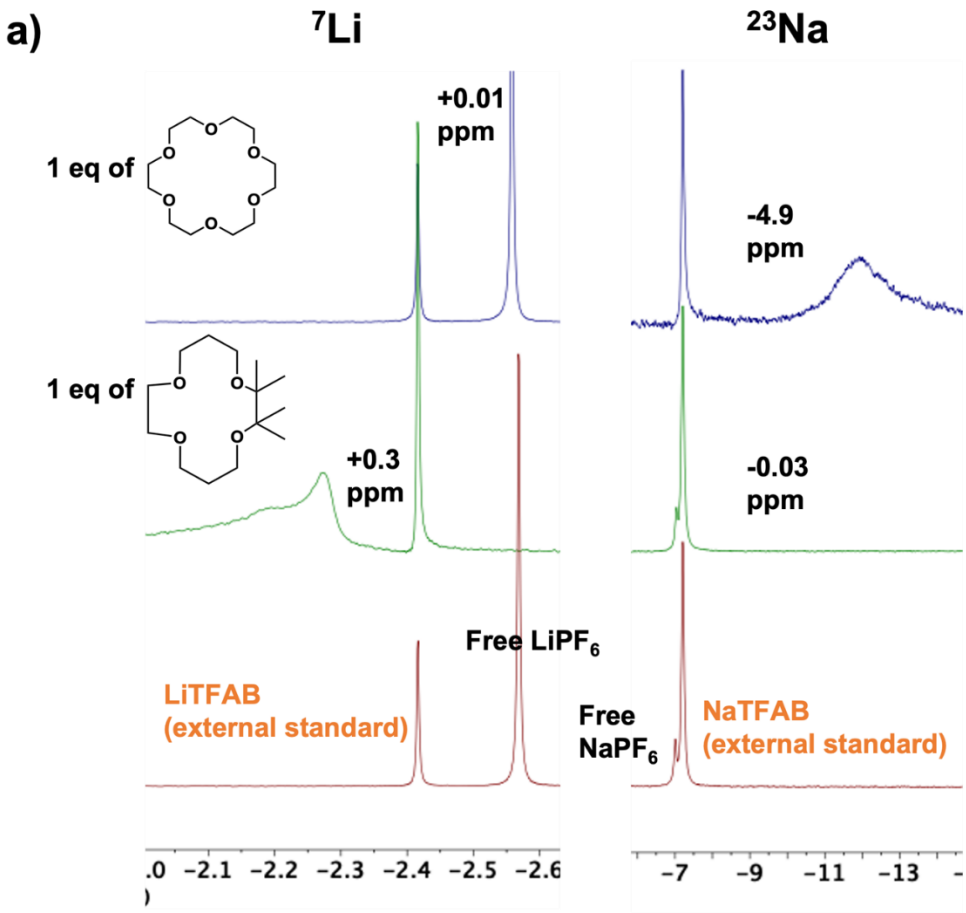

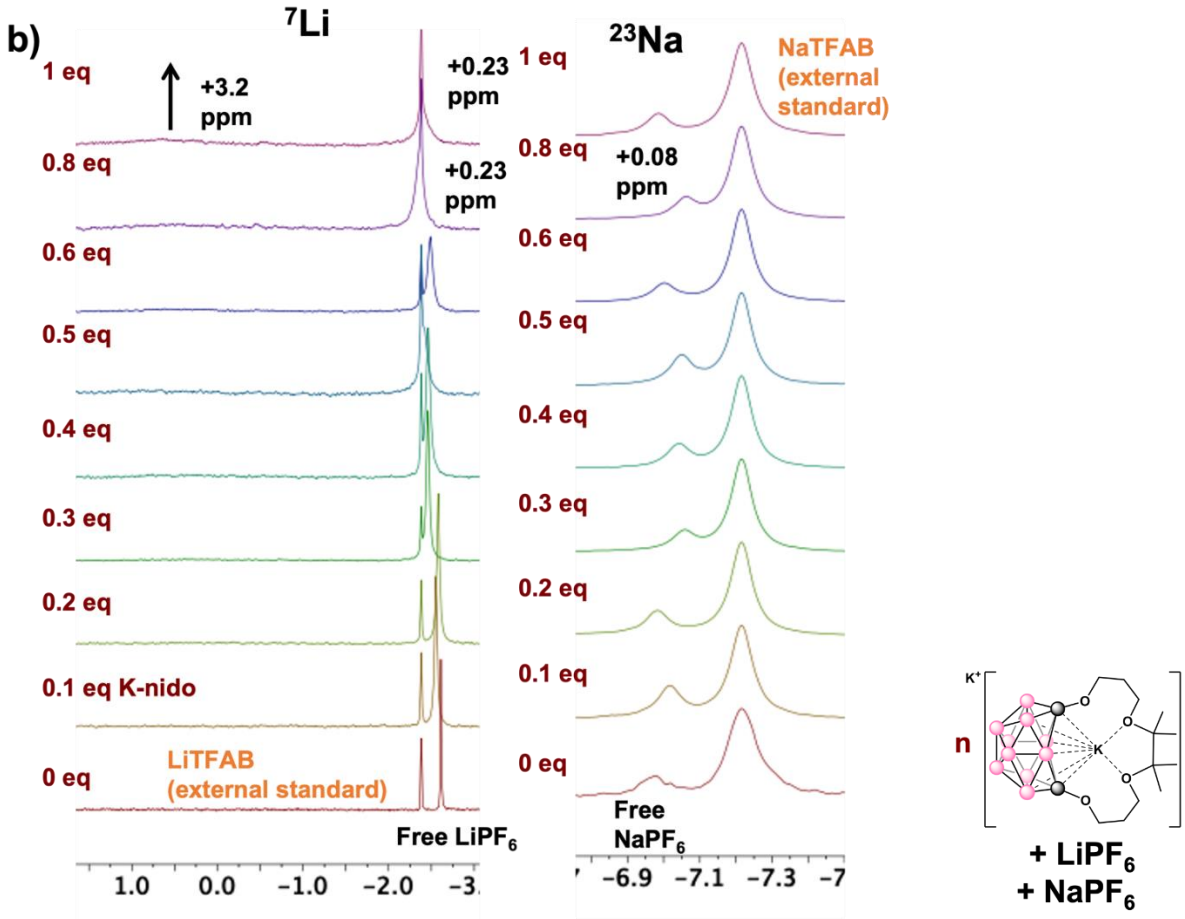

Figure 4.10. a) ^{7}Li (155 MHz) and ^{23}Na NMR (106 MHz) spectra of $LiPF_6$ and $NaPF_6$ with 1 equivs of synthesized 14-crown-4 and 18-crown-6 at r.t. b) ^{7}Li (155 MHz) and ^{23}Na (106 MHz) NMR spectra of 1:1 ratio of $LiPF_6$:$NaPF_6$ with different equiv of added **1-*nido*-K** at r.t.

4.2.4 Electrochemical measurements on *nido*-form of 1 in DMF

Although **1-*nido*-K** demonstrated strong Li^+ affinity, the K^+ counter cation could cause interference for accurate selectivity measurement. Therefore, we turned to electrochemistry to study the selectivity of metal free *nido*-form of 1 (**1-*nido***) using CV. In the presence of an alkali or alkaline-earth metal, the oxidation potential should shift anodically, indicating that

the oxidation becomes less thermodynamically favorable.[19-21] Additionally, we suspected that selectivity could be observed electrochemically by the formation of an oxidation potential corresponding to the preferred metal in a mixed-metal solution.

We recollected the CV of **1** in DMF using an $Ag_{(s)}$/AgOTf reference electrode. Then, to the same analyte solution containing **1**, we titrated different equivalents [Li] [PF_6], [Na][PF_6], or [K][PF_6] solution and scan at 50 mV/s (**Figure 4.11**). To avoid electrodeposition of the metals near the reduction potential of the Cb, the electrodes were polished between each scan.

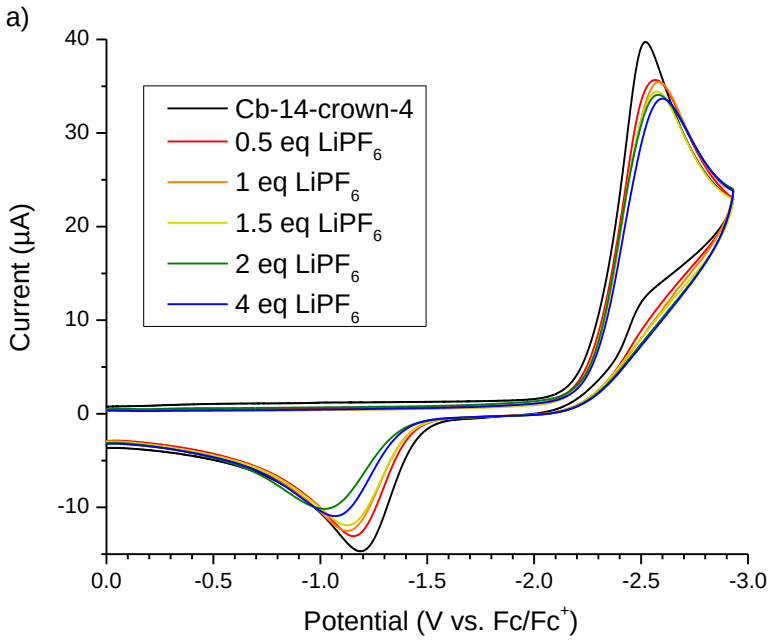

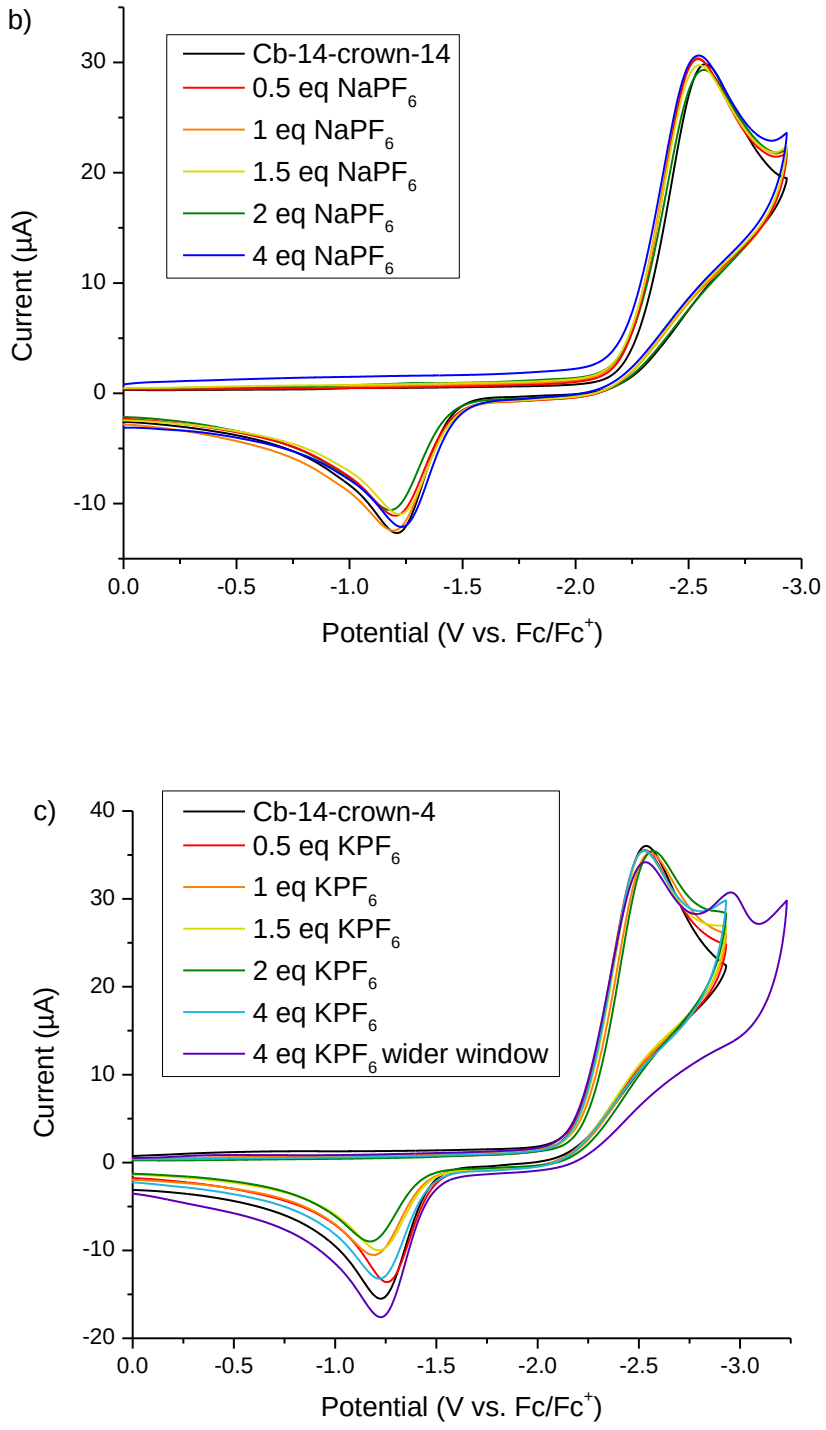

Figure 4.11. a) Cyclic voltammogram of **1** with varying equivalents of $LiPF_6$. b) Cyclic voltammogram of **1** with varying equivalents of $NaPF_6$. c) Cyclic voltammogram of **1** with

varying equivalents of KPF_6. All CVs were performed in DMF with 0.1M $[NBu_4][PF_6]$ and 2.9mM of analyte at a 50mV/s scan rate. Glassy carbon working electrode. Pt wire counter electrode. Ag/AgOTf reference electrode.

We observed that the oxidation wave shifted as equivalent of metal cation increased for all metal $[PF_6]^-$. The 2^- charged **1-*nido*** can interact with two alkali metal cations as shown in **1-*nido*-K**. Therefore, we compared the oxidative shift with 2 equivs of metal present for all metal cations (**Figure 4.12**). The stacked cyclic voltammograms indicated the oxidation peak shifted most by 215 mV anodically with Li^+ present in solution. Na^+ and K^+ shifts were smaller at 44 mV and 50 mV, respectively, suggesting a strong thermodynamic preference for Li^+ binding.[19, 20]

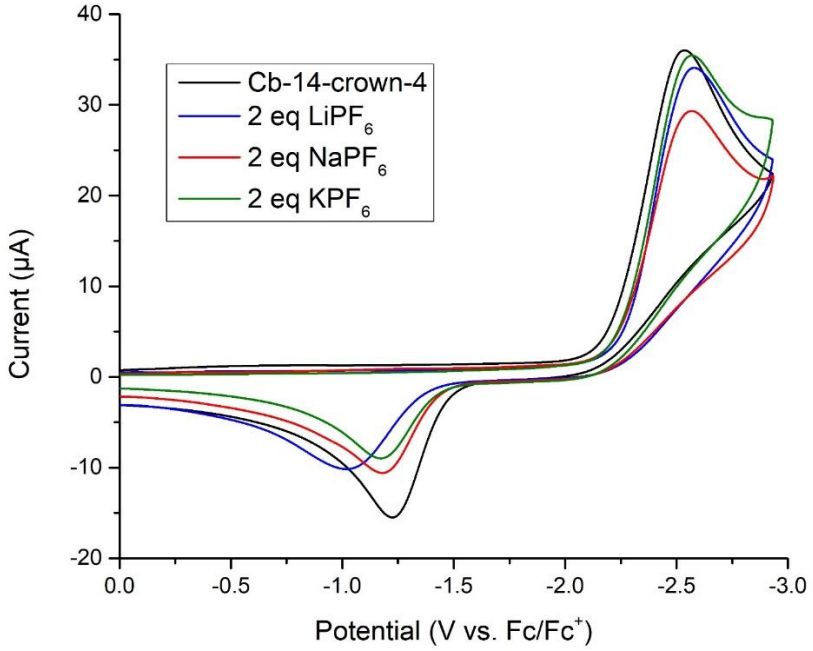

Figure 4.12. CV of 1 with 2 equivalents of $LiPF_6$, $NaPF_6$, or KPF_6 in DMF.

With the promising results from cyclic voltammograms, we began to probe Li^+ binding more accurately with electrochemically generated **1-*nido*** and monitored its oxidation event with different metal cation using differential pulse voltammetry (DPV). To avoid K^+ counter cations from chemical reduction of **1**, we performed a Galvanostatic bulk electrolysis on a 0.02 M solution of **1** in a 0.1 M tetrabutylammonium hexafluorophosphate solution in DMF (**Figure 4.26**). After charging for 24 hours, complete conversion of **1** to **1-*nido*** was observed along with the formation of side products that shared the same boron peaks as **1-*nido*-b** and **1-*nido*-H**, as shown in the unlocked ^{11}B NMR spectroscopy (**Figure 4.13** top). The solution containing **1-*nido*** was divided into 5 equal volume solutions DPV was performed after the addition of 2 equivalents of Li^+, Na^+, or K^+, or using a mixed metal or metal free solutions to measure selectivity of **1-*nido*** (**Figure 4.13** bottom).

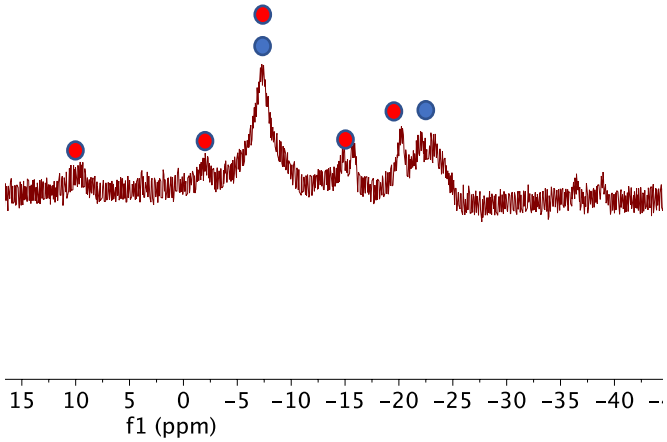

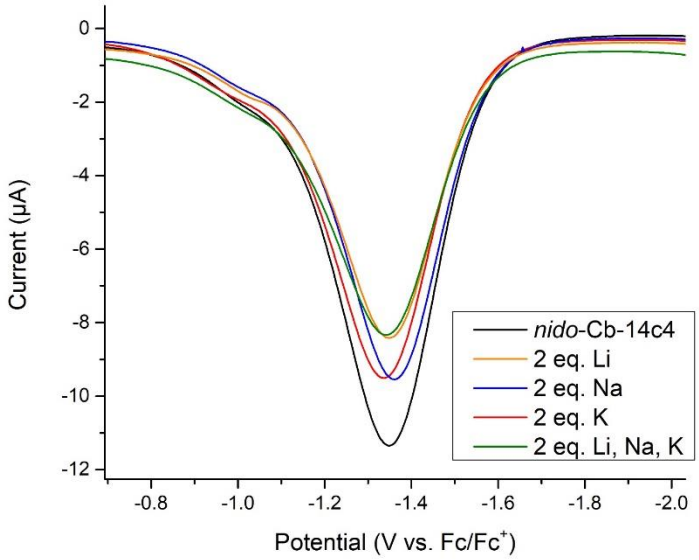

Figure 4.13. unlocked ^{11}B NMR spectrum of reaction solution after bulk electrolysis (top). **1-*nido*** and **1-*nido*-b** peaks labeled with blue and red dots, respectively. DPV of 0.003 M **1-*nido*** with 2 equivalents of $LiPF_6$, $NaPF_6$, KPF_6 or mixed metal in DMF with 0.1 M $[NBu_4][PF_6]$ (bottom). Glassy carbon working electrode. Pt wire counter electrode. Ag/AgOTf reference electrode.

The oxidation of **1-*nido*** occurs at -1.34 V vs. Fc/Fc^+ and DPV showed only small oxidation shifts with the presence of metal cations, contradicting the observed shifts in the previous CV experiments. Due to these observed inconsistencies, we repeated the CVs of **1** with and without 2 equivs $LiPF_6$ under the same conditions with polishing of the same glassy carbon electrode between each scan (**Figure 4.14**).

The CV of **1** shifted ~10mV between each scan when the same carbon working electrode was polished. With 2 equivalents of $LiPF_6$ present, and polishing between each scan, two of the scans overlap, but the third scan was shifted ~20 mV anodically. This data indicated the surface area of the electrode has a substantial effect on the CV. Additionally, we suspected

this inconsistency in potential may have resulted from solvent effects of DMF interacting with the metal cations. Therefore, we turned back to NMR spectroscopic measurements to study $LiPF_6$ interaction with **1-*nido*-K** in DMF under similar conditions as previous NMR experiments.

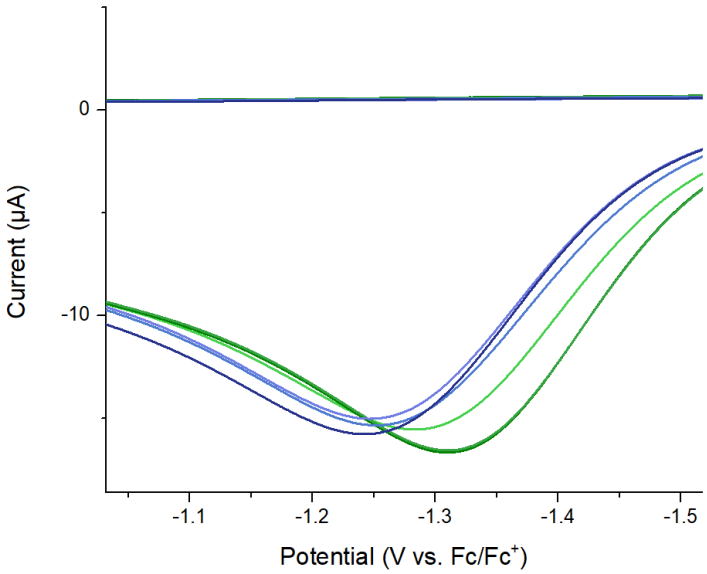

Figure 4.14. Cyclic voltammograms in DMF with 0.1M $[NBu_4][PF_6]$ and 2.9mM of **1** at a 50mV/s scan rate for consistency test. Glassy carbon working electrode. Pt wire counter electrode. Ag/AgOTf reference electrode. Blue - CV of 1. Green - CV of 1 with two equivalents of $LiPF_6$.

4.2.4 NMR spectroscopic measurements on *nido*-form of 1 in DMF

As shown in **Figure 4.15b**, the free $LiPF_6$ resonance was around 0.1 ppm in DMF, which was more downfield than MeCN-d_3. As we added 0.5 and 1 equiv **1-*nido*-K**, the changes in chemical shift were only 0.016 and 0.077 ppm, respectively. However, the control study of mixing 1 equiv 12-crown-4 and $LiPF_6$ shifted Li^+ resonance by a smaller number of 0.048 ppm, suggesting Li^+ interacted strongly with DMF than MeCN. To understand DMF ability to

interact with $LiPF_6$, we added an aliquot DMF into the MeCN-d_3 solution of $LiPF_6$ and the Li^+ resonance shifted 1.7 ppm as shown in **Figure 4.15a**, indicating DMF had a strong Li^+ interaction that affects the consistency of the previous electrochemical study.

Although the strong Li^+ affinity from DMF lessened the chemical shift change, **1-*nido*-K** resulted a bigger Li^+ resonance change than 12-crown-4 in DMF, further supporting the strong Li^+ affinity of **1-*nido*-K**. We noticed one 1 day after mixing $LiPF_6$ with **1-*nido*-K**, the Li^+ resonance shifted slightly downfield as we observed a formation of **1-*nido*-b** in unlocked ^{11}B NMR spectroscopy (**Figure 4.15c**). We purposely add $FcPF_6$ to oxidize the **1-*nido*-K**, which resulted a sharper Li^+ signal that shifted downfield and close to the free Li^+, suggesting that the captured Li^+ can be released due the poor Li^+ affinity of **1** in *closo*-form. Furthermore, this Li^+ resonance shift from captured and released Li^+ were also observed in ^7Li NMR spectrum of **1-*nido*-K** with both $LiPF_6$ and $NaPF_6$. After oxidation, we observed the formation of boron peaks from compound **1** with a byproduct that we proposed was the oxidized **1-*nido*-b**. These NMR spectroscopic measurements showed the redox switching **1** and **1-*nido*** system had capability to achieve Li^+ capture/release cycle.

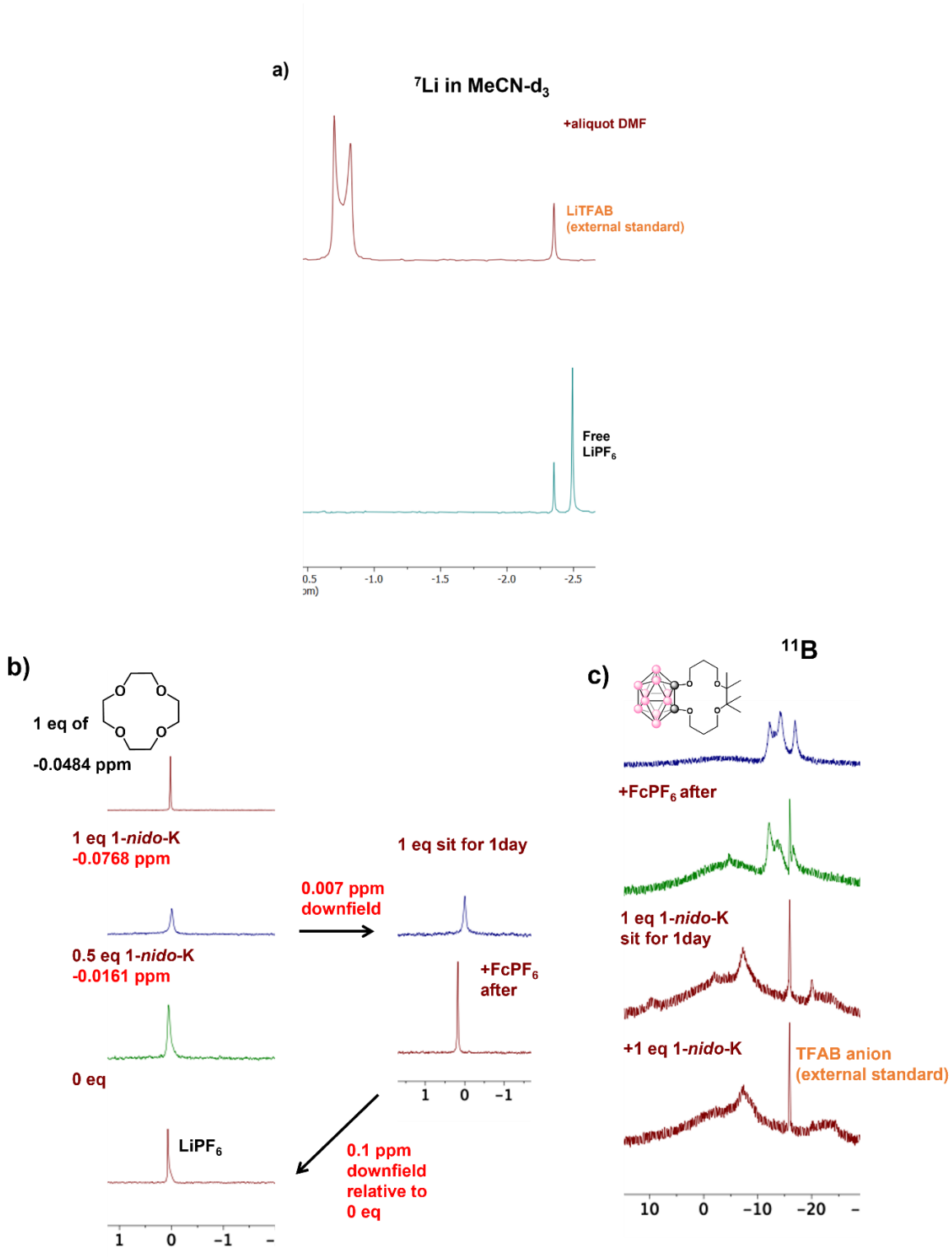

Figure 4.15. a) ^{7}Li NMR (155 MHz) spectra of $LiPF_6$ with aliquot DMF followed by 12-crown-4 in MeCN-d_3. b) Unlocked ^{7}Li NMR (155 MHz) spectra of $LiPF_6$ with different equiv

of **1-*nido*-K** in DMF at r.t. followed by addition of $FcPF_6$ (LiTFAB peak ignored for clarity). c) unlocked ^{11}B NMR (128 MHz) spectra of the **1-*nido*-K** with $LiPF_6$ before and after $FcPF_6$

4.2.5 Other lithium interaction with *nido*-form of 1

Although $LiPF_6$ provided more stability for Li^+ measurement of **1-*nido*-K**, formation of **1-*nido*-b** still occured, indicating *nido*-Cb cluster in **1-*nido*-K** underwent structural change in addition of chelating Li^+. We noticed the formation of **1-*nido*-b** (*nido*-Cb structural change) was avoided when mixing LiHMDS with **1-*nido*-K**, evidenced by the unchanged boron resonance in ^{11}B NMR spectroscopy, indicating the proposed rearrangement of *nido*-cage did not occur. The proton resonance from crown ether remained symmetric (no doublet of triplet) and coalesced like **1-*nido*-c** from addition of kryptofix-222. The shift of Li^+ resonance was also observed, further confirmed existence of Li^+ interaction. The smaller chemical shift change relative to $LiPF_6$ case was likely due to the more basic HMDS still coordinated to Li^+ in similar fashion as MeCN bonded to K^+ in **1-*nido*-K**.

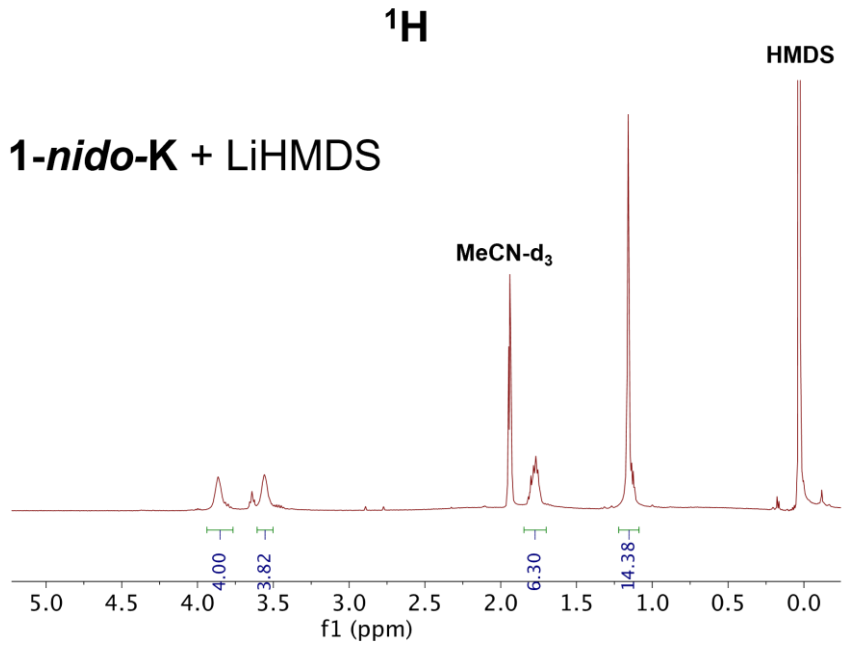

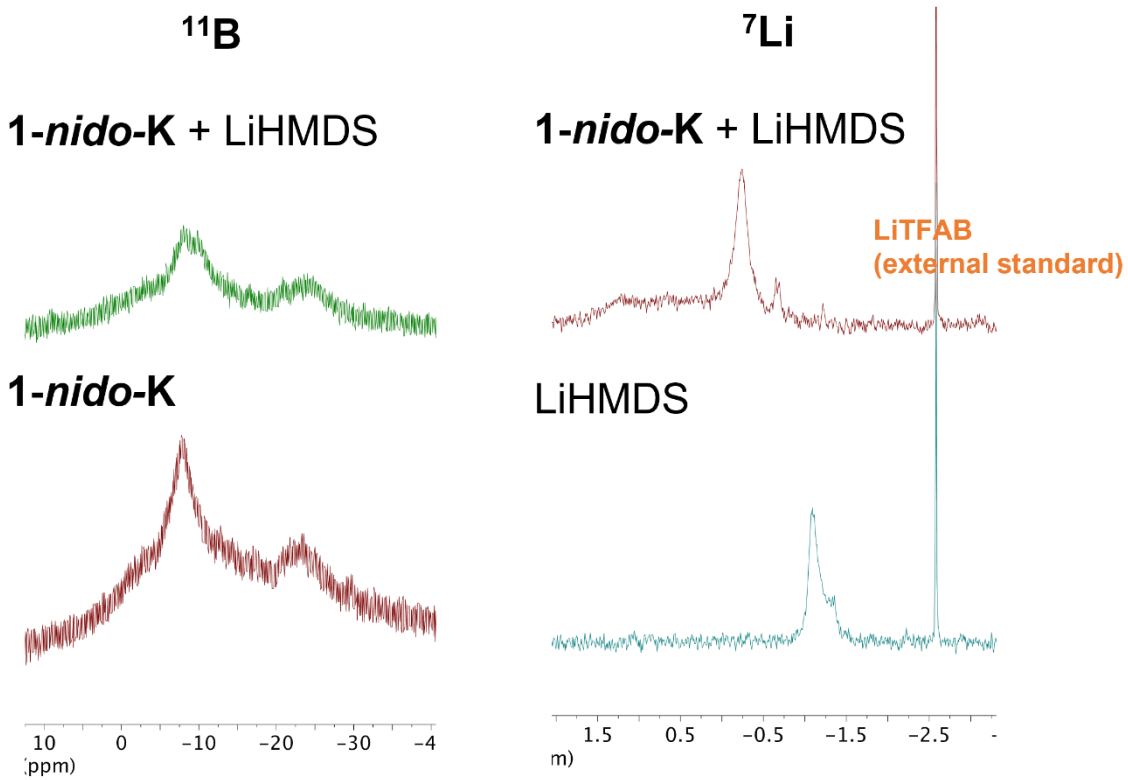

Figure 4.16. ^{1}H (400MHz), ^{11}B (128 MHz) and ^{7}Li (155 MHz) NMR spectra of **1-*nido*-K** with LiHMDS stacked ^{11}B NMR spectrum of **1-*nido*-K** and ^{7}Li NMR spectrum of LiHMDS

To further probe Li^+ interaction of **1-*nido***, we applied lithium naphthalenide[30] (in situ) to chemically reduce **1** in dry THF to produce its *nido*-form with Li^+ counter cations (**1-*nido*-Li**). **1-*nido*-Li** was soluble in THF, unlike **1-*nido*-K** that required MeCN to extract during purification. The shifted proton resonance in ^{1}H NMR spectroscopy and broad boron peaks in ^{11}B NMR spectra indicated formation of *nido*-Cb (**Figure 4.17**). Compared with **1-*nido*-K**, two crown ether proton signals in **1-*nido*-Li** were closer to each other than **1-*nido*-c** from addition of kryptofix-222. The broad Li resonance in ^{7}Li NMR spectroscopy was more upfield than free $LiPF_6$, suggesting the presence of a strong Li^+ interaction in **1-*nido*-Li**.

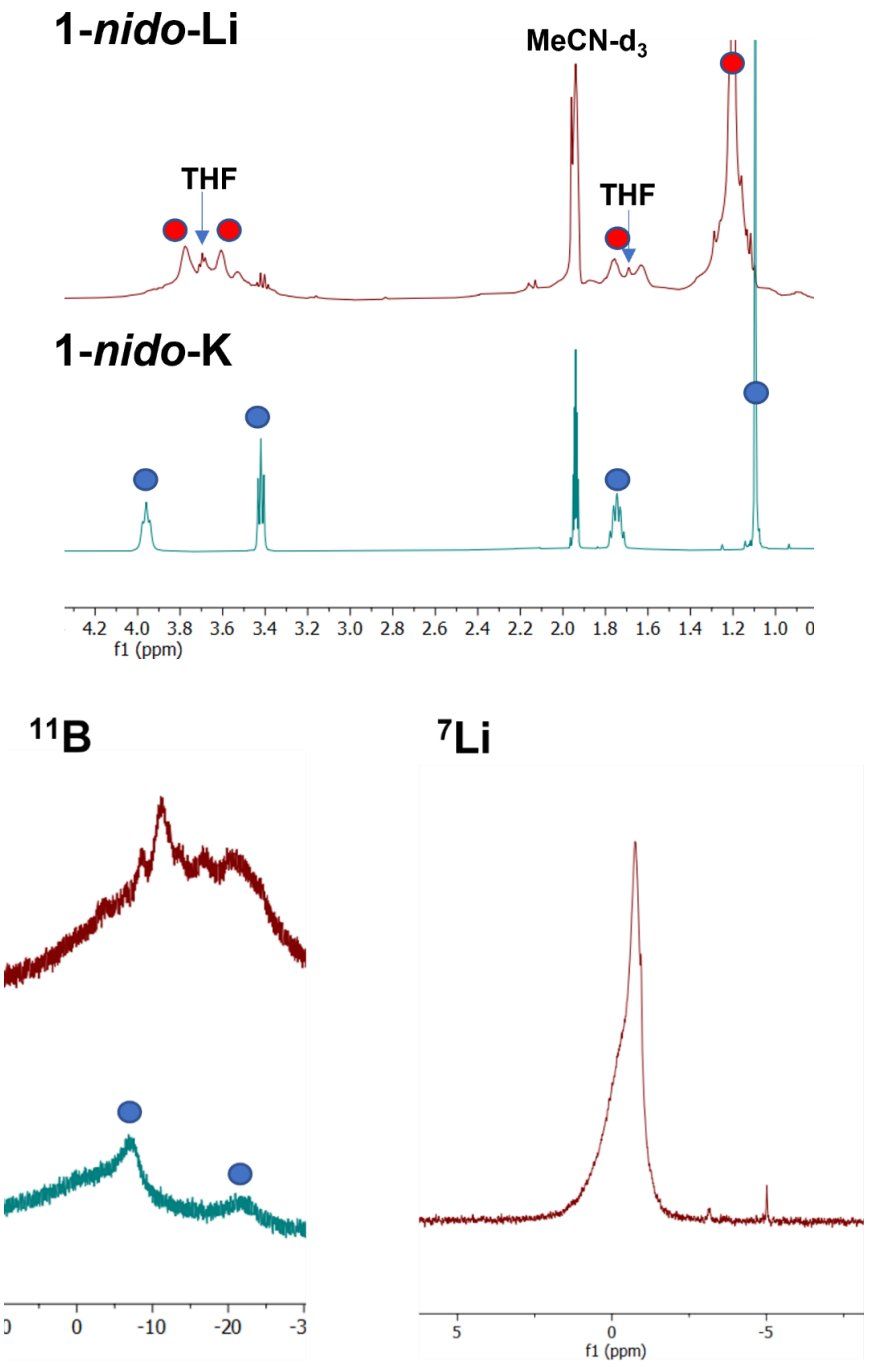

Figure 4.17. ^{1}H (400MHz), ^{11}B (128 MHz) and ^{7}Li (155 MHz) NMR spectra of **1-*nido*-Li** stacked with ^{1}H and ^{11}B NMR spectra of **1-*nido*-K.** Compounds peaks are labeled with blue and red dots.

For the second trail of this reduction reaction, the ^{7}Li NMR spectrum of **1-*nido*-Li** in d-THF showed the broad Li^{+} resonance at room temperature split into additional 4 peaks at -38°C, indicating multiple Li^{+} binding environment (**Figure 4.18**). Those addition Li^{+} peak at -38°C decreased as $FcPF_6$ was added to oxidized **1-*nido*-Li**, further confirming Li^{+} interaction with *nido*-Cb. The lithium naphthalenide in situ contained the mixture of mono reducing (green color, one Li per naphthalene) or di-reducing species (purple, two Li per naphthalene).[31] Therefore, equivalent of lithium naphthalenide was difficult to control, resulting the huge free Li^{+} peak in the ^{7}Li variable temperature NMR spectroscopic measurement.

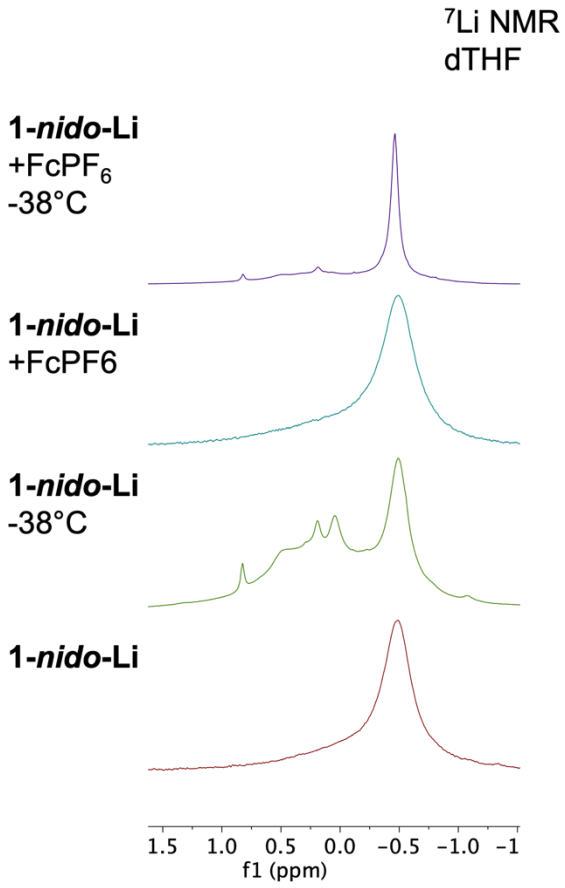

Figure 4.18. ^{7}Li NMR (155 MHz) spectra of **1-*nido*-Li** before and after addition of $FcPF_6$ at r.t. and -38°C in d-THF

The overall measurements showed **1** had weak Li^+ affinity and ***nido*-form** (**1-*nido*** and **1-*nido*-K**) showed strong Li^+ affinity with decent selectivity, indicating switching between *closo*- and *nido*- of **1** had capablility to achieve Li^+ capture/release cycle. These results on **1** provided important insights to improve Li^+ capture systems and demonstrated the potential of utilizing redox-active Cb based compounds to perform Li^+ extraction.

4.2.6 Li^+ measurements on *closo*- and *nido*-system of 2

With established methods for measuring Li^+ affinity and selectivity from **1**, we moved on to compound **2** to probe how two Cb cluster crown ether behave with Li^+. Due to the low solubility of **2** in MeCN-d_3, the NMR spectroscopic measurements were carried out in $CDCl_3$. The ^{7}Li NMR spectra of **2** with LiTFAB showed little crown/Li^+ interactions with increasing equivalents of LiTFAB (**Figure 4.19**). More precisely, the majority of LiTFAB remained unaffected and only very small amount of Li^+ interacted with **2**, unlike **1** where only one Li^+ resonance existed. This small Li^+ resonance shifted as equivalent of LiTFAB increased, confirming existence of crown/ Li^+ binding for the small amount of interacted Li^+. The NMR spectroscopic measurement suggested Li^+ affinity of **2** was weaker than **1** due to the additional electron withdrawing Cb cluster, which was beneficial for Li^+ release step like the study of **1** and **1-*nido*-K**.

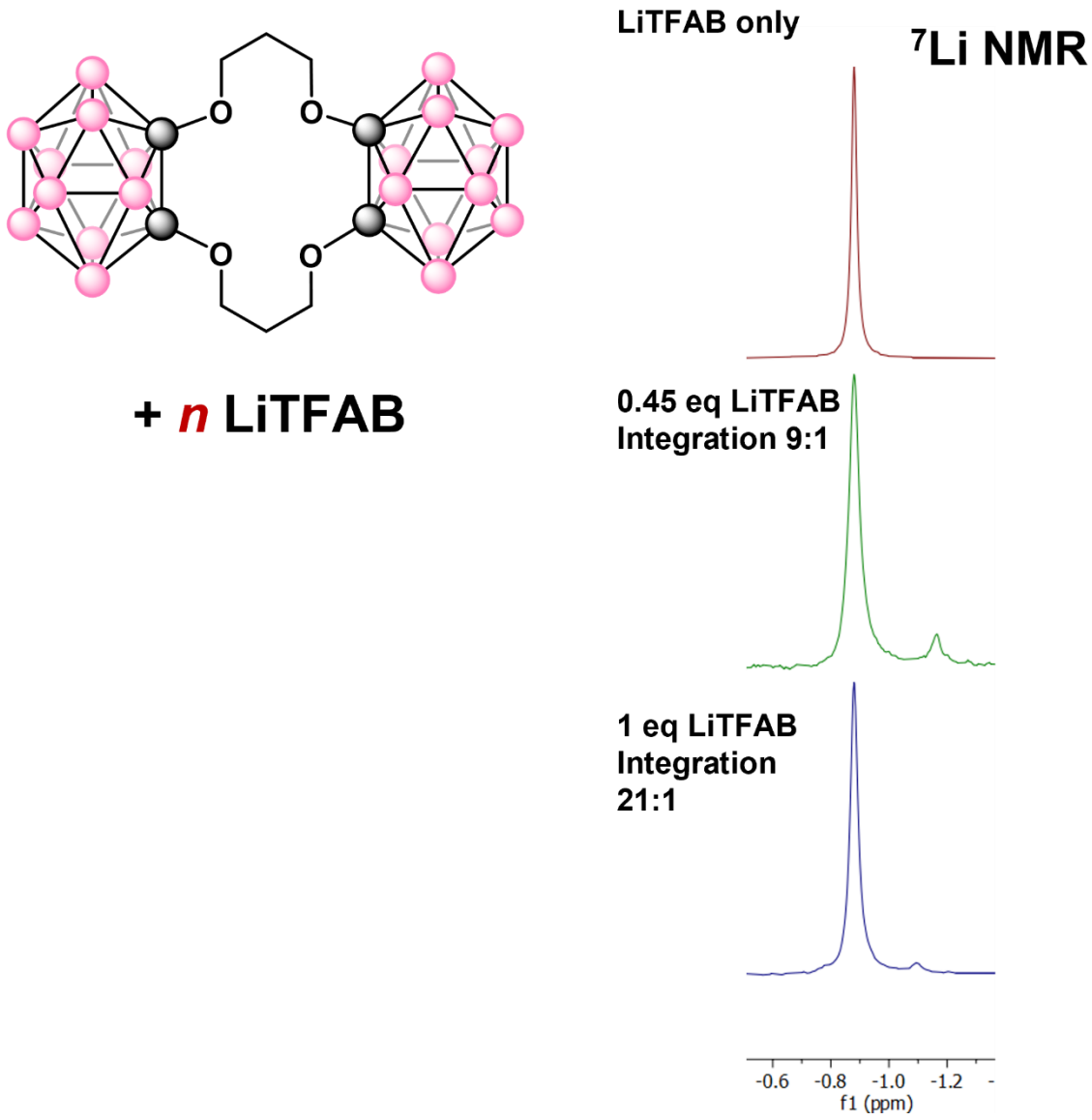

Figure 4.19. ^{7}Li NMR (155 MHz) spectra of **2** with different equivs of LiTFAB at r.t.

In contrast, **2-*nido*-K** appeared to have more interaction with LiTFAB as evidenced by the appearance of broad and shifted Li^+ resonances (**Figure 4.20**) in MeCN-d_3. The broadness of the Li^+ resonance was much more profound than **1-*nido*-K** in the same condition, indicating the existence of multiple Li^+ binding environments, which was further evidenced by the appearance of the second Li^+ peak as LiTFAB increased. The chemical shift changes of the

second Li^+ peak was remarkable ~ 1.5 ppm, which was much more than shift in NMR spectroscopic measurement of **1**, suggesting **2-*nido*** had a strong Li^+ affinity.

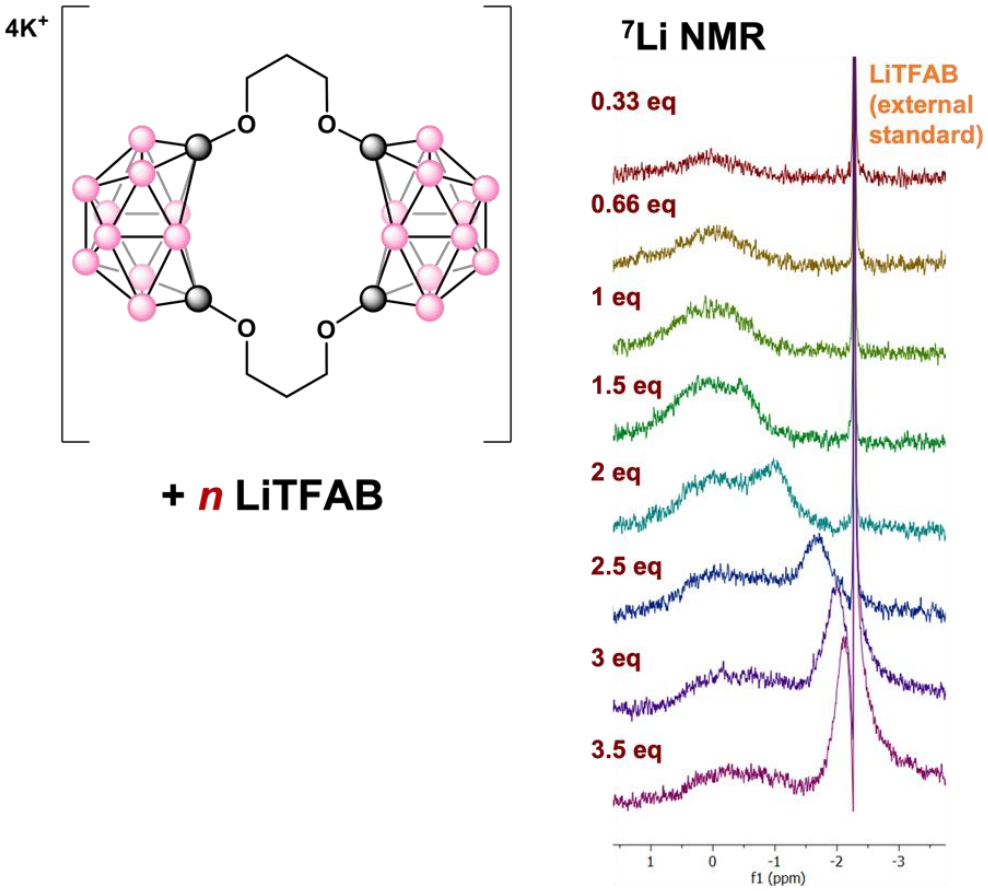

Figure 4.20. ^7Li NMR (155 MHz) spectra of **2-*nido*-K** with different equivalents of LiTFAB at r.t.

To study the selectivity of **2-*nido*-K**, 2.5 equiv of a mixture of LiTFAB, NaTFAB, and KTFAB were added to **2-*nido*-K** in MeCN-d_3 with LiTFAB, NaTFAB, and KTFAB in MeCN-d_3 as external standard. The broad Li^+ resonances remained and shifted in similar fashion as LiTFAB only case, whereas the in ^{23}Na NMR spectrum, only free Na^+ resonance was observed, suggesting **2-*nido*-K** was selective towards Li^+. These NMR spectroscopic measurements showed promising results of utilizing *closo*- and *nido*-form of **2** to achieve Li^+ capture/release

cycle and provided important insights for the optimization of Cb crown system to perform Li^+ extraction.

To reduce the competing affect from K^+ in **2-*nido*-K** for more accurate Li^+ affinity and selectivity measurements, electrochemical studies was also applied on **2**, similar as measurements of **1** that was discussed previously. The CV of **2** in presence of $LiPF_6$ in THF showed similar redox feature as **1** (**Figure 4.21**). After reduction wave where *nido*-from of **2** (**2-*nido***) was generated electrochemically, the oxidation event disappeared as equivalent of $LiPF_6$ increased, highlighting the presence of Li^+ interaction with **2-*nido***. The loss of the oxidation waves was similar to the CV of **1** with $LiPF_6$, which we proposed the similar rearrangement (**Figure 3.4**, Chapter 3) of *nido*-cage occurred after **2-*nido*** interacted with Li^+.

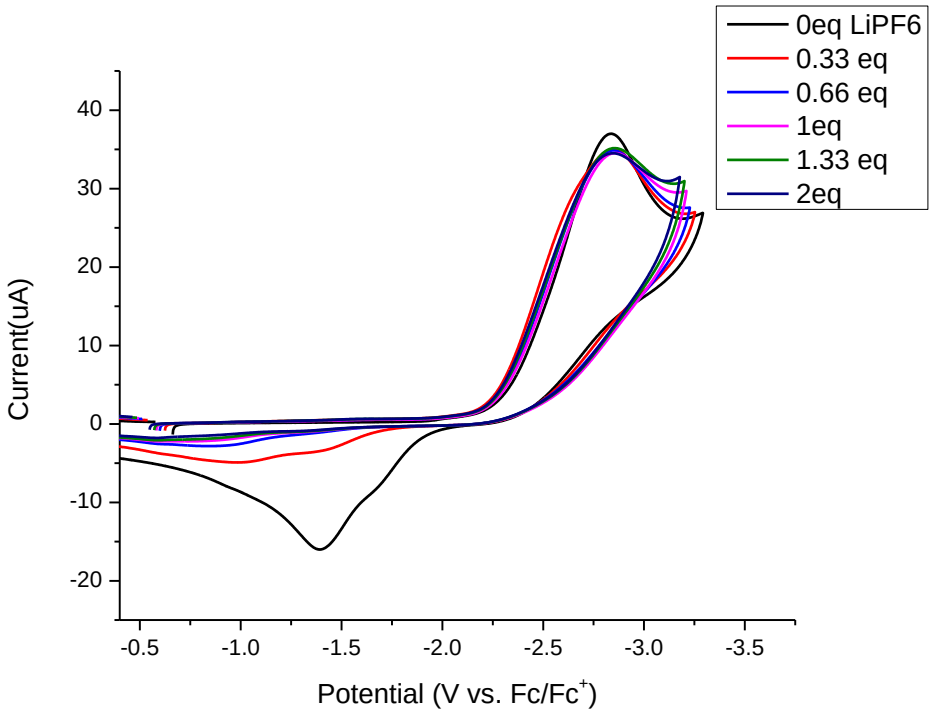

Figure 4.21. The cyclic voltammogram of **2** with different equivalent of $LiPF_6$ in THF at 100 mV/s scan rate. (Glassy carbon – WE, Pt wire – CE, Ag wire– RE)

Lithium naphthalenide (generated *in situ*) was also applied to chemically reduce **2** in dry THF in attempt to produce the *nido*-form with Li^+ counter cations (**2-*nido*-Li**). Following a MeCN wash, **2-*nido*-Li** had broad proton resonances that were often observed from crown/Li^+ interaction (**Figure 4.22a**). The broad boron peaks indicated the formation of the *nido*-Cb and minor impurities (**Figure 4.22b**). Two Li^+ resonances in **2-*nido*-Li** were almost identical as mixing LiTFAB with **2-*nido*-K**, suggesting the existence of a strong Li^+ interaction (**Figure 4.22c**). Due to the lithium naphthalenide in situ contained the mixture of mono reducing and di-reducing species,[31] different equivalent of Li was used to reduce **2** when the reaction was repeated. This resulted in the shift of the Li^+ resonance by ~0.8 ppm, which further confirmed existence of the Li^+ chelation.

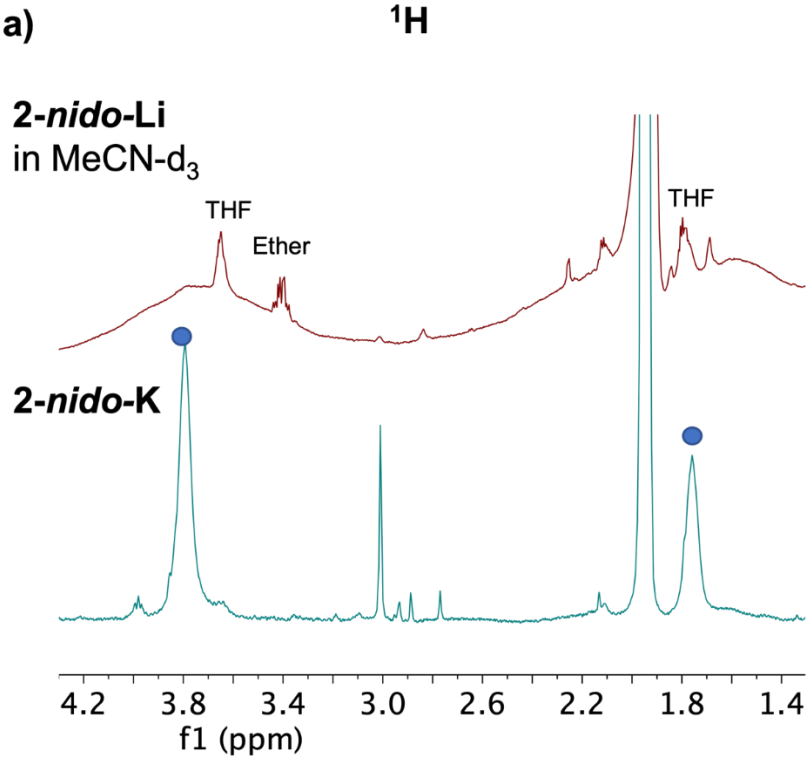

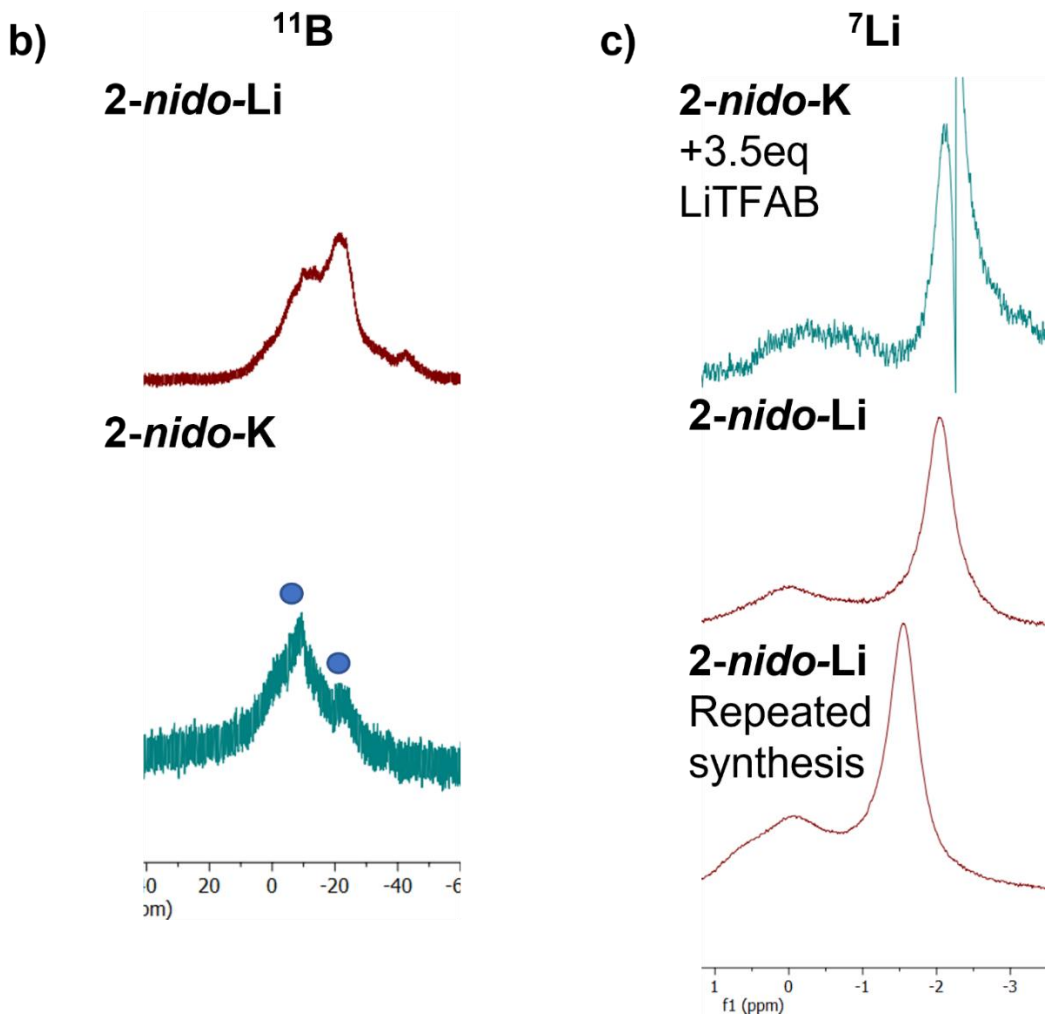

Figure 4.22. ^{1}H (400 MHz), ^{11}B (128 MHz) and ^{7}Li NMR (155 MHz) spectra of **2-*nido*-Li** stacked with NMR spectra of **2-*nido*-K** (labeled with blue dots). Note: proton resonances in **2-*nido*-Li** are broad

4.2.7 Li^+ measurements on other Cb crown ether 4, 5 and 8

Next, we turned our attention to the smaller silicon crown ether **4** and treated it with different equivalent of LiTFAB, which showed no changes in proton resonances (-Si(CH_3)$_2$). In the presence of the external standard LiTFAB in MeCN-d_3, additional Li^+ resonances were

not observed except after 0.33 equiv LiTFAB (**Figure 4.23**), suggesting **4** had a very poor Li^+ binding affinity with smaller crown ether chain.

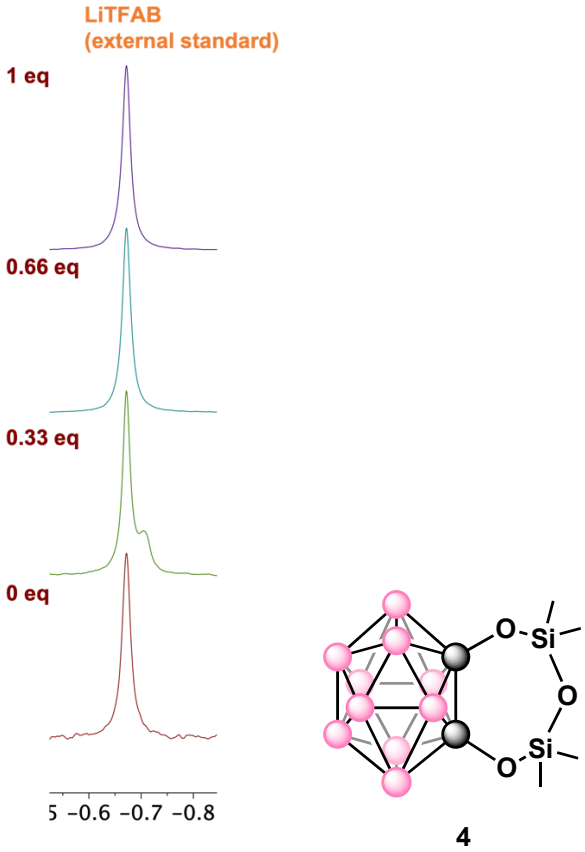

Figure 4.23. ^{7}Li NMR (155 MHz) spectra of 4 with different equivs of LiTFAB at r.t.

Next, we moved on to the Li^+ measurements of Cb 16-crown-4 (**5)** that contained carbon spacer. Due to the significant negative reduction potential (-3.15 V), the *nido*-form of **5** were challenging to access using chemical reduction. Therefore, the electrochemical measurements on the *closo*-form were carried out in the same condition as **2**. The CV of **5** in presence of $LiPF_6$ in THF also showed similar redox feature as **1** and **2** (**Figure 4.24**). The reoxidation event disappeared after addition of $LiPF_6$, suggesting the existence of Li^+ interaction with *nido*-form of **5**, which we proposed involving rearrangement of *nido*-cage.

However, due to the difficulty to chemically reduce **5**, the following NMR spectroscopic measurements on bind affinity and selectivity were unable to perform.

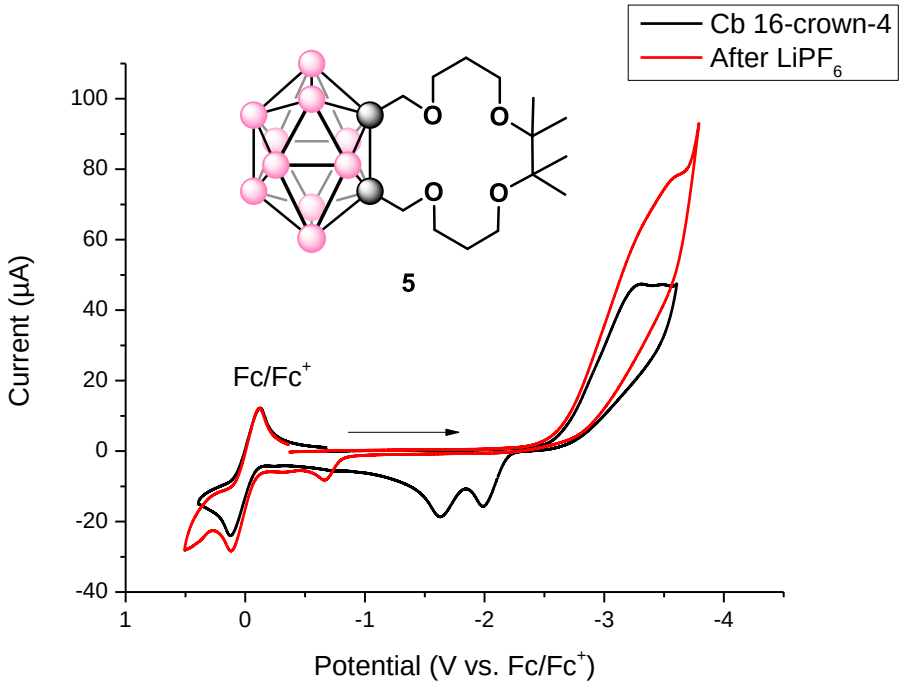

Figure 4.24. The cyclic voltammogram of **5** before and after addition of $LiPF_6$ in THF at 100 mV/s scan rate. (Glassy carbon – WE, Pt wire – CE, Ag wire– RE)

The CV of **8** (silicone crown with carbon spacer) in THF was slightly different before and after the addition of $LiPF_6$ (**Figure 4.25**). With the presence of $LiPF_6$, the possible small reduction event near -2.8 V completely disappeared. The increasing current near -2.8 V may originate from reaching solvent window instead of the Li^+ interaction. In addition, the chemical reduction of **8** failed to achieve its nido-form for NMR spectroscopic measurements. Therefore, **8** was not a good Cb crown candidate for Li^+ capture and release.

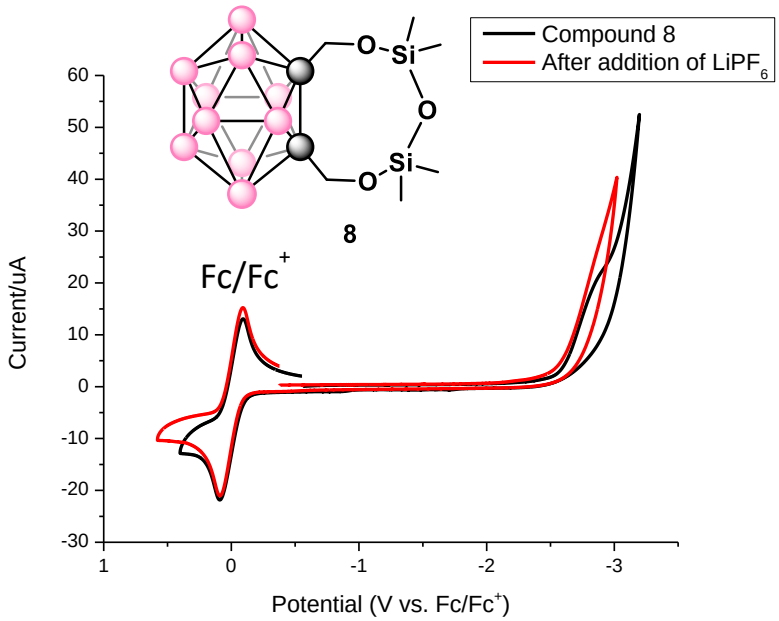

Figure 4.25. The cyclic voltammogram of **8** before and after addition of $LiPF_6$ in THF at 100 mV/s scan rate. (Glassy carbon – WE, Pt wire – CE, Ag wire– RE)

4.3 Summary

In summary, we described the NMR spectroscopic and electrochemical measurements for Li^+ binding affinity and selectivity of Cb crown ether species that was synthesized and characterized in Chapter 3. NMR spectroscopy method of constant Cb crown concentration with varying Li^+ equivalent offered initial fingerprint measurements on Li^+ interaction. The second NMR spectroscopy method involving fixed Li^+ concentration with increasing Cb crown equivalent provided more accurate Li^+ measurements by reducing the amount of free Li^+ gradually. Electrochemical measurements (mostly CV) allowed us to study Li^+ interaction with *nido*-Cb crowns without chemical reduction. The analytical measurement indicated all *closo*-Cb species had poor Li^+ binding affinity. On the other hand, the NMR spectroscopic studied showed both *nido*-Cb 14-crown-4 species demonstrated strong Li^+ affinity with decent

selectivity over Na^+. For this rare redox switchable scheme, we also developed electrochemical measurements to probe interaction between Li^+ and Cb crown ethers, further confirming their capability on Li^+ binding affinity and selectivity. These measurements from Cb crown ether compounds showed a great potential for utilizing Cb redox-switchable scheme for selective Li^+ capture and release, providing important insights on optimizing Cb systems to improve stability, effectiveness and selectivity of Li^+ binding. The future optimization of Cb crown ether includes attaching electron-withdrawing group (-C=O, $-NR_3^+$) on donor group and/or Cb cluster to shift reduction potential anodically for stability in water, followed by adjusting crown ether length to improve selectivity. The established analytical methods will be applied to measure new Cb compounds abilities to achieve selective Li^+ capture and release from seawater.

4.4 Experimental

General Considerations. All manipulations were carried out under an atmosphere of dry, oxygen-free N_2 within an MBraun glovebox (MBRAUN UNIlab Pro SP Eco equipped with a −35 °C freezer), or by standard Schlenk techniques. Pentane, hexanes, benzene, Et_2O, DCM, and THF (inhibitor-free) were dried and degassed on an MBraun Solvent Purification System and stored over activated 4 Å molecular sieves. All other solvents were degassed by freeze−pump−thaw and stored on activated 4 Å molecular sieves pubs.acs.org/IC Article prior to use. Celite and 4 Å molecular sieves were dried at 250 °C under dynamic vacuum (<0.1 Torr) for 24 h prior to use. Elemental analyses were recorded at the University of California, Berkeley, using a PerkinElmer 2400 Series II combustion analyzer. LiTFAB, LiCl, LiHMDS, $LiPF_6$, $NaPF_6$, KPF_6, 12-crown-4 and 18-crown-6 from Fisher Scientific or Sigma-Aldrich and

all were used with further purification (recrystallization). NaTFAB and KTFAB were prepared following previous reports.[32, 33] All other reagents were obtained from Sigma-Aldrich, Fisher Scientific, or VWR and used without further purification.

Spectroscopic Measurements. NMR spectra were obtained on an Agilent Technologies 400 MHz DD2, Varian Unity Inova 500 MHz, Bruker Avance NEO 500 MHz, or a Varian 600 MHz spectrometer, and referenced to residual solvent. Chemical shifts (δ) are recorded in ppm and the coupling constants are in Hz. J. Young airtight adaptors were used for air- and water-sensitive compounds. All measurements were carried out on recrystallized product. All stock solutions and dilutions were prepared by mass or volume.

Mass Spectrometry. Mass spectra were collected on a Shimadzu GC-2010 gas chromatograph coupled to a Shimadzu GCMS-QP2010 mass spectrometer. The instrument is equipped with a 30 m × 0.25 mm Agilent DB-1 column with a dimethylpolysiloxane stationary phase (0.25 μm). Helium was used as the carrier gas.

X-ray Crystallography. Data was collected on a Bruker KAPPA APEX II diffractometer equipped with an APEX II CCD detector using a TRIUMPH monochromator with a Mo Kα X-ray source (α = 0.71073 Å). The crystals were mounted on a cryoloop under Paratone-N oil, and all data were collected at 110 K using an Oxford nitrogen gas cryostream system. A hemisphere of data was collected using ω scans with 0.5° frame widths. Data collection and cell parameter determination were conducted using the SMART program. Integration of the data frames and final cell parameter refinement were carried out using SAINT software. Absorption correction of the data was carried out using SADABS. Structure determination was done using direct or Patterson methods and difference Fourier techniques. All hydrogen atom positions were idealized and rode on the atom of attachment. Structure

solution, refinement, graphics, and creation of publication materials were carried out using SHELXTL or OLEX.2

General procedure for lithium affinity studies (method 1 fixed [Li^+]): The stock solutions of Cb crown and Li^+ source (LiTFAB or $LiPF_6$) were prepared in 5 ml volumetric flask in MeCN-d_3. In different NMR tubes, the solution of Cb crown were mixed with different equivalent of Li^+ source solution and the total volume was made to 0.5 mL. A sealed capillary tube containing LiTFAB in MeCN-d_3 was then inserted into the NMR tube to serve as an external standard. ^1H, ^{11}B, ^{19}F and ^7Li NMR spectra were taken using different equivalents of LiTFAB at 25 °C.

General procedure for lithium affinity studies (method 2 fixed [Cb crown]): The stock solution of Cb crown and Li^+ source (LiTFAB or $LiPF_6$) were prepared in 5 ml volumetric flask in MeCN-d_3. In different NMR tubes, the solution of Li^+ source were mixed with different equivalent of Cb crown solution and the total volume was made to 0.5 mL. A sealed capillary tube containing LiCl in D_2O or LiTFAB in MeCN-d_3 was then inserted into the NMR tube to serve as an external standard. The reaction was monitored by ^1H, ^{11}B, ^{19}F and ^7Li NMR spectroscopy at 25 °C and -38.5°C.

General procedure for selectivity studies (method 1): The stock solution of Cb crown and metal cation mixture (LiTFAB, NaTFAB and KTFAB) were prepared in 5 ml volumetric flask in MeCN-d_3. In an NMR tube, the solution of Cb crown were mixed with 1 equivalent of metal cation mixture solution and the total volume was made to 0.5 mL. A sealed capillary containing LiTFAB, NaTFAB and KTFAB in MeCN-d_3 was then inserted into the NMR tube to serve as an external standard. ^1H, ^{11}B, ^{19}F, ^7Li and ^{23}Na NMR spectra were taken at 25°C.

General procedure for selectivity studies (method 2): The stock solution of Cb crown and metal cation mixture (LiTFAB, NaTFAB and KTFAB) were prepared in 5 ml volumetric flask in MeCN-d_3. In different NMR tubes, the solution of metal cation mixture were mixed with different equivalent of Cb crown solution and the total volume was made to 0.5 mL. A sealed capillary tube containing LiCl, NaCl and KCl in D_2O or LiTFAB, NaTFAB and KTFAB in MeCN-d_3 was then inserted into the NMR tube to serve as an external standard. The reaction was monitored by ^{1}H, ^{11}B, ^{19}F, ^{7}Li and ^{23}Na NMR spectroscopy at 25 °C and -38.5°C.

Electrochemical measurements. CV was performed on a CH Instruments 630E Electrochemical Analysis Potentiostat. The working electrode was a 3 mm diameter glassy carbon (CH Instruments) electrode and was cleaned prior to each experiment by sequentially polishing with a gradient of 1.0 μm, 0.3 μm, and 0.05 μm alumina (CH Instruments) on a cloth pad, followed by rinsing with distilled water and acetone. The $Ag/AgNO_3$ reference electrode was previous prepared in DMF solution and rinsed with DMF before the use for electrochemical experiments in DMF. The Ag wire pseudo-reference were rinsed with distilled water and acetone. The Pt wire counter electrodes were rinsed with distilled water and acetone and heated white-hot with a butane torch. All measurements were performed on recrystallized product and referenced to the Fc/Fc^+ redox couple unless otherwise stated.

4.5 Appendix

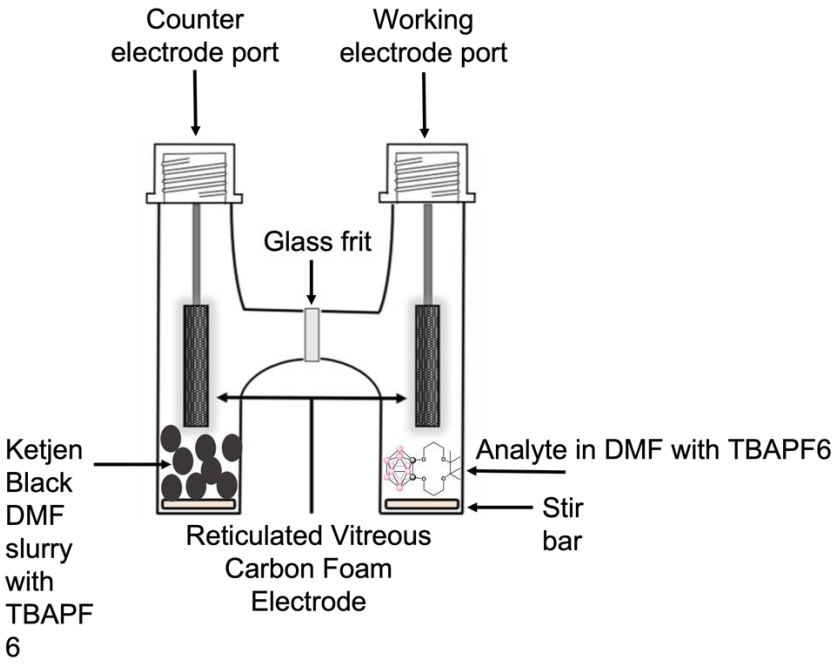

Figure 4.26. Bulk electrolysis set for electrochemical reduction of **1**

4.6 Reference

(1) Loganathan, P.; Naidu, G.; Vigneswaran, S. Mining valuable minerals from seawater: a critical review. *Environmental Science: Water Research & Technology* **2017**, *3* (1), 37-53, 10.1039/C6EW00268D.

(2) Battistel, A.; Palagonia, M. S.; Brogioli, D.; La Mantia, F.; Trocoli, R. Electrochemical Methods for Lithium Recovery: A Comprehensive and Critical Review. *Adv Mater* **2020**, *32* (23), e1905440, From NLM PubMed-not-MEDLINE.

(3) Yu, J.; Fang, D.; Zhang, H.; Leong, Z. Y.; Zhang, J.; Li, X.; Yang, H. Y. Ocean Mining: A Fluidic Electrochemical Route for Lithium Extraction from Seawater. *ACS Materials Letters* **2020**, *2* (12), 1662-1668.

(4) Dorn, F. M.; Ruiz Peyré, F. Lithium as a Strategic Resource: Geopolitics, Industrialization, and Mining in Argentina. *Journal of Latin American Geography* **2020**, *19* (4), 68-90.

(5) Nishihama, S.; Onishi, K.; Yoshizuka, K. Selective Recovery Process of Lithium from Seawater Using Integrated Ion Exchange Methods. *Solvent Extraction and Ion Exchange* **2011**, *29* (3), 421-431.

(6) Chitrakar, R.; Kanoh, H.; Miyai, Y.; Ooi, K. Recovery of Lithium from Seawater Using Manganese Oxide Adsorbent (H1.6Mn1.6O4) Derived from Li1.6Mn1.6O4. *Industrial & Engineering Chemistry Research* **2001**, *40* (9), 2054-2058.

(7) Keener, M.; Hunt, C.; Carroll, T. G.; Kampel, V.; Dobrovetsky, R.; Hayton, T. W.; Ménard, G. Redox-switchable carboranes for uranium capture and release. *Nature* **2020**, *577* (7792), 652-655.

(8) Keener, M.; Mattejat, M.; Zheng, S.-L.; Wu, G.; Hayton, T. W.; Ménard, G. Selective electrochemical capture and release of uranyl from aqueous alkali{,} lanthanide{,} and actinide mixtures using redox-switchable carboranes. *Chem. Sci.* **2022**, *13* (12), 3369-3374.

(9) Stubing, D. B.; Heng, S.; Abell, A. D. Crowned spiropyran fluoroionophores with a carboxyl moiety for the selective detection of lithium ions. *Organic and Biomolecular Chemistry* **2016**, *14* (15), 3752-3757.

(10) Li, E.; Kang, J.; Ye, P.; Zhang, W.; Cheng, F.; Yin, C. A prospective material for the highly selective extraction of lithium ions based on a photochromic crowned spirobenzopyran. *Journal of Materials Chemistry B* **2019**, *7* (6), 903-907.

(11) Pauric, A. D.; Jin, S.; Fuller, T. J.; Balogh, M. P.; Halalay, I. C.; Goward, G. R. NMR Determination of the Relative Binding Affinity of Crown Ethers for Manganese Cations in Aprotic Nonaqueous Lithium Electrolyte Solutions. *The Journal of Physical Chemistry C* **2016**, *120* (7), 3677-3683.

(12) Karkhaneei, E.; Zebrajadian, M. H.; Shamsipur, M. Lithium-7 NMR Study of Several Li+-Crown Ether Complexes in Binary Acetone-Nitrobenzene Mixtures. *Journal of inclusion phenomena and macrocyclic chemistry* **2001**, *40* (4), 309-312.

(13) Torrejos, R. E. C.; Nisola, G. M.; Song, H. S.; Limjuco, L. A.; Lawagon, C. P.; Parohinog, K. J.; Koo, S.; Han, J. W.; Chung, W. J. Design of lithium selective crown ethers: Synthesis, extraction and theoretical binding studies. *Chemical Engineering Journal* **2017**, *326*, 921-933.

(14) Harit, T.; Isaad, J.; Malek, F. Novel efficient functionalized tetrapyrazolic macrocycle for the selective extraction of lithium cations. *Tetrahedron* **2016**, *72* (18), 2227-2232.

(15) Sachleben, R. A.; Moyer, B. A. Ligand Design for Small Cations: The Li+/14-Crown-4 System. *ACS Symposium Series* **1999**, *716*, 114-132.

(16) Bartsch, R. A.; Czech, B. P.; Kang, S. I.; Stewart, L. E.; Walkowiak, W.; Charewicz, W. A.; Heo, G. S.; Son, B. High Lithium Selectivity in Competitive Alkali-Metal Solvent

Extraction by Lipophilic Crown Carboxylic Acids. *Journal of the American Chemical Society* **1985**, *107* (17), 4997-4998.

(17) C. Grossel, M.; G. Hamilton, D.; I. Fuller, J.; Millan-Barios, E. Alkali-metal binding properties of simple ferrocenyl- and ruthenocenyl-substituted aza-crown ethers. *Journal of the Chemical Society, Dalton Transactions* **1997**, (19), 3471-3477, 10.1039/A703597G.

(18) Scheibitz, M.; Winter, R. F.; Bolte, M.; Lerner, H. W.; Wagner, M. [1.1]Diborataferrocenophane: a highly efficient Li+ scavenger. *Angew Chem Int Ed Engl* **2003**, *42* (8), 924-927, From NLM PubMed-not-MEDLINE.

(19) Delgado, M.; Gustowski, D. A.; Yoo, H. K.; Gatto, V. J.; Gokel, G. W.; Echegoyen, L. Contrasting one- and two-cation binding behavior in syn- and anti-anthraquinone bibracchial podand (BiP) mono- and dianions assessed by cyclic voltammetry and electron paramagnetic resonance spectroscopy. *Journal of the American Chemical Society* **1988**, *110* (1), 119-124.

(20) Yao, Y.; Xing, F.; Zhu, S. Anthraquinone functionalized pseudocalixarene for high lithium loading and chromogenic ion-pair recognition in DMSO. *Inorganica Chimica Acta* **2021**, *525*, 120475.

(21) Kanamura, K.; Tamura, H.; Takehara, Z.-i. XPS analysis of a lithium surface immersed in propylene carbonate solution containing various salts. *Journal of Electroanalytical Chemistry* **1992**, *333* (1), 127-142.

(22) Spielvogel, K. D.; Stumme, N. C.; Fetrow, T. V.; Wang, L.; Luna, J. A.; Keith, J. M.; Shaw, S. K.; Daly, S. R. Quantifying Variations in Metal–Ligand Cooperative Binding

Strength with Cyclic Voltammetry and Redox-Active Ligands. *Inorganic Chemistry* **2022**, *61* (5), 2391-2401.

(23) Lewis, B. L.; Holt, P. D.; Taylor, S. W.; Wilhelm, S. W.; Trick, C. G.; Butler, A.; Luther, G. W. Voltammetric estimation of iron(III) thermodynamic stability constants for catecholate siderophores isolated from marine bacteria and cyanobacteria. *Marine Chemistry* **1995**, *50* (1), 179-188.

(24) Kulczynska, A.; Frost, T.; Margerum, L. D. Effect of PAMAM Dendrimer Size and pH on the Electrostatic Binding of Metal Complexes Using Cyclic Voltammetry. *Macromolecules* **2006**, *39* (21), 7372-7377.

(25) Johnston, D. H.; Thorp, H. H. Cyclic Voltammetry Studies of Polynucleotide Binding and Oxidation by Metal Complexes: Homogeneous Electron-Transfer Kinetics. *The Journal of Physical Chemistry* **1996**, *100* (32), 13837-13843.

(26) Karkhaneei, E.; Afkhami, A.; Shamsipur, M. NUCLEAR MAGNETIC RESONANCE STUDY OF LITHIUM ION COMPLEXES WITH SEVERAL CROWN ETHERS IN BINARY ACETONITRILE-NITROMETHANE MIXTURES. *Journal of Coordination Chemistry* **1996**, *39* (1), 33-42.

(27) Danil de Namor, A. F.; Ng, J. C. Y.; Llosa Tanco, M. A.; Salomon, M. Thermodynamics of Lithium−Crown Ether (12-crown-4 and 1-Benzyl-1-aza-12-crown-4) Interactions in Acetonitrile and Propylene Carbonate. The Anion Effect on the Coordination Process. *The Journal of Physical Chemistry* **1996**, *100* (34), 14485-14491.

(28) Kobiro, K. New class of lithium ion selective crown ethers with bulky decalin subunits. *Coordination Chemistry Reviews* **1996**, *148*, 135-149.

(29) Torrejos, R. E. C.; Nisola, G. M.; Song, H. S.; Limjuco, L. A.; Lawagon, C. P.; Parohinog, K. J.; Koo, S.; Han, J. W.; Chung, W.-J. Design of lithium selective crown ethers: Synthesis, extraction and theoretical binding studies. *Chemical Engineering Journal* **2017**, *326*, 921-933.

(30) Melero, C.; Guijarro, A.; Yus, M. Structural characterization and bonding properties of lithium naphthalene radical anion, [Li+(TMEDA)2][C10H8˙−], and lithium naphthalene dianion [(Li+TMEDA)2C10H8−2]. *Dalton Transactions* **2009**, (8), 1286-1289, 10.1039/B821119C.

(31) Tan, K. S.; Yazami, R. Physical-Chemical and Electrochemical Studies of the Lithium Naphthalenide Anolyte. *Electrochimica Acta* **2015**, *180*, 629-635.

(32) Nakajima, M.; Miyamoto, K.; Hirano, K.; Uchiyama, M. Diaryl-λ3-chloranes: Versatile Synthesis and Unique Reactivity as Aryl Cation Equivalent. *Journal of the American Chemical Society* **2019**, *141* (16), 6499-6503.

(33) Korshin, E. E.; Leitus, G.; Shimon, L. J. W.; Konstantinovski, L.; Milstein, D. Silanol-Based Pincer Pt(II) Complexes: Synthesis, Structure, and Unusual Reactivity. *Inorganic Chemistry* **2008**, *47* (16), 7177-7189.

Chapter 5

Utilization of the redox switchable ortho-carborane based crown ether on Cesium and group 2 metal capture/release

5.1 Introduction

With the previous published uranium work and promising results in Li^+ extraction, we extended our research interest with redox-switchable Cb scheme for other metal capture and release. Our new metal of interest are Cesium (Cs) and Strontium (Sr) for nuclear waste treatment purpose. To decrease emission of CO_2 for battling climate change, nuclear power has played an increasing role in energy production over the last several decades as an efficient, low-carbon energy source. The treatment of the resulting nuclear waste, however, is major concern for further establishment of nuclear power. Radioactive Cs and Sr are major contributors to radioactivity in the nuclear waste from fission with long lifetimes (>25 years). Due to their high solubility in water, if not handled properly, radioactive Cs and Sr can cause radiation risk to the environment as well as living organisms for centuries.[1-4] With increasing usage of nuclear energy, capturing Cs and Sr is an important step to properly treat nuclear waste for safer long-term storage. Analytical methods mentioned in Chapter 4 were commonly applied for metal binding affinity/selectivity measurements, and studies have shown crown ethers (18-crown-6 or bigger) contained complexes are popular candidates for capturing Cs and Sr.[5-7] The incorporation of additional coordination sites such as calixarene were often required to improve binding affinity and selectivity (**Figure 5.1**).[1, 6, 8] More specifically, for Cs^+ coordination with calixarene based crown ether, the oxygen atoms in crown ether provides ion dipole interaction and calixarene offers additional π interaction.

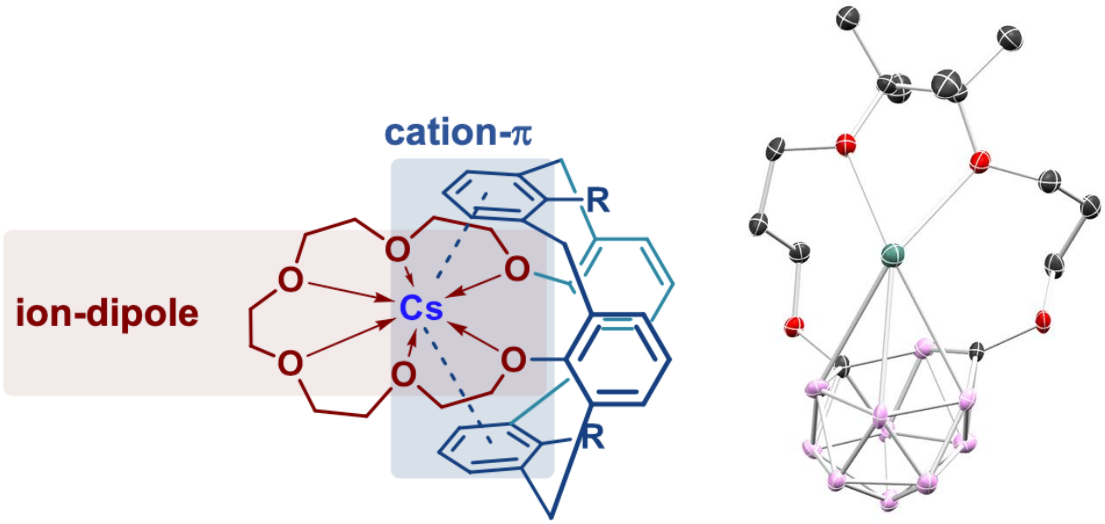

Figure 5.1. Calixarene attached crown ether Cs Selective Chelators (left). Solid-state structure of **1-*nido*-K** (right)

From our previous Cb crown study mentioned in Chapter 3, the solid-state structure of **1-*nido*-K** showed that *nido*-Cb cluster played a similar role as calixarene by serving as a second cationic coordination site in addition to ion-dipole interaction from 14-crown-4 for binding K^+ (**Figure 5.1**). We began to test the capability of using Cb crown scheme for capture/release of Cs and Sr, with detailed preliminary results presented in this chapter.

5.2 Preliminary results and discussion

5.2.1. Attempt Cs capture with Cb crown ethers

No reaction occurred after mixing $CsCO_3$ or $CsNO_3$ with **1-*nido*-K** in MeCN, as evidenced by ^1H and ^{11}B NMR spectroscopy, indicating the size of 14-crown-4 in **1-*nido*-K** was small for Cs^+ capture. Next, we investigated compound **3** featuring larger 18-crown-6 donor group. The ^1H NMR spectrum of **3** with addition of $CsNO_3$ showed very slight shift on

proton resonances (**Figure 5.2**) due to the electron withdrawing Cb cluster. The most upfield peak, which represented the crown ether proton closest to Cb cluster, changed the most at ~0.006 ppm, which was almost negligible but may suggesting a very small interaction between **3** and Cs^+. No changes were observed in the ^{11}B NMR spectrum before and after addition of $CsNO_3$.

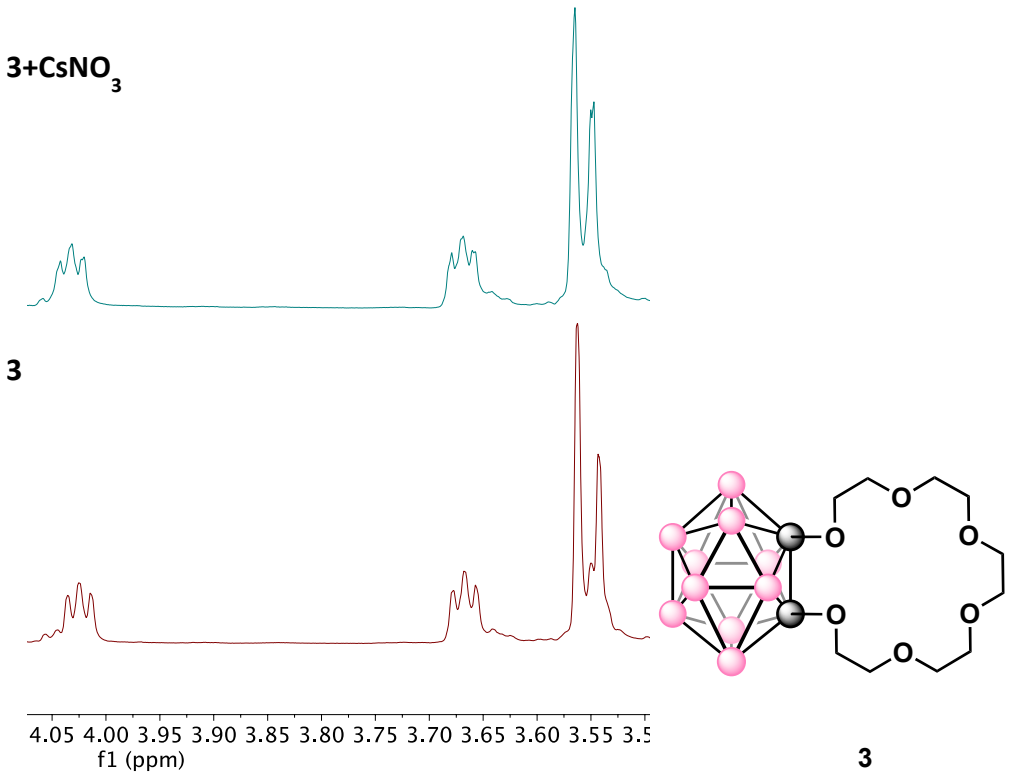

Figure 5.2. ^1H NMR (400 MHz) spectra of **3** before and after addition of $CsNO_3$

For chemically reduced form **3-*nido*-K** (Chapter 3), addition of $CsNO_3$ or CsF resulted in no change of the proton resonances and boron peaks in ^1H and ^{11}B NMR spectroscopy, suggesting 18-crown-6 pocket size at *nido*-form were more selective towards smaller K^+. Inspired by the solid-state structure of **1-*nido*-**K, we proposed two out of six oxygen in **3-*nido*-**

K did not participate ion dipole interaction, highlighting the importance of extend the size of crown ether (integrating spacer group described in Chapter 3) and utilize all oxygens.

Due to the difficulty on synthesis and purification of **6** featuring 20-crown-6 (carbon spacer) mentioned in Chapter 3, there was not enough material for chemical reduction to test Cs capture. The limited amount of material was used for electrochemical Cs capture cyclic voltammetry (CV) study. In presence of the $CsNO_3$, both waves from quasi-reversible reduction event shifted anodically ~0.15 V, suggesting a strong thermodynamic preference for Cs^+ binding.[9, 10]

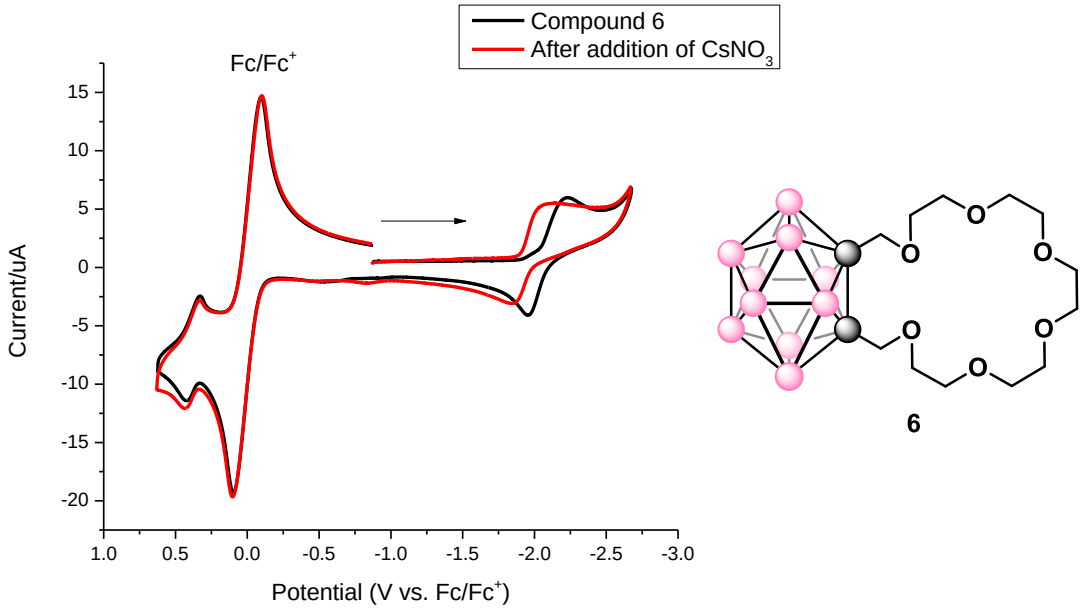

Figure 5.3. The cyclic voltammogram of **6** before and after addition of $CsNO_3$ in THF at 100 mV/s scan rate

5.2.2. Group 2 metal interaction with *nido*-Cb crown ethers

Two group 1 metal cations are required to balance the 2- charge in *Nido*-Cb, which can lead to different Cs binding interaction as shown in solid-state structure of **1-*nido*-K** with two

K^+. Ideally, 2+ charge in group 2 Sr^{2+} would promote 1:1 binding mode with *Nido*-Cb like other reported crown/Li^+ interaction. Likely due to the large Sr^{2+} size, the ^{1}H NMR spectrum showed no reactivity between $SrCl_2$ and **1-*nido*-K**. To further understand interaction between *nido*-Cb crowns and group 2 metal, Mg^{2+}, Ca^{2+} and Ba^{2+} compounds were added to **1-*nido*-K**. Addition of $Mg(OTf)_2$ or $CaCl_2$ resulted formation to **1-*nido*-b** described in Chapter 3 immediately and full conversion was finished after 2 days at room temperature, indicated by ^{1}H and ^{11}B NMR spectroscopy, showing the smaller metal cation had a stronger interaction with **1-*nido*-K**.

For 4- charge **2-*nido*-K**, the addition of $Mg(OTf)_2$ or $Ca(OTf)_2$ cleanly generated a new symmetric di-Cb crown species (**2-d**) with coalesced crown ether proton resonance (**Figure 5.4**). The broad boron resonances in **2-*nido*-K** became sharper, indicating a rearrangement was likely took place. Reaction with larger $Ba(OTf)_2$ resulted the same boron resonance with minor byproducts; however, more coupling was observed for the upfield crown proton resonance, indicating asymmetric proton chemical environments, which we proposed due to the large Ba^{2+} was coordinated out of the crown ether plane.

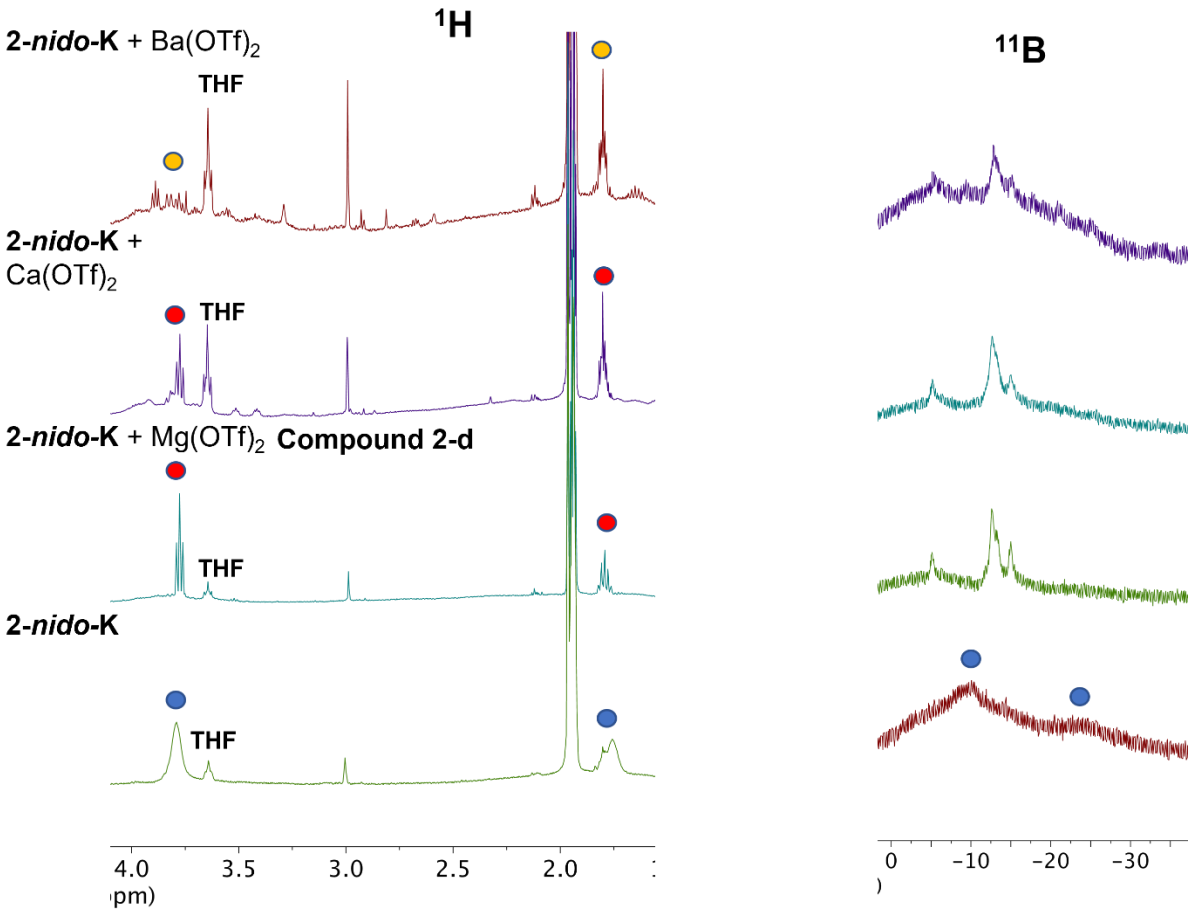

Figure 5.4. ^{1}H (400 MHz) and ^{11}B (128 MHz) NMR spectra of **2-*nido*-K** with group 2 triflate. **2-*nido*-K** peak labeled with blue dots and new compound **2-d** labeled with red dots. Mixture generated with $Ba(OTf)_2$ labeled with orange dots

Addition of $FcPF_6$ to **2-d** caused no change in boron resonances and formation of Fc was not observed in ^{1}H NMR spectroscopy, suggesting **2-d** was most likely the oxidized product after chemical rearrangement of **2-*nido*-K**. Currently, it was unclear how Mg^{2+} interacted before and after $FcPF_6$. To probe the interaction of 4+ charge metal Ti^{4+} with the di-*nido*-Cb system in **2-*nido*-K**, we added 1 equiv $TiCl_4$ and resulted in the oxidation on **2-*nido*-K** as **2** formed as the major product, indicated by ^{1}H and ^{11}B NMR spectroscopy.

5.3 Summary and future work

Our preliminary NMR studies showed little to no Cs or Sr interaction with the Cb crown for both 14-crown-4 and 18-crown-6 cases. Both Cb 14-crown-4 compounds demonstrated reactivity with smaller group 2 metal cations; however, these interactions promoted rearrangements or oxidizing *nido*-Cb in addition to metal coordination. These initial results provided us insights on optimizing Cb compounds for Cs and Sr capture in following directions. The first direction is increasing the crown ether donor length to improve Cs/Sr selectivity at *nido*-form. The second goal is to shift reduction potential anodically to avoid unwanted side reaction. Attaching a proper electron-withdrawing spacer group can achieve both purposes, e.g., -PhPO-. Further modification may be required depending on the results from the new Cb crown compound.

5.4 Experimental

General Considerations. All manipulations were carried out under an atmosphere of dry, oxygen-free N_2 within an MBraun glovebox (MBRAUN UNIlab Pro SP Eco equipped with a −35 °C freezer), or by standard Schlenk techniques. Pentane, hexanes, benzene, Et_2O, DCM, and THF (inhibitor-free) were dried and degassed on an MBraun Solvent Purification System and stored over activated 4 Å molecular sieves. All other solvents were degassed by freeze−pump−thaw and stored on activated 4 Å molecular sieves pubs.acs.org/IC Article prior to use. Celite and 4 Å molecular sieves were dried at 250 °C under dynamic vacuum (<0.1 Torr) for 24 h prior to use. Elemental analyses were recorded at the University of California,

Berkeley, using a PerkinElmer 2400 Series II combustion analyzer. All reagents were obtained from Sigma-Aldrich, Fisher Scientific, or VWR and used without further purification.

Spectroscopic Measurements. NMR spectra were obtained on an Agilent Technologies 400 MHz DD2, Varian Unity Inova 500 MHz, Bruker Avance NEO 500 MHz, or a Varian 600 MHz spectrometer, and referenced to residual solvent. Chemical shifts (δ) are recorded in ppm and the coupling constants are in Hz. J. Young airtight adaptors were used for air- and water-sensitive compounds. All measurements were carried out on recrystallized product. All stock solutions and dilutions were prepared by mass or volume.

Electrochemical measurements. CV was performed on a CH Instruments 630E Electrochemical Analysis Potentiostat. The working electrode was a 3 mm diameter glassy carbon (CH Instruments) electrode and was cleaned prior to each experiment by sequentially polishing with a gradient of 1.0 μm, 0.3 μm, and 0.05 μm alumina (CH Instruments) on a cloth pad, followed by rinsing with distilled water and acetone. The Ag wire pseudo-reference were rinsed with distilled water and acetone. The Pt wire counter electrodes were rinsed with distilled water and acetone and heated white-hot with a butane torch. All measurements were performed on recrystallized product and referenced to the Fc/Fc^{+} redox couple unless otherwise stated.

General procedure for mixing metal salt with Cb crown ether: In an NMR tube, the *nido*-Cb crown were dissolved in MeCN-d_3 and different equivalents of metal salts in MeCN-d_3 solution was added. ^{1}H and ^{11}B NMR spectra were taken at 25 °C.

5.5 Reference

(1) Wang, J.; Zhuang, S. Cesium separation from radioactive waste by extraction and adsorption based on crown ethers and calixarenes. *Nuclear Engineering and Technology* **2020**, *52* (2), 328-336.

(2) Kwon, S.; Kim, C.; Han, E.; Lee, H.; Cho, H. S.; Choi, M. Relationship between zeolite structure and capture capability for radioactive cesium and strontium. *Journal of Hazardous Materials* **2021**, *408*, 124419.

(3) Eun, S.; Ryu, J.; Kim, H.; Hong, H.-J.; Kim, S. Simultaneous removal of radioactive cesium and strontium from seawater using a highly efficient Prussian blue-embedded alginate aerogel. *Journal of Environmental Management* **2021**, *297*, 113389.

(4) Yang, H.-M.; Park, C. W.; Kim, I.; Yoon, I.-H.; Sihn, Y. Sulfur-modified chabazite as a low-cost ion exchanger for the highly selective and simultaneous removal of cesium and strontium. *Applied Surface Science* **2021**, *536*, 147776.

(5) Huang, D.; Zheng, H.; Liu, Z.; Bao, A.; Li, B. Extraction of rubidium and cesium from brine solutions using a room temperature ionic liquid system containing 18-crown-6. *Polish Journal of Chemical Technology* **2018**, *20* (2), 40-46.

(6) Liu, C.; Zhang, D.; Zhao, L.; Zhang, P.; Lu, X.; He, S. Extraction property of p-tert-butylsulfonylcalix[4]arene possessing irradiation stability towards cesium(I) and strontium(II). *Applied Sciences (Switzerland)* **2016**, *6* (8).

(7) Xu, C.; Wang, J.; Chen, J. Solvent Extraction of Strontium and Cesium: A Review of Recent Progress. *Solvent Extraction and Ion Exchange* **2012**, *30* (6), 623-650.

(8) Dozol, J. F.; Dozol, M.; Macias, R. M. Extraction of Strontium and Cesium by Dicarbollides, Crown Ethers and Functionalized Calixarenes. *Journal of inclusion phenomena and macrocyclic chemistry* **2000**, *38* (1), 1-22.

(9) Delgado, M.; Gustowski, D. A.; Yoo, H. K.; Gatto, V. J.; Gokel, G. W.; Echegoyen, L. Contrasting one- and two-cation binding behavior in syn- and anti-anthraquinone bibracchial podand (BiP) mono- and dianions assessed by cyclic voltammetry and electron paramagnetic resonance spectroscopy. *Journal of the American Chemical Society* **1988**, *110* (1), 119-124.

(10) Yao, Y.; Xing, F.; Zhu, S. Anthraquinone functionalized pseudocalixarene for high lithium loading and chromogenic ion-pair recognition in DMSO. *Inorganica Chimica Acta* **2021**, *525*, 120475.